Natuurlijke convectie in klassieke koellichamen en open-cellig metaalschuim

Natural Convection in Classical Heat Sinks and Open-Cell Metal Foam

Sven De Schampheleire

Promotor: prof. dr. ir. M. De Paepe
Proefschrift ingediend tot het behalen van de graad van
Doctor in de ingenieurswetenschappen: werktuigkunde-elektrotechniek

UNIVERSITEIT
GENT

Vakgroep Mechanica van Stroming, Warmte en Verbranding
Voorzitter: prof. dr. ir. J. Vierendeels
Faculteit Ingenieurswetenschappen en Architectuur
Academiejaar 2017 - 2018

ISBN 978-94-6355-048-2
NUR 910
Wettelijk depot: D/2017/10.500/83

Supervisors

Prof. Michel De Paepe

Members of the examination board

Chairmain:

Prof. Hendrik Van Landeghem - UGent

Secretary:

Prof. Jan Vierendeels - UGent

Reading committee:

Prof. Tom De Mulder - UGent

Prof. Tunde Bello-Ochende - University of Cape Town, South Africa

Prof. Peter De Jaeger - University College Dublin, Ireland

Dr. Henk Huisseune - Novy, Kuurne

Prof. Gilbert De Mey - UGent

Other members:

Prof. Michel De Paepe - UGent

Dankwoord

"What matters in life is not what happens to you but what you remember and how you remember it." **Gabriel García Márquez**

Ik heb altijd getwijfeld aan het nut van een doctoraat: een doctoraat laat je vooral twijfelen over jezelf. Bedankt aan zij die niet of minder aan mij getwijfeld hebben.

Zonder de hulp van de volgende mensen had ik dit doctoraat nooit tot een goed einde kunnen brengen:

. . . Aan prof. Michel De Paepe voor alle hulp en financiële mogelijkheden

. . . Aan Robert Gilles, Patrick De Pue, Hugo Bellinck, Frederik Martens en Yves Maenhout voor al hun technische, wetenschappelijke en praktische ondersteuning om dit werk mogelijk te maken. Ook bedankt voor de verschillende gesprekken die we gehad hebben.

. . . Aan Griet, Annie en Patricia voor al hun vriendschap en begrip (en uiteraard ook voor de administratieve hulp)

. . . Aan Bernd Ameel voor al het werk bij het nalezen van mijn papers en het bekijken van mijn wetenschappelijk werk, en zoeken naar nieuwe pistes en ideëen.

. . . Aan Peter De Jaeger om zoveel tijd in me te steken om me te leren hoe ik een beter onderzoeker wordt. Bedankt voor de vele avonden bij jou thuis.

. . . Aan mijn andere collega's om onze problemen mee te delen; bedankt Steven, Marnix, Henk, Özer, Hugo.

. . . Aan Veerle en Inge om me het gevoel te geven dat er nog andere mensen zijn in deze wereld.

. . . Aan de 3 katten in mijn leven voor hun warmte: Rune, Fluweel en Poenkie.

. . . Aan mijn ouders om me het gevoel te geven dat ik welkom ben, ook al was het niet altijd gemakkelijk.

. . . Aan Niels en Glen om vele Nederlandse teksten na te lezen en te luisteren naar mijn wetenschappelijke zever. Door dingen aan jullie te vertellen voelt het alsof het niet meer van mij alleen is, en dat lucht vaak op.

. . . Aan Kathleen, omdat jij de rijkste en meest warme persoonlijkheid hebt die ik ooit al heb mogen leren kennen. Zonder jou zou er geen doctoraat geweest zijn.

Gent, oktober 2017

"Ze loodst me langs een slapend dier - ik kan niet uitmaken wat voor dier het is, het ligt helemaal opgerold, het heeft een pels - en overal lopen mensen gearmd. Ze zegt: 'Ik denk dat alles goed komt.' 'Waarmee?' 'Met u.' " **Peter Verhelst**

Table of Contents

List of Figures

List of Tables

Nomenclature

Symbols

A	area	m^2
A_0	middle strut cross-sectional surface area	m^2
a_1	strut cross-section shape variation factor	-
a_2	strut axial cross-section variation factor	-
Bi	Biot number	-
c_M	molecular specific heat	J/Kmole
c_p	specific heat	J/kgK
d	(fin) diameter	m
d_1	large cell diameter	m
d_2	small cell diameter	m
d_c	mean cell diameter	m
d_h	hydraulic diameter	m
d_p	pore diameter	m
d_s	strut diameter	m
Da	Darcy number	-
E	radiant energy	J
E	simulation error	-
E_b	total emissivity power	W
$\mathcal{F}$	normalized axial strut area variation	m

f	friction factor	-
F_s	Safety factor	-
$F_{i,j}$	view factor	-
$\vec{g}$	gravitational acceleration	m/s^2
G_i	irradiation	-
GCI	Grid Convergence Index	-
Gr	Grashof number	-
H	(fin) height	m
h	heat transfer coefficient	W/m^{2}K
H_w	Heywood circularity factor	-
$\vec{\vec{I}}$	Identity tensor	-
I	current	A
I'	turbulence intensity	-
$\vec{J}$	flux vector	-
j	Colburn-j factor	-
J_i	radiosity	-
K	hydraulic flow resistance	-
k	thermal conductivity	W/mK
k_B	Boltzmann constant (k_B = $1.3806488 \times 10^{-23}$)	J/K
$\vec{l}_n$	translation vector	-
L	length	m
l	mean strut length	m
l_1	length short strut	m
l_2	length long strut	m
L_c	characteristic length	m
l_c	length scale	m
l_G	global length scale	m

l_n	natural length scale	m
l_μ	microscopic length scale	m
$\dot{m}$	mass flow rate	kg/s
m	mass	kg
M_w	molecular weight of the gas	kg/kmol
$\vec{n}$	normal vector	-
Nu	Nusselt number	-
P	power	W
P	pressure	Pa
p	order of convergence	-
p	parameter	-
p_{op}	operating pressure	Pa
Pr	Prandtl number	-
Q	heat transfer rate	W
q	heat flux	W/m^2 or W/m^3
$\vec{r}$	local position vector	-
$m(\vec{r})$	weighing function	1/m^3
R	universal gas constant (R = 8.3144621)	J/Kmol
r	constant grid refinement ratio	-
R_s	sphericity	-
R_{ij}	Reynolds stress term	-
R_{th}	thermal resistance	m^{2}K/W
Re	Reynolds number	-
S	Source term	-
Sp	Sparrow number	-
T	temperature	K
t	time	s

$\vec{U}$	large-scaled velocity	m/s
$\vec{u}$	small-scaled velocity	m/s
U	superficial velocity magnitude	m/s
U	thermal transmittance	W/K
u	energy density	J/m^3
$\dot{V}$	volumetric flow rate	m^3/s
$\vec{v}$	continuum-scaled velocity	m/s
V	voltage	V
V	volume	m^3
W	width	m
$\vec{x}_c$	measurement window centroid	-
x, y, z	Cartesian coordinates	-
$\vec{y}$	relative position vector	-

Greek symbols

α	spectral absorption component	-
α	thermal diffusivity	m^2/s
β	inertial loss factor	1/m
β	thermal expansion coefficient	1/K
Δ	difference	-
δ	uncertainty	-
δ_T	thermal boundary layer thickness	-
δ_μ	viscous boundary layer thickness	-
η	(fin) efficiency	-
η	Geometry factor	-
η_t	Kolmogorov scale	m

ε	radiative emissivity	-
Γ	general transport property	-
γ	phase distribution function	-
κ	permeability	m^2
κ_t	turbulence wave number ($\kappa_t = \frac{2\pi}{\lambda_t}$)	1/m
λ	wavelength	-
λ_c	small-scaled characteristic length	-
λ_t	turbulence wave length	m
λ_{mfp}	mean free path length	m
μ	dynamic viscosity	Pa.s
ν	kinematic viscosity	m^2/s
ν_t	turbulent eddy viscosity	m^2/s
Ω	foam domain	-
Φ	arbitrary kinematic quantity	-
ϕ	porosity	-
Ψ	arbitrary large-scaled quantity	-
ψ	arbitrary small-scaled quantity	-
φ	angular coordinate	rad
ρ	mass density	kg/m^3
ρ	spectral reflection component	-
ρ_r	relative density	-
$\vec{\vec{\sigma}}$	shear stress	Pa
σ_0	surface-to-volume ratio	m^2/m^3
σ_{SB}	Stefan-Boltzmann constant ($\sigma_{SB} = 5.670373 \times 10^{-8}$)	W/m^2K^4
τ	spectral transmission component	-
τ	tortuosity	-
τ_c	characteristic time	s

τ_r	relaxation time	s
τ_{mfp}	mean free path time	s
ξ	dimensionless axial strut position	-
ζ	loss coefficient	-

Sub- and superscripts

$node$	node
air	air
$bulk$	bulk characteristic
c	contact
CD	computational domain
cm	center of mass
$conv$	convective
cs	case-to-sink
d	dispersion
d_s	strut diameter
(e)	excessive
e	effective
eff	effective
end	boundary confining the foam domain
env	environment
f	fluid
fan	fan
fin	fin
$foam$	foam
fs	fluid-solid interface

H	heat
∞	outside boundary layer
i	intrinsic
in	inlet, input
ins	insulation
jc	junction-to-case
jmp	jump condition
l	liquid
l_c	characteristic length
$loss$	loss
M	molar
m	measurement window
max	maximum
min	minimum
o	other side
out	outlet, output
p	pressure drag
r	relative
rad	radiative
$**$	normalised
σ	solid
s	solid
s	substrate
s	superficial
sa	sink-to-ambient
sf	solid-fluid interface
$slip$	slip condition

$strut$	strut
t	total
tot	total
v	viscous drag
w	water
$wall$	solid wall
ζ	fluid
$*$	modified
i	intrinsic

Abbreviations

BCC	Body-Centred Cubic
BET	Brauner-Emmet-Teller
BS	Band Saw
CAD	Computer Aided Design
CFD	Computational Fluid Dynamics
CS	Circular Saw
CV	Control Volume
DNS	Direct Numerical Simulation
DOF	Degree Of Freedom
EDM	Electron Discharge Machining
ERG	Energy Research and Generation
eRMSE	expected Root Mean Square Error
HVAC	Heating Ventilation Air Conditioning
LED	Light Emitting Diode
LES	Large Eddy Simulation

LS Least Squares

LTE Local Thermal Equilibrium

μCT Micro Computed Tomography

NASA National Aeronautics and Aerospace Administration

PEC Performance Evaluation Criterion

PID Proportional Integral Derivative

PIV Particle Image Velocimetry

PPI Pores Per Inch

PU Polyurethane

PUC Periodic Unit Cell

RANS Reynolds Averaged Navier Stokes

REV Representative Elementary Volume

RMS Root Mean Square

SEM Scanning Electron Microscope

SGS Sub-Grid Scale

SIMPLE Semi-Implicit Method for Pressure-Linked Equation

SVR Surface-to-Volume Ratio

SW Sawing Wire

TCR Thermal contact resistance

UDF User Defined Function

UDM User Defined Memory

UDS User Defined Scalar

VAT Volume Averaging Theory

Nederlandse samenvatting –Summary in Dutch–

De aandacht voor energie en energie-efficiëntie is de laatste jaren sterk toegenomen. Een voorbeeld hiervan is de mate van vernieuwing op gebied van chipontwerp. De wet van Moore stelt dat de prestatie van een microprocessor elke 24 maanden verdubbelt. Dit zorgt ervoor dat de chips kleiner en kleiner worden en dat de vraag voor energie dissipatie ook groter en groter wordt. Vandaag de dag wordt een chip in een laptop of computer gekoppeld via een warmtepijp naar een koelvin. Deze koelvin wordt nog vaak gecombineerd met een ventilator en op deze manier wordt de energie geproduceerd door de chip gedissipeerd. Echter in vele applicaties gebeurt deze warmteoverdracht op een natuurlijke manier. In plaats van gebruik te maken van gedwongen warmteoverdracht met behulp van een ventilator gaat men de warmte overdragen met behulp van temperatuurverschillen (dit noemt men dan natuurlijke warmteoverdracht). Deze temperatuurverschillen zorgen voor een variatie in densiteit en dus een beweging van de vloeistof rond de koelvin. Nagenoeg alle zeer compacte toestellen zoals smartphones, gsms, tablets etc. werken via dit principe, maar in 2015 heeft Apple zijn 12 inch versie van de Macbook Pro op de markt gebracht zonder de aanwezigheid van een ventilator.

Bij natuurlijke warmteoverdracht (ook vaak natuurlijke convectie genoemd, naar een van de energieoverdrachtsmodes naast straling en conductie) wordt er uiteraard minder energie overgezet dan via gedwongen warmteoverdracht waar men gebruikt maakt van een ventilator. De voordelen van natuurlijke warmteoverdracht zijn echter duidelijk: geen onderhoud, geen kans op uitval, geen energieverlies van een ventilator en geen elektriciteitsgebruik.

In het verleden is er om deze reden al veel onderzoek gedaan naar koelvinnen die werken via natuurlijke warmteoverdracht. De koelvinnen verschillen van die van gedwongen warmteoverdracht aangezien ze een meer open structuur zijn: ze mogen het indringen van een vloeistof (lucht, water) namelijk niet te veel verhinderen. Bij gedwongen convectie kunnen de koelvinnen veel complexer zijn omdat de vloeistof over de koelvin geduwd wordt.

In dit werk wordt een overzicht gegeven van de mogelijkheden om koelvinnen te karakteriseren zowel op een experimentele manier als op een numerieke manier met behulp van een CFD (Computational Fluid Dynamics) software pakket. Hierbij wordt in de eerste plaats gekeken naar klassieke koelvinnen, bestaande uit rechthoekige structuren, of circulaire/hexagonale pinnen, etc. In de tweede plaats wordt aangetoond hoeveel complexer de berekenings- of metingstools worden

om koellichamen bestaande uit open-cellig metaalschuim te bestuderen. Deze heel complexe koelvin is gemaakt via een gietproces. Het kan eigenlijk het best vergeleken worden met een spons, maar dan gemaakt uit aluminium of koper.

Voor de experimentele studie van koelvinnen wordt een testopstelling ontwikkeld die specifiek bedoeld is om open cel metaalschuim op te testen. Dit zorgt er voor dat de testopstelling een grote lengte op breedte verhouding heeft, specifiek voor de beschikbare metaalschuimstalen. Er was namelijk geen tijd om een bijkomende opstelling te ontwikkelen om andere types koelvinnen mee te testen. De testopstelling is echter algemeen bruikbaar om de moeilijkheden te duiden voor onderzoekers die een experimentele studie aanvatten in natuurlijke convectie. De ideeën die in dit werk worden voorgesteld, worden ook gestaafd door een grondig literatuuronderzoek.

Een eerste aandachtspunt is de locatie waar een temperatuur wordt gemeten of gerapporteerd. Twee temperaturen worden bekeken: de temperatuur van de basisplaat, die in contact staat met de warmtebron (desnoods indirect) en de temperatuur van de omgeving ver weg van de koelvin. Deze temperaturen hangen af van diverse zaken, zoals de gebruikte materialen, het maakproces van de koelvin en de grootte ervan en de locatie van waar de temperatuur wordt genomen. Uiteraard worden deze temperaturen dan op hun beurt ook gebruikt om andere grootheden zoals warmteoverdracht coëfficiënt mee te berekenen. Afhankelijk van de testopstelling kan het effect van de locatie op de temperatuur gemakkelijk 5° zijn. Ook de noodzaak om hulpverwarmingselementen onderaan de koelvin te monteren wordt besproken. Het effect hiervan kan numeriek worden aangetoond, maar vele onderzoekers maken geen gebruik van deze hulpverwarmingselementen zodat er een energieverlies is naar de onderkant van de koelvin toe. Hierdoor kunnen de resultaten van de koelvin zelf overschat worden. Daarnaast is ook de geometrie waar de koelvin wordt ingeplaatst van belang. Dit effect is aangetoond door de doosgeometrie altijd aan kleiner te maken. Vanaf een bepaalde doosgeometrie begint de prestatie van de koelvin significant te wijzigen en effecten tot 7.5% op de thermische weerstand worden bekomen. Uiteraard is het van belang om de koelvin dus te testen in zijn doosgeometrie waar het in geplaatst zal worden.

Als laatste puntje, specifiek voor klassieke koelvinnen wordt het effect van de emissiviteit aangehaald. Heel wat onderzoekers bespreken dit effect zelfs niet en vermelden ook niet het gebruikte materiaal en of de koelvin in een niet-metaalkleur gespoten is. Ook de fabrikanten zijn hier niet altijd duidelijk in: vermelden ze de resultaten van hun gespoten koelvinnen of niet? Afhankelijk van de geometrie kan dit effect echter 30% bedragen.

Specifiek voor metaalschuim wordt ook nog het effect van verbindingstechnologie besproken (met lijm of gebrazeerd) alsook het effect van de bepaling van de geometrie. Er zijn verschillende methoden om het schuim te karakteriseren. Iedere onderzoeker doet dat op een andere manier, soms zelfs zonder aan te duiden hoe de geometrie bepaald werd. Zelfs fabrikanten van open cel metaalschuim karakteriseren het schuim op een verkeerde manier, waardoor de resultaten verkeerd kunnen geïnterpreteerd worden. In dit werk wordt er aangeduid dat het schuim zou moeten gekarakteriseerd worden met behulp van

μCT scans. Dit impliceert een bijkomende moeilijkheid om experimenteel op te meten.

Het grootste stuk van dit doctoraatswerk focust op numerieke bepaling en karakterisatie van koelvinnen. Hier wordt er terug gestart met klassieke koelvinnen. Numerieke studies maken gebruik van CFD software. Hier wordt de geometrie (of een deel van de structuur van de koelvin) in een simulatiepakket geïmplementeerd en gediscretiseerd met behulp van kleine eindige volumes. Hierop worden de behoudswetten dan toegepast. In dit werk werd het CFD-pakket Ansys-Fluent versie 15 gebruikt. In het literatuuroverzicht wordt aangeduid hoe diverse koelvinnen numeriek bestudeerd worden. Vele studies doen dat elk op hun manier: soms wordt er geen vloeistofdomein toegevoegd boven de top van het koelvin, soms wordt er geen rekening gehouden met straling, vrijwel nooit wordt er een onzekerheidsanalyse uitgevoerd op de discretisatie van de geometrie. In dit werk wordt aangetoond dat het vloeistofdomein boven de koelvin minimaal 1.3 keer de hoogte van de koelvin moet zijn, anders kunnen er fouten tot 35% worden gemaakt.

Ook wordt in dit werk beschreven hoe een onzekerheidsanalyse op de roosterdiscretisatie kan gemaakt worden. In dit werk wordt er gerekend met een onzekerheid van slechts 2% op het niveau van de roosterdiscretisatie. Indien men het rooster echter verdubbelt in grootte, dan kan die fout gemakkelijk oplopen tot 7%. Uit het literatuuroverzicht blijkt zelfs dat de discretisatie bij vele auteurs nog grover is, waardoor de fouten nog hoger kunnen oplopen. En hierbij bespreken we nog niet de turbulentiemodellen die sommige auteurs gebruiken, dewelke ook een effect kunnen hebben op de correctheid van de resultaten. Bijkomend worden net als bij experimentele studies sommige dingen vaak niet correct behandeld zoals de invloed van straling en de bepaling van de temperatuur.

Vaak wordt straling verwaarloosd bij numerieke studies, terwijl in dit werk duidelijk wordt aangetoond dat het effect van straling, afhankelijk van de geometrie en gebruikte temperaturen hoger kan zijn dan 35%. Ook de bepaling van de temperatuur is hieraan gelinkt. Als er straling wordt in rekening gebracht, dan zal de temperatuur van de koelvin ook dalen. Een bijkomende vraag, specifiek voor numerieke simulaties is: hoe bepaalt men de totale weerstand tegen warmteoverdracht? Bepaalt men dit op basis van de temperatuur van de omgeving, in de buurt van de koelvin? Of bepaalt men dit met een temperatuur op oneindig? Er wordt aangetoond dat dit effect tot 18% kan oplopen (voor de koelvinnen bestudeerd in dit werk).

Numerieke studie van metaalschuim maakt alles nog veel complexer. Metaalschuim wordt in de literatuur vaak ofwel via expliciete berekeningen gesimuleerd, ofwel via een model gebaseerd op de techniek van volume uitmiddeling. Beide technieken zullen geïllustreerd worden in dit werk. Voor de laatste techniek zal een representatieve eenheidscel gebruikt worden om alle parameters als permeabiliteit en inertiecoëfficiënt te bepalen. Deze parameters zullen dan gebruikt worden om een volledige koelvingeometrie te simuleren. In de literatuurstudie wordt uitgelegd hoe deze techniek kan gebruikt worden. Er zijn twee verschillende technieken gebaseerd op de

volume uitmiddelingsmethode: werken met vaste waarden voor permeabiliteit en inertiecoëfficiënt (de zogenaamde hybride methode) en werken met variabele waarden. Bij deze laatste methode zullen permeabiliteit en inertiecoëfficiënt variëren met de snelheid. In dit werk wordt enkel met de hybride techniek gewerkt, de tweede techniek heeft nog wat verfijning nodig en een aanzet wordt gegeven in Appendix D. Met de gebruikte techniek worden er vrij goede resultaten verkregen, met vrij correcte inzichten omtrent 3-dimensionale effecten. Zoals echter aangeduid wordt in Appendix D zijn er nogal wat beperkingen met de volume uitmiddelingstheorie, alhoewel ze vrij vaak gebruikt wordt. Een beperking is bijvoorbeeld dat deze theorie ervanuit gaat dat de stroming volledig ontwikkeld is van zodra deze intreedt in het schuim. Zeker in natuurlijke warmteoverdracht is dit echter niet het geval, zoals wordt geduid in Appendix D.

Om deze reden werd ook nog een expliciete berekening toegevoegd. In feite wordt hiermee bedoeld dat de volledige koelvin in CFD zou gesimuleerd worden, dit is echter verre van wat mogelijk is met de huidige computerkracht beschikbaar in deze wereld. Vandaar dat een beperkt gedeelte van de koelvin via een vereenvoudigde rechthoekige structuur in CFD werd geïmplementeerd om te berekenen. De resultaten zijn hierbij veelbelovend, maar er is nog meer werk nodig om dit verder op punt te stellen.

English summary

The attention for energy and energy efficiency has grown over the past years. An example of this is the number of innovations in chip design. Moore's law states that the performance of a microprocessor doubles every 24 months. Each innovation results in smaller transistors. As a result, the requirements for applications used to cool down the microprocessor increase more and more. In recent laptops or desktops, a heat pipe connects the microprocessor with a heat sink. This heat sink is often combined with a fan. In this way, the energy produced by the microprocessor is dissipated. Yet, in more and more applications, this heat transfer occurs in a natural way. Instead of using forced heat transfer with the help of a fan, the heat is transferred by means of temperature differences of the fluid (this is called natural heat transfer). These temperature differences cause a variation in fluid density which results in a movement of fluid around the heat sink, cooling down the device. Virtually all compact devices like smart phones, mobile phones, tablets... work through this principle. In 2015, Apple even launched a laptop (Macbook Pro 12 inch) without any fan inside.

Generally, natural heat transfer (often called natural convection, according to one of the energy transmission modes besides radiation and conduction) transmits less energy compared to forced heat transfer. However, the benefits of natural heat transfer are clear: there is no maintenance of the device (consequently, no chance of failure), no energy loss of the fan and no electricity usage.

In the past, a lot of research has already been done on cooling fins through natural convection. The heat sink fins in these applications differ from those used in forced heat transfer, as they are more open in structure: they should not prevent the penetration of a working fluid (air, water) too much. In forced convection, it is possible to use more complex fins because the working fluid is pushed over the heat sink by the fan.

This work gives an overview of the possibilities for characterizing heat sinks both in an experimental and numerical way (by means of CFD - Computational Fluid Dynamics - software). At first, classical heat sinks are considered in this work. These are heat fins with fins consisting e.g. of simple rectangular structures, or circular/hexagonal pins. Secondly, it is shown how the complexity of the calculation or measurement tools rises if heat sinks made with open-cell metal foam are studied. This fin material is made through a casting process. The most simple way of describing this material is to say it is a sponge made out of aluminium or copper.

For the experimental study of heat sinks, a test facility is developed to measure

the performance of open-cell metal foam. This results in a test facility with a large length-to-width ratio, as only metal foam samples with these dimensions were available in the lab. There was no time to develop an additional test rig which could test classical fin types in an accurate way. However, the discussion of the test facility is generally useful to indicate the difficulties especially for experiments on natural convection both for classical heat sinks and open-cell metal foam. The ideas presented in this work are also supported by a thorough literature review.

An important first parameter is the location where a temperature is measured (or reported). Two specific temperatures are considered: the temperature of the base plate, which is in contact with the heat source (if necessary indirectly through e.g. a heat pipe) and the temperature of the environment far from the heat sink. These temperatures depend on a vast amount of things, such as: the materials used, the process of making the heat sinks, the size of the heat sink and the location of the temperature. Furthermore, these temperatures are used to calculate other parameters, such as heat transfer coefficient. Depending on the test rig, the effect of the location on the temperature measurement can be easily up to 5°. This can have a big influence on the overall results.

A second issue is the necessity to use guard heaters at the bottom of the heat sink. The effect of using these heaters can be demonstrated numerically. However, many researchers do not use these guard heaters so there is an energy loss to the bottom of the heat sink. As a result, the performance of the heat sink can be overestimated.

Additionally, the geometry of the enclosure in which the heat sink is placed, is important. The effect of this box geometry is shown in this work. When this box is reduced in size, the effect on the performance of the heat sink can be up to 7.5% on the overall thermal resistance. Hence, it is important to test the heat sink in a similar box geometry as the one where it will be used in practical applications.

A final point of interest, especially for classical heat sinks, is the effect of the emissivity. Many researchers do not even discuss this effect properly, nor do they mention the material used and whether or not the heat sink is sprayed in a non-metallic color. Even manufacturers are not clear in the data they publish online. Yet, depending on the geometry this radiative effect can be up to 30%.

Specifically for open-cell metal foam, the effect of the bonding method is discussed (bonding through epoxy and brazing is considered) as well as the effect of characterizing the geometry. In case of open-cell metal foam, there are several methods to characterize the foam. Nearly every researcher does this differently, sometimes even without indicating how the geometry was determined. Even manufacturers of open-cell metal foam characterize the foam in a wrong way, in which the results can be misinterpreted. This work indicates that the foam should be characterized by μCT scans. This causes an additional difficulty.

The most important part of this work focuses on the numerical characterization of heat sinks. In the numerical study CFD simulation software is used, in which the geometry (or part of the geometry) is implemented and discretized using small finite volumes. Consequently, the conservation laws are applied. In this work, Ansys-Fluent15 was used. Again, the author starts by studying classical heat sinks.

The literature survey shows how various cooling fins are studied numerically. Many studies tackle this problem differently: sometimes no liquid domain is added above the top of the heat sink, in other cases radiation is simply neglected and hardly ever is there an uncertainty analysis performed on the grid discretization. In this work it is shown that the liquid domain above the heat sink must be at least 1.3 times the height of the cooling fin, otherwise errors up to 35% on the thermal performance can be made.

A description is also given on how such an uncertainty analysis can be made. In this work, it is shown that the used uncertainty on the grid discretization is 2%. However, if you double the size of the grid (coarsening), the uncertainty can increase up to 7% (for the heat sinks tested). Furthermore, based on the literature review it is shown that the grid discretization is even coarser in many studies in open literature, due to which the uncertainties will become even higher. Herein the effect of turbulence models is not even considered. Some authors do use these models, which will increase the uncertainty on the heat transfer results even further.

Additionally, as was the case in experimental studies, some aspects are often not properly treated in open literature, such as the influence of radiation and temperature determination. Often radiation is neglected in numerical studies, while in this work it is clearly demonstrated that the effect of including radiation can be higher than 35%, depending on the geometry and used temperature. The determination of the temperature is also linked to this. If radiation is taken into account, the temperature of the heat sink will be decreased. Furthermore, an additional question can be raised in case of numerical simulations: how is the overall resistance to heat transfer determined? Is this determined based on the temperature of the surroundings, near the heat sink? Or is this determined based on the temperature at infinity? It is shown (for the heat sinks studied in this work) that this effect can be up to 18%.

The numerical study of heat sinks made out of open-cell metal foam is even more complex. In open literature, metal foam is often simulated through explicit calculations or based on a model of volume averaging. Both ways of simulating the foam are discussed. The model based on volume averaging needs a representative unit cell to determine all parameters needed as permeability and inertial coefficient. These parameters will then be used to simulate the complete heat sink geometry. In the literature survey, this technique is explained. There are two ways to work with this volume averaging method: using fixed values for permeability and inertial coefficient (the so-called hybrid method) or working with variable values, where permeability and inertial coefficient e.g. will be determined depending on the Reynolds number of the working fluid. In this work, only the hybrid model will be discussed as the second method needs some refinements which is initiated in Appendix D.

When the hybrid technique is used, quite good results are obtained, yielding fairly correct insights in the three-dimensional effects. However, as indicated in Appendix D, there are quite some limitations on this volume averaging theory, although this technique is quite often used. For example, this theory assumes

that the flow is fully developed as soon as it enters to foam. Certainly in natural convection, this is not the case.

For this reason, an explicit calculation was also added. In fact, the complete heat sink could be implemented in a CFD software and simulated. However, with the current level of computational power this is not possible (even with the supercomputers now in operation). Hence, only a small part of the complete heat sink is implemented. For open-cell foam, this is a simplified rectangular structure. The results of this model are quite promising, however, some work is still needed to refine this method.

1 Introduction

1.1 Energy dissipation

1.1.1 What is energy?

Energy is commonly defined as 'the ability of a system to perform work' [1]. However, this definition can be misleading, as not all available energy does *useful* work. A simple illustration of this is the spinning of a water wheel. When kinetic energy is transferred past a water wheel, the wheel can only convert kinetic energy into mechanical energy. However, only a part of the inflowing energy can be converted into **useful energy**, the remainder is termed **rejected energy**.

In nearly all applications, there is a useful energy part and a rejected energy part. An illustration on how large this amount of rejected energy is, compared to the total inflowing energy is given in Figure 1.1. This figure reports the amount of energy used in 2015 in the United States of America in Quads (1 Quad = 1.055 EJ). On the left side of this figure the energy resources are shown, consisting of 81.5% fossil fuels, 8.5% nuclear energy and 10% renewable [2]. This shows the large dependency on fossil fuels. Next, this Sankey diagram also shows that of all inflowing energy, only 40% is used useful. The rest, more than half of the inflowing energy, is rejected.

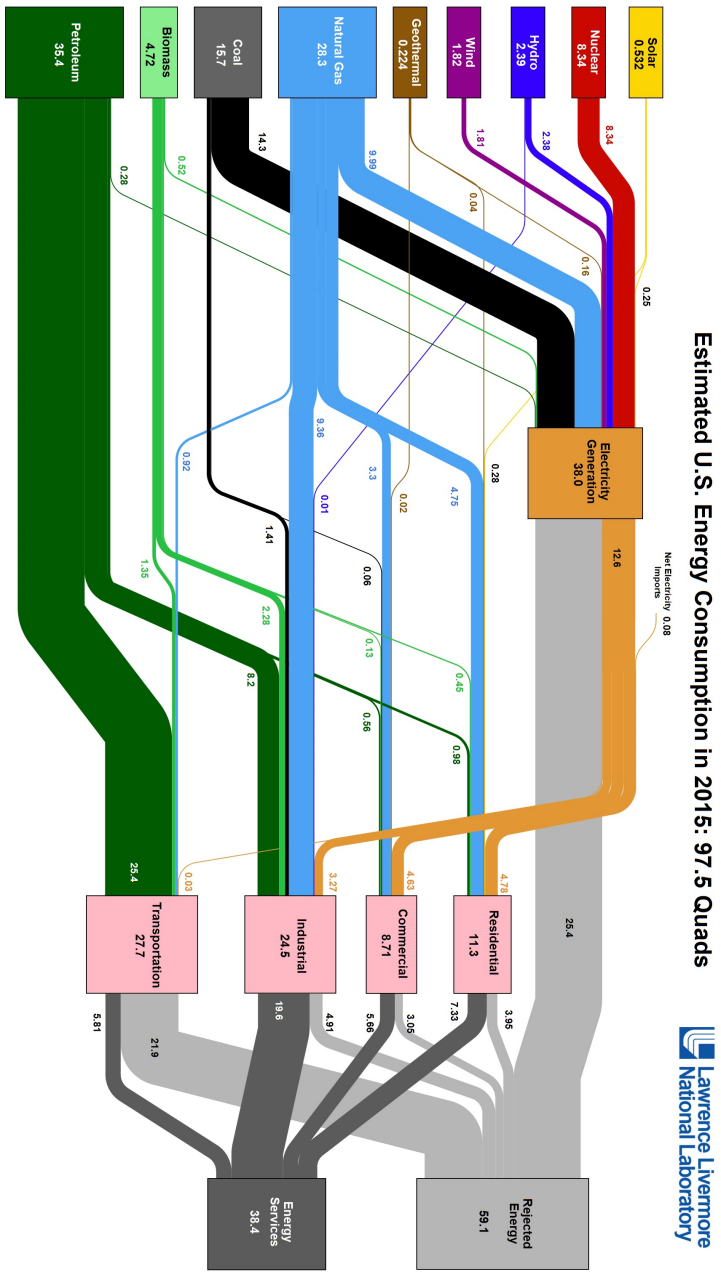

Figure 1.1: Sankey diagram of the energy flow for the United States of America in 2015 [2].

1.1.2 Dissipation systems

All of the inflowing energy for energy processes will sooner or later be dissipated into the atmosphere. Electricity generation facilities are using e.g. wet or dry **cooling towers** to dissipate the rejected energy to the ambient. A transportation system, like a car or a truck, cools its engine through a water-air **heat exchanger** which is placed in front of the vehicle or via exhaust gas discharge at the rear.

However, in this work the focus will be more on heat sinks rather than heat exchangers. Heat sinks are commonly used for the cooling of microprocessors. This specific kind of energy using device (the microprocessor) will be discussed in the next section (Section 1.2).

1.2 Power dissipation in microprocessors

1.2.1 Moore's law

In our highly automated environment microprocessors are omnipresent: in personal computers/laptops or industrial manufacturing, but also in e.g. residential applications. The evolution in the performance of microprocessors is very steep. Moore's law, named after Intel founder Dr. Gordon Moore, states that the transistor density, and hence the performance of a microprocessor, doubles roughly every 18 months [3]. In the past, this law was indeed able to predict the evolution in performance of the microprocessors, see Figure 1.2.

However, recently Moore's law started to flag, mainly because of the economics of making microprocessors. As originally stated by Dr. Moore, his law was not just about reductions in the size of transistors, but also cuts in their price. A few years ago, when transistors 28 nm length were the state of the art, chipmakers found their design and manufacturing costs beginning to rise sharply (see Fig. 1.2). In other words: transistors can be shrunk further, but they are now getting more expensive. And with the rise of cloud computing, the emphasis on the speed of the processor in desktop and laptop computers is no longer so relevant. The main unit of analysis is no longer the processor, but the rack of servers or even the data centre. The question is not how many transistors can be squeezed onto a chip, but how many can be fitted economically into a warehouse [4]. When the number of transistors per chip keeps increasing, the size of the chip shows a similar trend. The power dissipation in $\frac{W}{m^2}$, also called the heat flux, keeps on increasing.

Hence Moore's law will probably come to an end, although there is still quite some doubt on how microprocessors will evolve and which constraints will play the most important role (see Figure 1.3). And the question will be if Moore's law will come to an end or if it will become irrelevant to increase the number of transistors even more [4].

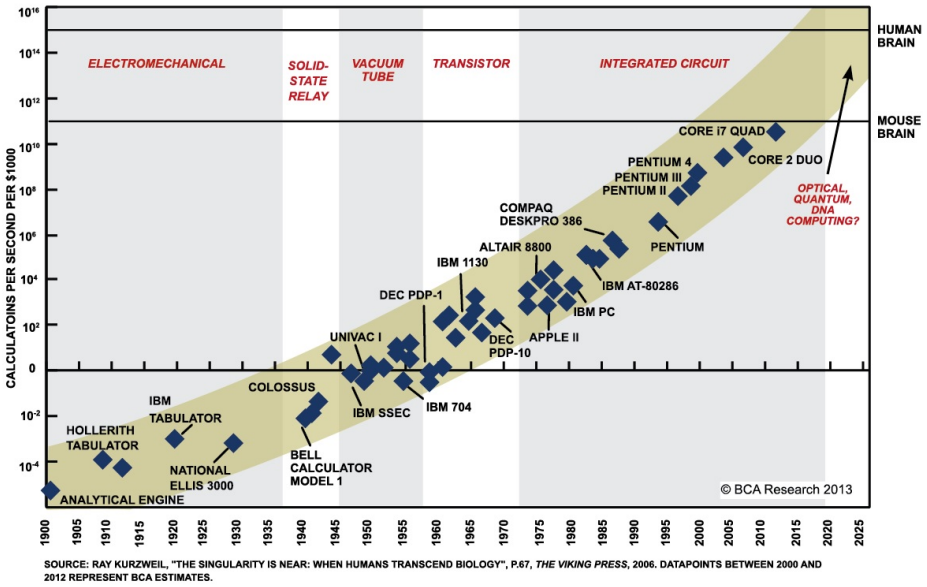

Figure 1.2: Illustration of Moore's law (existing processors are added) [3].

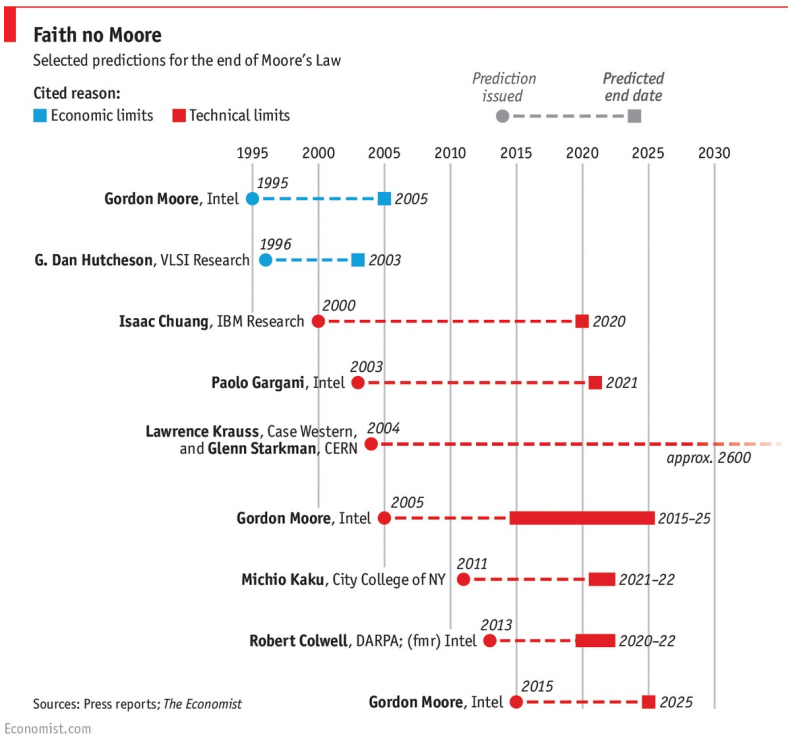

Figure 1.3: The end of Moore's law [4].

1.2.2 Dissipation systems

In the context of this work it is important to remember that the chip itself is very small (order of centimetres) and that all electricity that is required to operate the microprocessor has to be dissipated. For the last edition of the $i7$ core from Intel, Core i7-6700K-Skylake (width transistor: 14 nm), the nominal thermal design power is 91 W [5]. A microprocessor is typically cooled by a **heat sink**.

This heat sink is placed in contact with the device that needs to be cooled. Heat sinks typically have a large surface area compared to their volume, in order to dissipate as much heat as possible. This heat sink forms an extended surface to the device. The focus of this work is to study a number of existing and possible new extended surfaces. Nowadays, a fan is usually used to blow air over the heat sink. However, if one could increase the effectiveness of these extensions, it would also be possible to decrease the fan speed or eliminate the fan entirely from the design and create a passive cooling device.

There are many types of classical and more complex heat sinks and the work on these different types is endless and still ongoing. In this work the classical heat sinks studied consist mainly of plain fins and pin fins. The more complex heat sinks studied consist of open-cell metal foam, which is a material developed in the search to better extended surfaces. Heat sinks consisting of these fins (plain, pin and metal foam) will be studied in this work both through experiments and numerical research. Since there is still not so much commonly known about metal foam as an extended surface, this will be introduced in the next section.

1.2.3 Open-cell metal foam

In Figure 1.4 the nomenclature of open-cell foam is shown. The struts of the foam are interconnected in the nodes forming both cells and pores. It is clear that cells and pores are different in their definition as will be discussed later on.

There are different types of open-cell metal foam, this work will focus on the foam type which performs best in thermal applications: **casted open-cell metal foam**, which has *solid struts*. Conversely open-cell foam made through an electrophoretic deposition process has *hollow struts*. This significantly lowers its effective thermal conductivity up to one third of its casted alternative [6].

Casted foam originates from the late '60s and was invented by the "Materials and Aerospace" division of Energy Research and Generation (ERG) [7]. This invention has led to the patent of Walz [8] which describes the manufacturing process of casted open-cell metal foam based on an organic preform. Most of the time this preform consists of polyurethane. The metal foam by ERG Materials and Aerospace, was intended for military and aerospace applications.

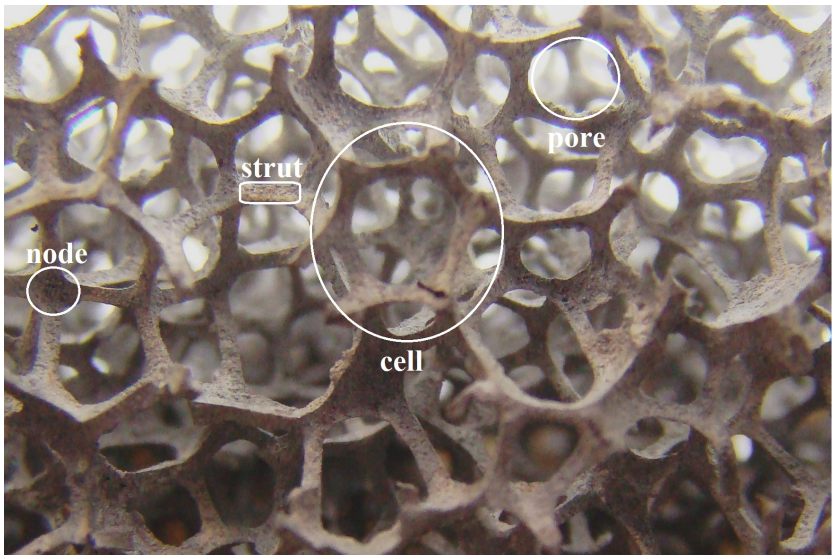

Figure 1.4: Nomenclature of casted open-cell metal foam.

Only since the mid '90s, the technology became generally available for non-classified military and industrial applications. It is from that time that the annual publication rate on the topic has increased steadily. From 2000 on the publication rate keeps increasing. This evolution has also triggered other manufacturers of casted open-cell metal foam to emerge. In 2000 the German company M-Pore GmbH [9] started making casted metal foam. Alveotec in France [10] and Constellium [11] in the Netherlands followed a few years later. Most of these companies are still closely related to the research industry. Constellium for example works together with The University of Sheffield, while Alveotec works closely together with the TEMISTh research group in Marseille (France).

Open-cell casted metal foam manufactured by either ERG Materials and Aerospace or M-Pore is made with an investment casting process based on a polyurethane preform. As the fabrication process of the organic preform is influenced by gravity, the resulting cells are oval shaped (see Figure 1.5(a)). A deterministic approach to obtain a model of such an organic preform is based on minimizing the total film energy of the surface between the solid and fluid phase.

On the other hand, the metal foam by Alveotec and Constellium is made by casting metal over a stacked bed of soluble spheres. These spheres can be either salt spheres or sand with a polymer bonding agent [10]. After solidification of the metal, the spheres are then simply washed away with water. This process is known as leachable bed casting. The metal foam that is created with this manufacturing process has a more uniform and spherical cell shape (see Fig.1.5(b)).

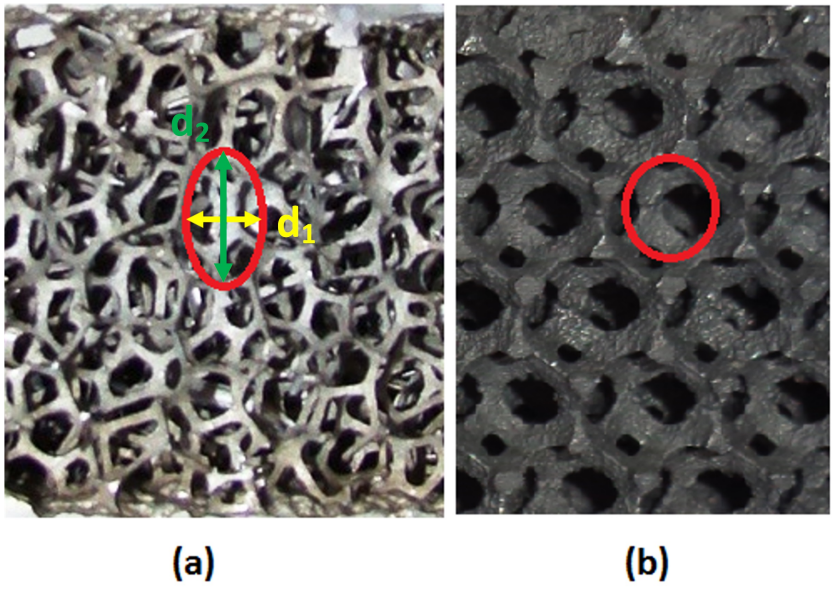

Figure 1.5: Two casted types of open-cell metal foam produced by (a) investment casting from a polyurethane perform and (b) leachable bed casting (exampled Alveotec, painted black to increase emissivity)

Several researchers from open literature mention that casted open-cell foam has a lot of interesting structural and functional properties, like:

- High porosity (higher than 80%; can go up to 95%). High porosity results in a low weight application.
- High interstitial surface area per unit volume.
- Good impact energy absorption [12].
- Excellent fluid mixing due to tortuous flow paths [13].
- Hybrid manufacturability: different foam materials (e.g. Al, Cu) can be sandwiched into one foam panel [14].
- Shapeable in three dimensions (obtainable via casting and/or co-casting techniques).
- Visually appealing.

There are two important parameters to which there will be referred to later in this work: (1) volumetric porosity, as defined in Eq. (1.1) with V_f the fluid

volume inside the foam structure and V_t the total volume of the foam structure ($V_t = V_s + V_f$). (2) the pore density, also called foam density, frequently defined with a PPI-value (which stands for Pores Per linear Inch), see Eq. (1.2). Foam manufacturers report this number as a whole number: e.g. 5, 10, 20 etc. However, in reality this is never the case.

$$\phi = \frac{V_f}{V_t} \tag{1.1}$$

$$PPI = \frac{numberofpores}{inch} \tag{1.2}$$

Thanks to these advantages the metal foam is already in use in systems like the Porifera LED (Light Emitting Diode) system from TAL Belgium (Technical Architectural Lighting) and LED cooling for LOUPI Lighting [15].

Small remark that needs to be mentioned in this introduction chapter: this PhD work does not want to compare a classical heat sink (pin fin or plain fin heat sink) with a heat sink made out of open-cell metal foam. The author just wants to discuss (the differences between) the experimental and numerical work of both types of heat sinks. More work on the comparison between classical heat sinks and open-cell metal foam can be found in a journal publication made by a master thesis student of the author, see Ref. [16].

1.3 Goals

This work focusses on energy dissipation through **heat sinks in buoyancy-driven flow**. As already mentioned a large amount of work was already done on different types of heat sinks. However, this work is very diffuse as will be shown in the following chapters. The aim of this work is to determine what is the best practice to characterize heat sinks both **experimentally and numerically**. This work focuses on laminar flow. No simulations were performed using turbulence models.

The approach to attain the goal of this work is to first study **classical heat sinks** both experimentally and numerically. In this study the effect of the different parameters on the experimental and numerical results will be assessed. As will be shown, this effect can be very significant. Hence a good design of the experimental and numerical research is paramount.

As already mentioned this work will study more complex heat sinks, made out of **open-cell metal foam**. This material was chosen because it is one of the more complex heat transferring structures. In this work it will be studied how this increase of complexity influences the necessary approach of the experimental and numerical tests. Specifically for numerical studies of open-cell metal foam, several techniques are available. Hence special attention was paid to these different techniques and how they can be applied to study this type of heat sink.

1.4 Outline of the PhD

Based on the objectives of these work, it was composed according to the following outline:

- In **Chapter 2** the basic principles of heat transfer are discussed
- In **Chapter 3** an overview of existing experimental work on heat sinks in buoyancy-driven flow is given
- In **Chapter 4** an overview of existing numerical work on heat sinks in buoyancy-driven flow is given
- In **Chapter 5** the test rig used in this work and the experimental test results for open-cell metal foams are discussed
- In **Chapter 6** the approach for numerical simulation and the results of simulations for classical heat sinks are given
- In **Chapter 7** the approach for numerical simulation and the results of simulations for heat sinks made out of open-cell metal foam are discussed
- In **Chapter 8** the main conclusions and outlook are given

This work also contains some appendices, the first two appendices contain the uncertainty analysis of this work and discussion of the emissivity measurements. The author of this work would like to attract the attention of the reader to appendices C and D, which contain some preliminary results of a DNS (direct numerical simulation) approach to study metal foam and a new interpretation of the Darcy equation. The results in the latter appendix have already been published in a peer-reviewed journal. In appendix E, an overview of all the publications related to this work is given.

2

Basic principles of heat transfer

Heat is defined as energy transferred by virtue of a temperature difference. According to the second law of thermodynamics there is a direction of natural processes. Heat, for example, flows from regions of higher temperature to regions of lower temperature. The different heat transferring modes will be discussed later. Heat itself is thus an energy transferring process.

The energy transfer process due to a temperature gradient can occur by two very different mechanics: **conduction and radiation**. Heat transfer due to conduction occurs through the interactions of molecular scale energy carriers within the material of interest. On the other hand, radiative heat transfer is energy transferred as electromagnetic waves. In a flowing fluid, the energy transferring system becomes even more complex: conductive heat transfer occurs in the presence of energy transfer due to bulk motion and this leads to a concept called **convection** [17]. Depending on how the fluid flow is generated, two types of convection can be identified: forced convection and natural convection. Forced convection means that the fluid flow is caused by a mechanical initiator, in most heat sink applications e.g. this is a fan. Natural or buoyancy-driven convection means that the temperature itself is causing a difference in density and thus a fluid flow without the use of any mechanical equipment. Often these convective heat transferring modes are classified as active and passive methods, respectively.

In this chapter, an overview is given on the different heat transferring modes in general. First, the basic principles of heat transfer will be discussed going from conduction, forced and natural convection to radiation. The focus of this work is electronics cooling with heat sinks. The basics as to how this is studied and

different particularities are discussed in Section 2.4 of this chapter. This work focuses on laminar flow. No simulations were performed using turbulence models, so no literature is overlooked studying the effect of different turbulence models.

2.1 Conduction

Conduction is the transfer of energy from one part of a body at a higher temperature to another part of the same body at a lower temperature. Or from one body at a higher temperature to another body, in physical contact with that other body, at a lower temperature. As mentioned in the introduction, the conduction process takes place at the molecular level and involves the transfer of energy from the more energetic molecules to those with a lower energy level. In a metal, the principal contribution to conduction is the motion of free electrons which move in a similar way to molecules in a gas. The equation to solve the transient heat conduction problem reads as Eq. (2.1). In this equation temperature T is function of the position (x, y, z) and time (t). Equation (2.1) is also called *the heat equation*.

$$\nabla \cdot (k \nabla T) + q = \rho c \frac{\partial T}{\partial t}, \tag{2.1}$$

In Eq. (2.1) q is the volumetric heat generation in $\frac{W}{m^3}$. At $t = 0$, $T = T_i(x, y, z)$ is called the initial condition to solve the partial differential equation. This initial condition is not required in the steady-state case where $\nabla \cdot (k \nabla T) + q = 0$ or for periodic heat transfer where q or the boundary conditions vary periodically with time and where the start of the transient behaviour is most of the time ignored.

The condition $q = 0$ simplifies the equation even more. However, a value of temperature T (in Eq. (2.1)) should also satisfy the boundary conditions. In case convection occurs at a boundary, following boundary condition (Eq. (2.2)) can be expressed where a derivative of T in a direction normal to a boundary is proportional to the temperature on that boundary [18]. Eq. (2.2) assumes the normal direction to the boundary in the x-direction.

$$-k \frac{\partial T}{\partial x}\Big|_{boundary} = h(T - T_\infty)_{boundary} \tag{2.2}$$

With this boundary equation for each space coordinate, the conduction problem can be solved. Also notice that convection and conduction are directly coupled here. Of course this convective boundary condition can be expanded to a combined convection-radiation boundary condition as it is typically the case in heat sink applications where the radiative heat transfer can not be neglected. In this boundary equation, Eq. (2.2), one can recognize the Fourier conduction equation, in the x-direction written as: $q = -k \frac{\partial T}{\partial x}$, with q the heat transfer rate per unit area normal to the direction of the heat flow in $\frac{W}{m^2}$. k is the thermal conductivity of

the studied material. Usually this conductivity can be considered as a constant, although it can also be dependent on the direction of the energy transfer [19]. The higher the thermal conductivity and/or the temperature gradient, the more energy transferred from one location to another.

The Fourier equation can also be written (for example for the x-direction) as Eq. (2.3), where $\Delta x/k$ assumes the role of the thermal conductive resistance ($R_{th,cond}$) and the temperature difference $T_{hot} - T_{cold}$ is the driving force for heat transfer. The relation shown in Eq. (2.3) now resembles the Ohm's law in electric circuit theory. This analogy will also be used later. In both equations below, Δx represents the outer boundary positions for which the equations are valid.

$$q = \frac{T_{hot} - T_{cold}}{\Delta x/k} = \frac{T_{hot} - T_{cold}}{R_{th,cond}} = \frac{\text{thermal potential difference}}{\text{thermal resistance}} \tag{2.3}$$

A small remark should be added as the thermal conductive resistance can also be written as:

$$R_{th,cond} = \Delta x/(kA_s) = (T_{hot} - T_{cold})/Q \tag{2.4}$$

Where A_s is the heated surface without taking into account the fin surface (= area of the substrate of the heat sink). Again this definition follows from the Fourier equation, but instead of working with q, one can write the equation in function of $Q = qA$.

2.2 Radiation

Radiation is a very different heat transfer process compared to conduction because energy is transferred without the benefit of any molecular interactions. E.g. radiation energy exchange can occur over long distances through a complete vacuum. A perfect example of this is the energy from the sun which brings life to our earth. It took until the early 1900s before a theory was developed on how the transport process occurs through radiation. The idea was the same as the energy dissipation induced when an object is dropped into water. The energy transport occurs through electromagnetic waves. However, the discrete nature of radiation emission is the basis for quantum theory: hence thermal radiation must be viewed as having both wave-like and particle-like behaviour [20].

Studying radiative heat transfer is quite complex. For a certain amount of radiant energy (E), a fraction will be reflected (ρE), a fraction is absorbed (αE) and a fraction is transmitted (τE) [17]. From the conservation of energy, following equation is obtained:

$$\rho + \alpha + \tau = 1 \tag{2.5}$$

Furthermore, also the body or surface itself will emit energy. According to the Kirchhoff law, the wavelength-specific emissivity of a body ε_λ equals the absorption α_λ of a body when they are in thermodynamic equilibrium. If that is not the case, both properties will depend on the incident angle.

2.2.1 Introduction: blackbody radiation

The examination of thermal radiation can be started best from the behaviour of a blackbody: a perfect absorber and emitter of radiation. Of course a perfect blackbody doesn't exist. The behaviour of a real surface is thus much more complex and will be discussed later. Thermal radiation is the portion of the electromagnetic spectrum between the wavelengths of approximately 0.2 μm and 1000 μm, while the wavelengths of visible light are within 0.38 μm and 0.78 μm [17]. Based on Wien's law, the wavelength of the maximum emissive power is related to the temperature according to: $\lambda_{max}T$ = 2897.8$\mu m - K$. So for the low temperatures studied in this work (< $100°C$) the wavelength of maximum emissive power will always be higher than 7.77 μm (see Figure 2.1).

How a surface emits or receives radiation is a complicated function of the orientation of the surface with respect to the other surfaces and whether the radiation is distributed *spectrally* and *directionally*. A diffuse body, for example, emits radiation uniformly in all directions. The spectral distribution for a black body, e.g., is a smooth curve depending on the wavelength, while for a real surface, this is a much more complicated function.

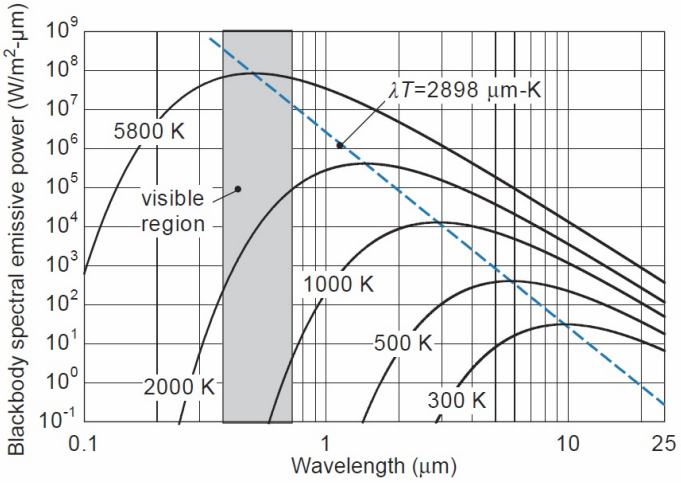

Figure 2.1: Blackbody spectral emissive power as a function of wavelength for various values of temperature [17]

For a black body, the total emissive power (E_b) is proportional to the fourth power of the temperature multiplied with a proportionality constant (σ), see Eq. (2.6) [20]. It was experimentally and theoretically proved by Stefan and Boltzmann, who have given their names to the proportionality constant σ: the Stefan-Boltzmann constant, equal to $5.670373\ 10^{-8} \frac{J}{sm^2K^4}$ [21]. The unit of E_b is W/m^2.

$$E_b = \int_0^\infty E_{b,\lambda} d\lambda = \sigma T^4 \tag{2.6}$$

To obtain the net rate of radiative heat transfer to a surface, the difference between the rate of radiation that is emitted by the surface and the rate at which the radiation that is incident on the surface is absorbed should be determined. Black surfaces are an ideal starting point for the analysis, as none of the radiation is reflected or transmitted from these surfaces. The amount of incident radiation can thus be determined by considering the radiation from all other surfaces and their geometric orientation with respect to the surface of interest. A so-called view factor is a dimensionless ratio that characterizes the degree to which two surfaces can 'see' each other.

A view factor $F_{i,j}$ is defined as the fraction of the total radiation that leaves surface i and goes directly to surface j. The words 'goes directly' excludes the possibility of radiation emitted by surface i reflecting off of a third surface before finally reaching surface j. The view factor between two (black) surfaces can be generally described through Eq. (2.7) [17].

$$A_i F_{i,j} = A_j F_{j,i} = \int_{A_j} \int_{A_i} \frac{cos(\theta_i) cos(\theta_j)}{\pi r^2} dA_i dA_j \tag{2.7}$$

For two black surfaces, the radiation exchange between surface i to surface j can be written as [17]:

$$Q_{rad,i\ to\ j,\ black} = F_{i,j} A_i \sigma T_i^4 - F_{j,i} A_j \sigma T_j^4 \tag{2.8}$$

2.2.2 Diffuse grey surface approximation

Compared to blackbody radiation, the determination of the radiative heat transfer for a real body is much more complicated. The total rate of radiation emitted per unit area of surface (dA) at a particular wavelength is the spectral emissive power of the surface (E_λ) and can be computed from the integral of the intensity over all angles intercepted by the hemisphere above the surface (see Eq. (2.9)) [17].

$$
\begin{aligned}
E_\lambda &= \frac{rate\ of\ radiation\ emitted}{dA\ d\lambda} \\
&= \int_0^{2\pi} Ie_{\lambda,\theta,\phi} cos(\theta) d\omega \\
&= \int_0^{2\pi} \int_0^{\pi/2} Ie_{\lambda,\theta,\phi} cos(\theta) sin(\theta) d\theta d\phi
\end{aligned}
\tag{2.9}
$$

In any real application, it is very complicated to calculate the intensity of the emitted radiation, which is formally defined as the rate of radiation emitted, $Ie_{\lambda,\theta,\phi}$, at wavelength λ per unit solid angle, ω and per unit surface area that is normal to the direction of emission defined by angles θ and ϕ. Therefore a lot of approximations are proposed for practical applications in order to calculate the radiative heat transfer rate. One approximation which is frequently used is the *diffuse grey surface approximation* [22]. Here the emissivity is supposed to be constant and independent of the direction (θ and ϕ) and the wavelength (λ). The most appropriate value of the emissivity to use for a diffuse grey surface model is the total hemispherical emissivity [17]. Later in this work, also this approximation will be used for the numerical simulations. This emissivity can be calculated through Eq. (2.10), if E_λ is given which is often not the case. Another option is to measure the total hemispherical emissivity. Eq. (2.10) is also frequently used in heat transfer calculations for radiation.

$$
\varepsilon = \frac{\int_0^\infty E_\lambda d\lambda}{\sigma T^4} \tag{2.10}
$$

In most applications, the material of interest is opaque. This means that no transmittance through the surface is possible [23]. For opaque materials, Eq. (2.5) can be rewritten as $\rho = 1 - \alpha$ and through the Kirchhoff law (for a system in thermodynamic equilibrium): $\rho = 1 - \varepsilon$.

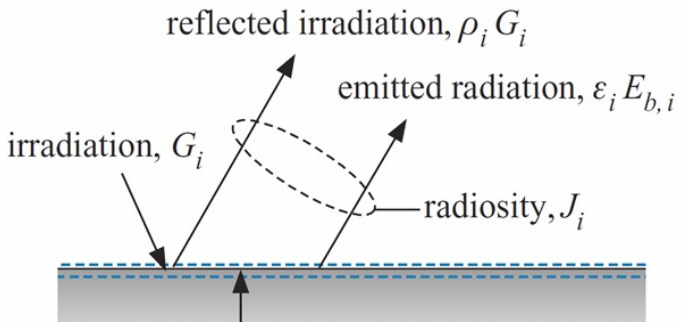

Figure 2.2: Illustration of radiative heat transfer from a surface i in case of a diffuse grey surface.

Consider now a grey surface i, shown in Figure (2.2), which is receiving incident radiation G_i (also called irradiation). A portion of this irradiation, $\rho_i G_i$, will be reflected. The surface itself will also emit some energy: $\varepsilon_i E_{b,i}$. The sum of the reflected and emitted radiation per unit area is called radiosity J_i, for an opaque structure calculated in Eq. (2.11).

$$J_i = (1 - \varepsilon_i)G_i + \varepsilon_i E_{b,i} \tag{2.11}$$

Hence the energy transfer to or from the grey surface i can be written as:

$$Q_i = A_i J_i - A_i G_i = \frac{\varepsilon_i A_i}{1 - \varepsilon_i}(E_{b,i} - J_i) \tag{2.12}$$

Note that the driving force for heat transfer is the difference between the surface's black body emissive power and its radiosity. The resistance to heat transfer is $(1 - \varepsilon_i)/(\varepsilon_i A_i)$. If two surfaces are involved, the net rate of radiation exchange between surface i and surface j can be written due to the reciprocity between view factors as Eq. (2.13).

$$Q_{i\ to\ j} = A_i F_{i,j}(J_i - J_j) \tag{2.13}$$

Again, the factor $1/(A_i F_{i,j})$ acts as a resistance against heat transfer, similar to the one defined in Eq. (2.4).

This means that in case of a diffuse grey surface, the only two parameters that need to be determined are the emissivity ε and the view factor $F_{i,j}$. The approach for radiative heat transfer in Computational Fluid Dynamics (CFD) is given in Chapter 4.

2.3 Convection

As explained in the introduction of Chapter 2 flow can pass past an object either with the aid of mechanical equipment such as a fan or without any auxiliary. For these two cases the heat transfer modes are called forced and natural convection, respectively. Forced convection is discussed in Section 2.3.1, while natural or buoyancy-driven convection is discussed in Section 2.3.2.

2.3.1 Forced convection

Convection is the transfer of energy between a moving medium and an object. The transfer of energy in a flowing fluid is not only due to conduction but also due to the enthalpy carried by the macro-scale flow. Enthalpy is the sum of the internal energy of the fluid and the product of its pressure and volume. This pressure-volume product is related to the work required to move the fluid across a boundary [17].

When fluid flows past a solid body a region of variable velocity must be built up between that body and the free fluid stream. This region is called a (velocity) boundary layer. The velocity boundary layer thickness δ is defined as the distance from the wall to the point where the flow velocity approaches within 1% of u_∞. The local velocity boundary layer thickness δ is a function of the velocity far away from the plate (u_∞), the density and dynamic viscosity of the studied fluid (ρ and μ) and the location on the solid body (x) as the boundary layer changes in thickness over the solid body (Eq. (2.14)) [20].

$$\delta = f(u_\infty, \rho, \mu, x), \tag{2.14}$$

The temperature of the solid body surface is called the wall temperature T_w. If T_w is different from the free stream temperature T_∞, there will also be a thermal boundary layer δ_t. Referring to Fig. (2.3), the heat conducted away from the solid at the wall can be equated to the heat transfer expressed in terms of a convective heat transfer coefficient, called h[1]:

$$-k_f \frac{\partial T}{\partial y}|_{y=0} = h(T_w - T_\infty) \tag{2.15}$$

Again the Fourier law for conduction is used to express the heat removal at the wall. The conductivity k is a property of the solid body material, conversely convective heat transfer coefficient h can vary in the fluid, depending on the heat transferred at the boundary. Eq. (2.15) can also be modified as:

$$\frac{\partial(\frac{T_w - T}{T_w - T_\infty})}{\partial(y/L)}|_{y/L=0} = \frac{hL}{k_f} \tag{2.16}$$

Eq. (2.16) can also be written for any location, x, along a flat surface. From Fig. 2.3 and Eq. (2.16) it can be seen that $\frac{hL}{k_f}$ can be written as L/δ_t. In other words, the convective heat transfer rate is inversely proportional to the thickness of the thermal boundary layer. L is the total length (characteristic length) over which the governing equations holds (the total length over which the boundary layer grows). The thermal boundary layer thickness depends on the velocity of the fluid u_∞.

[1] Remark that this is very similar to Eq. (2.2)

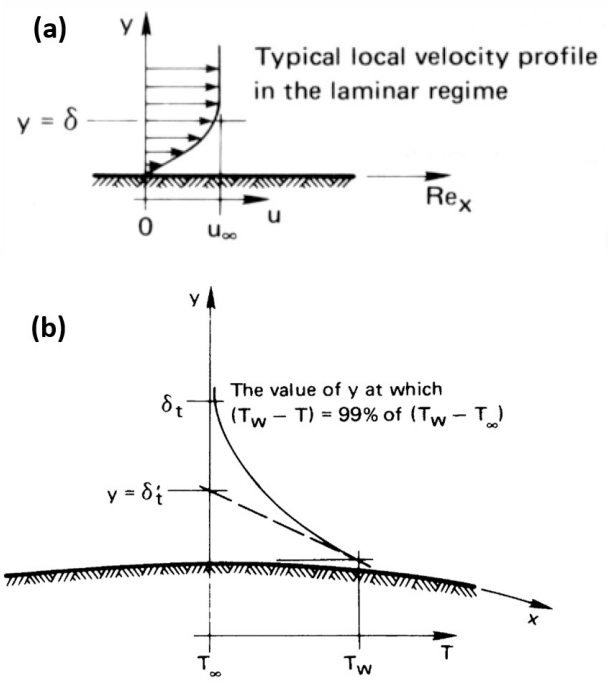

Figure 2.3: An illustration of the velocity (a) and thermal (b) boundary layer [24].

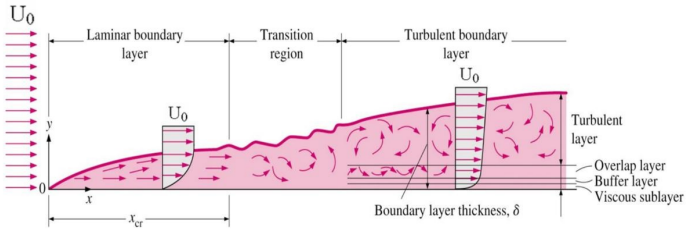

Figure 2.4: Boundary layer thickness for a laminar and turbulent flow.

In Figure 2.4, an illustration is made for the boundary layer thickness over a flat plate in case of a laminar and turbulent flow. This figure clearly shows that the increase in the turbulent boundary layer thickness is much sharper than that of the laminar boundary layer. Hence, the higher the incoming velocity over the plate the smaller the thickness of the thermal boundary layer and the higher the convective heat transfer coefficient (see Eq. (2.16)).

However, Figure 2.4 also shows that the boundary layer thickness along a flat plate keeps on increasing. This means that the heat transfer rate will decrease along

a flat plate: the thicker the boundary layer, the lower the convection coefficient and thus the lower the heat transfer rate. This decrease in heat transfer can be solved by adding obstructions which break up this boundary layer. If e.g. several pin-shaped obstructions (fins) are added to the surface, they will break up the boundary layer. However, the boundary layer will start to build up again after the each pin fin. The closer the pin fins are placed together, the smaller the boundary layer thickness will be and the better the heat transfer rate. This can be seen in Figure 2.5. Just before each pin fin, the fluid comes to a halt in one point just before the pin. Around the pin fin the fluid will accelerate, and a horseshoe vortex will be formed: the boundary layers will break up. See the previous PhD of Henk Huisseune in this research group on forced convection considering this topic [25].

Another reason for adding these fins is the need to increase the surface area of the body in contact with the flow, as $q = Q/A = h(T_w - T_\infty)$. The higher this surface area, the higher the heat transfer rate Q [26].

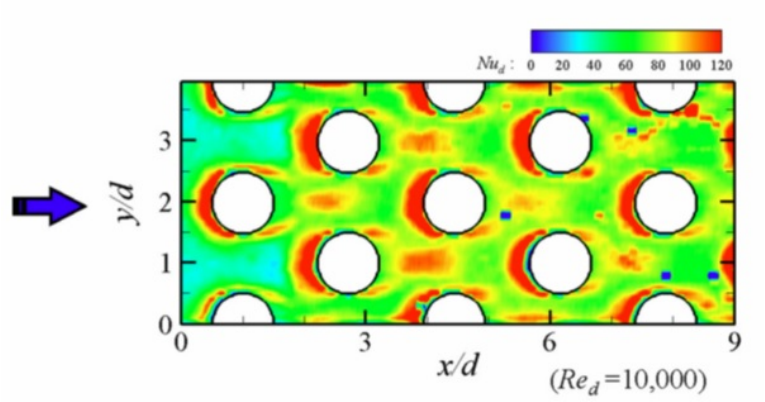

Figure 2.5: Illustration of the breaking up of (thermal) boundary layers [27]. The colors represent Nu_d (red indicates a high Nu_d)

The more the better? Optimization in forced convection

The last paragraph suggests that placing a very large amount of pin fins is the most optimal solution to increase the heat transfer rate. However, practically, this is never applied. First of all, there is the high manufacturing cost of making dense finned heat exchangers/heat sinks. Secondly, placing more obstructions increases the pressure drop over the heat exchanger/heat sink. In forced convection with air this pressure drop needs to be overcome with a fan. The bigger the fan, the more energy will be used. This pressure drop can also be seen as a hydraulic

resistance imposed by the fins on the fluid[2]. In the case of flow through a pipe, the hydraulic resistance κ can be written as a function of the Darcy friction factor f as: $\kappa = fL/D$ [18].

Practically, for all kinds of heat exchangers/heat sinks, researchers want to determine the heat transfer coefficient for different kind of fins and geometries. For this work only **heat sinks** are of interest. In a study on heat sinks, the authors typically work with one or a combination of the following options (each having their limitations which will be discussed in Chapters 3 and 4):

- Search for a correlation of a finned structure in open literature and use it to design the heat sink. Although the uncertainty on a Nusselt number correlation is quite high;
- Perform a numerical simulation of (a part) of the heat sink using CFD (most of the time to optimize the heat sink itself);
- Perform an experimental study by testing a specific heat sink.

The fluid that is mostly used in the study of heat sinks because of its omnipresence is air. Air-cooled heat sinks can be divided according to the manufacturing method. The production cost is proportional to the thermal performance. However, as discussed in the previous paragraph, the overall performance is a trade-off between pressure drop and heat transfer coefficient.

All heat sink types used in forced convection with air are summarised in Figure 2.6. These heat sinks are commercially available. **Forged heat sinks** (see Fig. 2.6a) are low cost and can be made in mass production. **Extruded fins** (see Fig. 2.6b) are most commonly used in thermal applications, they are mostly made of aluminium. Sometimes the produced extrusions are cross-cut to make rectangular pin fins. The drawback of this production method is that the width and height of the heat sinks are limited by the power required to extrude. Furthermore, there are so-called 'extrusion limits': a limited height-to-gap ratio, a maximum base-to-fin thickness and the minimum fin thickness-to-height. The maximum attainable height-to-gap ratio is 10 to 1 with a minimum fin thickness of 0.8 mm. **Bonded heat sinks** (see Fig. 2.6c) can overcome the maximum height-to-gap ratio and maximum size of the extruded heat sinks. However, the process to make bonded heat sinks is not automated, the fins are glued or brazed to the substrate, which makes them very expensive to manufacture.

[2]Similar reasoning will be made in case of buoyancy-driven convection.

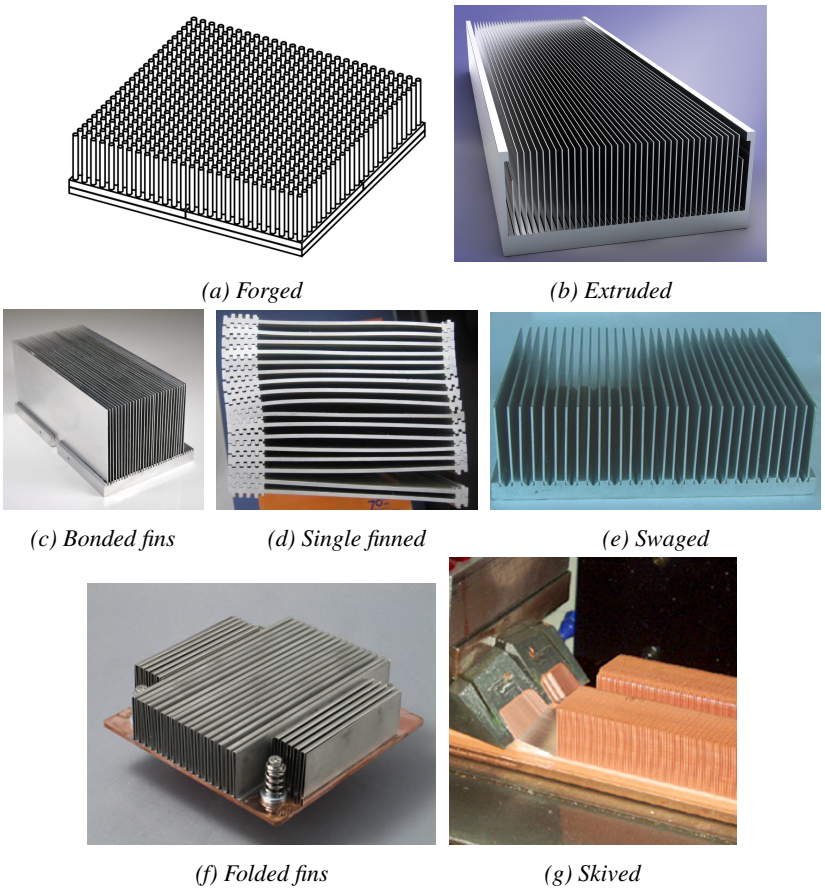

(a) Forged *(b) Extruded*

(c) Bonded fins *(d) Single finned* *(e) Swaged*

(f) Folded fins *(g) Skived*

Figure 2.6: Types of heat sinks for use in forced convection with air

A **swaged heat sink** (see Figure 2.6e) provides an alternative way to attach the fins to the substrate: here a double fin (folded sheet) is pressed in a machine groove. Sometimes the substrate is combined with the fins. These heat sinks are called **single fin heat sinks** (see Fig. 2.6d). The fins are alternately stacked with a spacer and everything is brazed together. **Folded fins** (see Fig. 2.6f) are made out of corrugated sheet metal glued or brazed to the substrate. Folded fins are mainly used with a ducted forced airflow and have a high performance. These heat sinks are very expensive but light. The last type of heat sink that can be used is the **skived heat sinks** (see Fig. 2.6g). These are made out of one piece of copper, resulting in very small fins. This will increase the thermal performance, cost and pressure drop penalty.

2.3.2 Natural convection

Natural convection refers to convection problems in which the fluid is thermally driven instead of mechanically. The fluid motion is buoyancy-driven, meaning that the flow is induced by density gradients in the fluid as it is heated or cooled. This heat transfer mode will also create a thermal and velocity boundary layer. As natural convection is the main focus of this work, the boundary layer equations for a flat vertical plate in natural convection will be discussed in more detail. One of the most used approximations to model a fluid in natural convection, the Boussinesq approach, will also be discussed.

For a vertical flat plate, where the gravitational term is aligned with the plate in the x-direction, the standard Navier-Stokes equation in steady-state is given as Eq. (2.17).

$$\rho\left(u\frac{\partial u}{\partial x}+v\frac{\partial u}{\partial y}\right)=-\frac{dp}{dx}+\mu\left(\frac{\partial^2 u}{\partial x^2}+\frac{\partial^2 u}{\partial y^2}\right)-\rho g \tag{2.17}$$

First of all, note that in case of a flat plate, the pressure gradient in the y-direction can be neglected [17, 24]. Far away from the plate, the fluid is stagnant everywhere. This leads to the following equation, in which all velocities are equal to zero:

$$\left(\frac{dp}{dx}\right)_{y\to\infty}=-\rho_{T=T_\infty}g \tag{2.18}$$

With the help of Eq. (2.18), Eq. (2.17) can be rewritten as:

$$\rho\left(u\frac{\partial u}{\partial x}+v\frac{\partial u}{\partial y}\right)=g\left(\rho_{T=T_\infty}-\rho\right)+\mu\left(\frac{\partial^2 u}{\partial x^2}+\frac{\partial^2 u}{\partial y^2}\right) \tag{2.19}$$

This equation is, most of the time, simplified through the Boussinesq approximation, which is a modelling approach for the density of the fluid (in this work: air). In natural convection, the density difference is driven by a temperature difference. The idea of the Boussinesq approach is that for *moderate* temperature changes, density depends almost linearly on temperature according to:

$$\rho_{T=T_\infty}-\rho_{T=T_s}=\left(\frac{\partial\rho}{\partial T}\right)_p\left(T_\infty-T_s\right) \tag{2.20}$$

Based on this the volumetric thermal expansion coefficient (β) can be defined:

$$\beta=-1/\rho\left(\frac{\partial\rho}{\partial T}\right)_p \tag{2.21}$$

In this way, $\rho_{T=T_\infty}-\rho_{T=T_s}$ can be written as $-\beta\rho(T_\infty-T_s)$. Although the volumetric thermal expansion coefficient is known for typical fluids that are

studied in natural convection, this simplification can only be used for *small temperature differences*, thus it is not always recommended. According to the manual of Ansys/Fluent [28], $\beta(T_\infty - T_s)$ has to be much smaller than 1. In Chapter 4, where the parameters of the numerical simulations will be discussed, the limitations of this approximation will be discussed further.

The more fins the better? Optimization in natural convection

As in the case of forced convection (Section 2.3.1), fins are generally added to a base plate in order to increase the surface area and break up the boundary layers. Although no mechanical equipment is used to generate the flow, the resistance against flow penetration through the heat transferring structure (similar to pressure drop) is very important in natural convection. In this perspective, very complex fins are not used in heat sinks for natural convection. Very densely packed plain or pinned fins are also not used as these will induce a very high hydraulic resistance which makes it impossible for the fluid to penetrate into the heat transferring structure.

Due to limited temperature differences between the substrate and the environment (max $80°C$) in electronics cooling, the density gradients will also be limited. This means that the resulting velocities over the fin structure in natural convection will be lower compared to forced convection. The boundary layer will also be thicker compared to forced convection. This means that the heat transfer coefficient will be lower, as is the maximum attainable heat transfer rate.

Still the aim for authors in open literature is to determine the heat transfer coefficient of different fin structures. As for forced convection, this can be extracted from correlations in literature, CFD simulations and/or experiments.

From the heat sinks presented in the section on forced convection (Section 2.3.1, Fig. 2.6), only the **extruded and forged heat sinks** can be used in natural convection. Even for these heat sink types, the fin density cannot be very high, otherwise no air will be able to penetrate into the fin structure. Typically two structures either made through extrusion or forging are commercially available and used in applications [29]:

- Plain finned heat sinks (see Figure 2.7c): these are rectangular fins, sometimes they are also interrupted.

- Pin finned heat sinks (see Figure 2.7a): all kinds of pin shapes are possible such as elliptical designs, circular, rectangular...

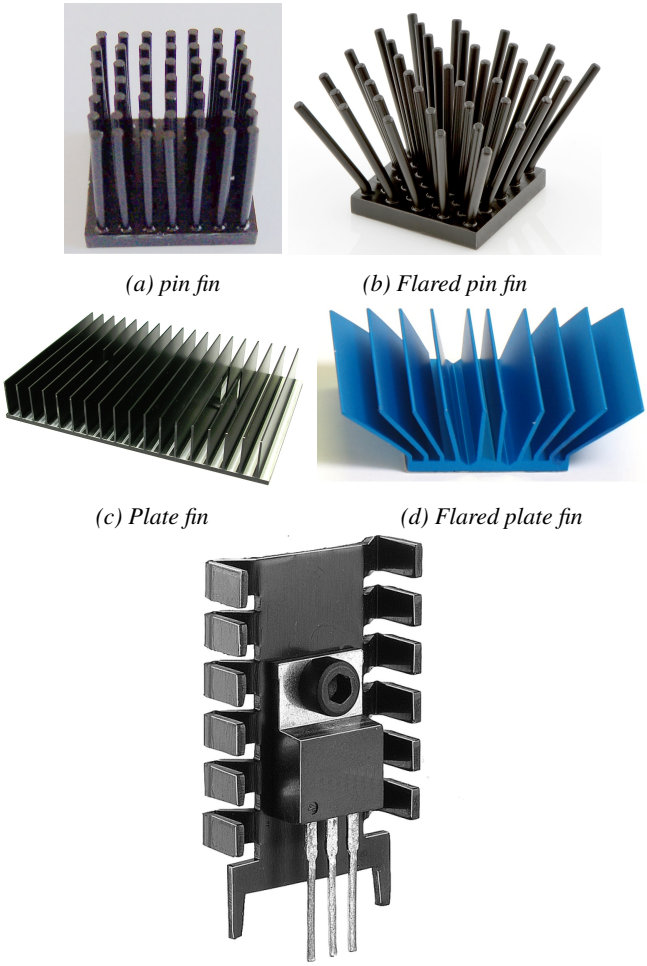

(a) pin fin *(b) Flared pin fin*

(c) Plate fin *(d) Flared plate fin*

(e) Stamped fin

Figure 2.7: Types of heat sinks for use in natural convection

In some cases, after producing the heat sink, the fins are pulled away from each other. They are called **flared heat sinks** (see Figs. 2.7b and 2.7d). According to some literature sources, flaring the heat sinks increases the heat transfer rate as it is easier for the air to penetrate into the heat sink. Of course the surface to volume ratio will become smaller, as the volume taken by the heat sink increases, while the heat transferring surface area remains the same.

Besides extruded and forged heat sinks, **stamped heat sink** can also be used in natural convection (see Fig. 2.7e). This is the cheapest air-cooled heat sink solution available because the mass production process is automated. Stamped heat sinks have also very simple shapes. However, due to the small

surface-to-volume ratio it has a low thermal performance.

2.4 Basics of electronics cooling with heat sinks in natural convection

2.4.1 Introduction

Electronic equipment is present in nearly every aspect of modern life, from toys and appliances to high-power computers. The reliability of the electronics is a major factor in the overall reliability of the complete system. To perform the duties of electronic components, an electric current has to pass through. Since current flow through a resistance is accompanied by heat generation (law of Joule) this creates potential sites of excessive heating. Furthermore, the continuous miniaturization of electronic systems has resulted in a dramatic increase in the amount of heat generated per unit volume.

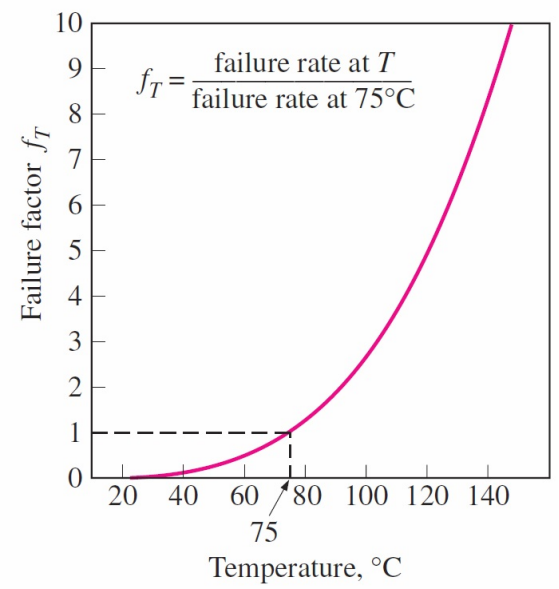

Figure 2.8: The increase in the failure rate of bipolar digital devices with temperature [30]

The narrow band where two different regions of a semiconductor (e.g. p-type and n-type regions) come in contact is called a junction. Junctions are sites of heat generation and thus the hottest spots in a component. In silicon-based semiconductor devices, the junction temperatures of the chip should be lower than

120°C in a continuous regime for safe operation [30][3]. However, even lower junction temperatures are desired for longer lifetime and lower maintenance costs. In Figure 2.8 the failure rate of a bipolar digital device is shown as a function of the temperature. Compared to the failure rate at 75 °C, the failure rate at 100 °C is already a factor 2 higher.

Figure 2.9 shows a simplification of an electronic component [30]. This component consists of the actual chip, the **lead frame**, the electrical connections (**leads**) and the **chip carrier**. This carrier can be made out of ceramic, plastic or glass in order to protect the circuit against environmental effects. The chip is secured in the carrier, bonded to the bottom surface. The thermal expansion coefficient of the plastic is about 20 times higher than that of silicon. Therefore, bonding the silicon chip directly to the plastic case would result in such large thermal stresses that the reliability would be seriously jeopardized.

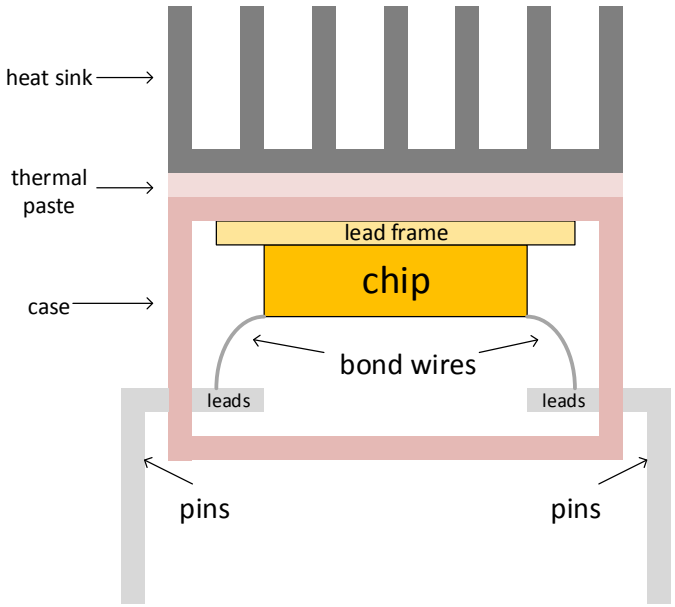

Figure 2.9: An illustration of the simplified thermal circuit for a chip

To avoid this problem, a lead frame made of a copper alloy with a thermal expansion coefficient close to that of silicon is used as the bonding surface. The design of the chip carrier is the first level in the thermal control of electronic devices, since the transfer of heat from the chip to the chip carrier (or case in

[3] peaks up to 300°C are easily manageable.

Fig. 2.9) is the first step in dissipating the heat generated by the chip. The heat generation by the chip is transferred to the case of the chip carrier through a combination of all heat transferring modes discussed in Sections 2.1, 2.2 and 2.3.

However, from Fig. 2.9, it is clear that in this chip carrier design, the thermal aspects were not the prime concern. The chip case itself will not be able to dissipate much energy as the cavity of the case is filled with an inert gas for protective reasons, which is a very poor heat conductor. Therefore, most energy will be dissipated through the lead frame to a heat sink on top of the chip (Fig. 2.9).

To calculate the temperature of an electronic device, an equivalent electrical scheme is assumed in Fig. 2.10 [30]. The maximum amount of heat Q_{chip} which the electronic device can dissipate, is specified in the data sheet. Between the ambient and the chip temperature (or junction temperature) there are three thermal resistances[4]: the **junction-to-case resistance** R_{jc} (Section 2.4.2), the **case-to-sink resistance** R_{cs} (Section 2.4.3) and the **sink-to-ambient resistance** R_{sa} (Section 2.4.4).

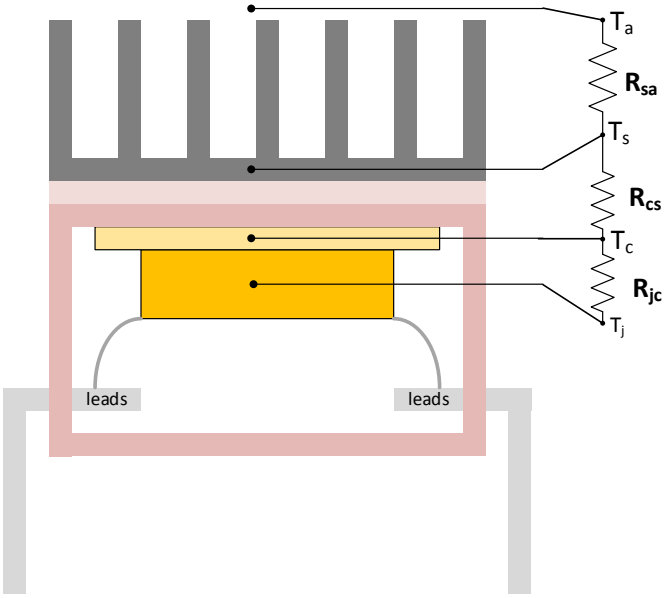

Figure 2.10: An illustration of the simplified thermal circuit for a chip in terms of thermal resistance.

[4]The use of thermal resistances was already introduction in Sections 2.1 , 2.2 and 2.3 e.g.

The maximum allowed thermal resistance, R_{sa}, to keep the junction temperature T_j below a certain threshold, can be calculated through Eq. (2.22). This value can be used to select the right heat sink. Most of the time heat sink manufacturers report this thermal resistance in their data sheets.

$$R_{sa} = \frac{T_j - T_a}{Q_{chip}} - R_{jc} - R_{cs} \tag{2.22}$$

Extra remark for sake of completeness

In practical applications, there will be not be a heat sink for each chip. In e.g. a laptop the two major energy users (the Central Processing Unit (CPU) and the Graphical Processing Unit (GPU)) will be placed on the evaporator side of a heat pipe, shown in Fig. 2.11. From the evaporator side of the heat pipe, the energy is transferred to a single heat sink, which is cooled in this specific case through a fan. In the latest design of laptops, like the 2016 edition of 12" Apple Macbooks, a fan is not even required [31].

The use of the heat pipe is extremely helpful here as it will not only transfer the dissipated energy away from the junction, it will also uniformise the heat sink temperature, there will be no hot spots; which will decrease the thermal resistance to ambient (R_{sa}).

In the following paragraphs, the thermal resistances presented in Figure 2.10 will be discussed further.

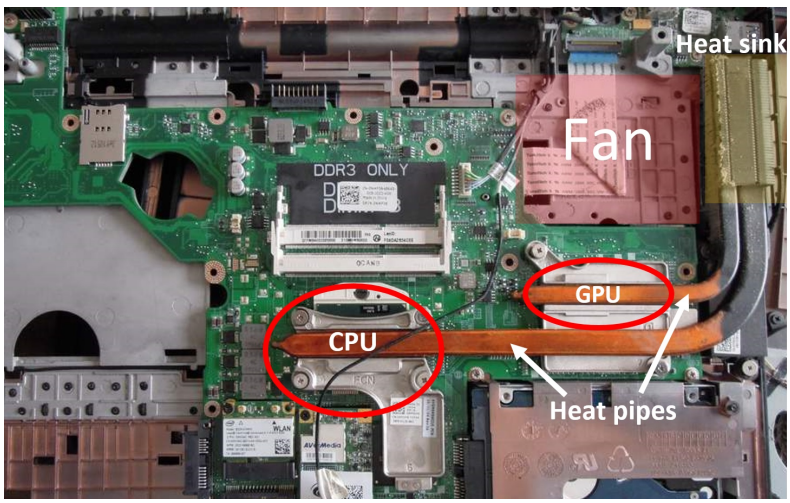

Figure 2.11: Heat pipe cooling system used in a Dell laptop

2.4.2 Junction-to-case resistance

The junction-to-case resistance (R_{jc}) depends on the material, size and geometry of the chip and its package. The resistance should be given in the data sheet by the chip manufacturer. However, there are different aspects in how to measure this junction-to-case resistance. The Joint Electron Device Engineering Council (JEDEC) published the EIA/JESD 51 series document in which they specify the conditions under which this resistance should be measured. However, sometimes these conditions are not followed and the deviations from the standards are not documented. Furthermore, in the JEDEC specification, two test board types are allowed. Moreover, depending on the tested package type, the allowed test board can result in a difference in junction-to-case resistance by a factor 2 [32].

However, as this resistance is not of interest to this work, this will not be discussed in further detail.

2.4.3 Case-to-sink resistance

The case-to-sink resistance (R_{cs}) consists of two resistances: the **interface (or contact) resistance** and the **spreading resistance**. Both resistances are very difficult to determine in practice.

2.4.3.1 Thermal interface (or contact) resistance

The interface resistance is a result of an incomplete contact between two surfaces. This is caused by imperfections in surface finish, which will always be present. For example in case of a heat sink this resistance occurs at the contact area between a fin structure and a substrate [33]. The energy flow through two surfaces is represented in Fig. 2.12. Heat transfer in between two 'imperfect' surfaces consists of three components [34]:

- conduction through the actual contact spots
- conduction through the interstitial medium, such as air
- radiation

In case of heat sinks, there will not be any influence of convection as the order of magnitude of the gaps is too small (around 1 μm). Radiation can also be neglected for temperatures under 300 °C [33]. However, the conduction through the interstitial medium is not negligible because the area that is in contact with this medium is 2 to 4 orders of magnitude larger than the contact area between the solids, as can be seen in Fig. 2.12.

Madhusudana [35] even mentioned that in case of forced convection with a heat sink, the thermal contact resistance can be up to 50% of the total thermal resistance of the system.

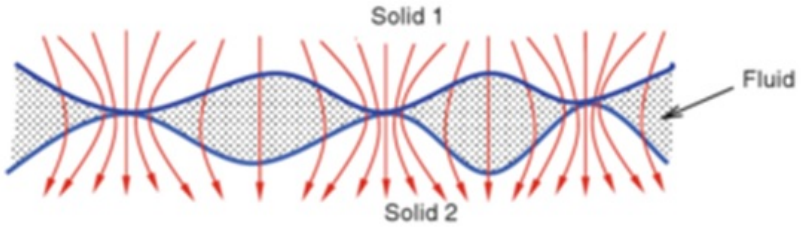

Figure 2.12: Heat flow through a joint [35]

In case of fins attached to a surface, several options exist to minimize the contact resistance [36]:

- Pay a lot of attention to the surface finish of each surface, as this will influence the surface roughness. With increasing surface roughness, the contact area between the two solids will reduce.

- Choose a better or more optimal contact technology. In case of pressed-fit the applied pressure can be increased. The higher the pressure, the smaller the contact resistance. Dependent on the micro-hardness of the material, the deformation caused by the applied pressure will be higher or smaller. Also another contact technology can be used, like glueing, brazing, soldering or co-casting.

- A thermal paste or pad can be used (see Fig. 2.13) this paste or pad fills the gaps between the two components. As this paste or pad has a higher thermal conductivity than the interstitial medium, the contact resistance is reduced. Also the thermal conductivity of both contacting solid materials is of importance.

Extensive studies have been performed to quantify the thermal contact resistance [37]. The different models are classified based on whether the deformation of the micro contacts are considered plastic or elastic in nature. The real contact area is proportional to the applied load, which implies that the deformation is plastic in nature. Hence all earlier theories were formulated based on the assumption that the deformations were plastic in nature and they did not account for the elastic deformations beneath the surface. This approximation is accurate if the elastic moduli of the contacting bodies were infinity or if the distances between the micro contacts were small such that the elastic deformation on both the micro contacts were the same. However, these assumptions are not true for most practical cases [36].

Figure 2.13: Illustration on how thermal paste is applied to heat transferring surfaces

2.4.3.2 Spreading resistance

The spreading resistance is a result of the mismatch in contact area. This is because the energy dissipater (e.g. a chip) does not have the same size as the heat sink. The way the heat is spread over the mismatched surface will have an impact on the thermal performance of the heat sink. In case of forced convection, this equivalent thermal resistance can be as high as 30% of the total value [38].

Depending on the spreading problem (namely: the specific mismatching areas), there are lots of ways how to calculate the spreading resistance. However, all of them are quite complicated to use. One of the most common used methods in case of a rectangular dissipater is the *fixed-angle spreading model*, as shown in Fig. 2.14. This method assumes that the heat flux from the source spreads to fill a cone where ϕ is the heat spreading angle. For steady and 2D heat transfer, and if the conduction cone from Figure 2.14 is not truncated before the outermost flux lines reach the bottom plane, the expression of the spreading resistance is quite simple [23]:

$$R_{spreading} = \frac{t}{k\Delta x(\Delta x + 2t\ tan\phi)}, \tag{2.23}$$

In this equation t denotes the thickness of the substrate, Δx the width of the dissipater and k the conductivity of the material. The angle ϕ will be influenced by all boundary conditions of the substrate/heat sink.

However, practical systems are much more complicated. For example, the heater itself is not uniform (even not in experimental setups). Hence the flux from the heater to the substrate is not uniform. Furthermore, the convective heat losses provided by means of the heat sink will also not be uniform, certainly in natural

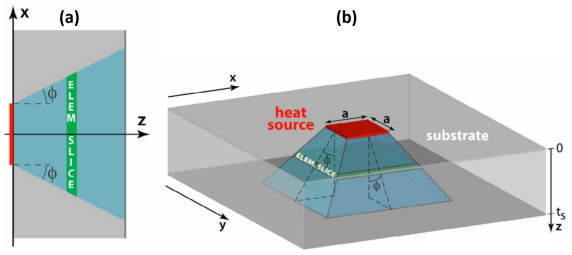

Figure 2.14: Fixed-angle heat spreading model for a square heat source on a rear-cooled substrate (a) illustration of spreading angle; (b) geometry [39]

convection where the middle of the heat sink will not be provided with fluid. Finally, the heat transfer can also be transient, making it even more complicated to calculate this resistance.

In case of fins that are attached to a surface, several options exist to minimize this spreading resistance:

- Use a thick and good conducting substrate. This can be explained with Eq. (2.23). If the thickness of the substrate increases above a certain level, the dependency of the conductive resistance on the convective one will be negligible. This is called Biot independency [38]. Furthermore, when the surface area of the electronic device is large compared to that of the heat sink, a much thicker substrate is needed to reach this state.
- Use heat pipes (so-called surface-embedded heat pipe heat sinks [40]) or vacuum chambers and liquid cold plates in order to uniformise the heat flux.

Furthermore, the substrate sometimes consists of multiple solid layers, for example to measure the temperature in between the layers [41]. In these cases, the case to sink resistance will be a very complex combination of both the interface and spreading resistance: firstly the heater itself will not be completely uniform. Secondly, there will be a contact resistance between the two solid layers. These point-wise resistances will give rise to spreading resistance for the following layer. Of course, for these applications, it is practically not possible to calculate these resistances theoretically.

2.4.4 Sink-to-ambient resistance

The sink-to-ambient resistance (R_{sa}) is the thermal resistance of the heat sink. Normally, it is this resistance that the manufacturers report (in K/W). Hence, this resistance is a combination of conductive, convective and radiative properties of the heat sink.

This resistance depends on:

- Temperature difference over the heat sink
- Box geometry: enclosure
- Fin structure: kind of material, kind of fins, emissivity of the material
- Orientation of the heat sink

This is also the main thermal resistance that will be modelled in this work.

2.5 Electronics cooling using (new) fin structures

As mentioned in the previous sections of this work, the addition of fins causes an increase in the initial price, weight and pumping power needed under forced convection conditions. For this reason, there are numerous research studies in open literature, searching for an 'optimal' fin style.

In optimization routines, researchers typically use two kinds of clusters [42]:

- The cluster involved in determining the profile of the fin for a given heat transfer rate, using a minimum of material
- A cluster working on the fin dimensions for a given fin form and desired heat transfer rate, using a minimum of material

In these routines, researchers typically use analytical expressions of the finned structures in their optimization algorithm. Other ways to find 'better' fin structures is studying them numerically (through CFD) or experimentally.

In forced convection fin structures can be **perforated** in order to decrease their friction coefficient [43] (Figure 2.15(a)). Of course, the convection coefficient will be lowered too, but as always, the performance is a combination of both thermal and hydraulic effects. In natural convection, perforation can increase the heat transfer rate because there are more possibilities for air to penetrate into the fin structure [44]. However this increase in heat transfer rate depends on the shape and structure of the fin (height, fin conductivity, fin spacing...) itself [45].

Dogan et al. [46] made some modifications to existing extruded fin shapes (Figure 2.15(b)). The numerical study was done for natural convection in a specific amount of fin material. It was shown that significant increases in heat transfer rate can be reached.

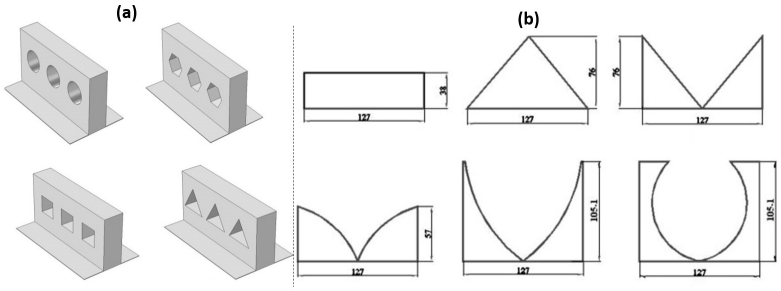

Figure 2.15: Illustration of new fin shapes studied (a) perforated fins [43]; (b) modified extruded fins [46]. The gravitational force vector is vertically downwards in the plane of the figure.

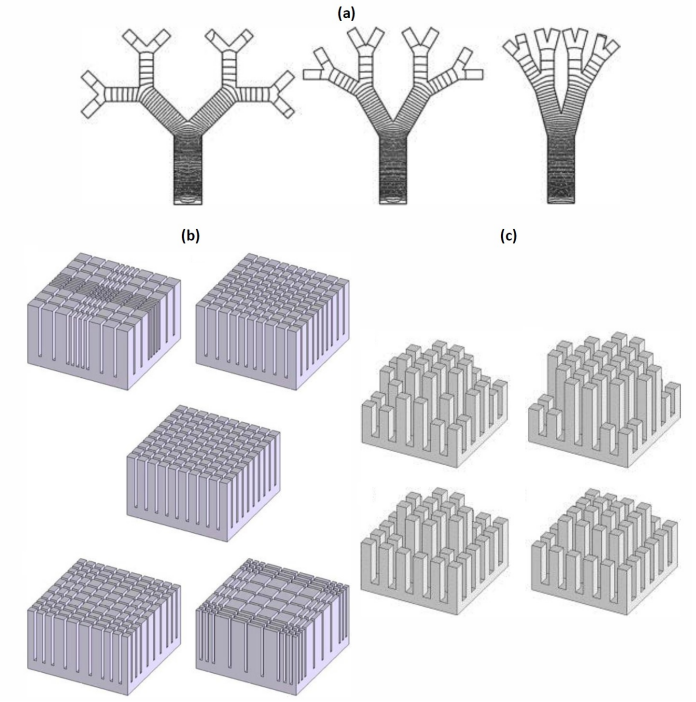

Figure 2.16: Illustration of new fin shapes based on optimisation (a) tree-shaped fins [47] ; (b) not uniform fin width designs [48] ; (c) not uniform fin height designs [49]. The gravitational force vector is vertically downwards in the plane of the figure.

Optimization routines result in much more complex fin shapes compared to the perforated types. Bejan [50] developed a solution for optimizing conduction

paths for an application in cooling a heat generating volume and found the paths forming a tree-like network [47]. The optimization technique of Bejan is known as the Constructal Theory. It states that finite-volume systems evolve to afford easier access to the imposed currents that flow through it. This explains the natural tendency of flow systems to evolve toward greater flow access. The resulting tree-shaped fins are shown in Figure 2.16(a). Yang et al. on the other hand tried to optimize an existing heat sink by either changing the width of it [48], or the height [49].

However, as can be seen in Figure 2.15 and 2.16, these new fin designs are quite difficult to manufacture. Therefore they are not commercially available. Even with 3D printing, these new fin designs will cost a lot more than the conventional designs and for some designs it will not even be possible to make them. It is in this new approach to novel fin designs that porous media came into play. Porous media on itself is not new, it is present in nature, e.g. the natural distribution and infiltration of water in rocks. In 1856, Darcy [51] was the first one to describe the flow of water through beds of sand based on experimental data. This resulted in the Darcy law, which will be discussed extensively later in this work.

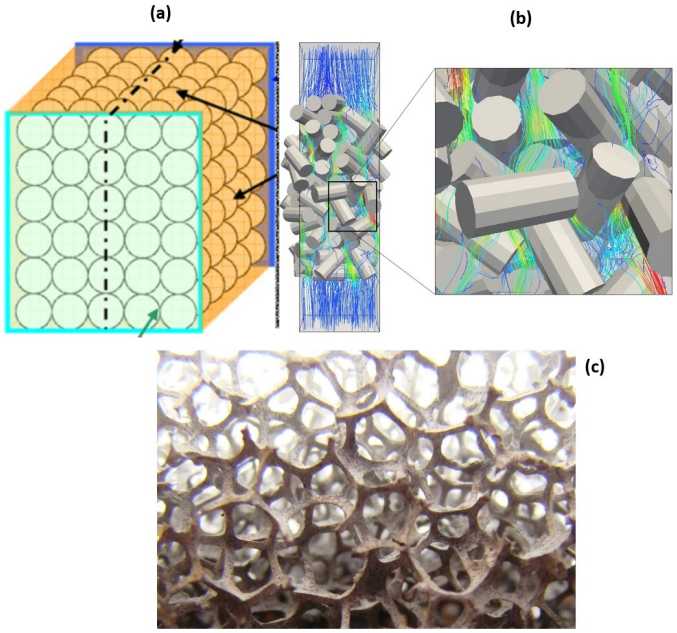

Figure 2.17: Illustration of new fin shapes made out of porous materials (a) a packed bed of spheres [52]; (b) bed of small diameter cylinders [53]; (c) open-cell metal foam

The first porous medium that was used as heat sink for electronics cooling was

a packed bed of spheres (see Figure 2.17(a)) and a fixed bed of small-diameter cylinders (see Figure 2.17(b)). This porous medium is characterized with a porosity around 60%. Another kind of porous medium which is more recent is metal foam and more specific: open-cell metal foams (see Figure 2.17(c)). This material is already discussed in Chapter 1, Section 1.2.3. In what follows, work towards modelling and testing this material as a heat sink will be discussed.

2.6 Dimensionless numbers

In this section the dimensionless numbers, that will be used later in this work, will be discussed.

2.6.1 Reynolds number

The Reynolds number Re_L (Eq. 2.24) is typically defined as a dimensionless ratio of the inertial forces to the viscous forces. The so-called critical Reynolds number determines whether or not the flow is turbulent or laminar.

$$Re_L = \frac{\rho v L}{\mu}, \tag{2.24}$$

In this equation ρ and μ are the density and dynamic viscosity of the fluid, respectively. v is a velocity, most of the time this is the mean velocity of the incoming flow and L is the characteristic length. This length is of course very dependent on the case/material that is studied.

2.6.2 Prandtl number

The Prandtl number Pr (Eq. 2.25) is a dimensionless ratio of momentum diffusivity to thermal diffusivity.

$$Pr = \frac{\nu}{\alpha}, with\ \alpha \ = \frac{k}{\rho c_p}, \tag{2.25}$$

In Eq. 2.25 k and c_p are the thermal conductivity and specific heat of the fluid, respectively. ν is the kinematic viscosity ($\nu = \mu/\rho$). When the Prandtl number is smaller than 1, like in the case of air, the thermal diffusivity dominates. This results in a thermal boundary layer thicker than the velocity boundary layer.

2.6.3 Grashof and Rayleigh number

The Grashof number Gr_L (Eg. 2.26) is typically used with buoyancy-driven convection. It is the dimensionless ratio of the buoyancy to the viscous forces.

$$Gr_L = \frac{g\beta(T_s - T_\infty)L^3}{\nu^2}, \tag{2.26}$$

In Eg. 2.26 β is the volumetric thermal expansion coefficient. T_s is the surface temperature and T_∞ is the bulk temperature of the fluid. It is not always straightforward to define this temperature. Again L is a characteristic length. In fact, the Grashof number is the equivalent of the Reynolds number in buoyancy-driven flows. If $\frac{Gr}{Re^2} \gg 1$

Furthermore, in most correlations, the Grashof number is not directly used. Instead the Rayleigh number Ra_L is used (Eq. 2.27).

$$Ra_L = GrPr \tag{2.27}$$

2.6.4 Nusselt number

The Nusselt number Nu_L (Eq. 2.28) is the ratio of convective to conductive heat transfer across a boundary.

$$Nu_L = \frac{hA\Delta T}{kA\Delta T/L} = \frac{hL}{k}, \tag{2.28}$$

In Eq. 2.28 k and h is the thermal conductivity and convection coefficient of the fluid, respectively. Typically the Nusselt number is used in a correlation of the form: $Nu_L = f(Re_L, Pr)$ or $Nu_L = f(Ra_L, Pr)$, dependent on whether active or passive systems are studied.

2.6.5 Darcy and Fanning friction factor

The friction factor f is a dimensionless number to express pressure drop in forced convection. There are two definitions for f: the Darcy/Weisbach friction factor f_D (Eq. 2.29) and the Fanning friction factor f_F (Eq. 2.30). Both definitions differ by a factor 4. As can be seen in Eq. 2.30 the Fanning friction f_F can also be expressed using the shear stress at the wall, given by τ.

$$f_D = \frac{\Delta p}{L/D\rho v^2/2} \tag{2.29}$$

$$f_F = \frac{\Delta p}{L/D2\rho v^2} = \frac{\tau}{\rho v^2/2} \tag{2.30}$$

2.6.6 Biot number

The Biot number Bi_L (Eq. 2.31) is the dimensionless ratio of the conductive resistance to the convective resistance of the heat sink. Very small Biot numbers lead to very uniform temperatures as convection to the ambient will be limited.

$$Bi_L = \frac{hL}{k_{material}} \tag{2.31}$$

2.6.7 Darcy number

The last dimensional number that will be used in this work is the Darcy number Da (Eq. 2.32). This number is typically used when working with porous materials. It is the dimensionless ratio of the permeability of the porous medium K and its substrate area L^2.

$$Da_L = \frac{\kappa}{L^2} \tag{2.32}$$

3

Experimental heat sink research in buoyancy-driven flow

As discussed in the review by Nagarani et al. [42], there are experimental, numerical and analytical methods to report investigations considering extended surfaces.

In this work, the focus will be on experimental (Chapter 3) and numerical methods (Chapter 4). In this chapter, the existing literature on experimental studies on classical heat sinks and heat sinks made out of open-cell metal foam in buoyancy-driven flow is discussed. However, in Section 3.3 the specific approach to study open-cell metal foam is also discussed.

To study buoyancy-driven heat transfer experimentally, many parameters need to be considered (some of these parameters were already discussed in Section 2.4.4):

- **Working fluid.** Of course, when using working fluids other than air, the heat transfer coefficient will change. In this work, however, only air is studied.
- **Geometrical characterization of the extended surface: used material, spacings, height, substrate dimensions and emissivity of the material.** These parameters are not always reported, this is certainly the case in studies on metal foam or numerical studies [41, 46]. For buoyancy-driven flows, the effect of the substrate dimensions (their length-to-width ratio) will be of importance, as it will influence the ability for the air to penetrate into the extended surface structure.

- **Box geometry.** This refers to the enclosure. Typically, an enclosure is mounted around a heat sink (e.g. a computer chip and its heat sink in a laptop). When a closed box is used, the heat exchange between the box and the surroundings (and thus the temperature in the box) will influence the heat transfer rate. Typically, this results in a Nusselt number correlation which is a function of the aspect ratio of the box geometry [20]. When the box is open on one or two sides, the dimension of the box will affect the intake of air, the flow pattern in the box and thus the resulting heat transfer rate.

- **Heat sink orientation.** This is a parameter of importance in case of orientation dependent fins.

- **Temperature of the surface.** Depending on the imposed surface temperature, different natural convection flow regimes can occur, which trigger a different thermo-hydraulic behaviour.

- **Bonding method between substrate and fins**. For example in metal foam heat sinks, the foam has to be connected to the substrate. This will introduce a significant thermal resistance against heat transfer to the extended surface [54]. This is a problem which is not encountered with extruded heat sinks.

- **Specific construction of the test rig**: e.g. the heat flux uniformity (quality of the heater), if a thermal paste is used and which type and the position of the thermocouples. Note that this is not only an issue for experimental studies. If numerical work is to be used to predict experimental performance of the heat sink, these parameters also need to be known.

At least two specific things need to be discussed in case of experimental research: the test rig and the comparison method of the results. Neither in industry, nor in academic literature, is there any standard in how to test heat sinks in buoyancy-driven convection. As will be illustrated later on, this makes it very difficult to compare results from different authors.

3.1 Test rig design

Firstly, some experimental test facilities are discussed to test extended surfaces in buoyancy-driven convection. Also the test rigs used to study open-cell metal foam heat sinks are discussed. In section 3.1.1 the information on test rigs used in industry is discussed. In the following sections 3.1.2, 3.1.3 and 3.1.4 test rigs used in academic research are discussed. Generally, more information is known about academic test facilities compared to industrial research.

3.1.1 Test rigs used by heat sink manufacturers [29, 55, 56, 57]

In this section, an overview of the test rigs used by common heat sink manufacturers is given. The heat sink manufacturers discussed in this section are limited compared to the total amount of existing manufacturers. This limited number of manufacturers is discussed, because some information on their testing methods was available and the types of heat sinks they offer are similar to the heat sinks of interest in this work.

3.1.1.1 Coolinnovation and Advanced thermal solutions

These two manufacturers are discussed in the same section, because both gave very little or no information on the used test facilities. Advanced thermal solutions only mentioned the maximum heat input Q for each available heat sink type. Coolinnovation doesn't give any information at all, they just mention the possible application for each heat sink and the thermal resistance. However, it is not clear which thermal resistance is given.

3.1.1.2 Aavid

In the data given by the manufacturer, little information is given about how the heat sinks are tested. The only information given is that the heat sink was tested at 75 $^{\circ}C$ above ambient temperature, the length of the heat sink was 150 mm and the heat source only covered a small part of the heat sinks' base plate. This makes it very difficult to determine the effective thermal resistance of the heat sink itself, as the spreading resistance will have a big influence on the results. Furthermore, no information is given on: the orientation in which the heat sink was tested, the finishing of the heat sink (anodized or not) and whether or not insulation is used at the back of the heat sink.

3.1.1.3 Alpha heat sinks (Japan)

Alpha heat sinks are more clear in the data they provide (see Fig. 3.1). For each heat sink, they report the heated area, orientation and heat input. However, no guard heaters are used and no information is given upon the thickness and quality of the insulation, although according to their test rig description they have used insulation material.

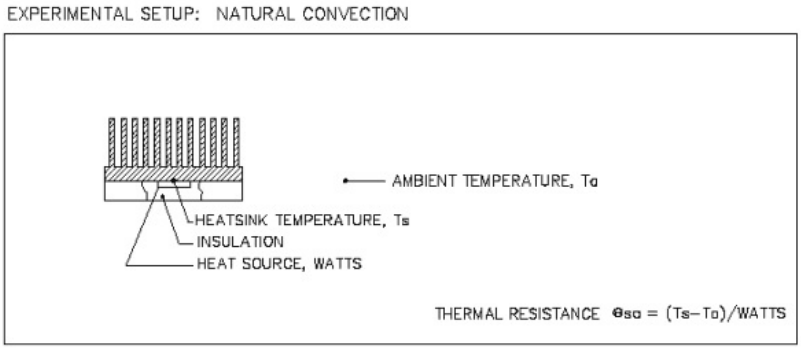

Figure 3.1: Test rig used by Alpha heat sinks (Japan)

3.1.2 Test rigs in open literature without guard heating [58, 59, 60]

The test rig as presented and used by Bhattacharya and Mahajan [58] (see Fig 3.2(a)) is a typical example of how test rigs are presented in academic literature. However, in many cases no more information is given, like in Refs. [61, 62, 63, 64]. In this case, Styrofoam (k = $0.03W/mK$) was used as insulation material with a thickness of 50 mm. The tested sample was 63.5 mm in width (thickness was not reported) and the enclosure that was used measured 304.8 x 304.8 x 457.2 mm^3. The uncertainty on the heat input Q was taken 1.5% neglecting the heat losses through the Styrofoam insulation. No information was given on possible non-uniformities of the test samples and/or use of thermal paste. The uncertainty on the heat transfer coefficient is a combination of the uncertainty on Q, A_s and ΔT and is found to be max. 1.8%.

Similar to Bhattacharya and Mahajan [58] is the work of Joo and Kim [59] (Fig. 3.2(b)) and Li and Byon [60] (Fig. 3.2(c)), although these researchers go a step further.

Joo and Kim [59] measure the temperatures at different locations. This is important, because depending on the heat sink and the heater, non-uniformities will appear over the substrate. The authors use an insulating material with a higher thermal conductivity (k = $0.25W/mK$) and tried to estimate the heat loss by measuring the temperatures at two locations as can be seen in Fig. 3.2(b). However, neither on the uncertainty analysis, nor the uniformity of the substrate or the dimensions of the insulating material, any information was given.

Li and Byon [60] did more or less the same as Joo and Kim [59] and references like [44, 65]. They also calculated Q_{loss} over the 50 mm-Bakelite insulation. This heat loss is maximally 8% according to the authors. Although, they do not report any uncertainty analysis, the maximum uncertainty on $Q_{heat\ sink}$ is 5%.

Remark that the two last authors (Refs. [59, 60]) did not use any enclosure around the heat sink.

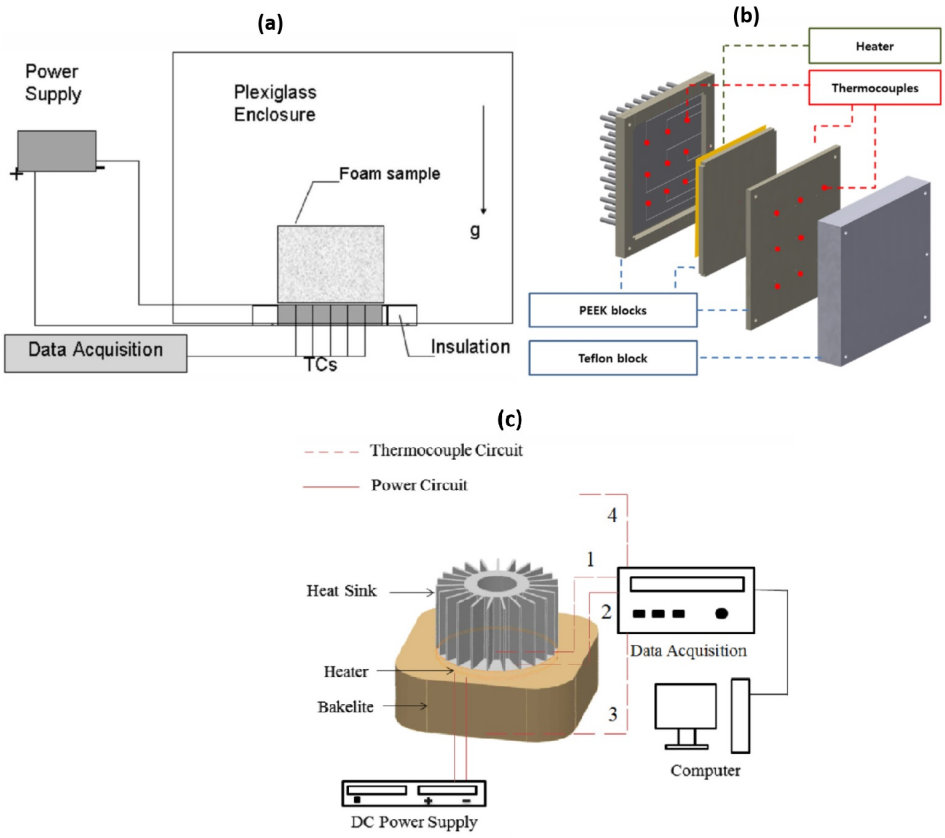

Figure 3.2: Illustration of different kind of test rigs with few information. (a) Bhattacharya and Mahajan [58]; (b) Joo and Kim [59]; (c) Li and Byon [60]

3.1.3 Test rig in open literature with guard heating in one direction [66]

The test rig reported in Sikka et al. [66] was used to test straight-fin heat sinks (see Fig. 3.3). An electrical film heater is used. One guard heater is used at the back of the heat sink to reduce heat losses (see Fig. 3.3(a)). The guard heater is kept at the temperature of the main heater in a controlled manner. Apparently, guard heaters are rarely used in natural convection test rigs. Nevertheless, authors like Zhao et al. [6] state that guard heaters are 'essential to ensure a one-dimensional heat flux through the test sample'. Furthermore, there exists a standard to design guard heaters: ASTM C1044-90 and ASTM C177. Our own research group have tested

the influence of not using guard heaters through Computational Fluid Dynamics (CFD), when no guard heaters are used, Q_{loss} can be higher than 15%, depending on the temperature difference with the ambient [16].

Furthermore, the assembly is insulated with 101.6 mm thick insulation material (again Styrofoam). To reduce the influence of the environment, a cubic insulation box is placed over the test rig as can be seen in Fig. 3.3(b).

However, no uncertainty analysis is given. The authors only mention that the uncertainty on the Nusselt number is maximally 4%.

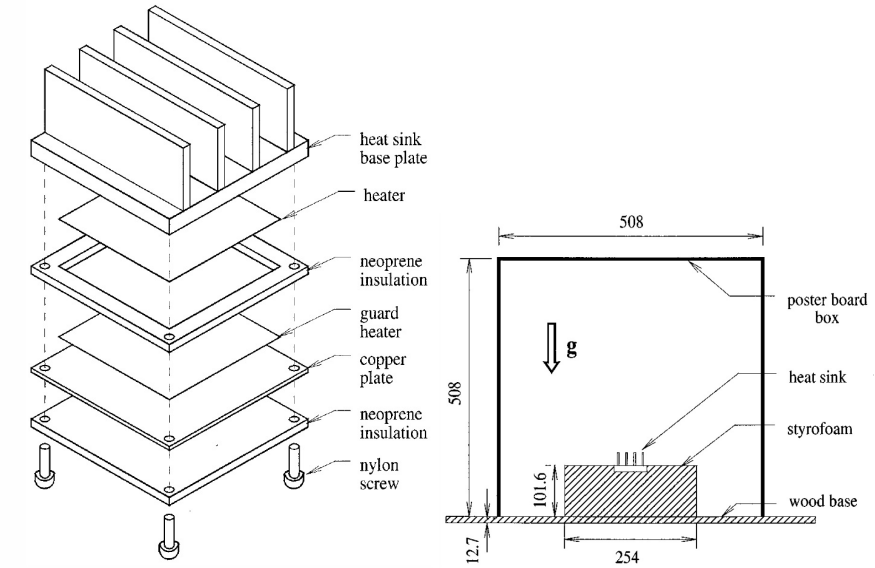

(a) heater assembly *(b) experimental setup*

Figure 3.3: Illustration of the test rig used in Sikka et al. [66]

3.1.4 Test rigs in open literature using a heater sandwiched between two heat sinks [67, 68]

Both Kamath et al.[67] and Awasarmol and Pise [68] use a similar test rig (see Fig. 3.4). The same extended surface/heat sink is placed on either side of the heater. This method has some advantages: there is no need for insulation, nor do they need to install guard heaters.

However, there are also disadvantages. For example: what is the effect of the heater on the incoming flow? What about horizontal inclination? What about thermocouple wiring and consequently their influence on the flow pattern.

Kamath et al. [67] didn't report any uncertainty analysis. The resulting maximum uncertainty on the heat flux is 4.2% and for the heat transfer coefficient

up to 6%.

Awasarmol and Pise [68] report an uncertainty on their heat flux of 1% and a maximum uncertainty on their heat transfer coefficient of 2%, without going into detail on the uncertainty analysis.

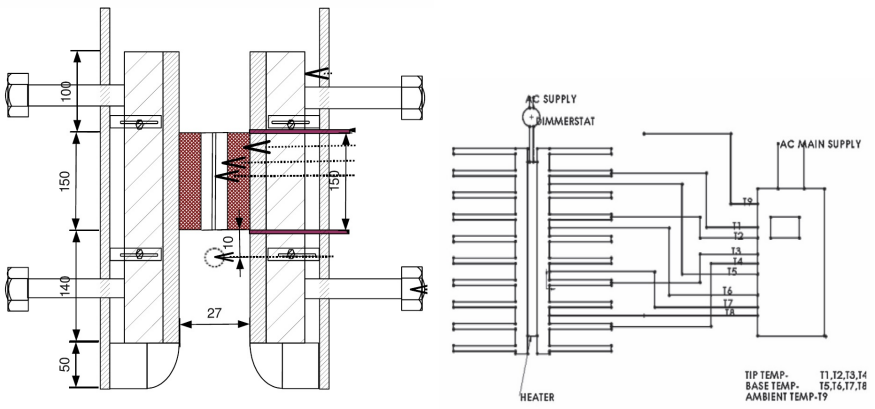

(a) Test rig of Kamath et al. [67] *(b) Test rig of Awasarmol and Pise [68]*

Figure 3.4: Illustration of an alternative approach. The gravitational force vector is vertically downwards in the plane of the figure.

3.2 Results & discussion for classical heat sinks

In open literature, many different methods are used to compare the performance of one heat sink to another. Generally a comparison between heat sinks is made based on two parameters plotted against each other graphically. However, the parameters used for this comparison can vary greatly depending on the author. Below, there is a list of possible graphs that are made to compare different heat sinks with each other:

- $Q_{in\ or\ conv}$ **vs** ΔT [16, 60]
- h or Nu **vs** ΔT or Q_{in} [58, 68]
- Nu **vs** Ra [58, 66]
- $R_{tot\ or\ conv}$ **at** T_s / $Q_{in\ or\ conv}$ [29, 55, 56, 57]

The definition and evaluation of these different parameters also differs in open literature. In the following sections, the different parameters listed above are discussed in more detail.

3.2.1 The use of different definitions of heat input

The heat input Q_{in} is a commonly used parameter. However, it is not always clear how it is defined. In this work, Q_{in} will be defined as the sum of three elements:

$$Q_{in} = Q_{conv} + Q_{loss} + Q_{rad} \tag{3.1}$$

However, it is not always clear which Q is reported and how it is defined. In fact one could expect that Q_{conv} is plotted against ΔT or the Rayleigh number Ra to compare different heat sinks. By using Q_{conv}, one is able to make a proper comparison between different literature sources and heat sinks. This is because Q_{conv} is independent of the radiative influences Q_{rad} and thermal losses Q_{loss} of the test rig that is used. However, it is quite rare to find studies that report Q_{conv}.

Authors like Harahap and Setio [69], Taji et al. [70] and Shen et al. [71] do calculate the heat loss Q_{loss} and the radiative influence Q_{rad}. They report a correlation of the Nusselt number based on the convective heat transfer rate Q_{conv}.

In contrast, in the review paper of Charles and Wang [72] the heat loss Q_{loss} is taken into account and the radiative heat transfer rate Q_{rad} is neglected. Furthermore, to calculate the convection coefficient h, the authors use Q_{in} which leads to an overestimate of h (Q_{in} is of course higher than Q_{conv}).

Guvenc and Yunch [73, 74], do correct for Q_{rad}, but they don't calculate Q_{loss}. The same is the case for Harahap et al. [75], Zografos and Sunderland [76], Rao et al. [77], Huang et al. [78] and Sertkaya et al. [79], amongst many others. Of which the latter use the Boltzmann equation[1] to estimate Q_{rad}. According to Sertkaya et al., the radiative heat transfer from surfaces through air can be of a comparable magnitude as convection (in case of heat transfer based on buoyancy).

Furthermore, how this radiative influence is determined is also important. Although a lot of studies are performed on the thermal performance of fin heat sinks, only very few deal with radiation and study the effect of thermal radiation. Khor et al. [65] discussed the difficulties in calculating the view factor. Additionally, finding an accurate value for the emissivity is quite difficult. This problem can be solved if the emissivity can be measured, but this was not the case in all above mentioned references. Khor et al. [65] showed that a bad determination of the view factor will result in even larger uncertainties compared to completely neglecting radiation. So, even if the authors calculate the radiative term, the question remains with which uncertainty this parameter (Q_{rad}) can be determined.

Sahray et al. [80] found that for a given fin height, the relative contribution of radiation is usually higher for both sparse (12 mm free space in between the pins) and dense (6 mm free space) sinks compared to the intermediate heat sinks.

[1] Please refer to Chapter 2, Section 2.2.1: $Q_{rad} = \sigma \varepsilon A(T_{hot}^4 - T_{env}^4)$. The equation only holds if the environment is a black body.

This was explained by the fact that sparse surfaces have a higher exposure to the surroundings, while in a dense sink, the inter-fin spacing behaves like a cavity, and the 'effective emissivity' is much higher than the nominal one. For pin fins, radiative contributions up to 45% of the total heat transfer rate were found. Sparrow and Vemuri [81] studied the effect of orientation and radiation on natural convection/radiation heat transfer in pin fins. The fractional contributions of radiation to the combined-mode heat transfer were generally in the 25-40% range, with the larger contributions occurring for the smaller temperature differences between substrate and environment.

Even in case of a very simple geometry, like a flat horizontal plate, there are large deviations between the different correlations that can be found in open literature. This also makes it very hard to compare numerical data with experimental data. Corcione [82] discussed this in his review paper. According to Corcione, these deviations can go up to 50%. He explains this by (1) the surface heating system, since the test setup with only a single heater as is often used does not ensure at all that the condition of uniform wall temperature is actually achieved, as the heat transfer performance of the plate is not uniform and (2) the accuracy in the evaluation of the thermal power really convected from the plate to the adjacent fluid, due to the difficulty to calculate the heat losses through the electric cables and the support assembly.

Furthermore, referring to Khor et al. [65], the determination of the radiative heat transfer will also play an important role. Table 3.1 shows the results for the heat transfer coefficient using different correlations and two different temperatures at the substrate. One can notice relative differences up to 17%.

Correlation	$h_{without\ radiation}$ for T_{hot} = $323.15K$	$h_{without\ radiation}$ for T_{hot} = $353.15K$
Ref. [17]	5.1165 $[W/(m^2K)]$	6.1832 $[W/(m^2K)]$
Ref. [83]	5.0554 $[W/(m^2K)]$	5.8226 $[W/(m^2K)]$
Ref. [84]	4.627 $[W/(m^2K)]$	5.3291 $[W/(m^2K)]$
Ref. [82]	5.1308 $[W/(m^2K)]$	6.2037 $[W/(m^2K)]$

Table 3.1: Differences of h over different correlations for a flat horizontal plate available in literature.

For the sake of completeness, the work of Singh and Patil [63] is also mentioned. These authors do calculate the convective heat transfer coefficient h to calculate the Nusselt number Nu, taking into account Q_{loss} and Q_{rad}. However, they plot this Nusselt number against Q_{supply} = Q_{rad} + Q_{conv}, taking only Q_{loss} into account.

3.2.2 The use of ΔT

To the knowledge of the author of this work, the temperature difference ΔT that is reported represents the difference between the substrate temperature T_s and the environmental temperature T_∞. An alternative choice could be the fin temperature T_{fin}, as the fin efficiency η_{fin} in buoyancy-driven convection is quite high. However, the authors generally do not define which temperatures are used to calculate ΔT. It is important to know how ΔT is defined for reproducibility and comparison with simulations. This temperature difference is also needed to calculate the heat transfer coefficient h ($h = \frac{Q_{conv}}{A_s \Delta T}$, with $\eta_{fin} = 1$).

To indicate the location where the substrate temperature T_s is measured, most authors add a figure showing that the temperature is measured somewhere around the heater. However, they do not specify where. The only exception here is the work of Joo and Kim [59] (see Fig. 3.2(b)). Furthermore the type of thermocouple is also important, for example stick-on thermocouples do not measure the substrate temperature directly; this will induce an extra uncertainty on the determination of ΔT.

Very rarely the location where ambient temperature T_∞ is measured is given. The only exception is the work of Khor et al. [65]. The lack of this information can have a bigger effect than the choice of the location where the substrate temperature is measured. This is certainly the case if the heat sink assembly is enclosed, as seen in the work of Bhattacharya and Mahajan [58], for example. As previously described, there is no standard as to how ΔT should be determined.

3.2.3 The use of heat transfer coefficient h

Different literature sources reported a heat transfer coefficient h. However, the definition of this coefficient is not unambiguous. Authors like Li et al. [60] and Sikka et al. [66] use Eq. (3.2) to calculate the heat transfer coefficient, while Joo and Kim [59] take into account the fin efficiency η_{fin} according to Eq. (3.3). The fin efficiency η_{fin} is defined as the ratio of the heat transfer to the fin to the heat transfer of an ideal fin. An ideal fin is made of an infinitely conductive material and therefore this limit corresponds to a fin that is entirely at a temperature of T_s. The fin efficiency depends on the boundary condition at the tip and the geometry of the fin. The fin efficiency for simple geometries like plate fins or pin fins has to be calculated iteratively through Eq. (3.4). As mentioned above, the Q that is used here should be Q_{conv}. However, most authors use simply Q_{in}.

$$h = \frac{Q}{A_s \Delta T} \tag{3.2}$$

$$h = \frac{Q}{A_s \eta_{fin} \Delta T} \tag{3.3}$$

$$\eta_{fin} = \frac{tanh(mH)}{mH},\ with\ m = \sqrt{\frac{2h}{k_s w}}\ or\ \sqrt{\frac{2h}{k_s d}}, \tag{3.4}$$

where H is the fin height, w is the width in-between the plate fins, or d the fin diameter in case of pin fins.

3.2.4 The use of thermal resistance R

Reporting the thermal resistance is quite common for heat exchangers and heat pipes. For heat sinks this is done less often in academic literature, especially in case of natural convection. However, heat sink manufacturers use this parameter frequently (see [29, 55, 56, 57]). The thermal resistance R_{tot} is defined as $\frac{\Delta T}{Q_{in}}$. For extruded profiles in natural convection, Aavid [29] only measured one heat sink with a length of 150 mm and a substrate temperature of 75°C. On their website it is also mentioned that the heater only partially covered the substrate. For longer or shorter heat sinks and a higher or lower substrate temperature, there are correction curves published on their website [29]. Aavid doesn't report the orientation of the heat sink nor is it stated whether the heat sink is anodized or not.

Alpha [57] also reports thermal resistances. However, this manufacturer reports the Q_{in} and the surface area where the heater is located for each heat sink separately. Also the orientation is given, most heat sinks are measured horizontally. All results are reported for anodized samples.

3.3 Results & discussion for open-cell metal foam heat sinks

The approach for open-cell metal foam is quite similar to that for regular extended surfaces. Therefore no separate paragraph is added on the general approach of studying open-cell metal foam as heat sinks in natural convection.

However, due to the complex structure of open-cell metal foam, two extra concerns need to be discussed:

- The **contact resistance**. This issue is already discussed in Chapter 2. However, due to the complex structure, the strut finish will have an important impact on the contact resistance. Hence, the method used to cut the metal foam can affect its thermal performance. This is almost never discussed in open literature. Partly because the researchers frequently just buy the foam without slicing it. How the strut is fixed to the substrate can also give rise to an important thermal resistance. Some authors have tried to assess the influence of this contact resistance. However, experiments are always done with a fan (active cooling). De Jaeger et al. [54] give an expression for

the thermal contact resistance in case of several bonding methods such as pressed-fit, epoxy, brazing and co-casting. Furthermore, they also discuss the effect that cutting the foam has on the contact resistance. Sadeghi et al. [85] studied the contact resistance in case of a pressed-fit contact. DeGroot et al. [86] studied the influence of the contact resistance numerically. They increase the contact resistance to such high levels that the heat transfer is found to go to an asymptotic value as conduction into the solid constituent of the foam is completely blocked. It is also found that for most reasonable interface materials, such as thermal epoxies, the impact of thermal contact resistance on the heat transfer performance in comparison with that for an ideal bond is small.

- The **fin efficiency** in case of open-cell metal foam is not straight-forward to calculate. Ghosh [87] developed an expression of this fin efficiency for a simplified cubic representation of the foam, see Figure 3.5. The model, in the microscopic level, takes account of the forced convective heat transfer coupled with heat conduction through the foam struts. Analytical expressions have been derived for the gas-solid temperature difference, total heat transfer through the foam and efficiency of foam as an extended surface. The resulting expressions show a strong resemblance with those of the conventional finned surface. The effect of porosity and foam density on the heat transfer in metallic foam has been established through parametric studies. Significant heat transfer augmentation due to cross connections in metal struts has been noticed. The porosity is defined as the ratio of the fluid volume (V_f) and the total volume (V_t) of the heat transferring structure. The foam density (or also called pore density) is typically given in Pores per linear Inch (PPI). In fact, this value given in indication how dens the foam structure is.

The number of experimental studies in buoyancy-driven convection with open-cell metal foam is limited. As the research is limited, the author prefers to give an overview of all experimental studies done with open-cell metal foam heat sinks. Bhattacharya and Mahajan [58] studied influences of pore density (5, 10, 20 and 40 PPI) and porosity (ranging between 89% and 96%) for open-cell aluminium foam with substrate temperatures up to 75°C (limited by the used insulation). The authors found that the heat transfer rate increases with a decrease in porosity or an increase in metal content (see Figure 3.6(a)). Although the flow resistance will be higher for a metal foam with lower porosity, the effective thermal conductivity is higher too. The latter effect is found to be more important. This is also shown by Kathare et al. [88] for natural convection in water-saturated metal foam.

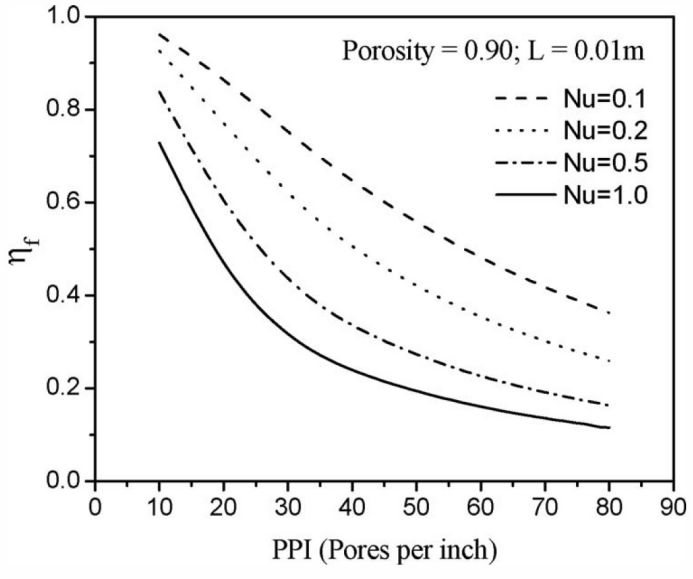

Figure 3.5: Effect of pore density and Nusselt numbers on the fin efficiency of aluminium foam [87].

Furthermore, when the porosity is kept constant, higher pore densities result in a higher flow resistance and a higher interstitial heat transferring surface area. In this case, the first effect is found to be dominant, showing a lower heat transfer rate when using higher pore densities. However, as mentioned in the Section 3.1, only the length of the heat sink is reported. This makes it very difficult to compare with other results. The foam was bonded to the substrate with a single epoxy. Although the authors recognised the relative importance of the bonding method, no further research has been performed on this. The horizontal and vertical orientation is studied, but no significant difference between both is observed. Next to pure foam heat sinks, they also studied plate finned heat sinks with metal foam in-between the fins and compared this with correlations from commercial Aavid heat sinks. The finned metal foam heat sinks outperformed the commercial heat sinks by almost 25% (see Figure 3.6(b), depending on the temperature difference). The finned foam heat sinks even outperform the regular foam heat sink. The authors explained that the low effective thermal conductivity is the basic constraint for heat transfer, so if fins are used in-between the foam samples, than the effective conductivity increases. However, the flow resistance will also increase. Apparently for the cases studied by [58], it seems to have a positive effect.

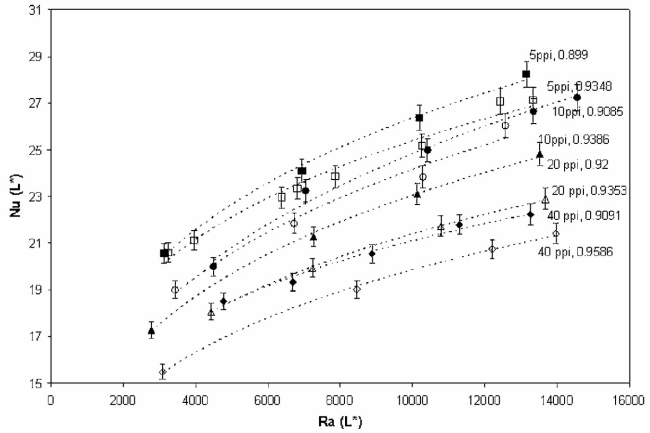

(a) Experimental data for natural convection in metal foams in horizontal orientation

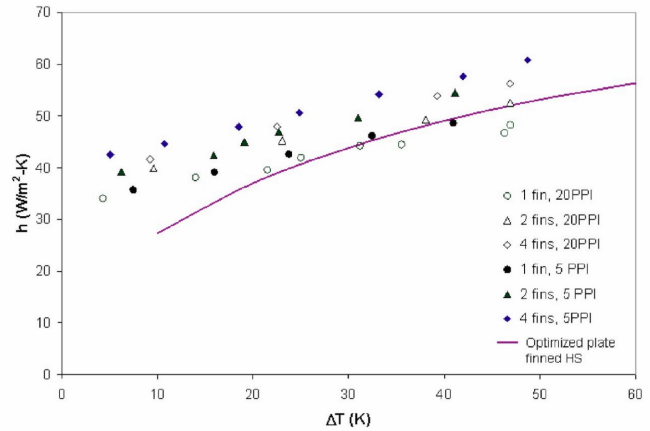

(b) Thermal performance of the finned metal foam heat sinks in horizontal orientation

Figure 3.6: Results from Bhattacharya and Mahajan [58] (L^* is the characteristic length, in this case equal to A/P, with A the area of the base and P the perimeter of the base)

Recently, Qu et al. [89] studied the influence of the inclination angle (from vertical to horizontal upward in steps of 15°), the pore density (10, 20, 40 PPI), the porosity (90% to 95%) and the aspect ratio (the ratio of foam height to sample length) is varied from 0.1 to 0.5, for copper foam square heat sinks (100x100 mm^2). The heat flux was varied from 300 to 3000 W/m^2 in order to obtain different Rayleigh numbers and substrate temperatures. The foam was sintered to the substrate. Dimensions of the Plexiglas® housing are not mentioned. The effect of the height variation is found to be significant in their test rig: for a foam height

variation from 10 to 50 mm, an increase of 38% in heat transfer rate is observed (see Figure 3.7(b)). The additional heat transfer rate decreases with increasing foam height. The dependence of the heat transfer rate on the inclination is found to be very small: up to 6% for the Nusselt number, with an uncertainty of 4.4% (see Figure 3.7(a).)

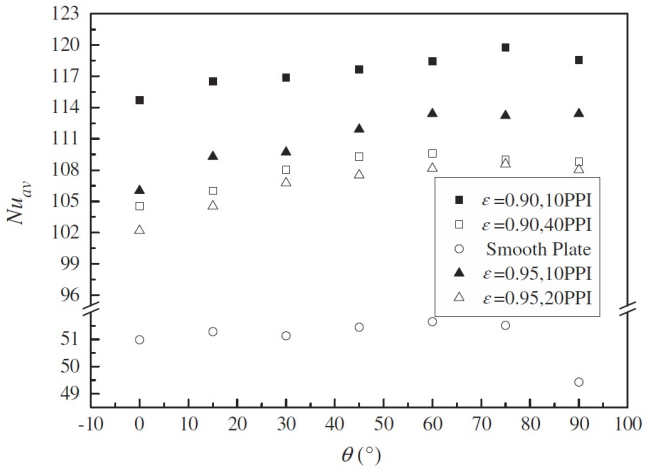

(a) Experimental data for natural convection in metal foams in different orientation and different types of foam.

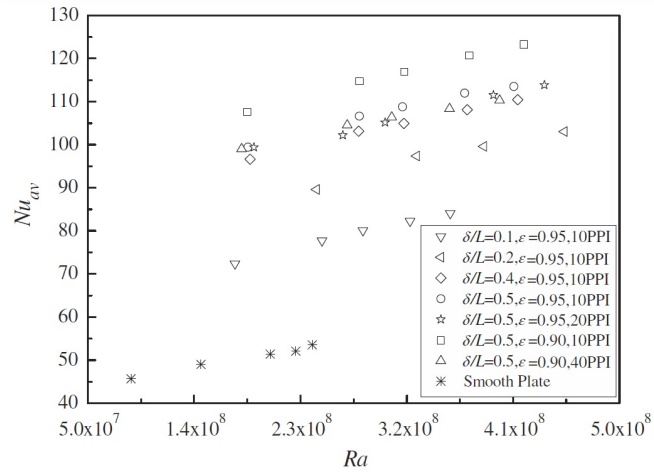

(b) Experimental data for natural convection in metal foams for different foam heights and different types of foam.

Figure 3.7: Results from Qu et al. [89]

Mahdi et al. [90] studied an AL6101 heat sink for an Intel 200 MHz Pentium processor in natural convection and compared it with pin fins. The surface area of the processor and the heat sinks is 2.54 x 2.54 cm^2 and 5.08 x 5.08 cm^2, respectively. The maximum required dissipation is 30 W. Foam samples with a PPI value of 10, 20 and 40 were studied. The box dimensions were again not mentioned. The authors found that the total thermal resistance of the foam heat sink was 70% lower compared to the finned heat sink, indicating that a foamed heat sink could be beneficial per unit volume. In contradiction with other researchers, Mahdi et al. [90] reported an inverse proportionality of the thermal resistance with the pore density, indicating that the increased heat transferring area prevails over the increase in flow resistance (see Figure 3.8).

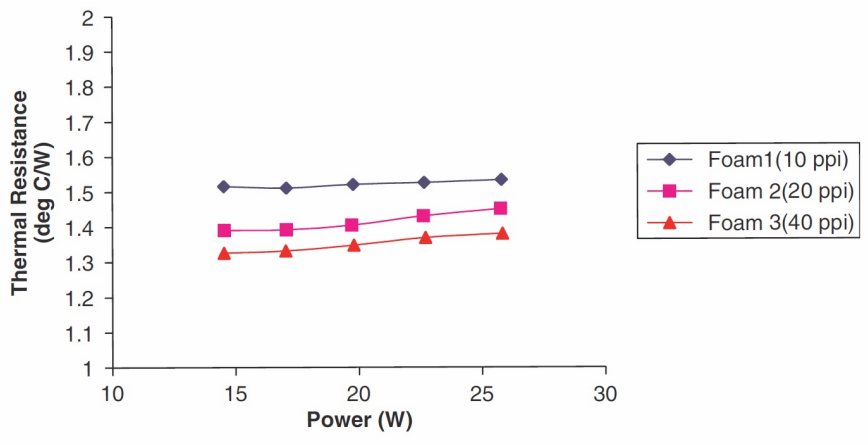

Figure 3.8: Results by Mahdi et al. [90]

4

Numerical heat sink research in buoyancy-driven flow

In this chapter, the existing literature on numerical studies on general heat sinks in buoyancy-driven flow is discussed. Additionally, the approach to study open-cell metal foam is discussed in section 4.2.

4.1 Geometry, boundary conditions and fluid models for classical heat sinks

4.1.1 Introduction

Table 4.1 gives an overview of the available numerical work in open literature on standard heat sinks with simple fin shapes in buoyancy-driven heat transfer and for low Rayleigh numbers. Table 4.1 focusses only on recent publications in open literature and tries to show the diversity in the geometry/mesh, the boundary conditions and fluid models/domains.

Author (Year)	Geometry	Simulation (dimensionality - fluid - turbulence model - radiation)	Finest discretisation used	Mesh
Ahmadi et al. [91] (2014)	Rectangular interrupted fins	2D - Boussinesq approximation - no turbulence model - included	'optimum size': 1 mm. Presumed shape: rectangular mesh	One fin row is simulated. Calming section before fins, no calming section after last fin
Dialameh et al. [92] (2008)	Rectangular fins	3D - constant properties, except $\rho(T)$ - no turbulence model - not included	Length: 2 mm, height: 1 mm, depth: 0.5 mm. Presumed shape: rectangular mesh	A half fin row is simulated. Calming section before and after. Only one fin is taken into account, other side is open.
Shen et al. [71] (2014)	Rectangular fins	3D - incompressible ideal gas - no turbulence model - included	2 mm. Presumed shape: rectangular mesh	Several half fin rows are simulated. Calming section before, after and underneath
Tari et al. [93, 94] (2013)	Rectangular fins	3D - air is ideal gas - zero order turbulence model - included	Non-conformal mesh, not discussed	Complete heat sink is simulated together with insulating material. Square box with 3m-edges
Dogan et al. [46] (2014)	Thin-fin arrays with various shapes	3D - constant properties except $\rho(T)$ - no turbulence model - included	Approximately 0.5 mm/cell (and higher)	One fin row is simulated. Complete fin is simulated. No symmetry plane. No calming section before or after.
Work of Lee et al. [95, 96, 97, 98] (2012 - 2015)	Radial heat sinks	3D - constant properties except $\rho(T)$ - $k-\varepsilon$ turbulence model - not included	Hexahedral mesh, not discussed	One unit cell is simulated. Fluid domain at each side of the fins.

Table 4.1: Overview of numerical work on heat sinks operating in buoyancy-driven convection.

Ahmadi et al. [91] study natural heat transfer in vertically-mounted rectangular interrupted fins. The authors use a 2D numerical model (see Figure 4.1). They simulate only one fin row and use symmetrical boundary conditions. The authors use a cell size of 1 mm. However, no picture of the grid itself is shown. A so-called *calming section* is implemented before the interrupted fins, no calming section is implemented after the last fin. The term calming section is used here to indicate an amount of fluid domain before the actual heat sink. It is the section where the flow develops to the outlet of the flow domain. All calculations were performed for steady state with no turbulence model. The flow is modelled through the Boussinesq approximation.

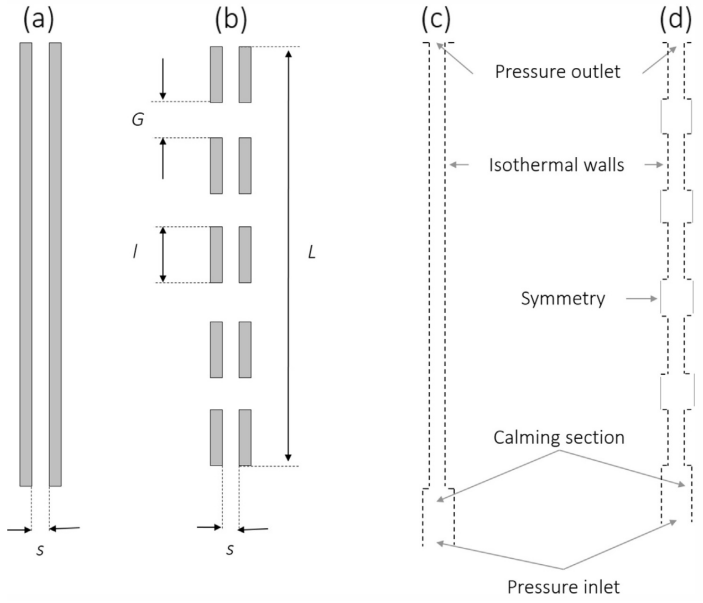

Figure 4.1: Schematic of the numerical domain, (a) continuous fins, (b) interrupted fins; (c) boundary conditions for continuous fins, (d) boundary conditions for interrupted fins [91].

Dialameh et al. [92] study thick rectangular fins with a short length. The thickness of the fins varies between 3 mm and 7 mm, while the length of the heat sink is always smaller than 50 mm. Only half of one fin row is simulated in 3-D, and only one fin is taken into account (see Fig. 4.2). According to the authors, radiation is negligible. Although the mesh itself is not given, the authors do state that a different spatial resolution is used for the height (1 mm), length (2 mm) and depth (0.5 mm) of the heat sink. The authors use this grid size because they tested 20 x 40 x 45, 19 x 50 x 55 and 24 x 50 x 60 discretization schemes and observed ”no impact on the average heat transfer coefficient”. The fluid properties

are assumed to be constant, except for the density, which is a function of the temperature.

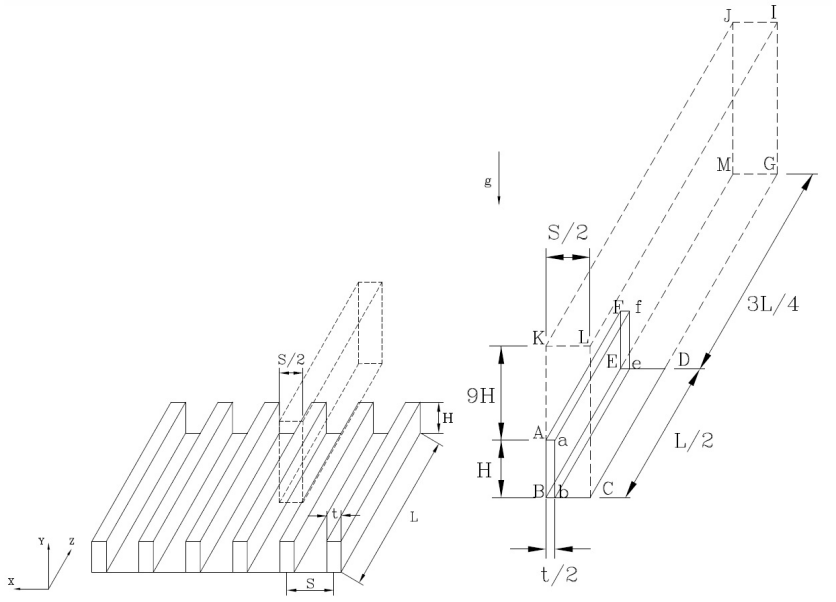

Figure 4.2: Schematic drawing of fin arrays and computational domain [92].

Shen et al. [71] study rectangular fins in 3-D by simulating only half of the complete heat sink (other part is symmetrical). Their geometry is shown in Figure 4.3. A calming section is provided at the sides, top and bottom of the heat sink. No turbulence model is used and radiation is taken into account. Again the mesh is not shown. The geometry is meshed with 2 mm cells. The authors determined this discretization by testing two different schemes (16 x 25 x 60 and 12 x 20 x 50) and observing a deviation in overall heat transfer coefficient of 1.9%. Air is modelled as an incompressible ideal gas.

Tari et al. [93, 94] simulate a complete heat sink (see Figure 4.4). The authors placed the heat sink and insulating material in a square box with an edge of 3 m. A non-conformal mesh is used, as the authors mention this in the paper, but it is unclear as to how the mesh itself was generated. The authors used a zero order turbulence model. This is a turbulence model based on the mixing length hypothesis. Radiative heat transfer is taken into account. The complete grid has 2.8M cells for a fluid domain of 9 m^3. Air is modelled as an ideal gas.

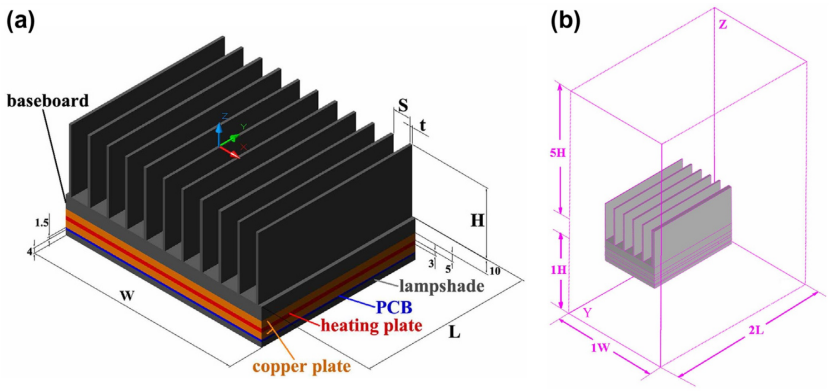

Figure 4.3: (a) Isometric view of the lamp (to be cooled) and (b) the computational domain [71]. The gravitational force vector is vertically downwards in the plane of the figure.

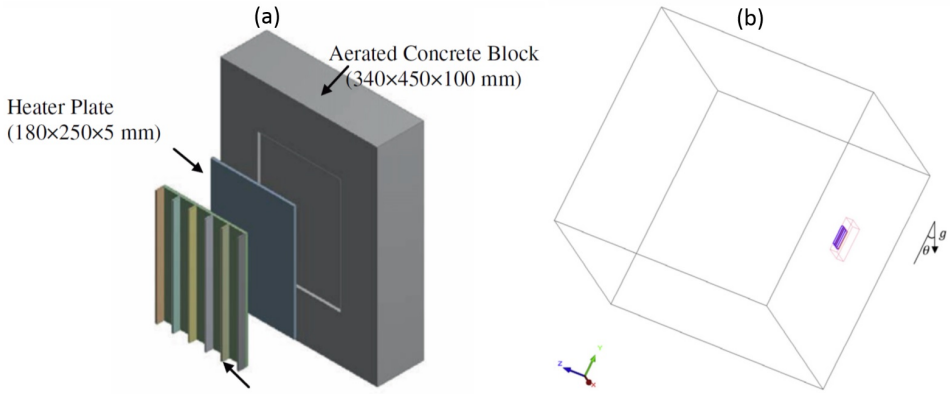

Figure 4.4: (a) Schematic view of the model for the heat sink with a length of 250 mm. (b) 3-D view of the computational domain (cube with edge of 3 m) [94]

Dogan et al. [46] compare a rectangular shape with five different fin shapes. For this, the authors simulate one fin row with a fin at each side as shown in Figure 4.5. This approach is different in comparison with the work by Dialameh et al. [92] where only one fin is taken into account and the other end is open. No calming section is provided before or after the heat sink, as can be seen in Figure 4.5. The finest mesh consists of 1 mm cells. No turbulence model is used but a radiation model (S2S) is included.

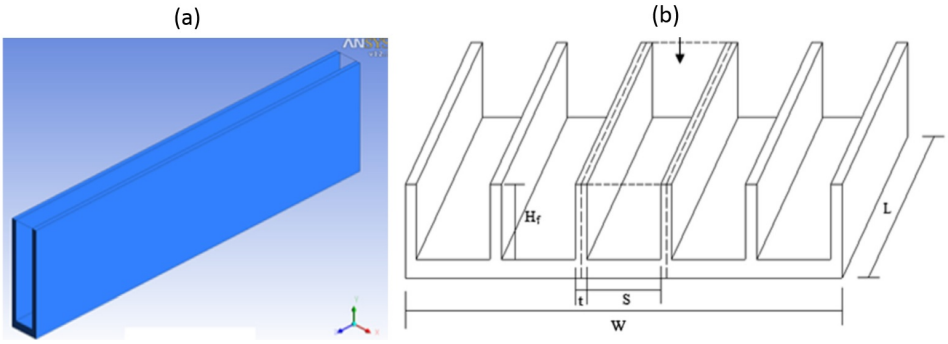

Figure 4.5: A detailled view of the computational domain that is used [46]. The gravitational force vector is vertically downwards in the plane of the figure.

The work by **Lee et al.** [95, 96, 97, 98] studies different radial heat sinks. The authors simulate only one unit cell, with one fin row, as shown in Figure 4.6 for example. A calming section is provided before and after the heat sink. In order to compare with experimental results, a circular plate made of heat-resistant glass was installed under the film heater to minimize the heat loss (and measure Q_{loss}). The authors used a $k - \varepsilon$ turbulence model and radiation is neglected.

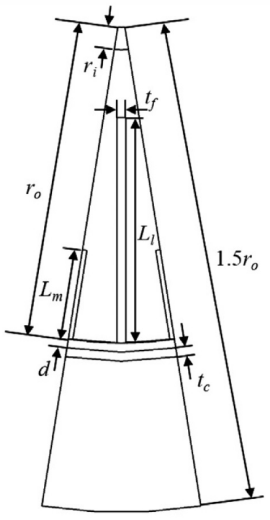

Figure 4.6: 2D illustration of the computational geometry [95].

As can be seen in Table 4.1, different authors in open literature use different approaches to simulate heat sinks in natural convection. However, these different

approaches do not all yield the best quality of results. Despite the numerous results for numerical studies of heat sinks in open literature, very little of these studies use a good approach, as will be explain and shown later in this PhD work. Therefore, a focus of this work is to show what a proper technique to simulate heat sinks through CFD can be. All the calculations of the cited literature sources are done using the solver Fluent from Ansys. Hence, what follows there will sometimes be pertinent terminology of Ansys/Fluent.

A discussion of the different elements in literature seen for the following aspects of numerical research will be given:

- Which fluid models can be used (Section 4.1.2).
- How to determine the discretization error for the used grid (Section 4.1.3).
- Effect of turbulence models (Section 4.1.4).
- Influence of radiative heat transfer (Section 4.1.5).

4.1.2 Different fluid models

As is illustrated in Table 4.1, different authors use different fluid models. For natural convection, the most important parameter in the fluid model is the fluid density ρ, as in case of natural convection the fluid flow is density-driven. In this work, the working fluid is always air. Hence the following discussion is focussed on air as a working fluid.

The **Boussinesq approach** is used by e.g. Ahmadi et al. [91], amongst many others, for calculating the density. This approach is introduced in Section 2.3.2. However, this approximation can only be used when the actual changes in density are small [28]. Specifically the Boussinesq approximation is only valid when $\beta(T - T_0) \ll 1$. Hence the question remains: what is sufficiently lower than 1? In the work of Ahmadi et al. [91] the studied temperature difference varies between 50 K and 90 K. For an operational temperature of 20 $°C$, the values for β range between $3 \cdot 10^{-3} 1/K$ and $2.68 \cdot 10^{-3} 1/K$, consequently $\beta(T - T_0)$ varies between 0.15 and 0.24.

Other authors model air as an **ideal gas** [93, 94] or an **incompressible ideal gas** [71]. In both models the density ρ is calculated as:

$$\rho = \frac{p_{op} + p}{R/M_w T}, \tag{4.1}$$

In the above equation R is the universal gas constant, M_w is the molecular weight of the gas, p is the local relative pressure ($p = 0$ for an incompressible ideal gas) and p_{op} is the operating pressure[1].

[1] By default, this is taken as the atmospheric pressure in Ansys/Fluent.

If the Boussinesq approach is not used, there is still one term in Eq. (2.17) unknown: $\rho_{T=T_\infty}$. This is called the specified operating density in Ansys/Fluent. However, none of the authors who use an (incompressible) ideal gas model report which value they chose for this parameter. If this operating density is *not* specified, Ansys/Fluent will compute the operating density by averaging over all cells. If this default calculation is not used and a specified operating density is used, than the operating density at T_{env} has to be used. This will lead to the only correct interpretation of the hydrostatic pressure at the inlet of the heat sink. Otherwise, a user defined function has to be selected as hydrostatic pressure[2] at the inlet.

The simplest model is keeping **all the fluid properties constant except the density**, which is function of the temperature $\rho(T)$. This type of model is used by Refs. [46, 92, 95, 96, 97, 98], amongst many others. In Ansys/Fluent itself there are different options to define the density as a function of the temperature: piecewise-linear, polynomial, ideal gas law, incompressible ideal gas law. However, none of the explored sources in Section 4.1.1 report how this $\rho(T)$ was defined. Two frequently used models are: incompressible ideal gas and the Boussinesq approach, as discussed in the previous Chapters.

4.1.3 Uncertainty analysis on numerical results

Although many researchers use numerical techniques, none of them reports an uncertainty on their numerical discretization scheme. However, this is important in order to evaluate the accuracy of the numerical results. Therefore Section 4.1.1 gives no details upon the uncertainty of the simulations, in contrast with Section 3.2 for the experimental results.

When the grid is refined and the grid cells become smaller, the spatial discretization errors should approach to zero, excluding computer round-off errors. When the time steps are approaching to infinite small numbers, the temporal discretization errors should also approach to zero. Furthermore, the order of grid convergence involves the behaviour of the solution error. Methods to examine the spatial and temporal convergence are presented in the book by Roache [99] and are based on the Richardson extrapolation. The order of convergence is defined as the difference between the discrete solution (in function of a grid spacing measure h) and the exact solution (f_{exact}):

$$E = f(h) - f_{exact} = Ch^p + H.O.T. \tag{4.2}$$

In the above equation C is a constant and p is the order of convergence (H.O.T. are the higher order terms).

[2]Hydrostatic pressure is the pressure that is exerted by a fluid at equilibrium at a given point within the fluid, due to the force of gravity. Hydrostatic pressure increases in proportion to depth measured from the surface because of the increasing weight of fluid exerting downward force from above.

The theoretical order of convergence in case of a second-order upwind algorithm is 2 according to Roache [99]. Therefore p theoretically equals 2. However, the observed order of convergence will be likely lower. Without going into the mathematical details, a more direct evaluation of p can be obtained from three solutions using a constant grid refinement ratio r (see. Eq. (4.3)). Roache recommends using r = 2 [99]. This means that three grids are required, each with a grid refinement ratio of 2. For each grid, the simulated result should be in the asymptotic region. Hence, the discretization for each grid has to be fine enough. In three dimensions, the grid size will thus increase each time with a factor 8 which can lead to very large grid sizes. As this requires a lot of computational power, the uncertainty is studied on only 2 grids with r = 2 and p is taken theoretically on 2 as all calculations use a second-order upwind algorithm.

$$p = ln\left(\frac{f_3 - f_2}{f_2 - f_1}\right)/ln(r), \tag{4.3}$$

In Eq. 4.3 f_1 is the solution of a specific parameter of interest for the finest grid size studied and f_3 for the coarsest grid.

Roache [99, 100] suggests a grid convergence index GCI to provide a consistent manner in reporting the results of grid convergence studies and provide an error band on the grid convergence of the solution. The GCI can be computed using *two levels of grid*. However, three levels are recommended in order to accurately estimate the order of convergence and to check that the solutions are within the asymptotic range of convergence.

When using 2 grids, the grid convergence index for the finest grid GCI_{fine} is:

$$GCI_{fine} = \frac{F_s|\varepsilon|}{(r^p - 1)}, \tag{4.4}$$

In the above equation F_s is a safety factor. F_s is 3, when comparing only 2 grids, and 1.25, when comparing 3 (or more). ε is the relative error between two grids, depending on the parameter of interest: $\frac{f_2 - f_1}{f_1}$[3].

In case the coarsest grid is used, GCI_{coarse} is expressed as Eq. (4.5) which is a factor r^p larger than GCI_{fine}.

$$GCI_{coarse} = \frac{F_s|\varepsilon|r^p}{(r^p - 1)} \tag{4.5}$$

Finally, one has to make a clear difference between the discretization error that can be calculated with the GCI, and the uncertainty when comparing with experiments. In cases, only the GCI is of importance, because it is not always the aim to compare numerical studies to experimental studies. So, the GCI only

[3]The parameter of interest in this PhD will be the heat transfer coefficient. However, this could also be local parameters like flow angles, temperatures or velocities at specific locations etc.

gives an indication of the uncertainty on the grid discretization that is used. Effects of boundary conditions (fluid models, addition of fluid domain, use of turbulence models etc.) still need to be considered separately.

4.1.4 Impact of turbulence modelling

When using a large geometry, like e.g. in Tari et al. [93, 94], an unsteady plume far away from the heat sink appears. In this case, the results are more difficult to be calculated without the use of a turbulence model[4]. In this turbulent flow, both velocity and pressure fields can be decomposed into a mean part and a fluctuating part. Averaging the Navier-Stokes equations (Eq. (2.17)) with these decomposed parts yields the Reynolds-averaged Navier-Stokes equations (RANS). These equations govern the mean flow [101]. However, the nonlinearity of the Navier-Stokes equations implies that the velocity fluctuations still appear in the RANS equations. This is in a nonlinear term $-\rho\overline{v_i' v_j'}$ from the convective acceleration. This term is also called the Reynolds stress R_{ij}, as its effect on the mean flow is the same as the effect of a stress term [101].

Turbulence modelling means obtaining equations that contain only the mean velocity and pressure. One need to close the RANS equations by modelling the Reynolds stress term R_{ij}. This gave rise to the concept of turbulent eddy viscosity ν_t, for which different models were proposed. Prandtl was the first one to propose a model in order to calculate ν_t:

$$\nu_t = |\frac{\partial u}{\partial y}| l_m^2 \tag{4.6}$$

This model is called the **mixing length hypothesis** and is only accurate for wall-bounded and attached flow field with small pressure gradients. The mixing length hypothesis is not frequently used in Ansys/Fluent. However, it is implemented under the name: 'zero order turbulence model'. This model is used by Tari et al. [93, 94].

For recirculating flows the $k-\varepsilon$ **model** is used, like in Refs. [95, 96, 97, 98] ($\nu_t = C_\mu k^2/\varepsilon$). This model is widely used and is validated for specific applications. Also the $k-\omega$ **turbulence model** is frequently used ($\nu_t = k/\omega$).

In each case, when turbulence modelling is used extra diffusivity is added to the system. A turbulence model can only be trusted for a specific case if it is validated by experiments. This induces some limitations to the model.

[4] Of course, this is still possible. For example, through the selection of a very coarse grid; introducing extra numerical viscosity and thus error on the numerical simulation. Or one can also do an unsteady calculation; though this will of course increase the total computational time.

4.1.5 Influence of radiation

Based on the experimental results in open literature (Sections 3.1 and 3.2) it is clear that even for low substrate temperatures, radiative heat transfer can have a large effect. For this reason, most commercially available heat sinks are anodized in a non-metallic color. In numerical studies, there are several authors who neglect the radiative influence (see Table 4.1). This leads to an underestimation of the total heat transfer potential and most of the time the convective influence will be overestimated, as the temperature of the fin material will be higher than in case of combined convection-radiation. Later in this work, this issue will be discussed further.

Authors who do take radiation into account, generally use the standard **surface-to-surface ($S2S$) radiation model** used for gray, diffuse and opaque surfaces. This is the recommended model in case of non-participating media. Emissivity and absorptivity of a gray surface are independent of the wavelength. Also, by Kirchoff's law, the emissivity equals the absorptivity and for a diffuse surface, the reflectivity is independent of the outgoing (or incoming) directions. In this way (from conservation of energy) the reflection $\rho = 1 - \varepsilon$. The energy flux leaving a given surface can be decomposed into a component which is directly emitted and a component which is reflected:

$$q_{out,k} = \varepsilon_k \sigma T_k^4 + \rho_k q_{in,k} \tag{4.7}$$

where the subscript k is the radiative surface.

In the above equation $q_{out,k}$ is the energy flux leaving the surface, ε_k is the emissivity, σ is the Boltzmann constant and $q_{in,k}$ is the energy flux incident on the surface from the surroundings.

The amount of incident energy upon a surface from another surface is modelled with the view factor F_{jk}, as explained in 2.2 and with this view factor the incident energy flux $Q_{in,k}$ can be expressed as:

$$A_k q_{in,k} = \sum_{j=1}^{N} A_j q_{out,j} F_{jk} \tag{4.8}$$

In Ansys/Fluent other radiation models are also proposed [102] (but not usable in this work). However, these are practically never used in the numerical study of heat sinks. The discrete transfer radiation model (DTRM), the P-1 radiation model and the Rosseland model from Fluent are most of the time used in combustion processes. The DTRM also assumes gray radiation, no scattering and a diffuse object, however it can not be used in parallel calculations. The P-1 radiation model is explicitly used for combustion processes as here the optical thickness (the natural logarithm of the ratio of incident to transmitted radiant power through a material, and spectral optical depth or spectral optical thickness is the natural

logarithm of the ratio of incident to transmitted spectral radiant power through a material) is large. The Rosseland model has been tested in this work but it appears not usable. The results for a flat plate were significantly different compared to correlations. Probably because the optical thickness should be larger (< 3 according to Fluent). The DO-model is for non-gray bodies.

4.2 Results & discussion for classical heat sinks

After the discussion of all the used parameters and the way experimental researchers study extended surfaces in natural convection in open literature, it is clear that a whole range of approaches are used. The same holds for the results that can be found in open literature.

A lot of different methods are used to compare one heat sink to another[5]:

- ΔT or T_{wall} **vs** $Q_{in\ or\ conv}$ [91, 94]
- h **vs** ΔT or S (fin spacing) or L (length of the fin) or $Q_{in\ or\ conv}$ [46, 92]
- Nu **vs** Ra [71]
- $R_{tot\ or\ conv}$ (at T_s) **vs** $Q_{in\ or\ conv}$ [95]
- visualisation of temperature/velocity field and/or v **vs** x [46, 71, 94]

4.2.1 The use of different definitions of heat input

A similar discussion can be given as for the experimental results: the question remains which Q is reported? As discussed in Chapter 3, there are different Qs that can be reported, this is also shown in Eq. (3.1). First of all the initial boundary conditions and geometry used by the authors should be considered. In fact, if reseachers want to compare their findings with experimental results, they need to simulate the insulation material along with the heat sink itself. This is done in Tari et al. [94]. Lee et al. [95] installed a heat-resistant glass to measure the heat loss to the environment, something similar is done by Shen et al. [71]. Otherwise the Q_{loss}-term will not be taken into account. Some authors also neglect the radiative heat transfer in numerical simulations (see Table 4.1). The Q reported in this case will then lump convective and radiative heat transfer. In fact, to compare heat sinks it is not necessarily bad to use the lumped heat transfer rate $Q = Q_{conv} + Q_{rad}$. However, it is difficult for other authors to use the reported data. In fact both Q_{conv} and Q_{rad} should be reported separately.

Ahmadi et al. [91] are well aware of the impact of thermal radiation. They try to report Q_{conv} only. To compare their results with literature correlations, they tried

[5]This list is very comparable with the list given in Section 3.2 for experimental research

to estimate Q_{rad}. This value is determined by estimating the emissivity value. However, as pointed out in Section 3.2, it is not always clear if Q_{rad} is minimized or not during the experiments by for example polishing surface.

Dogan et al. [46] report the lumped Q which is send to the heat sink, although they did take radiative influences into account. The authors did not simulate any insulation.

Lee et al. [95] report a lumped Q too. As explained in Section 4.2, Lee et al. implemented a heat-resistant glass underneath the film heater in order to measure Q_{loss}. The authors are in fact reporting $Q_{conv} + Q_{rad}$.

Shen et al. [71] studied the heat sink together with the fitting of a LED lamp. In this way, the authors are also able to calculate $Q_{conv} = Q - Q_{rad} - Q_{loss}$.

4.2.2 The use of ΔT

ΔT is typically determined as $T_{solid\ or\ wall\ or\ s} - T_\infty$[6]. In case of numerical simulations, T_∞ is a temperature which is applied to the boundaries. Most of the time, the authors also report this temperature. For the other temperature in ΔT ($T_{solid\ or\ wall\ or\ s}$) it is not always clear which temperature is exactly used. One can either choose for T_{solid}, T_{wall} and T_s, for all three can be easily accessed in a program like Ansys/Fluent. However, the difference between the temperatures will be limited as only studies in natural convection are considered. Hence the effect will be probably be limited. Dialameh et al. [92] and Shen et al. [71] use T_s, while Ahmandi et al. [91], Tari et al. [94] and Dogan et al. [46] use T_{wall}.

4.2.3 The use of heat transfer coefficient h (or Nu)

Similar to the discussion in Section 3.2, the question is how h and consequently Nu are determined. Again this is linked to how ΔT and Q is determined. Dialameh et al. [92] reported h vs ΔT, where h is calculated as $\frac{Q}{A\Delta T}$, with A the total heat transfer area of the fin arrays, ΔT calculated based on T_s and Q the total heat transfer rate (as radiation was neglected here). Shen et al. [71] calculated Nu based on $h_{fin} = \frac{Q_{fin}}{A_{fin}\Delta T}$. Q_{fin} is calculated as in Eq. (4.9), while ΔT is calculated based on T_s. The heat transfer coefficient as reported in Dogan et al. [46] is determined using Ansys/Fluent through $h_{avg} = 1/A \int_A h_i dA$. h_i is calculated based on T_{wall}.

$$Q_{fin} = Q - Q_{rad} - Q_{loss} \tag{4.9}$$

[6]The subscript $solid$ stands for: the average temperature of the complete heat sink, the subscript $wall$ is the average temperature of the exposed wall of the heat sink (partly fins and substrate) and finally, the subscript s stands for the average temperature of the substrate (base plate).

4.2.4 The use of thermal resistance R

A thermal resistance is only very rarely reported in numerical simulations. However, Lee et al. [95, 96, 97, 98] do report the thermal resistance. Here R is defined through Eq. (4.10), where T_{solid} is the volume averaged temperature over the complete heat sink and $q_{heatsink\ base}$ is calculated as $q - q_{loss}$ with the q_{loss} calculated over a heat-resistant glass placed under the film heater (as explained earlier). Hence the thermal radiation is taken into account for the calculation of R in Eq. (4.10).

$$R = \frac{T_{solid} - T_{\infty}}{q_{heatsink\ base} A_{heatsink\ base}} \tag{4.10}$$

4.3 Approach for open-cell metal foam heat sinks

In comparison with the experimental approach as discussed in Chapter 3, the approach to study open-cell metal foam (or porous media in general) is different compared to the approach described in Section 4.1. Two techniques are frequently used in open literature to numerically simulate open-cell metal foam:

- Directly simulating (a part of) the application with open-cell metal foam.
- Using an upscaling approach in which only the macroscopic scale will be solved.

With the first technique, the complete foam structure is implemented in the CFD software and solved. Sometimes, this can lead to a direct direct numerical simulation or DNS. A direct numerical simulation (DNS) is a simulation in computational fluid dynamics in which the NavierStokes equations are numerically solved without any turbulence model. This means that the whole range of spatial and temporal scales of the turbulence must be resolved. All the spatial scales of the turbulence must be resolved in the computational mesh, from the smallest dissipative scales (Kolmogorov microscales), up to the integral scale, associated with the motions containing most of the kinetic energy. Although a full DNS is very computational intensive. In this work, a calculation will be done on a simplified foam structure, using the steady state Navier Stokes: this will not be a DNS calculation as the grid cells are way too large. In each case, up to a certain height, the micro-scale has to be resolved.

With the upscaling method the micro-scale level doesn't need to be solved, which simplifies the problem. The principle of upscaling is the basically the same as turbulence modelling used to model the Reynolds stress term (as briefly explained in Section 4.1.4)[7].

[7]The behaviour of turbulence scales, at the highest wave-numbers, is found to posses a considerable degree of universality which makes it amenable for modelling. This is accomplished by filtering the

The most common multi-scale feature is illustrated in Figure 4.7, which represents a typical porous medium (e.g. open-cell metal foam). On the micro-scale, two phases can be differentiated: the fluid phase ζ and the solid phase σ [103]. Both phases have their own micro-scale characteristic length resp. l_ζ and l_σ. However, the macro-scale doesn't show any difference between the fluid and solid phase, as displayed in Fig. 4.7[8]. For this reason, *effective properties* have to be used in the macro-scale at a characteristic length scale L. To be able to use this macro-scale upscaling approach, there has to be a clear length scale separation, implying that $(l_\zeta, l_\sigma) \ll r_0 \ll L$. With r_0 an intermediate scale at which macro-scale variables are defined. If there is no clear length scale separation and L is too close to $l_\zeta or l_\sigma$, only direct numerical simulation (or meso-scale approaches [104]) can be used. A detailed discussion on length scale separation is given in the PhD thesis of Peter De Jaeger [105].

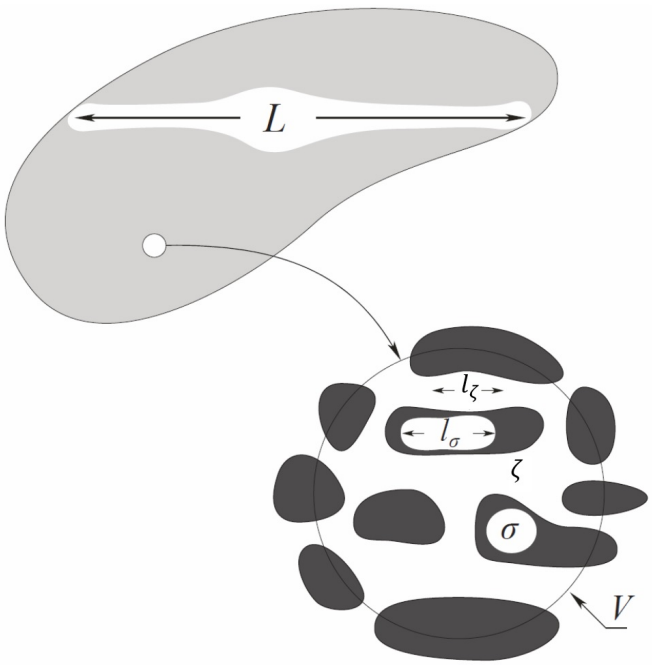

Figure 4.7: Micro- and macro-scale description of a porous medium [103].

smaller scaled eddies, by means of space averaging. Space averaging in its simplest form is done by volume-averaging.

[8]Small footnote: in this work two energy equations for fluid and solid phase are used. The convection coefficient (not assumed to be infinitly large) is used to couple both energy equations. Thus a thermal non-equilibrium model is used.

Already in 1993, Lakes [106] catalogued open-cell aluminium foam as a material with a structural hierarchy. The existence of a representative elementary volume (REV) for open-cell aluminium is shown in the PhD of Brun [107] and further processed by De Jaeger [105]. A REV consists out of several periodic unit cells (PUC). A large amount of research was spent on characterizing such a unit cell. Cushman et al. [108] suggest that the presence of the solid matrix in the flow domain alters the general hierarchy between the micro- and macro-scale. This facilitates the derivation of a macroscopic model.

Deriving the macroscopic model requires an upscaling technique. Different techniques can be found in literature [103]. The most important ones are the **volume averaging technique** (VAT) and the **homogenization theory**. The first technique will be used in this work and is also mostly used for open-cell metal foam. The VAT technique was developed for any kind of porous medium (with a clear length scale separation) by Whitaker [109]. The second theory uses asymptotic methods based on the mathematics of studying differential operators involving rapidly oscillating coefficients. It is difficult to give a complete picture of this homogenization technique, as it is very dependent on the used boundary conditions [110].

Before discussing the volume averaging theory, a discussion will be given on the geometrical characterization of open-cell foam. Before being able to upscale, one needs to characterize a PUC for the foam of interest. This characterization can be used for both direct numerical simulations and/or the volume averaging technique. The VAT technique averages the applicable conservation laws over a representative elementary volume. In some practical applications, only direct numerical simulations (DNS) will be usable, e.g. in a case where there is no clear length scale separation. However, some authors also use DNS in other cases. Therefore also a discussion will be given upon the grid cell sizes that are applicable for PUC (geometry used to upscale) or DNS (geometry consisting of multiple PUC to simulate metal foam as such). The most important range of results for both approaches will be given in Section 4.4.

4.3.1 Geometrical characterization of PUC

As illustrated in Chapter 1, there are many differences between different types of casted open-cell metal foam. The geometrical characterization, as will be discussed here, will focus on the casted foams made from a polyurethane preform (see Fig. 1.5(a)), as is produced by manufacturers such as MPore and ERG Materials and Aerospace. These foams are most commonly used in thermal applications, as the struts are solid as opposed to foam made via electro-deposition in which the struts are hollow.

Generally it is quite difficult to make an unambiguous characterization of

the metal foam based on the information provided by the manufacturer. These manufacturers characterize their metal foam products by reporting both the numbers of **Pores Per linear Inch (PPI)** and the **volumetric porosity** ϕ (1 – $\frac{m_{solid}/\rho_{solid}}{V_{tot}}$)[9]. The volumetric porosity ϕ is quite easy to measure with a relatively low uncertainty of 2-3%. In theory the number of PPI should be quite easy to measure too. However, as the foam structure is inherently three-dimensional, the PPI value heavily depends on the direction in which the PPI value is measured. This is also evident in Fig. 1.5(a). At least three different PPI values should be reported for each foam sample: one in every dimension. Furthermore, the reported PPI values in open literature are mostly a multiple of five (5, 10, 15...) which is certainly not representative for the complex and three-dimensional structure of (casted) open-cell metal foam. However, the integration of the PPI value has led to a large commercial value for manufacturers. For actual foam samples, these PPI values are far from a multiple of five as shown in Billiet et al. [16].

Properties that are of interest to reconstruct the foam or to use in calculations/correlations are:

- The strut diameter d_s
- The pore diameter d_p
- The surface-to-volume ratio σ_0
- The tortuosity τ (sometimes this parameter is necessary to determine the other mentioned parameters): this value represents the ratio of the chord length between two points and the effective pathway.

Authors like Hooman et al. [111] and Ghosh [112] use a **cubic cell representation** to study open-cell foam (see Fig. 4.8). The properties needed for this representation are d_p and d_s. In Hooman et al. [111], this strut diameter is determined through a correlation as a function of the PPI value. Considering the issues with the use of a PPI value as discussed earlier, this does not seem to be an accurate approach. Furthermore, it should be noted that the strut diameter varies over the strut length as shown in Fig. 4.9 for a foam made by ERG Materials and Aerospace. A detailed study of this axial variation was carried out by Jang et al. [113].

[9]This characterization method is frequently adopted in academic work in open literature too.

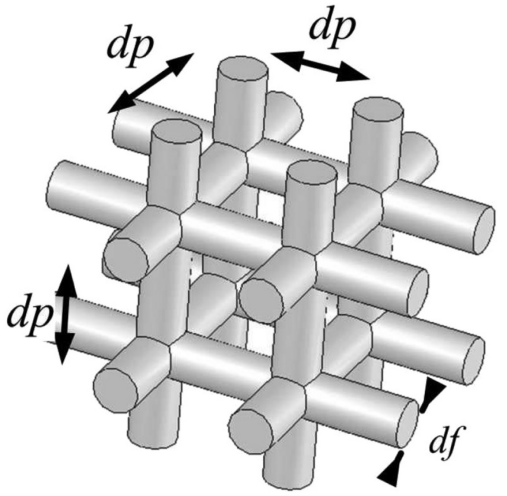

Figure 4.8: Periodic unit cell according to Hooman et al. [111] ($d_f = d_s$, d_s is used in this work.)

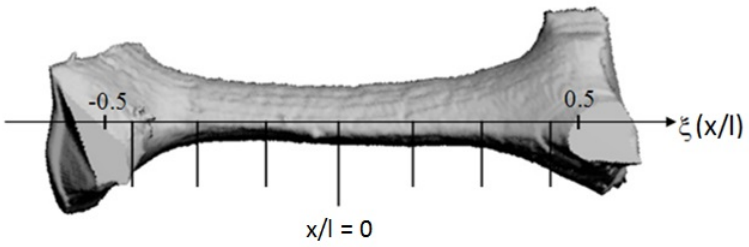

Figure 4.9: An illustration of the axial thickness variation along the strut length for a foam made by ERG Materials and Aerospace [105].

Dukhan et al. [114] simplified the metal foam geometry even more. They only considered a staggered bank of cylinders (see Fig. 4.10(c))

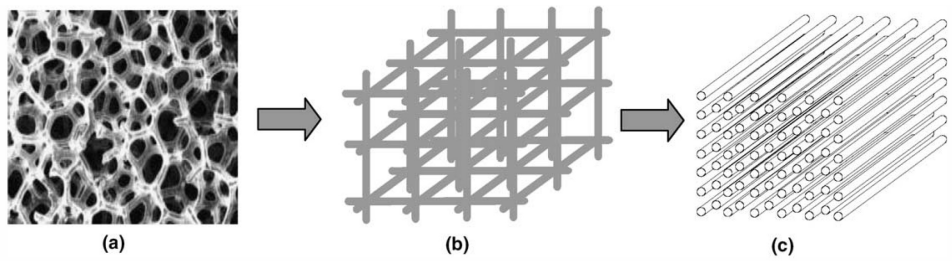

Figure 4.10: Metal foam representation as a bank of cylinders [114]

A first assumption of a more precise methodology to reconstruct the geometry of open-cell foam could stem from the **theory of space minimization**. Casted foam by e.g. MPore and ERG Materials and Aerospace is made based on a polyurethane preform. To make this preform, a foaming agent is added to polyurethane. How this preform then solidifies is influenced by the surface tension, resulting in a minimal surface area. Since the resulting metal foam is a copy of the polyurethane preform, one should consider shapes with a minimal surface energy to make an approximation of the metal foam structure. A tetrakaidecahedron was found by Lord Kelvin as that optimum (minimum) surface for a formulation of polyurethane [115]. It consists of six planar quadrilateral faces and eight non-planar hexagons of zero net curvature (see Figure 4.11(a)). Later, Weaire and Phelan [116] proved that the optimum formation was rather a combination of 6 tetrakaidecahedra and 2 irregular dodecahedra (see Figure 4.11(b)). The surface energy here is 0.3% compared to the model of Kelvin. This so-called WP cell, after the name of the discoverers, is then used by e.g. Kopanidis et al. [115] to reconstruct the foam.

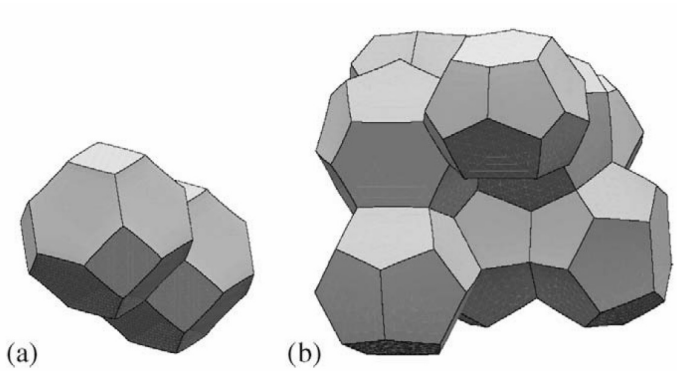

Figure 4.11: Illustration of (a) Kelvin cells and (b) W-P cells [115]

Fig. 4.12 shows that two parameters are used to describe the foam based on the

WP-cell: a pore diameter (d_p) and a strut diameter (d_l in this figure). The strut cross section is considered to be triangular and the strut diameter is assumed to be constant along the struts' length.

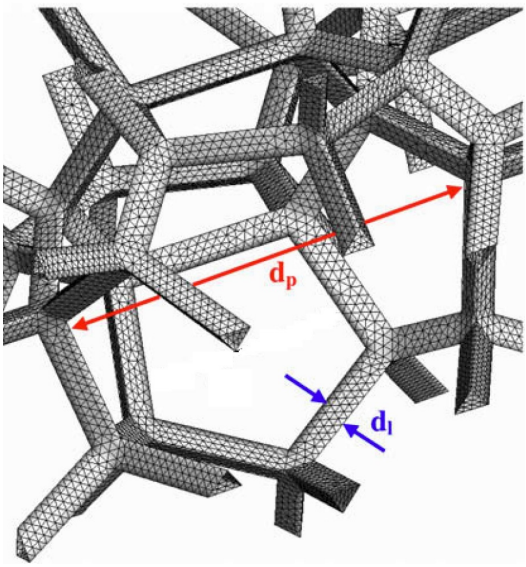

Figure 4.12: Detail of surface grid on foam's pore and ligaments [115]

Another approach is given by Krishnan et al. [117]. They assumed the shape of the pores to be spherical and these spheres of equal volume are arranged according to three **lattice structures**: body face-centered cubic (BCC), face-centered cubic (FCC) and A15 lattice. The BCC structure resembles the Kelvin cell, while the A15 lattice represents a WP cell. The PUC is obtained by subtracting the unit-cell cube from the spheres at various lattice points (see Fig. 4.13). The authors assumed the strut cross section to be triangular and they recognized the non-uniform distribution of metal along the struts' length. A similar approach is used for the PUC-determination in Dukhan et al. [118]. Krishnan et al. [119] have illustrated that the thermal conductivity is represented well with the BCC and A15 model PUC. Yet, the authors also stated that there should be more research for an accurate representation of the struts' cross-sectional area to length ratio. For the friction factor and local Nusselt number, all three models perform good if the surface-to-volume ratio is captured well with the unit cell model that is used. The authors compared their findings with the surface-to-volume ratio from correlations of Calmidi and Mahajan [120].

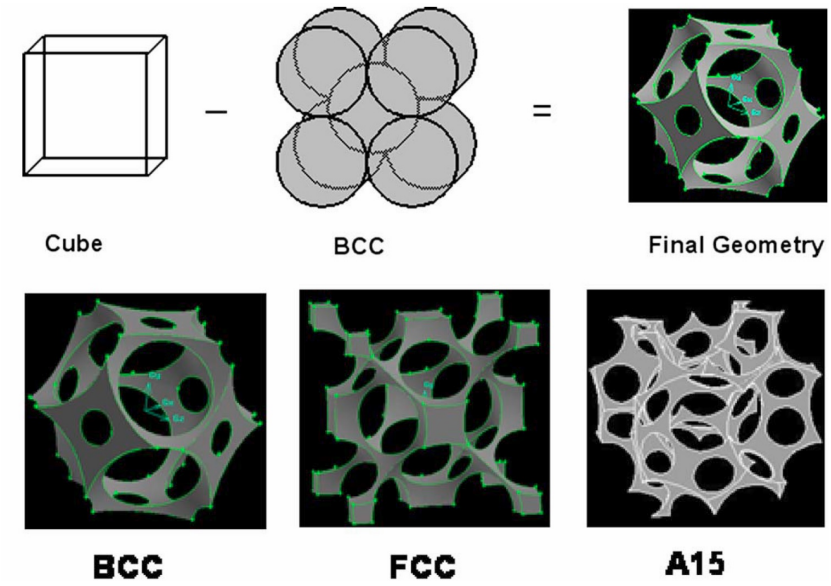

Figure 4.13: Sample images of PUC created for BCC, FCC and A15 arrangements of spherical pores [119]

Another very powerful method to characterize the foam is a **micro tomography (μCT) scan**. This method has recently gained some interest, as quite some recent work in open literature deals with this topic [121, 122, 123, 124]. However, it is still not common practice to use. A μCT scan virtually divides the solid structure in slices of equal thickness. Each slice is divided into a number of three-dimensional pixels which are called voxels. Each voxel is appointed a grey value, which depends on the interaction of X-rays with the material in that voxel. After combining the digital slices to a full three-dimensional model the foam's structure can be determined.

Once a virtual structure is available, structural characteristics of the structure can be obtained in a systematic way through image processing techniques and dedicated algorithms.

The X-rays used in the scanning equipment interact significantly different with a solid compared to a fluid (or vacuum), allowing for a clear distinction between both phases. However, voxels at the solid-fluid interface contain both phases. Therefore, their grey values can span a large range. For further image processing, they need to be binarised, i.e. allocated to either the solid (1) or fluid (0) phase. This operation is called grey scale segmentation or thresholding [107]. An overview of different segmentation algorithms is given by Linquist [125] and recently by Ohser et al. [126]. In this work, the algorithm is based on a so-called dual threshold which defines a threshold interval, combined with a

labelling operation [127]. This means that neighbouring voxels with grey values within the threshold interval, are treated as a subset and are all assigned to a phase. The phase assignment is done by comparing grey values with the averaged threshold level of the interval. Grey values smaller than this averaged value are assigned to the fluid phase, while voxels with larger values are considered as solid material.

With the help of μCT scans on real foams from ERG Materials and Aerospace, Perrot et al. [128] illustrated that the foams are orthotropic in nature. This means that they have different characteristics in different directions. Figure 4.14 illustrates this for a 20 PPI foam, however, this will be discussed later on. Based on μCT scans authors like De Jaeger et al. [129] were able to build more accurate models for the PUC representation, which will later be used in this work. Their orthotropic wire-frame representation is shown in Figure 4.15a. It is based on the Kelvin cell representation. The longest struts (l_2) make an angle α with a horizontal plane, which is given by:

$$tan\alpha = \frac{2l_2 sin\alpha}{d_1 - \sqrt{2}l_1} \tag{4.11}$$

Considering a hypothetical case, l_1 and l_2 are equally sized and $\alpha = \pi/4$. If this assumption is applied to Eq. 4.11 it yields:

$$l_1 = \frac{d_1}{2\sqrt{2}} \tag{4.12}$$

Consequently, Eq. 4.11 for the proposed geometry becomes: $tan\alpha = d_2/d_1$. This is based on μCT scans. This allows to find an expression for the longer strut in the orthotropic structure reading:

$$l_2 = 1/4\sqrt{d_1^2 + d_2^2} \tag{4.13}$$

The importance of using anisotropic models (on the thermal conductivity) is shown by Kumar and Topin [130].

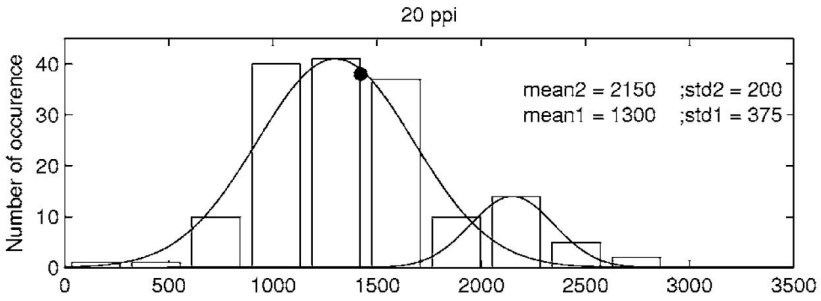

Figure 4.14: Ligament length and thickness distribution of the struts in lateral direction for 20 PPI ERG Materials and Aerospace Duocel foam [128]

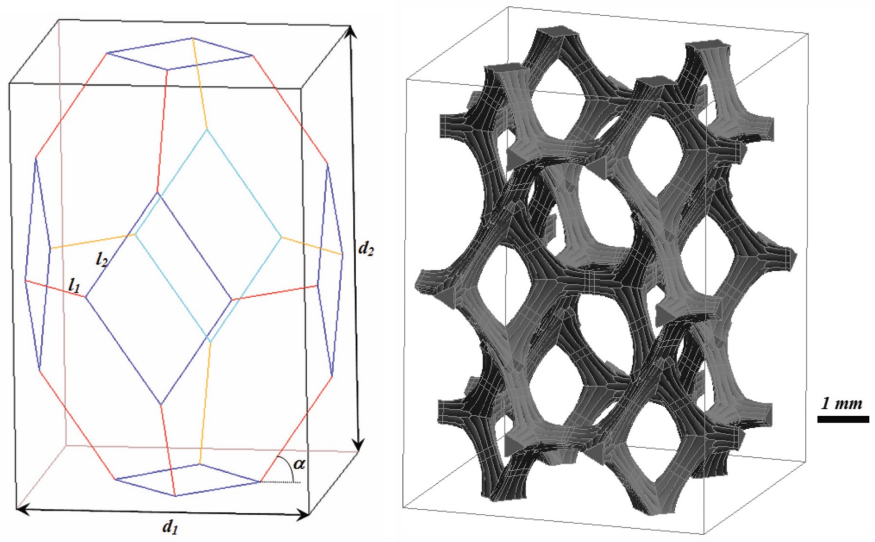

(a) with straight edges *(b) CAD model*

Figure 4.15: Orthotropic cell representation according to De Jaeger et al. [129]

Both strut lengths are derived from the two characteristic cell diameters. Additionally, the strut shape also needs to be determined. As already mentioned, the strut cross sectional shape is not assumed to be circular by all authors. In fact it depends on the porosity of the foam, linked with the Heywood circularity factor ($H_W(\phi) = 0.971 \cdot (1 - \phi)^{-0.09}$). High Heywood factors will result in a more triangular shape of the cross section, while a Heywood factor of one represents a completely circular strut shape [129]. Another issue is the variation of the strut diameter along the strut lengt. The way De Jaeger [105] addresses

this issue was based on the work of Kanaun and Tkachenko [131]. They found that the strut cross-sectional area in the middle between two nodes was the most critical parameter. It inspired De Jaeger [105] to analytically describe the strut size variation along the struts' length based on one parameter: the area A_0 measured in the middle of the strut. With this De Jaeger et al. [129] where able to construct a geometrical model based on just three input parameters: d_1, d_2 and A_0. With this model one is also able to calculate the surface-to-volume ratio σ_0 and the porosity of the foam ϕ.

Thanks to μCT scans one can determine these properties (also σ_0 can be determined through μCT as explained in De Jaeger et al. [132]). Although μCT scans are used more often to characterize the foam, this is still only by a minority of the researchers. If researchers want to use a geometrical representation or they want to determine parameters like tortuosity or surface-to-volume ratio, they will need to determine the properties either by a microscope (with limited uncertainty) or find them through correlations found in literature.

For a cubic unit cell representation, authors use an average pore diameter d_p or a so-called equivalent diameter $d = d_s + d_p$. Often it is not clear which of these two parameters is used. The average pore diameter (d_p) can be calculated either based on the PPI value provided by the manufacturer ($0.0254/PPI$) or through a correlation based on the average diameter. The review paper by Mahjoob and Vafai [133] gives an overview of some correlations to determine d_p. The correlation by Du Plessis et al. [134, 135] for d_p is a frequently used example of such a correlation (Eq. (4.14)). In Eq. (4.14) d_p is a function of both the tortuosity and the equivalent diameter of a cubic unit cell volume d. Another frequently used correlation for d_p is proposed by Calmidi [136] and depends on the strut diameter d_s and the porosity ϕ (Eq. (4.15)).

$$d = d_p \frac{2}{3 - \chi} \tag{4.14}$$

$$d_f/d_p = 1.18\sqrt{(1-\phi)/(3\pi)} * 1/(1 - e^{-(1-\phi)/0.04}) \tag{4.15}$$

The surface-to-volume ratio is also a parameter which is frequently used. In open literature, this surface-to-volume ratio is often calculated through a correlation like the one by Calmidi and Mahajan [120] (requiring the strut diameter d_s, the pore diameter d_p and the porosity ϕ) or the one by Fourie and Du Plessis [135] (depending on the tortuosity χ of the foam sample and the equivalent diameter d), see Eq. (4.16) and Eq. (4.17), respectively. If the correlation by Fourie and Du Plessis [135] is used, the tortuosity χ is also required and again calculated through a correlation (see Eq. (4.18)) [134].

Both correlations are frequently used in open literature. The paper by Calmidi and Mahajan is cited over 500 times and is still in use as can be seen from these

recent citations: Refs [89, 137, 138]. The work by Fourie and Du Plessis [135] is cited over 150 times, and is only rarely used in open literature.

$$\sigma_0 = \frac{3\pi d_f}{(0.59 d_p)^2[1 - e^{-((1-\phi)/0.04)}]} \tag{4.16}$$

$$\sigma_0 = \frac{3}{d}(3 - \chi)(\chi - 1) \tag{4.17}$$

$$\frac{1}{\chi} = \frac{3}{4\phi} + \frac{\sqrt{9 - 8\phi}}{2\phi} * cos[\frac{4\pi}{3} + 1/3 cos^{-1}[\frac{8\phi^2 - 36\phi + 27}{(9 - 8\phi)^{3/2}}]] \tag{4.18}$$

Properties that can be measured through μCT scans are e.g. porosity (ϕ), surface-to-volume ratio (σ_0), cell diameters (d_1, d_2), pore diameter (d_p) and axial variation of the strut thickness. Table 4.2 reports the values measured with a μCT scan for five different foam samples [129]. A_0 is the interfacial strut area as measured in the middle of the strut. The relative experimental uncertainty on the porosity and surface-to-volume ratio is at most 2% and 8%, respectively. Note that the reported properties are averaged values as the μCT scan is performed over 16 cells of the foam sample. The surface-to-volume ratio (σ_0) is calculated with the marching cube algorithm, as described by Lindblad [139]. The interfacial strut area (A_0) is calculated as described in De Jaeger et al. [129].

Note that all uncertainties in this work are expressed as 95% confidence intervals. Uncertainties are calculated according to Moffat [140].

In Table 4.2, the correlations for surface-to-volume ratio from Calmidi and Mahajan [120] and Fourie and Du Plessis [135] are compared with results from μCT scans. For this comparison the porosity and pore diameter from in-house μCT scans are used (Table 4.2) together with correlations for the surface-to-volume ratio, strut diameter and tortuosity as reported in Ref. [134] and [136]. Furthermore a comparison with the work of De Jaeger et al. [129], the so-called hybrid model, is also made in Table 4.2.

Table 4.2 shows a large deviation between results obtained through correlations and the results obtained through a μCT scan. The correlation of Calmidi and Mahajan [120] is the least accurate with differences up to 133%. Also the correlation of Fourie and Du Plessis [135] deviates up to 22% from the experimental results of the full μCT data. Also note that both correlations consistently overestimate the measured surface-to-volume ratio at the 8.5 μm scale. As previously discussed, the surface-to-volume ratio at this scale is actually already an overestimation of the surface-to-volume ratio which is relevant for the heat transfer and pressure drop.

Foam	PPI	ϕ	d_1	d_2	A_0	σ_0	d_p	Calmidi & Mahajan [120] σ_0	Fourie & Du Plessis [135] σ_0	De Jaeger et al. [129] σ_0
		–	$[mm]$	$[mm]$	$[\times 10^{-1} mm^2]$	$[mm^{-1}]$	$[m]$	$[m^{-1}]$	$[m^{-1}]$	$[m^{-1}]$
1	10	0.932± 0.02	4.22± 0.18	6.23± 0.18	0.998± 0.08	462± 35	2.56± 0.13	1062	528	482
2	10	0.951± 0.02	4.28± 0.13	6.42± 0.13	0.615± 0.13	380± 30	2.61± 0.11	884	462	403
3	20	0.913± 0.02	2.52± 0.06	3.78± 0.06	0.463± 0.04	860± 69	1.53± 0.05	2000	951	860
4	20	0.937± 0.02	2.77± 0.05	4.15± 0.05	0.377± 0.05	720± 58	1.69± 0.05	1549	781	694
5	20	0.967± 0.02	2.6± 0.05	3.67± 0.05	0.126± 0.02	580± 46	1.55± 0.05	1218	669	573

Table 4.2: Properties of studied foam samples, determined through a μCT scan with a voxel size of 8.5 μm [129]. All reported foam samples were made in-house [129].

Despite their limited accuracy, these correlations are often used in open literature [141]. Furthermore, also note that the comparison made in Table 4.2 is based on input parameters that are determined through μCT and not according to the common practice as discussed in the paper of Mahjoob and Vafai [133]. As a result, the deviations will be even higher if the uncertainty on the input parameters for the correlations are larger, e.g. if they are determined through a microscope or the naked eye. This will not only influence the repeatability of the experiments, it will also influence the results. Both in numerical and experimental work, parameters such as σ_0 are used as input.

Furthermore, the results from the model of De Jaeger et al. [129] show a much better agreement with the μCT scan data. With a relative uncertainty level of 10% [129], the values for σ_0 match the experimental values.

However, μCT scan data is still necessary in the model of De Jaeger et al. [129] to determine the input parameters (d_1, d_2 and A_0). Hence the method by De Jaeger et al. [129] requires a greater amount of effort compared to correlations. Yet, considering the correlations currently available, μCT scans are the only way to ensure a relative error which is smaller than 10%.

As will be discussed later, the pressure drop of the metal foam can be characterized by the permeability and the inertial coefficient (a proper definition will be given later on). In their turn, these quantities are mainly determined by the geometric foam properties that have been discussed so far. Since it has been shown that the uncertainty on these geometrical properties is rather large, it is not surprising that a large discrepancy can be found between the experimental results for the permeability and inertial coefficient in open literature [142]. Furthermore, the smaller the fluid mass flow rate, the larger the discrepancies. These properties are frequently seen as bulk properties of the porous medium. In Section 4.3.3, these properties will be discussed more extensively. Next to the geometrical characterization of the foam, there are also other factors which determine the permeability and inertial coefficient: interpolation details, wall boundary layer effects, entrance/exit effects, dependency of the velocity range over which the quadratic correlation is taken to calculate permeability and inertial coefficient for example [105]. However, these parameters (permeability and inertial coefficient) are also used in numerical calculations or experimental investigations, as shown by the recent review by Yang et al. [143]. The uncertainty on the permeability and the inertial coefficient will result in an uncertainty on the performance of the metal foam.

Other methods exist to (more effectively) determine the properties of foam samples. For example, the surface-to-volume ratio σ_0, can be determined indirectly via the Brunauer, Emmet and Teller (BET) method [144]. This is a technique based on the gas adsorption/desorption at the interfacial surface area. Using this method, the entire surface area down to nanometer scale is measured.

This means that the BET method can be used for analyses on nanometer scale only. However, thermal analysis is performed on continuum scale. It is important to note that the continuum assumption is only valid when the Knudsen number is smaller than 0.01 [145]. Consequently, for the continuum hypothesis to hold, the smallest characteristic dimension that can be considered is around 5 μm in case of air as heat transferring medium. Hence, the BET method will result in too large surface areas for the intended analysis [146], as nanometer scale variations do not influence the continuum scale behaviour.

The BET method is also used by ERG Materials and Aerospace for calculating their surface-to-volume ratio σ_0 as reported on their website. Therefore, this σ_0 value by ERG Materials and Aerospace is often cited by authors [147], disregarding the fact that this is a strong overestimation of the actual value especially in regards with thermal applications [105, 146].

A **drawback of these** μCT **scans** is that they are quite expensive and not straightforward to use in comparison with a microscope or the naked eye. The main difficulty lies in the choice of the averaged threshold level to allocate the voxels to either the solid (1) or fluid (0) phase. A different threshold can yield significantly different allocation of fluid volumes [105], and thus a significantly different foam model. Furthermore, the voxel size itself can also significantly influence the results (as shown in Figure 4.16). Figure 4.16(a) is constructed with a voxel size of 37.5 μm, while Fig. 4.16(b) - which clearly shows more detail - is made through a scan with a voxel size of 8.5 μm. The surface-to-volume ratio of both reconstructions in Fig. 4.16 is 720 (a) and 860 (b) m^{-1}: a relative difference of 19%. In this example, the scan is done on at least 16 foam cells. The reported values are averaged. This shows that the voxel size, besides thresholding, is an important parameter [54]. The heat transfer performance of a fixed volume of metal foam is determined by the product of the heat transfer coefficient and the surface-to-volume ratio. The heat transfer coefficient is determined based on the measured performance and the determined surface-to-volume ratio. As long as the thermal performance is reconstructed using the same surface-to-volume ratio σ that was used to determine the heat transfer coefficient h, the correct thermal performance $h \cdot \sigma$ will be obtained. This is not always the case as the heat transfer coefficient is most of the time reported separately.

It is clear that the geometry obtained with a 37.5 μm voxel size and a 8.5 μm voxel size is fundamentally different on the continuum scale. This leads to the question whether this continuum scale roughness has a significant impact on the pressure drop and heat transfer behaviour. Generally this is not the case, as long as the flow is laminar, or the roughness peaks are smaller than the thickness of the viscous sublayer in turbulent flow [148]. For numerical simulations, the relevant surface-to-volume ratio is the one obtained on a scale that does not resolve the roughness effects which do not influence the flow.

Schmierer and Razani [149] scanned metal foam samples with four different voxel sizes, ranging from 115 to 58 μm. They found an asymptotically converging surface-to-volume ratio. Another restriction on the voxel size is imposed by the continuum assumption with no-slip boundary conditions, upon which thermal and hydraulic analysis are commonly based (as is the case for this work). If the continuum hypothesis holds and with air as a working fluid, it is not necessary to have a finer spatial discretization than voxel sizes in the order of 5 μm. Hence, the high resolution scan with voxel size 8.5 μm of Figure 4.16(b) can be considered highly accurate [54].

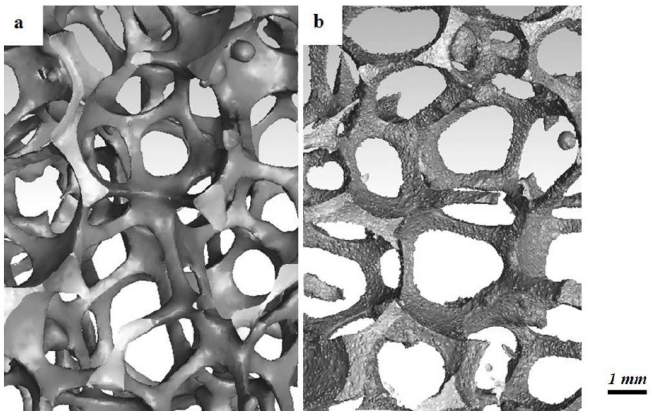

Figure 4.16: An illustration of the effect of voxel size for a μCT scan reconstruction with respectively (a) 37.5 μm and (b) 8.5 μm voxel size. Foam samples are made in-house. Picture copied from the work of De Jaeger [129].

4.3.2 Typical grid cell sizes

This section is included to illustrate the large number of cells that are needed to study foam structures in a direct numerical simulation. First of all, it should be mentioned that most researchers report an 'uncertainty' on their results by refining their grid once and reporting the difference in the obtained numerical result for one specific parameter. However, as explained in Section 4.1.3 this method will underestimate the uncertainty on the simulation results. In fact they only compare two grid refinements with each other, and this doesn't give any information upon the uncertainty against an infinitely small grid size.

Kopanidis et al. [115] simulated a metal foam block with dimensions 2.82 x 2.82 x 5.82 mm^3. They studied conjugated heat transfer (describing the heat transfer between fluid and solid as an interaction between two 'objects'). The base case was meshed with $1.5\ 10^6$ elements. Dukhan et al. [118] simulated a sample size with dimensions 5.08 x 5.08 x 127 mm^3. They used a mesh with $1.2\ 10^6$

elements. Krishnan et al. [119] only studied one PUC and their analysis was done dimensionless. They studied thermal conductivity and pressure drop. They used 200 000 elements. Ranut et al. [150] performed a thermo-hydraulic analysis on a 12 x 12 x 20 mm^3 sample. For this they used a grid of $4.1\ 10^6$ elements. Magnico [151] studied hydrodynamic properties using DNS simulations on pore scale. The dimensions of his sample were 10.08 x 11.67 x 11.67 mm^3 and the computational domain contains 6.7 million cells. This is much higher than the previous discussed work.

When aiming to perform a real DNS simulation, an important aspect is resolving the velocity boundary layer, for which the numerical approximation of the velocity gradient is required. A proper estimation of the velocity divided by the distance from the CV-centroid normal to the boundary is therefore important. This is denoted as y_c and a good estimation for this value is:

$$y_c \sqrt{\frac{\rho_f U}{\phi \mu x_0}} \leq 1, \tag{4.19}$$

In the above equation x_0 is the distance in flow direction, parallel to the boundary. Considering the flow along a strut as flow along a flat plate with length d_s and requiring that 95% of the boundary layer is resolved accurately, then x_0 can be written as $(1 - 0.95)d_s$. For Re_{d_s} = 200 this yields a y_c of around $4\ 10^{-6}m$. This sets the grid spacing adjacent to the interstitial surface to $8\mu m$. For the same Reynolds number, the required CV size for a fully resolved DNS, based on the Kolmogorov scale would be in the order of η_t = $23\mu m$[10]. For a second order central differencing scheme the grid spacing needs to be limited to $0.26\eta_t$. For one 3D PUC cell this would take at least $1 \cdot 10^9$ cells, which is computationally too expensive. Della Torre et al. [152] have preformed DNS simulations to determine the flow regimes inside open cell foam. First they measured the foam through μCT, then they make a $2D$ projection and only simulated one cell. Even with a $2D$ approach this already gave rise to a grid of $4.1 \cdot 10^6$ elements.

Calculating the results with a coarser grid can be thought of as an implicit LES and introduces numerical diffusion. Therefore a grid uncertainty analysis has to be performed. For the finest grid size (start size: $8\mu m$, max. size: $100\mu m$) chosen by De Jaeger [105], the cell count for one PUC was around 120 million cells.

This discussion indicates large differences exist in the grids used by different authors. Furthermore, of all the authors only De Jaeger has reported an uncertainty analysis for the numerical discretization, like the one described in Section 4.1.3.

[10]The Kolmogorov scale is linked to the smallest scale in the spectrum of the viscous sub-layer. These smallest scales are causing turbulence. Kolmogorov is only relevant if the flow is turbulent. In case of geometrical unsteadiness, without turbulence, it is possible to calculate the Kolmogorov scale; however, it does not exists physically.

4.3.3 A short introduction to the volume averaging theory

Based on the discussion in the previous paragraph, it is clear that the full geometry of an application with metal foam cannot be simulated accurately in CFD. Therefore, instead of using the microscopic model, a macroscopic model is determined. A general approach to one possible upscaling method is given by Whitaker [109]: volume averaging. It provides a mathematical framework in which the porous properties like depicted in the famous Darcy-Forchheimer equation get a clear physical meaning.

Large parts of this literature survey were adapted from the previous PhD work of P. De Jaeger at this research group [105].

The volume averaging theory starts with the microscopically scaled model, as described in the introduction of Section 4.3. The continuum, momentum and energy equations can be averaged over a representative elementary volume, based on the volume averaging process as described by Whitaker [109]. As discussed in Section 4.3, the porous medium consists of two phases indicated by σ (solid) and ζ (fluid). An arbitrary quantity ψ of the ζ phase is indicated by ψ_ζ. The intrinsic average[11] of ψ_ζ, evaluated at a location $\overrightarrow{x_c}$, is then given by $\langle\psi_\zeta\rangle(\overrightarrow{x_c}) = \int_{V_\zeta} m(\overrightarrow{x_c} - \overrightarrow{r})\psi_\zeta(\overrightarrow{r})dV$. Here, $m(\overrightarrow{x_c} - \overrightarrow{r})$ is a filter function, which is normalized on the REV volume V_m and which is zero outside of the REV. Using Gray's decomposition [153], the arbitrary quantity can be written as a function of the porosity ϕ, the intrinsic average and the microscopic scale deviation from the average:

$$\psi_\zeta = \phi\langle\psi_\zeta\rangle + \widetilde{\psi_\zeta} \tag{4.20}$$

This averaging process results in the following volume averaged equations in

[11] There is a difference between intrinsic properties and superficial properties. The superficially averaged velocity for example is preferred in the foam domain, since an intrinsically averaged velocity would require a velocity jump because of the sudden contraction of the flow area when the air enters the foam. The difference between both average operations is thus the porosity of the material.

local thermal non-equilibrium (the superscript i stands for intrinsic) [105]:

$$\nabla \cdot \langle \vec{v} \rangle^i = 0 \tag{4.21}$$

$$\begin{aligned} \rho \frac{\partial \langle \vec{v} \rangle^i}{\partial t} + \rho \langle \vec{v} \rangle^i \cdot \nabla \langle \vec{v} \rangle^i &= -\nabla \langle P \rangle^i + \mu \nabla^2 \langle \vec{v} \rangle^i + \rho \vec{g} \\ &\quad -\rho \nabla \cdot \langle \widetilde{\vec{v}} \widetilde{\vec{v}} \rangle^i \\ &\quad -\frac{1}{\phi} \int_{A_{fs}} m(\vec{x}_c - \vec{r}) \widetilde{P}(\vec{r}) \vec{n}_{fs} dA \\ &\quad +\frac{1}{\phi} \int_{A_{fs}} m(\vec{x}_c - \vec{r}) \mu \nabla \widetilde{\vec{v}}(\vec{r}) \cdot \vec{n}_{fs} dA \end{aligned} \tag{4.22}$$

$$\begin{aligned} \phi (\rho c_p)_f \left[\frac{\partial \langle T_f \rangle^i}{\partial t} + \langle \vec{v} \rangle^i \cdot \nabla \langle T_f \rangle^i \right] &= \phi k_f \nabla^2 \langle T_f \rangle^i \\ &\quad -\phi (\rho c_p)_f \nabla \cdot \langle \widetilde{\vec{v}} \widetilde{T}_f \rangle^i \\ &\quad +k_f \nabla \cdot \int_{A_{fs}} m(\vec{x}_c - \vec{r}) \widetilde{T}_f(\vec{r}) \vec{n}_{fs} dA \\ &\quad + \int_{A_{fs}} m(\vec{x}_c - \vec{r}) k_f \nabla \widetilde{T}_f(\vec{r}) \cdot \vec{n}_{fs} dA \end{aligned} \tag{4.23}$$

$$\begin{aligned} (1-\phi)(\rho c_p)_s \frac{\partial \langle T_s \rangle^i}{\partial t} &= (1-\phi) k_s \nabla^2 \langle T_s \rangle^i \\ &\quad +k_s \nabla \cdot \int_{A_{sf}} m(\vec{x}_c - \vec{r}) \widetilde{T}_s(\vec{r}) \vec{n}_{sf} dA \\ &\quad + \int_{A_{sf}} m(\vec{x}_c - \vec{r}) k_s \nabla \widetilde{T}_s(\vec{r}) \cdot \vec{n}_{sf} dA, \end{aligned} \tag{4.24}$$

With a normal vector on a surface pointing out of the adjacent volume. Note that this convention is used throughout this work. An advantage of the VAT approach is that it offers a rigorous framework, which allows to indicate the conditions for which the macroscopic transport equations hold.

The main assumptions for these equations are [105, 109]:

- The variation of μ within the averaging volume is neglected.
- Length-scale constraints: $l_\zeta \ll r_0$ and $r_0^2 \ll L^2$, in which l_ζ is the characteristic length for the ζ-phase, r_0 the radius of the averaging volume and L a generic length-scale associated with the averaged quantities.
- Terms involving $\nabla \phi_\zeta$ and $\nabla^2 \phi_\zeta$ can be neglected (this is more a consequence than a assumption). This is derived from comparing terms between one another, like shown in Ref. [109]. When this is not the case, no simple solution to the closure problem can be given. These are the boundary conditions of the porous medium, which can be described (if necessary) with the momentum jump conditions as given by Ochao-Tapia and Whitaker [154].

- No-slip boundary condition and quasi-steady flow (no time dependency).

Next step is to transform Eqs. 4.21 to 4.24 with the help of closure term modelling. Closure modelling is based on mapping the spatial deviations of microscopic quantities to its macroscopic counterpart. This simplifies the closure problem to solving the quasi-steady transport equations on a REV representation of the porous medium in order to find its appropriate mapping function. Determination of the closure terms will require a lot of computational power. However, once the closure terms are calculated, they can be used in any simulation based on the volume averaged equations (as will be discussed later). This technique is also used in most of the numerical studies found in literature.

4.3.3.1 Momentum dispersion

The term 'momentum dispersion' represents the mixing and remixing in the fluid phase ζ. It is caused by the splitting and rejoining of streamlines, as a fluid passes through a porous medium. Inspired by LES turbulence modelling a gradient-type model will be employed to model momentum dispersion. In this model, the diffusion is governed by the effective viscosity μ_e. This effective viscosity is estimated to be μ/ϕ by Ochoa-Tapia and Whitaker [109] together with Magnico [151]. It expresses how macroscopic shear strain rates are equalised due to the presence of the solid matrix in the flow domain. This model reads as Eq. 4.25.

$$-\rho\langle\widetilde{\vec{v}}\widetilde{\vec{v}}\rangle^i = (\mu_e - \mu)\nabla\langle\vec{v}\rangle^i, \tag{4.25}$$

4.3.3.2 Viscous and pressure drag closure

Whitaker has theoretically proven that the well-known Darcy-Forchheimer equation is a closure term model for the volume-averaged momentum equation. Therefore the closure modelling can be done as (like in the previous PhD work of De Jaeger at this research group [105]):

$$\langle\vec{v}\rangle^s\overline{\overline{\kappa}}_*^{-1} = \frac{1}{\mu}\frac{1}{V_m}\int_{A_{fs}}\mu\nabla\widetilde{\vec{v}}(\vec{r})\cdot\vec{n}_{fs}dA \tag{4.26}$$

$$\langle\vec{v}\rangle^s\overline{\overline{\beta}}_* = \frac{1}{\rho|\langle\vec{v}\rangle^s|}\frac{1}{V_m}\int_{A_{fs}}\widetilde{P}(\vec{r})\vec{n}_{fs}dA \tag{4.27}$$

Note the subscript asterisk in the equations above, this indicates that both properties are determined by a direct numerical formation. This differs from the common approach in open literature, where the properties are determined through experiments. Eqs. 4.26 and 4.27 are valid independent of the way the closure terms are determined (experimental or numerical). For this reason, the asterisk subscript will be omitted in further equations, unless there is an explicit reference

to numerically determined closure terms [12]. Some authors e.g. De Jaeger [105] developed a way to determine these parameters numerically by recognising that the permeability can be linked to the viscous forces acting on the surface, while the pressure forces are linked to the inertial coefficient. Indeed, a distinction needs to be made with the experimentally defined permeability $\overline{\overline{\kappa}}$ and inertial coefficient $\overline{\overline{\beta}}$. These experimentally defined parameters are described as a material property and assumed to be independent of the velocity. In contrast, in the numerical simulation no assumptions are made on the dependency of these properties on the velocity. The only assumption that is invoked is that the permeability is associated with the viscous forces and the inertial coefficient with the pressure forces.

4.3.3.3 Thermal dispersion

Similar to the momentum dispersion term, Quintard et al. [103] also discussed a closure scheme for the thermal dispersion. The interpretation is similar to the momentum term, only that this term describes the splitting and rejoining of energy flows in the solid phase σ.

$$-(\rho c_p)_f \langle \widetilde{\vec{v}} \widetilde{T}_f \rangle^i = \overline{\overline{k_d}} \cdot \nabla \langle T_f \rangle^i, \tag{4.28}$$

In the above equation $\overline{\overline{k_d}}$ is the dispersion tensor where the subscript d denotes dispersion.

The resulting macroscopic flow and energy equations for incompressible flow with constant fluid properties in the REV, stationary solid phase and constant porosity are then given by Eqs. (4.29) to (4.32) [105]. According to Minkowycs et al. [155] thermal equilibrium equations can only be used when $Re_{d_f} < 0.1$. This means that the convection coefficient cannot be assumed to be infinitely large and two energy equations (for the fluid and solid field) have to be solved. An interstitial convection coefficient makes the connection between the solid and fluid domain. In these equations, the closure terms $\overline{\overline{\kappa}}$, $\overline{\overline{\beta}}$, $\overline{\overline{k_d}}$ (thermal dispersion), h_{fs} (interstitial heat transfer coefficient) appear. The determination of these terms is discussed in the next paragraph. Furthermore, as can be seen from these equations some terms are tensorial.

[12] Note that there is a significant difference between numerically and experimentally determined closure terms. In experimentally determined closure terms it is assumed that $\overline{\overline{\kappa}}$ and $\overline{\overline{\beta}}$ are constant. In a numerical approach this is not the case. However, independent of a numerical or a experimental approach, the sum of $\langle \vec{v} \rangle^s \overline{\overline{\kappa}}^{-1}$ and $\langle \vec{v} \rangle^s \overline{\overline{\beta}}$ should be identical.

$$\nabla \cdot \langle \vec{v} \rangle^i = 0 \tag{4.29}$$

$$\begin{aligned} \rho \frac{\partial \langle \vec{v} \rangle^i}{\partial t} + \rho \langle \vec{v} \rangle^i \cdot \nabla \langle \vec{v} \rangle^i &= -\nabla \langle P \rangle^i + \mu_e \nabla^2 \langle \vec{v} \rangle^i + \rho \vec{g} \\ &- \mu \overline{\overline{\kappa}}^{-1} \cdot \langle \vec{v} \rangle^i \\ -\rho \overline{\overline{\beta}} \cdot |\langle \vec{v} \rangle^i| \langle \vec{v} \rangle^i & \end{aligned} \tag{4.30}$$

$$\begin{aligned} \phi (\rho c_p)_f \frac{\partial \langle T_f \rangle^i}{\partial t} + \phi (\rho c_p)_f \langle \vec{v} \rangle^i \cdot \nabla \langle T_f \rangle^i &= \phi \nabla \cdot (\overline{\overline{k_d}} + \overline{\overline{k_{f,e}}}) \cdot \nabla \langle T_f \rangle^i \\ &+ h_{fs} \sigma_0 (\langle T_s \rangle^i - \langle T_f \rangle^i) \end{aligned} \tag{4.31}$$

$$\begin{aligned} (1-\phi)(\rho c_p)_s \frac{\partial \langle T_s \rangle^i}{\partial t} &= (1-\phi) \nabla \cdot (\overline{\overline{k_{s,e}}} \cdot \nabla \langle T_s \rangle^i) \\ &- h_{fs} \sigma_0 (\langle T_s \rangle^i - \langle T_f \rangle^i) \end{aligned} \tag{4.32}$$

Simulating porous media numerically basically comes down to determining the closure terms.

4.3.3.4 Results from the PhD of De Jaeger [105]

In this section, the results of the PhD of De Jaeger are discussed, because this was the best state of the art at the moment of writing this work. However, further research is necessary before this method by De Jaeger can be widely used. This is shown in Appendix D, in this appendix a start of this further research is also made.

Determination of momentum closure terms

In Eq. (4.26) and (4.27) the superscript s stands for superficial and subscript m for measured (volume).

Recognizing that the integrals in these equations are the viscous and the pressure force, respectively, which act on the fluid-solid interface gives a physical interpretation to both parameters. The subscript asterisk indicates that both properties are determined by a direct numerical formation. Indeed, a distinction needs to be made with the *phenomenologically* defined permeability $\overline{\overline{\kappa}}$ and the inertial coefficient $\overline{\overline{\beta}}$. These phenomenological parameters are described as a material property and assumed to be independent of the velocity. In contrast, in the numerical simulation no assumptions are made on the dependency of these properties on the velocity. The only assumption that is invoked is that the permeability is associated with the viscous forces and the inertial coefficient with

the pressure forces. Note that in a macroscopical fully developed and steady flow, the momentum balance becomes a pure force balance between the pressure gradient and the drag forces which act on the interstitial surface. Therefore, one could argue the need to characterize both drag forces separately through porous properties, i.e., why not insert a direct dependency between the total drag force and the geometrical characteristics?

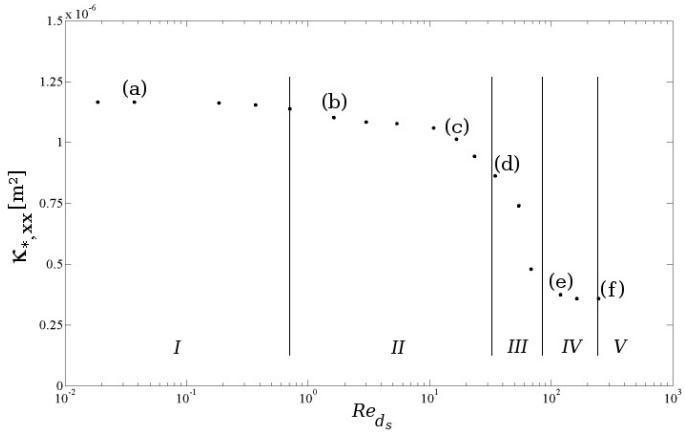

Figure 4.17: Permeability ($\kappa_{*,xx}$) versus Reynolds number for Foam 1 in Table 4.2. The five flow regimes are indicated (I-V)[105]

Based on this idea, one can calculate the permeability and the inertial coefficient by applying different pressure gradients in each direction (ranging from 0.05 Pa/m to 50 kPa/m). For the higher pressure gradients, the calculation is unsteady. For this unsteady calculation, the computational time is quite high. It takes 1 month to calculate the data on a machine with dual hex core Xeon X5690 3.46 GHz processors with 12 MB Cache and an on-board memory of 96 GB DDR3-1333 MHz RAM. However, this calculation only has to be done once. In Figures 4.17 and 4.18, the results for the x-direction are shown. It is apparent that both properties *depend on the Reynolds number*. The characteristic length for the Reynolds number reported here is the strut diameter (d_s) which is based on the interfacial strut area in the middle of the strut (A_0 as reported in the work of De Jaeger et al. [129]). The characteristic velocity used in the Reynolds number is the superficial velocity.

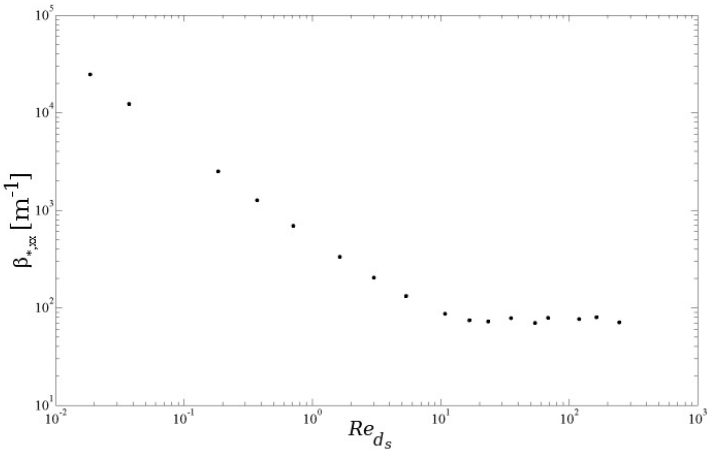

Figure 4.18: Inertial coefficient ($\beta_{*,xx}$) versus Reynolds number for Foam 1 in Table 4.2 [105]

For the first three points ((a)-(c)) in Figure 4.17, the flow is laminar and steady. For the lowest Reynolds number, point (a), an inertial core starts to form in the pores. The core does not span the complete flow domain and therefore has no influence on the struts downstream (see Figure 4.19(a)). This changes for the second point (b) (see Figure 4.19(b)), where the inertial core now spans the complete flow region. The permeability shows a slight decrease, as can be seen in Figure 4.17. Recalling the relation between permeability and viscous drag force, this decrease in permeability implies that the strain rate (and thus the shear stress for a Newtonian fluid) increases more than the intrinsic velocity increases, i.e. the effect of the inertial core formation is traced downstream in the foam sample.

In the third steady-laminar case, point (c) in Figure 4.17, recirculation zones are formed in the wake behind the struts (see Figure 4.19(c)). Note that in an actual foam sample, where the struts are not as aligned as in the idealised PUC representation, this formation of recirculation zones can be understood by recognizing that the regions containing these zones have a very limited contribution to the mass flow rate through the foam volume. On the other hand, the mass flow rate increases compared to the previous point (b). As the majority of the increase in mass flow rate has to pass through a decreased volume, the inertial core is compacted. This results in a larger increase of the strain rate near the solid-fluid interface than of the filtration velocity. In point (d), the flow has entered the unsteady laminar regime: see Figure 4.19(d). This is slightly above the critical value of Re_{d_s} = 31.5 as also reported by Ref. [151].

Increasing the Reynolds number further makes the flow enter the transitional

regime and for $Re_{d_s} > 120$ (in this case) there is an equilibrium between the increment of filtration velocity and strain rate: the permeability tends to a constant value. This is characterized by the highly unsteady flow, resembling turbulence. This is visualized in points (e) and (f) in Figure 4.19.

In Figure 4.18, the inertial coefficient is defined as the ratio of the pressure force density to the kinetic energy of the fluid (Eq. (4.27)). This pressure force is determined by the pressure distribution over the surface area of the solid-fluid interface. Upstream of a strut, there is a stagnation zone, where kinetic energy reduces to zero and results in a region with high pressure. Downstream, a distinction has to be made between flow regimes with or without recirculation regions in the wakes behind the struts. In case of no circulation ($Re_{d_s} < 10$), the inertial coefficient decreases with an increasing Reynolds number. This means that the pressure force increases at a lower rate than that of the averaged kinetic energy in the flow domain. When the recirculation regimes in the wakes downstream the struts start to appear ($Re_{d_s} > 10$), the increment of pressure force and averaged kinetic energy is equal. This is characterised by a nearly constant inertial loss factor.

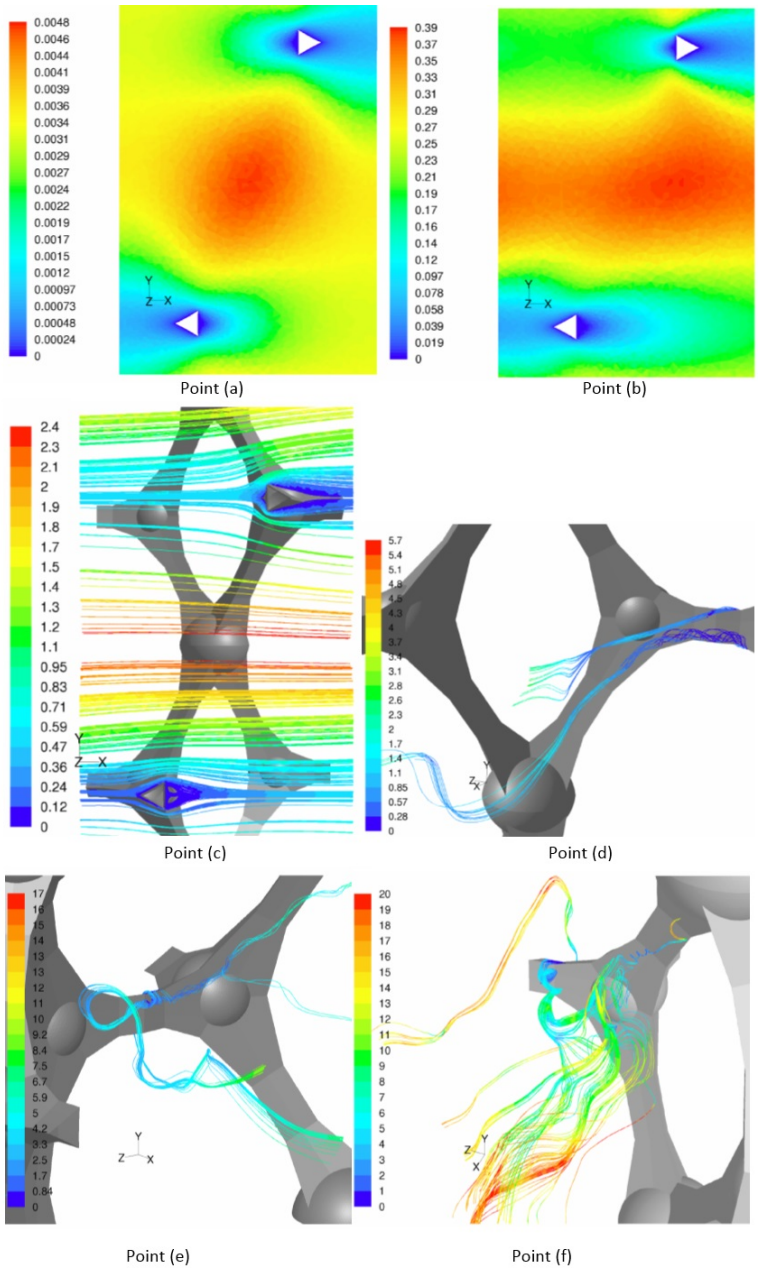

Figure 4.19: Illustration of the different flow regimes as indicated in Fig.4.17 and Fig.4.18 [105]

Determination of energy closure terms

A numerical study of the **thermal dispersion** term $\overline{\overline{k}}_d$ is performed by imposing a periodic temperature change in each direction, subjected to specified heat flux condition at the interstitial surface.

The commercial solver now assumes a constant temperature gradient, similar to the pressure gradient given in the previous paragraph on the determination of the momentum closure terms.

For the quarter-PUC these gradients are given by [102][13]

$$\begin{aligned}
\frac{T(x+\frac{l_{n,x}}{2},y,z)-T(x,y,z)}{\frac{l_{n,x}}{2}} &= \frac{T(x+l_{n,x},y,z)-T(x+\frac{l_{n,x}}{2},y,z)}{\frac{l_{n,x}}{2}} = \frac{\Delta T}{\frac{l_{n,x}}{2}} \\
\frac{T(x,y+l_{n,y},z)-T(x,y,z)}{l_{n,y}} &= \frac{T(x,y+2l_{n,y},z)-T(x,y+l_{n,y},z)}{l_{n,y}} = \frac{\Delta T}{l_{n,y}} \\
\frac{T(x,y,z+\frac{l_{n,z}}{2})-T(x,y,z)}{\frac{l_{n,z}}{2}} &= \frac{T(x,y,z+l_{n,z})-T(x,y,z+\frac{l_{n,z}}{2})}{\frac{l_{n,z}}{2}} = \frac{\Delta T}{\frac{l_{n,z}}{2}}
\end{aligned}$$

Note that the thermal dispersion term is modelled similar to momentum dispersion, through a gradient-type diffusion model. The applied gradients are constant in all three directions. When fluid flow is considered in a single direction, along the x or y coordinate, this temperature gradient is practically only significant in the applied direction. In the other directions, it can be assumed to be negligibly small. This allows specifying the constant gradient. For example, for an x directed flow, it reads:

$$\frac{\Delta T}{\frac{l_{n,x}}{2}} = \frac{\dot{q}A_{fs}}{\dot{m}c_p}\frac{1}{\frac{l_{n,x}}{2}} = \frac{T_{bulk,x=\frac{l_{n,x}}{2}} - T_{bulk,x=0}}{\frac{l_{n,x}}{2}}, \tag{4.33}$$

In the above equations the subscript $bulk$ is the mass weighted average at the indicated face.

For the determination of the thermal dispersion, it is common practice to consider the dispersion diffusivity $\overline{\overline{\alpha}}_d = \frac{\overline{\overline{k}}_d}{(\rho c_p)_f}$ $[m^2/s]$ instead of the thermal dispersion itself. It is typically assumed that this tensor is symmetrical [156]. Furthermore, its principal directions are assumed to be aligned with the small and large cell diameter.

Whitaker [109] has shown that for discrete hierarchical structures, the thermal diffusivity in the x direction can be determined from the local data by applying Eq. (4.34) [105]. The numerator of this equation, $\langle \widetilde{v}_x \widetilde{T} \rangle^i$, is determined by $\langle \widetilde{v}_x \widetilde{T} \rangle^i = \langle v_x T \rangle^i - \langle v_x \rangle^i \langle T \rangle^i$.

[13] Remark that the gradient boundary conditions in x and z-direction are related to half a length, this is the way the foam samples were cut and reordered to produce a quarter unit cell. See Ref. [105].

$$\alpha_{d,xx} = -\frac{\langle \widetilde{v}_x \widetilde{T} \rangle^i}{\frac{\Delta T}{\frac{l_{n,x}}{2}}} \tag{4.34}$$

The method to solve this problem is based on the discussion of the mesh in Section 4.3.2, where it was explained that a non-conformal mesh has to be used because of the periodic boundary conditions around the PUC. Concerning the macroscopic temperature gradient in the denominator of Eq. (4.34), in practice the bulk temperatures are obtained by considering a place which is located a distance of the dimension of one control volume from the periodic plains. This ensures that no interpolation errors, due to the non-conformal mesh, are present. Doing so, this results in a heat balance closure within 1.5%, between the imposed heat transfer rate at the interstitial surface and the retrieved thermal energy in the air flow.

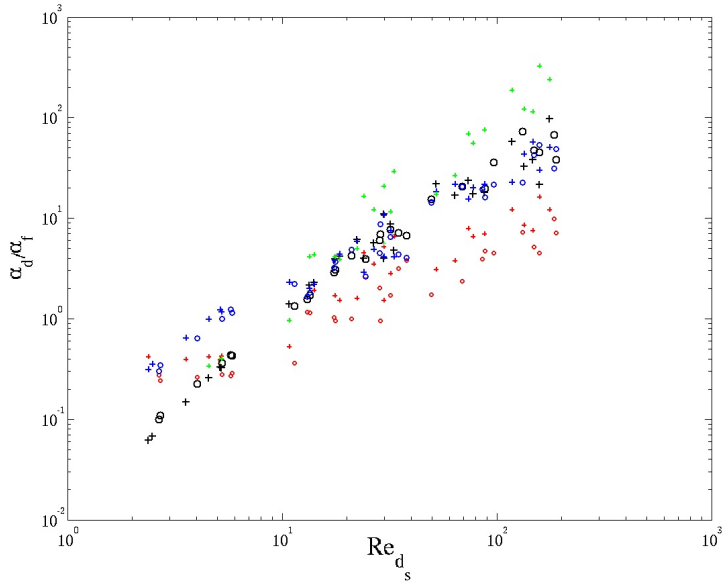

Figure 4.20: Validation of thermal dispersion diffusivity. The symbols + and ∘ represent respectively $k_{d,xx}$ and $k_{d,yy}$ results. The colours distinct between data from Calmidi et al. [120] (red), Kaviany [157] (blue), Steven et al. [158] (green) and the CFD results obtained in this work (black).

Validation of the obtained results is performed by comparing them with data given in open literature. Often cited is the work of Calmidi et al. [120], who proposed following correlation under the assumption of an isotropic foam:

$$\frac{\alpha_d}{\alpha_f} = 0.06\frac{1}{\alpha_f}|\langle\vec{v}\rangle^i|\sqrt{\kappa} \tag{4.35}$$

This correlation was obtained through an inverse technique by varying the coefficient in the correlation until the modelled and the experimental heat transfer yielded the same value for a given foam (the resulting value of the coefficient is thus 0.06). As can be seen in Figure 4.20 (red symbols), the agreement with the CFD results from the work of De Jaeger is poor. However, Calmidi et al. [120] reported a low sensitivity of their correlation towards the thermal dispersion and hence indicate that the obtained number of 0.06 (in Eq. (4.35)) gives an order of magnitude. It allows the authors to assess the importance of thermal dispersion with respect to the solid phase effective thermal conductivity, which is assumed to account for the major part of conductive heat transfer in foams. It was shown that at $Re_{d_s} \approx 30$, thermal dispersion merely amounts for 3% of the conductive heat transfer in foam. Based on this, the authors neglect thermal dispersion for $Re_{d_s} < 30$. For higher Reynolds numbers, thermal dispersion needs to be taken into consideration.

A general correlation for thermal dispersion, derived from a large amount of experimental data and for a variety of porous media, is given in the textbook of Kaviany [157]. Amongst others, it is based on the work of Koch et al. [159] which deals with metallic fibrous media. The resulting correlation is as follows:

$$\frac{\alpha_{d,xx}}{\alpha_f} = \frac{3}{4}Pe + \frac{1}{6}\pi^2(1-\phi)Pe\ln Pe, \tag{4.36}$$

In the above equation the Peclet number is given by $Pe_{d_p} = \frac{|\langle\vec{v}\rangle^s|d_p}{\alpha_f}$. The data depicted in Figure 4.20 (blue symbols) is based on this Peclet number (based on the pore diameter), but shown with respect to Re_{d_s} on the abscissa. Good agreement is found for $Re_{d_s} > 10$. For lower Reynolds numbers, a major deviation is observed. Recalling the flow regimes, as treated in Figure 4.19, this corresponds to the Reynolds number where recirculation zones in the wakes behind struts emerge. Note also that the results depicted in Figure 4.20 suggest that the thermal dispersion and molecular diffusion become equal at $Re_{d_s} \approx 10$. The same effects have been observed and reported by Steven et al. [158] in a numerical study on open-cell foams. Based on the data, the authors proposed the following correlation:

$$\frac{\alpha_{d,xx}}{\alpha_f} = \frac{1}{1.14} + \frac{1}{206}\left(\frac{|\langle\vec{v}\rangle^i|\frac{4\phi}{\sigma_0}}{\alpha_f}\right)^{1.81} \tag{4.37}$$

This correlation shows a good agreement with the CFD results given here, but only for $Re_{d_s} < 10$. The large deviation for higher Reynolds numbers, most likely can be attributed to the geometrical model used by these authors which consisted

of an isotropic Kelvin cell with equilateral triangular fibres representing the struts (and the nodes).

To calculate the **interstitial heat transfer coefficient**, the PUC can be used again. When imposing a constant heat flux, only two temperatures need to be computed for the determination of the interstitial heat transfer coefficient through Eq. (4.38). This only requires determining the bulk temperature of the solid and the fluid based on the microscopic data.

$$h_{fs} = \frac{\dot{Q}}{A_{fs}(\langle T_s \rangle^i - \langle T_f \rangle^i)} \tag{4.38}$$

For the solid phase temperature, further simplification is possible by considering the Biot number, given by Eq. (4.39).

$$Bi = \frac{h_{fs} d_s}{k_s} \tag{4.39}$$

The Biot number gives an indication of the temperature distribution inside the struts, when they are subjected to a heat transfer towards the fluid phase. Due to the latter, the strut boundaries can be at a significantly different temperature than the solid material at the centreline of the strut. For an aluminium AA4260 alloy, a conservative estimate of the heat transfer coefficient of 10 W/m^2K and a typical foam with ϕ = 0.93 and σ_0 = $500m^{-1}$ the resulting Biot number is smaller than 10^{-4}. Hence, it can be safely assumed that knowing the mean interstitial surface temperature is a sufficiently accurate representation of the intrinsically averaged solid phase temperature. For this reason, it is not required to solve the conjugate heat transfer problem. h_{fs} is thus given by Eq. (4.40).

$$h_{fs} = \frac{\dot{Q}}{A_{fs}(\langle T_{fs} \rangle^{fs} - \langle T_f \rangle^i)} \tag{4.40}$$

In this equation $\langle T_f \rangle^i$ is easily subtracted from the microscopic simulation. $\langle T_{fs} \rangle^{fs}$ denotes the mean interstitial surface temperature given by Eq. (4.41).

$$\langle T_{fs} \rangle^{fs} = \frac{1}{A_{fs}} \int_{A_{fs}} T_{fs} dA \tag{4.41}$$

Again, this closure term depends on the Reynolds number.

From the large number of Nusselt correlations published for open-cell foams (see e.g. [133, 160, 161] for a survey on the subject), a correlation which strongly resembles the correlation for a bank of staggered tubes [162] is found to be appropriate. Experimental validation for this study is provided by Calmidi et al. [120], Ghosh [112] and Tamayol et al. [163]. This correlation by Zukauskas [162] is given by equation (4.42).

$$Nu = 0.52 Re_{d_s}^{0.5} Pr^{0.37} \tag{4.42}$$

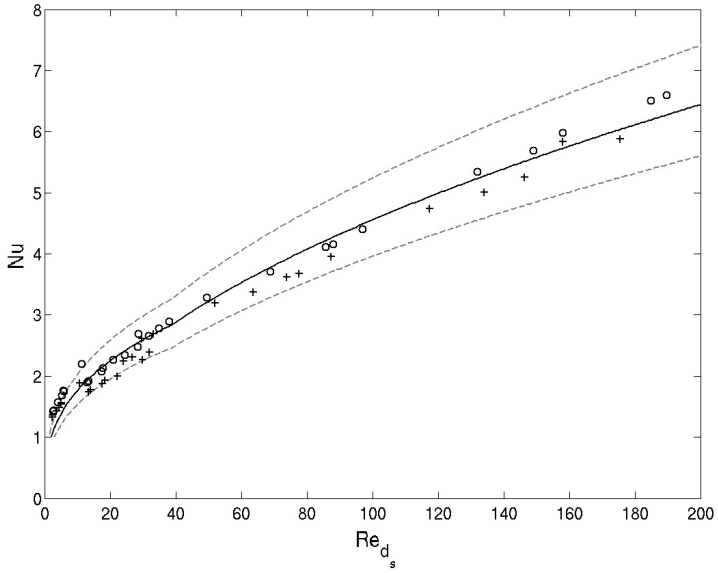

Figure 4.21: Validation of interstitial heat transfer coefficient. The symbols + and ∘ represent respectively Nu_x and Nu_y results. The solid line gives correlation (4.42) [120]. The dashed lines indicate ±15% uncertainty.

After accounting for the aforementioned geometrical differences, it can be deduced from Figure 4.21 that the obtained CFD results indeed show a good agreement with the Zukauskas correlation (4.42). The largest relative deviation is observed at the lower Reynolds numbers, i.e. for $Re_{d_s} < 30$.

A comparison of the interstitial heat transfer coefficient between the x- and y-directed flow shows only a limited difference between both.

4.4 Results & discussion for open-cell metal foam heat sinks

Numerical results using the volume averaging technique (VAT) for open-cell metal foam in natural convective heat transfer using CFD software is very limited. Yet many studies are presented using VAT for simulation applications in forced

convection (see Refs. [164, 165, 166] amongst others)[14].

First of all, it should be noted that none of the authors that are discussed include any effect of radiation. Either they neglect it or ignore.

In 2002, **Phanikumar and Mahajan [141]** were the authors to present a study of metal foam heat sinks in natural convection using VAT. They compared their numerical results with the experimental one from Bhattacharya et al. [58]. They also studied the difference between local thermal equilibrium (LTE) and local thermal non-equilibrium (LTNE). Their results indicate that the thermal non-equilibrium even for natural convective applications provides the best solution of heat transfer in metal foams. This is also stated in the work of De Jaeger, based on a evaluation of the Sparrow number. For thermal equilibrium to hold and in case of an aluminium foam is used together with air as working fluid, it is concluded that the Reynolds number (with d_s as characteristic length) has to be smaller than 0.1. Even in natural convection, this is not (always) the case.

The closure terms in the momentum equation are determined as:

- For the momentum dispersion, the authors used the same expression as proposed by Whitaker. The effective viscosity is also modelled as $\mu_e = \mu$.
- The values for permeability κ and inertial coefficient β are mentioned in their paper. However, it is not mentioned how these properties were determined.

The closure terms for both energy equations are determined as:

- The effective solid and fluid conductivities $k_{eff,\ solid}$ and $k_{eff,\ fluid}$ are estimated using the correlation from Calmidi and Mahajan [169].
- The interstitial heat transfer coefficient h_{fs} is estimated based on the correlation proposed by Zukauskas for air passing over a cylinder [162]. The Reynolds number is based on the strut diameter d_s. However, the authors noted that the Zhukauskas correlation is only valid for circular cylinders. For non-circular cross-sections they mentioned that Eq. (4.43) could be used. The exponent m was found to lie between 0.5 and 0.78 [141]. The authors fixed m at 0.5 and studied the effect of a varying cross sections by means of C_T. They studied different values of C_T until the point where the Nusselt number ceases to increase with further increasing C_T (this was at $C_T = 0.52$). Remark that this results in the same equation as proposed by De Jaeger (Eq. 4.42).

$$Nu = C_T Re_{d_s}^m Pr^{0.37} \tag{4.43}$$

[14]There are also other methods to study metal foam numerically (next to other upscaling techniques or DNS calculations through CFD, as described in Section 4.3.3). An upcoming simulation technique is the lattice Boltzmann. Some work on metallic foams can be found in literature [167, 168]

- For the thermal dispersion, the authors use the analysis from Koch and Brady [159]. However, they don't discuss how they have determined k_d for the specific foams studied.
- Finally, for the surface-to-volume ratio σ_0 they used the correlation from Calmidi and Mahajan [169].

The simulations were performed in 2D. The boundary conditions are shown in Figure 4.22. The authors observed differences with the experimental results up to 15%. The effect of the permeability is studied in Figure 4.23. Here the effect of the Darcy number on the amount of flow penetration is studied. Fig. 4.23(a) shows that for a Darcy number of 10^{-8} almost no flow can penetrate into the foam, while for $Da = 10^{-3}$ (Fig. 4.23(b)) there is certainly some air going inside the foam structure. The low Da heat transfer asymptote represents the physical limit of an almost impervious porous block. This study indicates that the results are quite sensitive to this parameter, while they are less sensitive to h_{fs} for example.

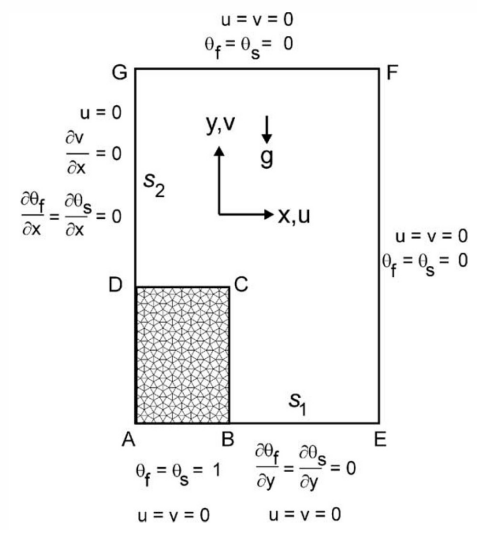

Figure 4.22: Illustration of the boundary conditions used in Phanikumar and Mahajan [141] (θ stands for a dimensionless temperature.)

In 2005, **Zhao et al. [170]** also published numerical work using the VAT for Porvair foam in natural convection. Porvair foam is made through electro-deposition, therefore the struts will be hollow. To model the variation of density, the Boussinesq approach is used.

This is how the authors determined the closure terms (calculations were done in two dimensions):

- According to the authors, it is very difficult to determine the permeability κ. Most correlations for this closure term were determined in forced convective applications, so the velocity range is too high. Furthermore, they also notice that the permeability can be seen as a velocity-dependent parameter. So in this paper, they study the effect of the permeability by changing the Darcy number Da (function of κ).
- The inertial coefficient β is set to zero.
- The momentum dispersion is modelled in a similar way as in Phanikumar and Mahajan [141]. However, they did not mention how μ_e is determined.
- The thermal dispersion k_d is modelled based on the work of Georgiadis and Catton [171].
- The surface-to-volume ratio σ_0 is based on arrays of parallel cylinders intersecting other arrays in the other orthogonal directions: $\sigma_0 = \frac{3\pi d_f}{d_p^2}$. Here the cross-relation between porosity ϕ, pore diameter d_p and strut diameter d_s is adopted from Paek et al. [172]
- The effective solid conductivity $k_{eff,\,solid}$ is calculated from the model by Boomsma and Poulikakos [173]. This model is made for casted metal foams (from ERG Materials and Aerospace e.g.). As the struts are hollow, this effective conductivity is recalculated as $k_{eff,\,solid}(1-r)^2$ with r the inner-to-outer radius ratio of the hollow struts.
- For the effective fluid conductivity $k_{eff,\,fluid}$ the authors did not mention how they determined this closure term.
- The interstitial heat transfer coefficient h_{fs}, was found through a correlation based on the work by Churchill and Chu [174] for natural convection in a bank of staggered cylinders. The Rayleigh number is based on the strut diameter d_s.

The authors were not able to compare their findings with experimental results.

In 2012, **Piller and Stalio [175]** also studied metal foam in natural convection. They studied an inclined parallel-plate channel partly filled with metal foam. Again the authors used the Boussinesq model. The permeability κ and inertial coefficient β are determined from the model of Calmidi [169]. Momentum dispersion is neglected. The effective thermal conductivity is calculated with the model of Singh and Kasana [176] while assuming local thermal equilibrium. Finally the thermal dispersion is modelled as in Alazmi and Vafai [177]. The authors showed that there was no effect of channel inclination, while the results do depend on the solid-to-fluid thermal conductivity and the thickness of the porous layer.

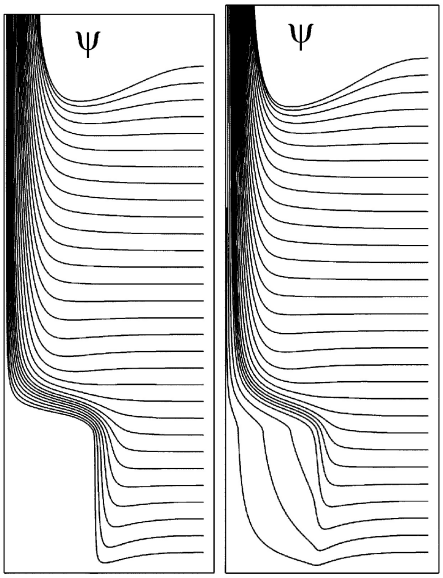

(a) $Da = 10^{-8}$ *(b)* $Da = 10^{-3}$

Figure 4.23: Illustration of the influence of the Darcy number on the flow peneration into the foam structure [141]

Finally, in 2013 **Su et al. [178]** proposed to use a geometry factor for metal foam in natural convection. This factor η (Eq. (4.44)) is defined as the ratio of the product of the microscopic length scale and the solid fluid interface area to the solid volume in a REV. The authors linked this geometry factor to the microscopic drag coefficients and permeability and used this geometry factor as a parameter in their simulations based on VAT. The focus of this study is an enclosure filled with metal foam which is heated from one end.

Although this geometry factor can be linked to different coefficients/closure terms, it is very hard to unambiguously determine this factor (see Section 6.2.1 for the discussion on determining the PPI-value).

$$\eta = \frac{dA_{fs}}{V_s} \approx \frac{6PPI^2[\pi d_p l + 3\sqrt{3}(d_p + d)^2/4 - \pi d_p^2/2]d}{(1-\phi)0.0254^3} \tag{4.44}$$

5 Experimental test rig & results

5.1 Introduction

In this chapter, an experimental test rig to test heat sinks without the use of a fan is discussed (Section 5.2). Due to practical and timing considerations, only one test setup was built. This test setup is specifically built for open-cell metal foam samples. Because open-cell metal foam has a considerable flow resistance, the tested samples are long and narrow. For this reason, it was not possible to test classical heat sinks in the same setup. A second test setup would be required to test these conventional heat sinks. However, this was not possible within the scope of this work due to the effort and time necessary to build a qualitative setup. Considering the fact that there is already a large amount of experimental data available on conventional heat sinks, the author opted to only test open-cell metal foam. Despite the fact that is was built for a specific type of heat sink, the test rig that is built for this work summarizes all needs for a proper test facility. Furthermore, the main focus of this work was to numerically study heat sinks, as is also evident from the publications of the author (Appendix E). This also contributed to the decision to only build one test setup. The heat sinks tested on this test facility are discussed in Section 5.3.

In Section 5.2.1 and 5.2.2 the used procedure and uncertainty analysis are discussed, respectively. The procedure describes how the data is gathered and which results are obtained. The uncertainty analysis is only briefly explained in this chapter. In Appendix A this is done more profoundly.

In Section 5.4 the results obtained with the test rig are discussed. The results from these tests were already published by De Schampheleire et al. [41]. The influence of the thermal contact resistance, foam height, substrate temperature etc. is studied for two types of metal foam.

5.2 Discussion of the test facility

Figure 5.1(a) depicts the test assembly, with a horizontal flat aluminium plate mounted as a heat sink (indicated by the dashed rectangle) above the main heater (not shown on the figure)[1]. For this work, the master thesis of Robin Reynders also needs to be acknowledged, see Ref. [179].

The plate measures 254 x 25.4 x 4 mm^3 and this same base plate is used for all samples. The top surfaces of both the plate and the surrounding insulation are at the same level. On this plate, different kinds of extended surfaces are placed. In Section 5.3, the studied heat sinks will be discussed. When an extended surface is placed over this plate, it acts as a *substrate* or *base plate*. This assembly is placed in an enclosed box, measuring 700 mm in length, 600 mm in width and 450 mm in height. This box is closed with Plexiglas® on two sides (at front and back end of the test section - the Plexiglas® panels are not mounted in Figure 5.1(a)) - and insulation on the other sides (shown in Fig. 5.1(a)). Eurofloor® (50 mm thick) insulation from Recticel with a thermal conductivity of 0.023 W/mK is used. The Plexiglas® plates are 35 mm thick and have a thermal conductivity of 0.2 W/mK. As it is a closed system, it is ensured that there is no momentum exchange with the environment. The solid line in Figure 5.1(a) indicates where the cross-section is taken. A frontal view of this cross section is given in Figure 5.1(b).

As illustrated in Figure 5.2(a), two copper plates (254x25.4x5 mm^3) and the main heater are mounted underneath the substrate. The copper plates are used to uniformise the heat flux from the heater to the substrate. Figure 5.3 shows an image - taken by an infrared camera - of the substrate which is painted with a high emissivity paint (ε =95%). This figure illustrates the uniformity of the heat flux: the temperature along the substrate varies less than 0.3°C. If no copper plates were used there would be a significant spreading resistance, which is very difficult to calculate accurately as discussed in Section 2.4.3.

[1] Also note that due to the construction of the test rig, only *horizontal* heat sinks can be tested with this test facility.

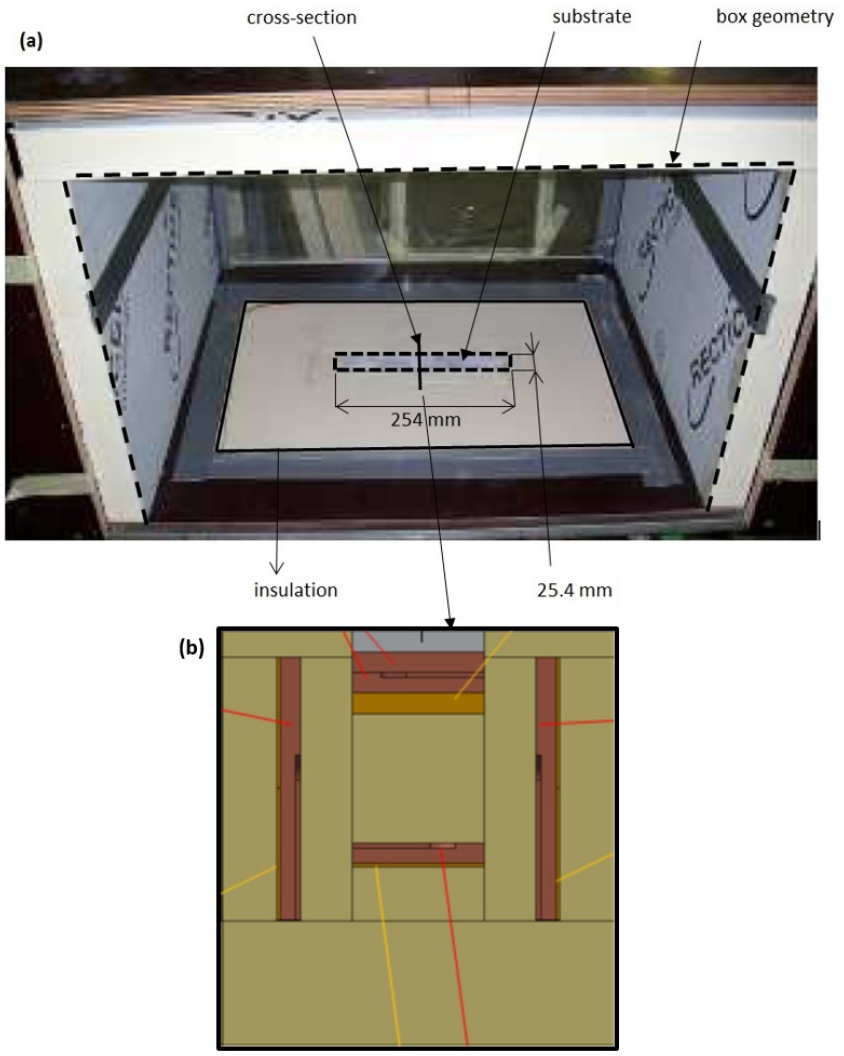

Figure 5.1: (a) Top view of the heater assembly in the box. The full line indicates where the cross section shown in (b) is taken. Outside the dashed line in subfigure (a) is insulation. The gravitational force vector is vertically downwards in the plane of the figure.

The copper plates were also machined by Bekaert Engineering (Kortrijk, Belgium).The flatness of the plates was achieved after grinding multiple times each side alternately. If they were cut with a guillotine, the tolerances would be much higher.

The bottommost copper plate (just above the main heater) is machined to house

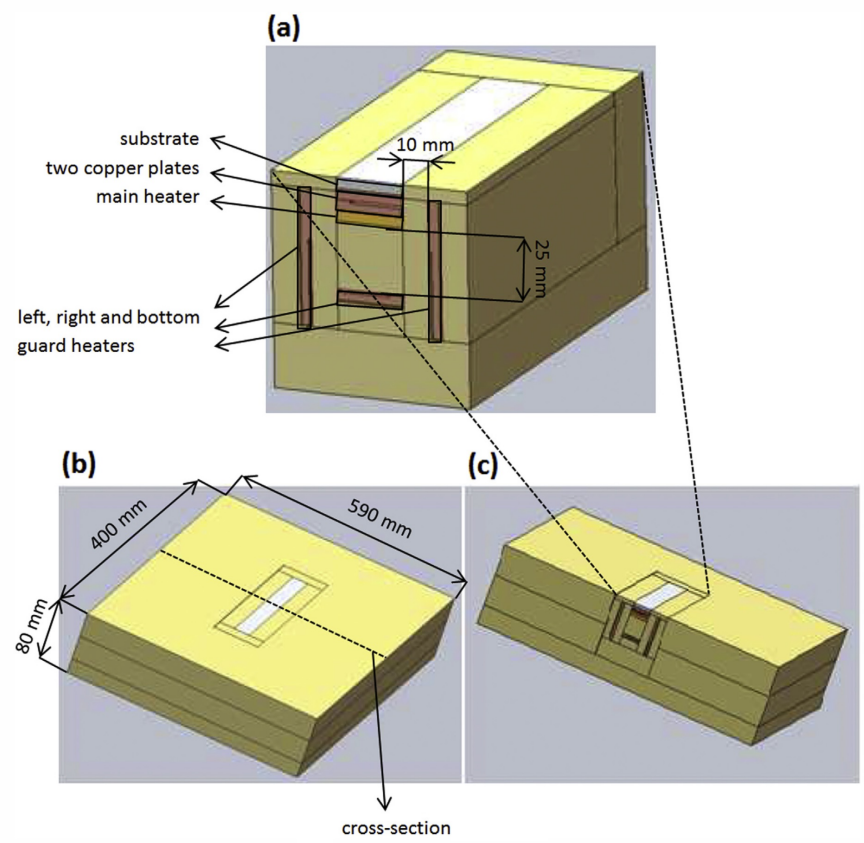

Figure 5.2: Insulation of the test assembly. (a) shows the specific construction of the guard and main heaters, whereas (b) and (c) illustrate the surrounding insulation.

six flat K-type thermocouples (see Fig. 5.4). These thermocouples are used to measure the **substrate temperature** (T_s). The slots in the plate are 1 mm in depth, 10 mm in width and have a variable length. Special care was taken in manufacturing the copper plates, to assure a good thermal contact. To further enhance this contact, a thermal paste is used. Silicon thermal conductive paste V5312 from Assmann WSW-Components® is used with a thermal conductivity of 0.8 W/mK. In the selection of the thermal paste not only the conductivity is of importance, but also the viscosity. This is also studied in one of the master theses guided by this author [180].

The **surrounding air temperature** in the closed box (T_{env}) is measured with twelve thermocouples which are placed near the walls of the box (two on each side of the box). For all measurements, the differences between these thermocouple

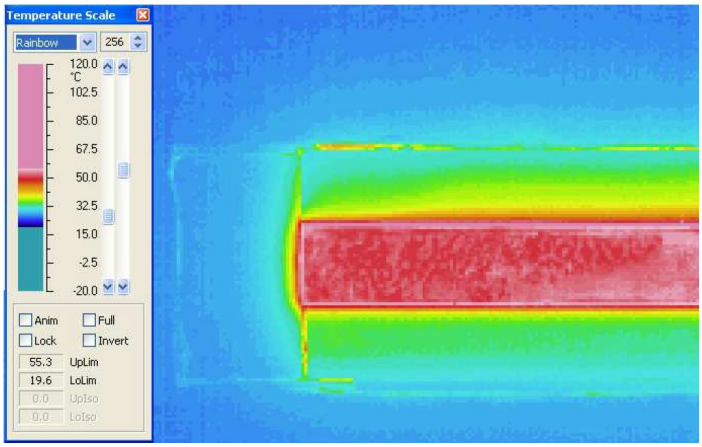

Figure 5.3: Illustration of heat flux uniformity (measured through a thermal image camera).

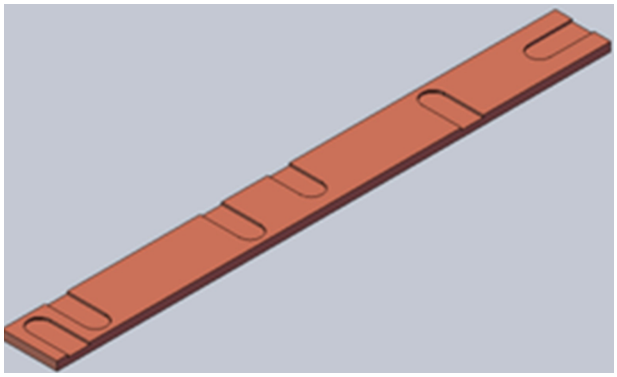

Figure 5.4: Upper copper plate, as shown in Figure 5.1(b) and 5.2(a), placed just above the main heater.

readings are less than 0.5°C.

The **main heater** (see Fig. 5.2(a)) is PID-controlled in LabVIEW® with the substrate temperature as a set point. This heater is a flexible heater with silicone rubber encapsulation from Watlow Manufacturing Company®. According to the specifications, this heater is able to deliver 100 W for a 240 V voltage supply. The resistance of the heater is 580 Ω with an uncertainty of ± 15%. To be able to generate a one-dimensional heat flux to the sample, following the recommendations of Zhao et al. [6], Kathare et al. [88] and Willockx [181], three **guard heaters** were installed at the left, right and bottom side of the main

heater. The purpose of the guard heaters is to keep the temperature difference with the main heater as small as possible, which consequently minimises heat losses of that main heater to the surroundings. In this way, the main heater sends a one-dimensional heat flux to the substrate (heat sink). An illustration of how effective the guard heaters work is given in Appendix A where an uncertainty analysis for Q_{conv} is given based on computational fluid dynamics (CFD).

The guard heaters are also accompanied by a copper plate and three thermocouples. The guard heaters are again PID-controlled. The bottom copper plate measures 254 x 25.4 x 5 mm^3 and both side copper plates measure 254 x 50.8 x 5 mm^3. Note that no guard heaters were installed in front and at the back of the main heater. The heat losses in these directions are calculated (as a $2D$ conduction problem) and found to be less than 0.2% of the total heat transfer rate.

Three **power supplies** are used: one for the main heater, one for the bottom guard heater and one for both side guard heaters. All three supplies are voltage controlled to ensure that the average temperature on each copper plate matches the set point. The power supply for the main heater is a Sorenson DCS 150-8E from AMETEK® and is able to deliver 150 V. Both sources of the three guards heaters are integrated in one unit (of the type PL303 QMB from AIM&Thurbly Thandar Instruments®) and can deliver a maximum of 30 V. To measure the power supplied to the main heater, both voltage and current are measured. For the current this is done by measuring the voltage difference over a 10 Ω precision resistor. This resistor can dissipate 150 W, in all tests the dissipation was limited to 0.63 W. In this way, the temperature dependency of the resistor can be neglected.

As shown in Figure 5.2, the complete assembly is mounted in high quality **insulation** material, surrounding the actual test rig. This is done with Promalight 1000R insulation by Microtherm® with a thermal conductivity of 0.022 W/mK. Between the bottom guard heater and the main heater the insulation is 25 mm thick. Between the main heater and the side guard heaters 10 mm of insulation is placed (see Fig. 5.2(a)). The two top plates in Figure 5.2(b) are 30 mm and the bottom plate is 20 mm. The outer dimensions in Figure 5.2(b) are 590 x 400 x 80 mm^3.

5.2.1 Procedure

The temperature of the substrate (T_s) is varied between 55°C and 95°C. The required heat flux (q) is generated by the main heater. All measurements are performed in steady-state. This is reached when all temperatures (including T_{env}) vary less than 1% during a period of 5 minutes. Reaching this stage takes several hours per set point. Every test sample is measured twice in a random sequence and turned 180° around its axis perpendicular to the main heater. This is done in order to observe potential sample or heater non-uniformities.

The data is gathered via a National Instrument® Data Acquisition System. For every sample, a dataset is obtained by sampling all relevant quantities during 300 seconds at a sampling rate of 1 Hz. A thermal transmittance (U) can be determined through:

$$U = \frac{Q}{A_s(T_s - T_{env})}, \tag{5.1}$$

In the above equation the surface of the substrate (A_s) is taken as the heat transferring surface ($254 \cdot 25.4\ mm^2$). This thermal transmittance U includes the influence of the thermal conductive resistances of the copper and aluminium plates, thermal paste and thermal contact resistance of foam. The 'lumped' Nusselt number, as reported by the reviewed literature sources [58, 89, 90, 141, 182], is given by:

$$Nu = \frac{UL}{k_f}, \tag{5.2}$$

In Eq. 5.2.1 the characteristic length L is defined as the ratio of the plate surface ($254.0 \cdot 25.4\ mm^2$) to its perimeter ($(254.0 \cdot 2)+(25.4 \cdot 2)\ mm$).

However, in this work (if not otherwise stated) a 'modified' Nusselt number (Nu^*) will be reported. This Nusselt number is the dimensionless form of the product of the convection coefficient and the fin efficiency [87]. Hence, the fin efficiency is not separated from the convection coefficient, following the recommendations of Moffat et al. [183]. This is especially interesting when working with open-cell metal foam. This modified Nusselt number is determined as:

$$Nu^* = \frac{\eta h^* L}{k_f}, \tag{5.3}$$

In the above equation ηh^* is defined by:

$$\eta h^* = \frac{R_{conv}}{A_s}, \tag{5.4}$$

With the convective resistance (Eq. (5.5)) defined as the total thermal resistance minus the conductive resistances between the heater and the foam (respectively two copper plates, aluminium substrate and thermal paste between the plates) and the thermal contact resistance between the foam and the substrate. The thickness of the thermal paste is measured at the beginning of each series of heat sinks tests.

$$R_{conv} = R_{tot}(\frac{Q}{\Delta T}) - R_{cond,Al} - 2R_{cond,Cu} - R_{thermal\ paste} - R_{contact} - R_{fouling} \tag{5.5}$$

The fouling resistance ($R_{fouling}$) is not of interest for this study. As no durability tests are performed, there is no visible fouling on the studied extended surfaces, hence $R_{fouling}$ is considered to be 0. Furthermore, before using any kind of contact technology (like brazing or epoxy bonding) the different surfaces are cleaned using a degreasing spray (*Loctite 7063*).

The thermal contact resistance ($R_{contact}$) in Eq.(5.5) depends on the applied bonding method. There are different possible contact technologies. The used contact technology is discussed for each heat sink separately in Section 5.3. For casted aluminium foam, De Jaeger et al. [54] studied this for four different contact technologies: pressed-fit, epoxy, brazing and co-casting. The authors defined the contact resistance on the plate surface to which the foams are connected. For epoxy the contact resistance is $1.25 \times 10^{-3} m^2 K/W$ and for brazing $0.7 \times 10^{-3} m^2 K/W$. The relative uncertainty on these values is 11.4%.

For the results (see Section 5.4), as suggested, the calculations for $R_{contact}$ by De Jaeger et al. [54] (based on experiments) are used.

The other conductive resistances in Eq. (5.5), like $R_{cond,Al}, R_{cond,Cu}$ and $R_{thermal\ paste}$, can simply be calculated analytically.

Finally, the convection coefficient (or Nusselt number) is typically related to the flow regime. In natural convection, the flow regime is expressed by a Rayleigh number, defined as:

$$Ra = \frac{g\beta(T_s - T_{env})L^3}{\alpha_f \nu_f}, \tag{5.6}$$

In the above equation $\beta = 1/T_{avg}$ represents the thermal expansion coefficient for an ideal gas ($T_{avg} = \frac{T_s+T_{env}}{2}$) and $\alpha_f = \frac{k}{\rho c_p}$ the thermal diffusivity, determined at $T_{air,\ avg}$. In this work, either the lumped or the modified Nusselt number will be plotted against the Rayleigh number. The dependence with the Prandtl number is neglected here as only air is studied as fluid medium.

5.2.2 Analysis

To assess the quality of the measurements, a thorough uncertainty analysis was performed. An extensive overview of the uncertainty calculations is given in Appendix A for the interested reader. This section discusses the general approach.

Standard error propagation rules as described by Taylor [184] and Moffat [140] were used to calculate the overall uncertainty (root-sum-square method). As in this work a lot of samples were taken for each measuring point, it is assumed that the distribution of these measurements is Gaussian (normal distribution). The error on the dimensions of the heat sink measurements varies between 0.5 and $1\ mm$. The uncertainty on the thermodynamic properties of air is determined based on recommendations in open literature [185]: a relative uncertainty of

2% for the thermal conductivity, dynamic viscosity and specific heat capacity. The uncertainty on the air density is calculated from the uncertainty on the air temperature and the atmospheric pressure (± 50 Pa). Note that all uncertainties in this work are expressed as 95% confidence intervals.

Prior to the measurements, all thermocouples were calibrated using a Druck DBC150 temperature calibrator furnace to eliminate systematic errors. The reference temperature is measured with a FLUKE1523 PT100 with an accuracy of 0.064°C. The resulting uncertainty on all thermocouples is $0.2K$ conservatively. Thus the uncertainty on the temperature differences will be around $\sqrt{0.2^2 + 0.2^2} = 0.28K$ as the measurements are assumed to be independent from each other.

5.2.3 Validation

The validation of the test rig is done by (i) comparing with the literature results for a horizontal flat aluminium plate and (ii) studying the sensitivity of the results to the box geometry.

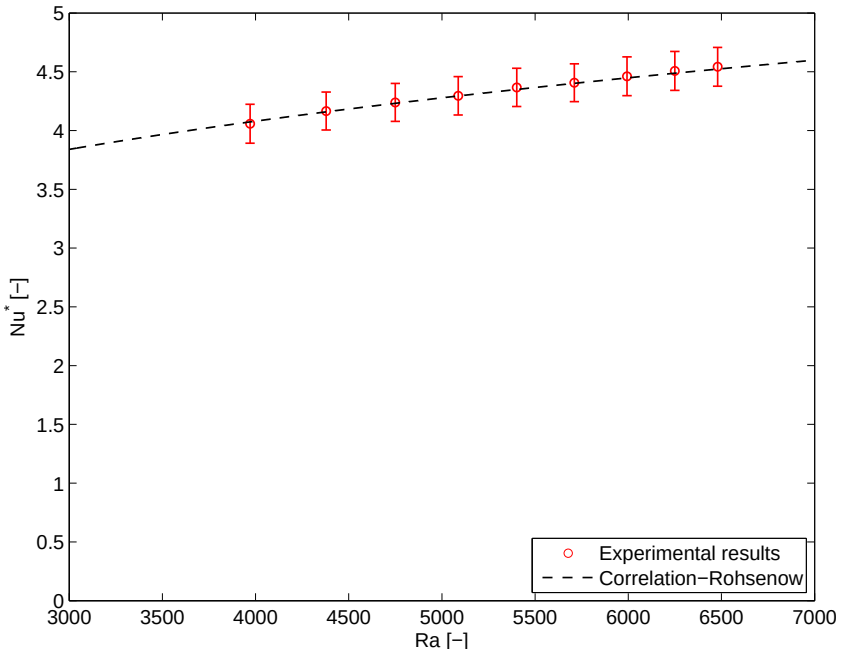

Figure 5.5: Comparison of experimental results for a bare plate with literature data of Rohsenow et al. [20].

The flat horizontal aluminium plate, as depicted in Figure 5.1(a), is used as a validation case for the test facility. The modified Nusselt number is determined

for substrate temperatures ranging between 55 and 95°C, resulting in a Rayleigh number varying from 3970 to 6480. The result is depicted in Figure 5.5 and shows a good agreement with the correlation for a flat horizontal plate given in the textbook of Rohsenow et al. [20].

Foam height $[mm]$	Box height/width $[mm]$	Ra [-]	T_s [°C]	Nu^* [-]	δNu^* [-]
18	450/500	4537	60	14.04	0.81
	75/500	4472		12.87	0.74
	450/125	4425		14.24	0.85
	ref	4472		14.23	0.77
	75/125	5467	75	12.78	0.82
	ref	5329		15.21	0.86
	150/250	6336	90	16.60	1.06
	450/500	6304		17.09	1.13
	75/500	6337		15.71	0.99
	ref	5963		16.02	0.96
12	75/250	4438	60	10.21	0.49
	ref	4243		11.26	0.52
	150/250	5387	75	11.71	0.64
	150/500	5359		11.89	0.72
	150/250	5375		11.70	0.59
	ref	5161		12.15	0.58
	450/125	6264	90	13.47	0.74
	ref	5954		12.80	0.61
6	450/500	4226	60	8.80	0.40
	75/500	4267		7.95	0.35
	150/125	4261		8.31	0.37
	ref	4162		8.82	0.37
	450/250	5343	75	9.51	0.45
	ref	5110		9.41	0.40
	450/500	6222	90	10.03	0.48
	75/125	6243		8.52	0.39
	ref	5972		9.87	0.40

Table 5.1: Influence of box geometry on the heat transfer rate. ***Ref*** *represents to reference case with dimensions 700 x 600 x 450* mm^3

The influence of the box geometry is studied for the brazed 20 PPI sample in Table 5.1, this is based on 18 additional experiments. The foam height (18 - 12 - 6 mm) is varied for different box heights (75 - 150 - 450 mm) and box widths (125 - 250 - 500 mm) around the heat sink. For these additional experiments, the box is open on the other two sides (at the left and right in Figure 5.1(a)). The

temperature of the substrate is fixed at 60°C, 75°C and 90°C. The results for the modified Nusselt number are compared to the closed box (*reference case*), with dimensions 700 x 600 x 450 mm^3. Table 5.1 shows that the influence of the foam height is more important than the influence of the box width in this case, where δNu^* indicates the uncertainty on the modified Nusselt number. It is clear that only a box height of 150 mm results in a significantly lower heat transfer rate. The limited height of the box will decrease the Bénard-like cells that will arise in natural convection. However, as soon as the box height reaches a certain level (higher than 150 mm), the influence of the box height on the heat transfer is found to be negligible.

5.3 Studied heat sinks

As already mentioned the heat sinks tested in the test facility (discussed in Section 5.2) are exclusively open-cell metal foam samples. In these tests the influence of contact technology, foam height and foam density is studied. The samples that are used in this work are illustrated in Figure 5.6. They have a dimension of 10 inch on 1 inch. The height is varied along the different samples.

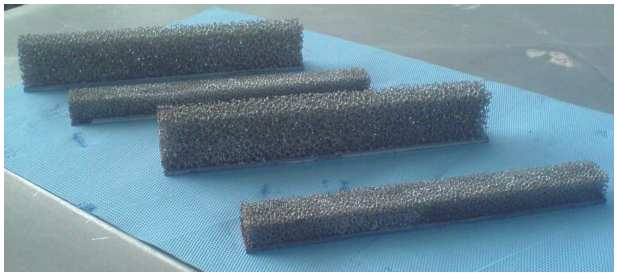

Figure 5.6: Illustration of the used metal foam heat sinks with different PPI values.

Foam PPI	ϕ –	d_1 $[mm]$	d_2 $[mm]$	A_0 $[\times 10^{-1} mm^2]$	σ_0 $[m^{-1}]$
10	0.933± 0.002	4.22± 0.18	6.23± 0.18	0.998± 0.08	462± 35
20	0.937± 0.002	2.77± 0.05	4.15± 0.05	0.377± 0.05	720± 58

Table 5.2: Properties of studied foam samples. All properties were determined through a μCT scan.

The foam samples used here are manufactured in-house and made of an AL1050 alloy, which consists of 99.5% pure aluminium. This material has a very high

thermal conductivity (220 W/mK) and is brazeable. The properties of the two studied open-cell aluminium foams are obtained with a μCT scan and are given in Table 5.2. Two types of metal foam are studied, each with a different **foam density**. The studied samples will be denominated based on their PPI value (10 PPI sample and 20 PPI sample). However, as already mentioned, this value does not characterize the flow unambiguously. One should always refer to Table 5.2 for the characteristics of the samples. The **height** of the (brazed) 10 PPI and 20 PPI samples is varied between 6-40 mm and 6-18 mm, respectively. The height of the foam samples is altered through a destructive method with an angle grinder. Two different **bonding technologies** were used for the 10 PPI foam: a single epoxy layer and a brazing process. For the 20 PPI sample, only brazing is studied as a bonding technique. The selected heights, applied bonding techniques and imposed substrate temperatures are summarised for each sample in Table 5.3.

foam PPI	bonding technique	H $[mm]$	T_s [°C]
10	brazed	40	55-60-65-70-75-80-85-90-95
10	brazed	25.4	60-67.5-75-82.5-90
10	brazed	18	60-65-67.5-70-75-80-82.5-90-95
10	brazed	12	60-65-70-75-80-85-90
10	brazed	6	60-65-70-75-80-85-90
10	epoxy	25.4	60-67.5-75-82.5-90
10	epoxy	18	60-65-67.5-70-75-80-85-89
10	epoxy	12	60-65-70-75-80-85-90
20	brazed	18	55-60-65-70-75-80-85-90-95
20	brazed	12	60-65-67.5-75-80-82.5-85-90
20	brazed	6	60-65-67.5-75-80-82.5-85-90

Table 5.3: The selected pore densities, used bonding techniques, foam heights and imposed substrate temperatures for the tested AL1050 foam samples.

For the *epoxy bonding*, epoxy is applied on the substrate and the foam is pressed onto it. Then this assembly is heated to 150°C and the epoxy is allowed to cure for 1 hour. Bondmaster ESP110 (single part epoxy) is used, because of its high viscosity (400 $Pa.s$ at 25°C) combined with a relatively high thermal conductivity (up to 0.66 W/mK). Bondmaster ESP110 is also used because De Jaeger et al. [54] used the same epoxy for determining the thermal contact resistance. Therefore, it is possible to calculate R_{conv} by subtracting this contact resistance from the total thermal resistance (Eq. (5.5)).

The bonding method *brazing* is more favourable compared to epoxy, despite its higher complexity. The aluminium brazing is performed on an AL1050 substrate,

combined with a lower melting point AA4xxx Al-Si alloy filler material as the brazing material. The assembly is heated to the eutectic temperature of the filler material (577°C). Because the substrate and the foam consist of an aluminium alloy which melts at a higher temperature (and because the gradient on the temperature is found small), the assembly does not distort. Together with a proper fluxing (to remove surface metal oxides and protect against re-oxidation before the contact is made), a joint is achieved in a controlled atmosphere brazing furnace. During brazing, a metallic plate (separated from the foam through a graphite foil) is placed on top of the foam to apply a constant pressure and to ensure a good contact between the foam and the substrate. A detailed discussion on how the samples were brazed can be found in Ref. [179]. The impact of different brazing technologies is extensively studied in Sekulic et al. [186]. To obtain a good brazed contact, the brazing is done in cooperation with the company Solvay using their NOCOLOK® flux.

5.4 Results & discussion

An overview of the performed measurements is given in Figure 5.7, where the lumped Nusselt number is reported, as this number has the highest industrial relevance.

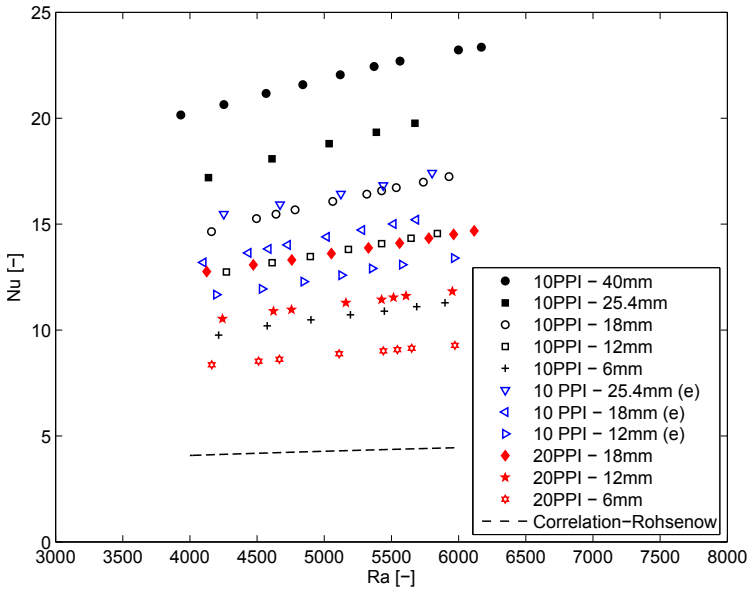

Figure 5.7: An overview of the thermal performance of the studied foamed heat sink (Table 5.2), compared with a bare aluminium plate. (e) in the legend stands for epoxy.

foam height	$\Delta T[^\circ C]$	$\delta\Delta T[^\circ C]$	$T_s[^\circ C]$	$\delta T_s[^\circ C]$	$Q[W]$	$\delta Q[W]$
40 mm	33.2	0.67	54.9	21.8	10.10	0.17
	37.4	0.73	59.9	22.5	11.76	0.20
	41.8	0.8	64.9	23.1	13.58	0.22
	46.2	0.88	69.9	23.7	15.40	0.25
	50.6	0.95	74.9	24.1	17.42	0.28
	55.4	1.03	79.9	24.5	19.47	0.31
	59.7	1.09	84.9	25.2	21.39	0.34
	66.1	1.20	89.9	23.8	24.33	0.39
	70.6	1.25	94.9	24.3	26.34	0.42
25.4 mm	36.6	0.57	60.0	23.3	9.6	0.16
	43.3	0.65	67.5	24.1	12.07	0.20
	50.2	0.73	75.0	24.8	14.7	0.24
	56.9	0.83	82.4	25.5	17.33	0.28
	63.6	0.93	89.9	26.3	20.00	0.32
18 mm	36.8	0.69	60.0	23.2	8.21	0.14
	41.3	0.77	65.0	23.6	9.68	0.17
	43.5	0.82	67.4	23.9	10.38	0.18
	45.8	0.86	69.9	24.2	11.09	0.19
	50.4	0.96	74.9	24.6	12.60	0.21
	55.0	1.06	79.9	25.0	14.15	0.23
	57.2	1.11	82.4	25.2	14.92	0.24
	59.5	1.16	84.9	25.4	15.71	0.26
	64.1	1.26	89.9	25.8	17.31	0.28
	68.7	1.36	94.9	26.2	18.97	0.31
12 mm	37.5	0.63	59.9	22.41	7.28	0.13
	42.1	0.70	64.9	22.8	8.52	0.15
	46.6	0.77	69.9	23.4	9.69	0.25
	51.2	0.86	74.9	23.7	11.00	0.19
	55.8	0.94	79.9	24.1	12.30	0.21
	60.3	1.02	84.9	24.6	13.63	0.23
	64.9	1.10	89.90	25.0	15.00	0.21

Table 5.4: Experimental results for different foam heights ('10 PPI' foam with brazed contact technology)

It is shown that a foamed heat sink has a significant improvement when compared to a bare aluminium plate. In this case, the improvement depends on the used bonding method, pore density and foam height. A 10 PPI brazed heat sink with a similar space constraint as a 20 PPI sample (18 mm height) performs on average 3.69 times better against a bare plate. A 20 PPI sample performs only 3.18 times better. When a brazed 10 PPI sample is compared with an epoxy bonded

10 PPI sample with the same space constraint (12 mm height), the brazed sample performs 3.16 times better than a bare plate, whereas the epoxy bonded sample performed only 2.89 times better.

Compared with the measured bare aluminium plate, the heat transfer rate of the studied sample with the lowest PPI number and largest height (10-PPI sample with 40 mm height) is 4.95 times higher. This is comparable with the results found by Bhattacharya et al. [58].

A more detailed study of the influence of bonding method, pore density and sample height on the heat transfer rate is treated in the next sections.

5.4.1 Influence of the bonding method

First the influence of the bonding method is discussed. The impact of the bonding method is only studied for the 10 PPI foam. As reported by De Jaeger et al. [54], the results can also be used for a 20 PPI foam. For the sake of simplicity, only the results for a foam height of 25.4 mm and 12 mm are shown in Figure 5.8.

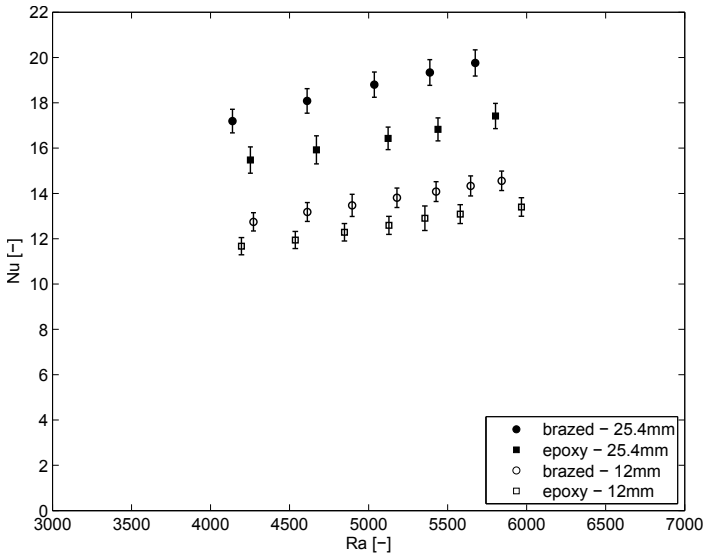

Figure 5.8: Influence of bonding method for 10 PPI foam of 25.4 mm and 12 mm height.

It can be observed that brazing has a significant influence on the measured heat transfer. For a foam height of 25.4 mm, the increase of the lumped Nusselt number varies between 11.1 and 14.9%. While for a foam height of 12 mm there is a less pronounced augmentation, varying between 9.2 and 10.4% (comparing the averaged values). The relative increase is defined as the ratio between the brazed

sample on the epoxy sample. For 18 mm (not shown on Figure 5.8) the increase in lumped Nusselt number varies between 11 and 11.9%. This result can be attributed to a more qualitative thermal bonding between a brazed and an epoxy sample. Although the epoxy is enriched with alumina particles, its thermal conductivity (0.8 W/mK) remains much smaller than that of AL1050 (220 W/mK). This is also indicated by De Jaeger et al. [54] where the authors found a difference of a factor 1.64 in thermal contact resistance between a brazed and an epoxy sample. As the convective thermal resistance decreases with increasing foam height, the relative importance of the thermal contact resistance increases in the total thermal resistance. The contribution of the contact resistance to the total thermal resistance is relatively small. For epoxy bonded samples it ranges between 3.4% and 5.4% and for a brazed contact, between 1.6% and 4.05%. This is a result of the inferior heat transferring properties in natural convection applications when comparing natural & forced convective applications (resulting in high resistances against heat transfer).

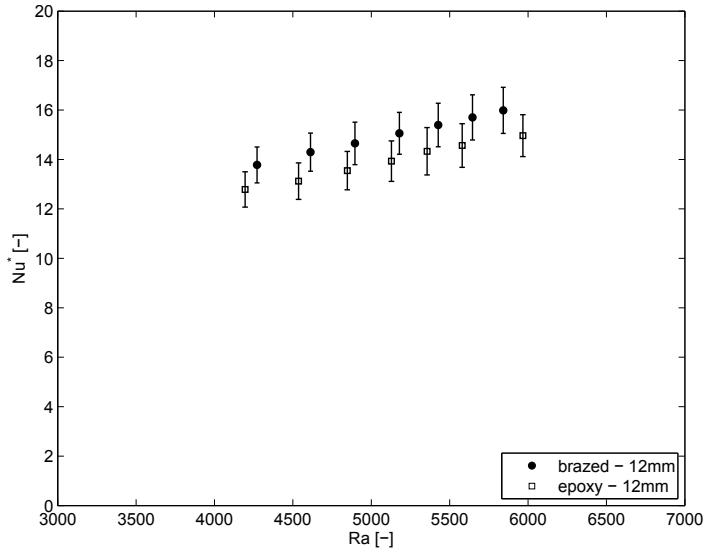

Figure 5.9: The modified Nusselt number is plotted against the Rayleigh number for 10 PPI foam of 12 mm height for two bonding methods.

The impact of thermal contact resistance is completely different in case of forced convection foam applications, like in the foam covered tubes studied by T'Joen et al. [13]. The authors conservatively estimated the contact resistance by modelling a layer of epoxy around a cylinder, yielding a relative contribution of the contact resistance to the total resistance between 6 and 55%. Even higher

contributions (up to 70%) are reported in De Schampheleire et al. [41] for a pressed-fit metal foam fin-and-tube heat exchanger for air-side velocities up to 3 m/s.

For the following results, the modified Nusselt numbers are reported. Figure 5.9 plots Nu^* against Ra for a brazed and epoxy bonded 10 PPI foam with a height of 12 mm. It should be noted that the data for the epoxy and brazed samples show statistically the same result, indicating the good quality of the data reduction. However, the modified Nusselt number for the brazed sample is systematically higher compared to the epoxy sample. This is related to the fact that the epoxy layer covers the complete substrate. This results in an additional thermal resistance near the substrate and between the struts (which is not the case for the brazed samples where there is a metal-metal contact).

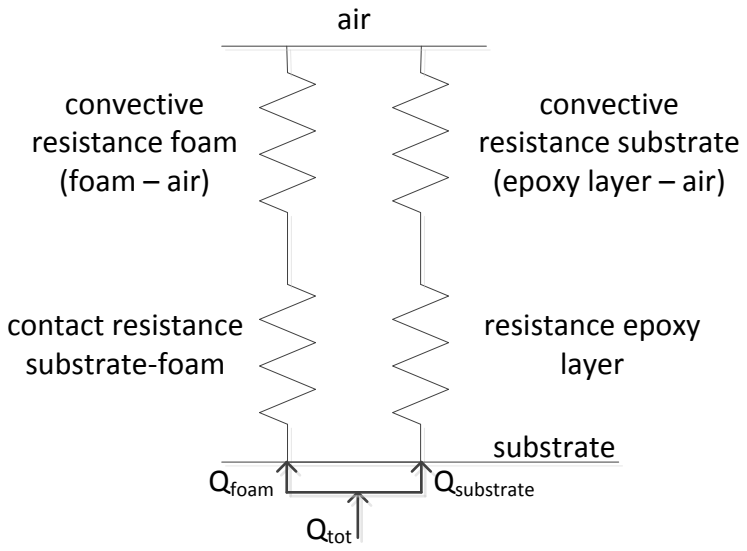

Figure 5.10: Illustration of the two way dissipating in case of an epoxy bonding.

This is illustrated in Figure 5.10. As the foam only has point contacts on the substrate, there are two ways to dissipate the heat: (i) from the substrate to foam and through convection to the air, and (ii) from the substrate through an epoxy layer and convectively to the air. These two ways have been taken into account in the experimentally determined thermal contact resistance in open literature. However, this resistance was determined in forced convection [54]. As the right branch in Figure 5.10 is dependent on the convection coefficient, this thermal resistance will be slightly underestimated. This is shown in Figure 5.9, where the epoxy sample

always remains under the Nusselt number for the brazed sample.

5.4.2 Influence of pore density

As depicted in Figure 5.11, a 10 PPI foam of the same height will yield higher Nusselt numbers compared to a 20 PPI sample. For the largest comparable foam height (18 mm) the increase in Nusselt number varies between 12.7 and 18.9%, while for a foam height of 12 mm, it ranges between 22.3 and 25.1%. The improvement of the heat transfer for smaller pore densities can be understood by recognising that the cells of the 10 PPI are larger than those of 20 PPI foam, as shown in Table 5.2. This makes the foam more permeable. Consequently, buoyancy driven air flows easier through the structure, enabling an interfacial heat transfer between the solid and fluid phase. The effective thermal conductivity, which is of importance in transporting the heat to the solid phase (enabling convective heat transport), is mainly influenced by the porosity of the foam. As the porosities of both foams are (nearly) equal and as the heat transferring surface area is even higher for the denser foam, the differences in heat transfer are largely attributable to the flow resistance in the foam. The conclusions are the same as obtained by Bhattacharya et al. [58]. However, the differences between 10 and 20 PPI are observed to be much smaller (< 10%).

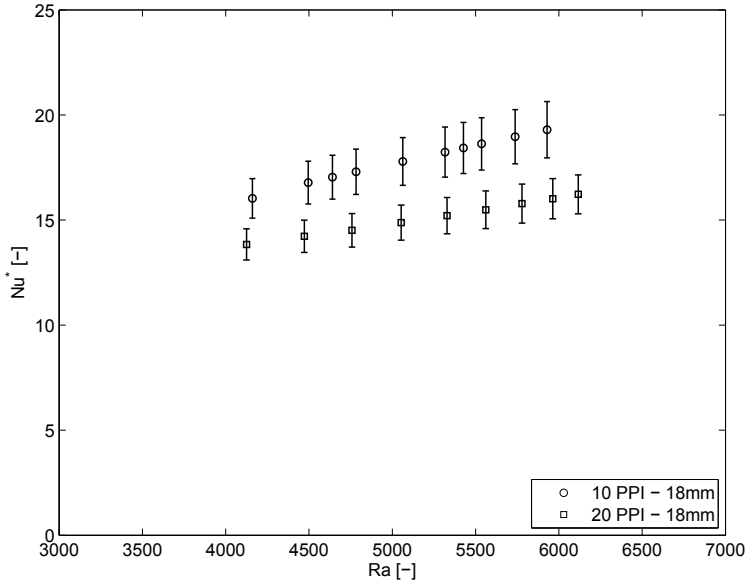

Figure 5.11: Illustration of the influence of pore density (10 PPI versus 20 PPI) for a 18 mm high brazed foam.

Furthermore, in a forced convective application, Ghosh [87] calculated that the fin efficiency for a 85%-porous foam and an air side velocity of 3.5 m/s decreases from 72 to 50% when moving form a 10 PPI to a 20 PPI foam. The combination of a lower fin efficiency and an increased flow resistance results in a smaller heat transfer rate for 20 PPI foam, even though the heat transferring surface is larger.

Note that based on these results and on a comparison of the average values, it is also clear that the influence of the pore density is slightly higher than the influence of the bonding method.

5.4.3 Influence of foam height

Figures 5.12(a) and (b) show the impact of varying the foam height for both 10 and 20 PPI foam. For the 10 PPI, the brazed sample is used, as for this sample the largest height variation is studied (see Table 5.2). Increasing the foam height results in an increase of the heat transfer rate. Increasing the foam height for a 10 PPI sample from 6 mm to 18 mm results in a rise of the heat transfer by a factor 1.55 (on average), whereas for the 20 PPI sample an augmentation by a factor 1.62 (on average) is obtained when increasing the foam height from 6 to 18 mm. This shows that, within the uncertainty, a 10 and 20 PPI sample have a similar improvement in heat transfer due to an increased height.

It should be noted that this increment is reduced for larger foam heights. This can be attributed to an increased flow resistance for the buoyancy-driven air flow in upward direction and a decreasing fin efficiency (as the fin efficiency decreases with foam height [87]).

For the 10 PPI sample the averaged increase in thermal performance from 6 to 12 mm is 31.8% (5.3% per mm), from 12 to 18 mm 17.9% (2.99% per mm), from 18 to 25.4 mm 19% (2.6% per mm) and from 25.4 to 40 mm 21% (1.4% per mm). However, no conclusions can be drawn as the absolute uncertainty on these ratio ranges between 9.5 and 12.9%. For the 20 PPI sample, the augmentation between 6 and 12 mm is 29% and between 12 and 18 mm 25.3%. The absolute uncertainty on these values ranges between 7.9 and 9.3%. Similar conclusions were observed in Qu et al. [89]. However the measurements in this study show a more significant influence of the foam height.

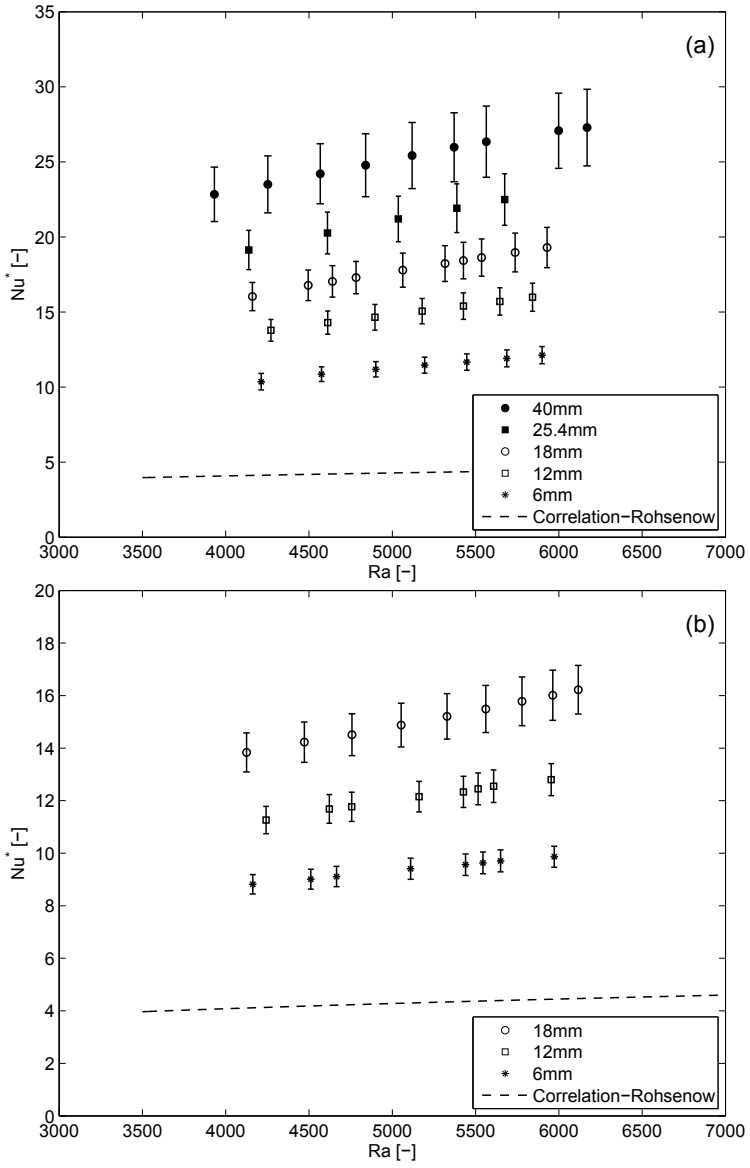

Figure 5.12: Influence of foam height of different pore densities (a) 10-PPI foam (b) 20-PPI foam. The dashed line indicates the Nusselt correlation for a bare plate from the textbook of Rohsenow et al. [20].

5.4.4 Correlation

Finally, based on the obtained data for the reference box geometry, a heat transfer correlation is derived for each foam. This is done through basic regression, in which the lumped Nusselt number is the depending variable and foam height and Rayleigh number are the two independent variables. The foam height is made dimensionless by taking its ratio to the foam's averaged cell diameter ($\frac{2d_1+d_2}{3}$ as can be found in Table 5.7), i.e. $\varsigma = H/d_c$. All parameters to determine this parameter can be found in Table 5.2 and Table 5.3. Thus, an expression of the following form is aimed at:

$$Nu = a\varsigma^{b_1} Ra^{b_2}, \tag{5.7}$$

In this equation a, b_1 and b_2 are the regression coefficients. The regression coefficients are given in Table 5.5 and are calculated according to Fernandez-Seara et al. [187], i.e., based on the *log*-values. The maximum relative deviation for the 10 PPI correlation is 2.65% and is 3.23% for the 20 PPI correlation. Please remark that this correlation is valid for foam in between the dimensions studied in this work (see Table 5.2), furthermore, this correlation valid in the range of Rayleigh numbers (Eq. 5.2.1) studied in this work: from 4000 to 6500.

Pore density	a	b_1	b_2
10-PPI	0.2125	0.4283	0.4546
20-PPI	0.2963	0.422	0.3729

Table 5.5: Regression coefficients for the Nusselt correlation for both pore densities, according to Eq. (5.7).

5.5 Conclusion

In this chapter a general approach for experimental testing of classical heat sinks and heat sinks made out of open-cell metal foam was discussed. This approach was only applied for open-cell metal foam heat sinks. This was due to lack of time. However, this approach can also be used to experimentally test other heat sinks in general.

Because this approach is generally valid, some general points of interest can be summarized for experimental tests on all types of heat sinks. Even with a well designed test facility special attention should be reserved for the following parameters, due to their large impact (as also explained earlier in this chapter):

- Location of temperature measurements: depending on the bonding method, the used materials and the dimensions of those materials, the impact of the

location on the measured temperature can be significant. This is mainly the case for the base temperature and the environmental temperature. This large variation of the measured temperature is due to the non-uniformities in the test setup. The effect depends on the setup and the measurement location, but can be estimated conservatively at a difference of up to 5°C.

- Guard heaters and the location of the guard heaters: to limit the losses and non-uniformities in the test setup, the use of guard heaters is imperative. Also the location of the guard heaters in the setup has a large effect on their usefulness. There are no general rules on how these heaters should be placed, this has to be investigated for each set up individually.This can be done through numerical simulations.

- The box geometry: generally the effect of the box geometry on the test results is limited. However, for small box geometries this effect can become significant. Hence, it is important to pay attention to this parameter. In this work, the effect of the box geometry was up to 7.5 %.

- Effect of the emissivity of the material: this was not studied in this chapter. Due to the difficulties of studying radiation experimentally in an accurate way. However, this was studied numerically, as will be discussed later on in this work (see Chapter 7). As will be shown in the numerical study, the effect of radiation can be up to 30 % depending on the fin geometry.

The test rig built for this work was designed specifically for testing open-cell metal foam heat sinks. The influence of several parameters on the performance of the heat sinks was investigated. Some of these parameters are general for all types of heat sinks as discussed above. The following parameters are specific for open-cell metal foam heat sinks and form additional points of interest for testing these heat sinks:

- The most important parameter found in this study, is the **foam height**. The difference between a 6 and 12 mm 10 PPI foam is already 32%. However, this increase in heat transfer rate decreases for larger foam heights. Furthermore, the foam height is a parameter that is highly restricted due to the space constraints around the heat sink.

- The **pore density** has a lower impact on the heat transfer. 10 PPI foam performs up to 25% better in heat transfer compared with the same-dimensioned 20 PPI foam.

- The **bonding method** has - of all studied parameters - the lowest impact on the heat transfer: up to 15%. The larger the foam height, the lower the overall thermal resistance and the higher the relative impact of the bonding

method. The brazed foam has a higher Nusselt number because of the better thermal contact between struts and substrate.

6

Numerical study on classical heat sinks

6.1 Introduction

The numerical results on classical heat sinks is discussed in this chapter. Numerical work for metal foam heat sinks is discussed in Chapter 7.

Firstly, the influence of the numerical fluid domain above the finned surface itself is discussed in Section 6.2. As depicted in Table 4.1 (Chapter 4), authors in open literature use different heights for the fluid domains above the heat sink in numerical studies. In Section 6.2, the effect of the height of the fluid domain on the results for heat transfer coefficient will be discussed. The author also tries to give a dimensionless expression to the required minimum fluid height for simulations.

Secondly, the procedure to simulate conventional heat sinks is discussed in Section 6.3. Here, an uncertainty analysis on the grid discretization is given, together with the fluid properties and models which are used to simulate the different heat sinks.

Next to the geometry of the fluid domain and the uncertainty analysis, there are additional parameters which affect the numerical results. These parameters such as the temperature and the effect of radiation are influenced by the specific heat sink that is studied. For this reason, different commercially available heat sinks are studied. The studied heat sinks are summarized in Section 6.4. As explained in Chapter 5 no experimental measurements were performed for these heat sinks in this work. These heat sinks are experimentally characterized by the manufacturer. However, as explained in Section 3.1.1 the manufacturers give little information

on the experimental setups used.

Finally, in Section 6.8 some extra simulations are performed to bridge the gap with open-cell metal foam heat sinks. One will make some simulations to study the effect of in-line and staggered fin shapes and the effect of some other variations that resemble open-cell metal foam.

In this chapter, the pressure-velocity coupling is used with the SIMPLE algorithm. Also the COUPLED algorithm could be used, however, the simulation time will increase. Momentum and energy equations are discretizated second order upwind. Air is modelled as an incompressible ideal gas, and the operation density necessary to use this model is determined at environment temperature. The residuals are automatically calculated each iteration step and have to be lower than 10^{-6} before the results can be accepted (all residuals have to be lower than 10^{-6}). Most of the time the residuals are **much** lower than 10^{-6}. As all simulations are done laminar, the presented results are thus valid for Rayleigh numbers smaller than 10^{8}.

Different to the previous chapter (chapter 5), where a fixed temperature is attempted at, the results in this chapter were calculated based on a fixed heat flux at the substrate of the heat sink. This is frequently used as a boundary condition in open literature, although there are some back draws: when the temperature, instead of the heat flux, is fixed at the substrate of the heat sink, the heat flux at the sides will be different compared to the heat flux in the middle of the heat sink. The heat flux is then non-uniform and most of the time in practical circumstances, this is also the case. As a rule of thumb, the temperature at the substrate of the heat sink is more constant than the heat flux. However, the author has chosen to follow the boundary condition that most other authors in open literature are using.

As also explained in Section 3.2.1, it is very difficult to compare numerical data with experimental one. Therefore it is also very difficult to compare or verify our numerical experiments with correlations from literature. For a flat plate, the obtained convective results for the heat transfer coefficient were: 5.36 W/m^2K, while the combined convective and radiative results were 5.9 W/m^2K. These results are quite comparative with the correlations reported in Section 3.2.1.

6.2 Influence of fluid height

Even in most recent results in open literature (see Section 4.1.1, Chapter 4), there are quite some ambiguities and variability on how heat sinks or fin rows are studied numerically with CFD. In this work, the case of Dogan et al. [46] will be taken as a starting point as this is is a fairly recent work (2014). It is an interesting paper to focus on (i) **influence of the fluid domain** as the authors didn't add any fluid domain in their simulations and (ii) the **influence of the uncertainty due to grid resolution**.

In this publication by Dogan et al. several fin shapes are compared. The studied heat sinks are similar to the heat sinks discussed in Tari et al. [94]. Similar fin shapes will be considered in this work. In open literature, it is stated that the fluid domain itself has to be far enough from the heat sink itself, similar to the Saint-Venant principle in mechanics [188]. However, the question here is: what is far enough?

Comparing different sources in open literature, there is little consensus on this topic. As shown in Table 4.1 (Chapter 4), the extra fluid domain which is added to the side of the heat sink varies between 0 and 6 times the length of the fin, while the amount of extra fluid domain that is added on top of the heat sink varies between 0 and 116 times the fin height. In this section, the influence of the fluid domain on the thermal results will be discussed and the dependency of these parameters (side & height) on the studied fin shape. Three different fin shapes, displayed in Section 6.2.1, will be studied. Only the horizontal orientation of the substrate of the heat sink will be considered.

6.2.1 Used geometry

The used reference geometry is based on the case simulated by Dogan et al. [46], except that in this work only half of the heat sink is simulated. The simulated fin structures are shown in Figure 6.1.

In Figure 6.1, only half of the fin rows are shown, as their symmetry boundary conditions are already depicted in this figure. The symmetry planes are indicated by a dashed rectangle in Figure 6.1. The other boundary conditions will be explained in the next section (Section 6.2.2). In this work, the considered fin structures are:

- A **rectangular fin shape** (see Fig. 6.1(a)) with a length (L) of 127 mm, a fin spacing (S) of 6.4 mm and a height (H) of 38 mm.

- An **interrupted fin shape** (see Fig. 6.1(b)), all characteristics are the same as for the rectangular fin shape, except that in the middle of the fin, a 7 mm long part is cut away. It seems valuable to study this interrupted fin design since the simulations by Dogan et al. [11] show that the temperature in the middle of this fin was approximately the same as the substrate temperature.

- An **inverted triangular fin shape** (see Fig. 6.1(c)) with a length (L) of 127 mm, a fin spacing (S) of 6.4 mm and a height (H) of 76 mm.

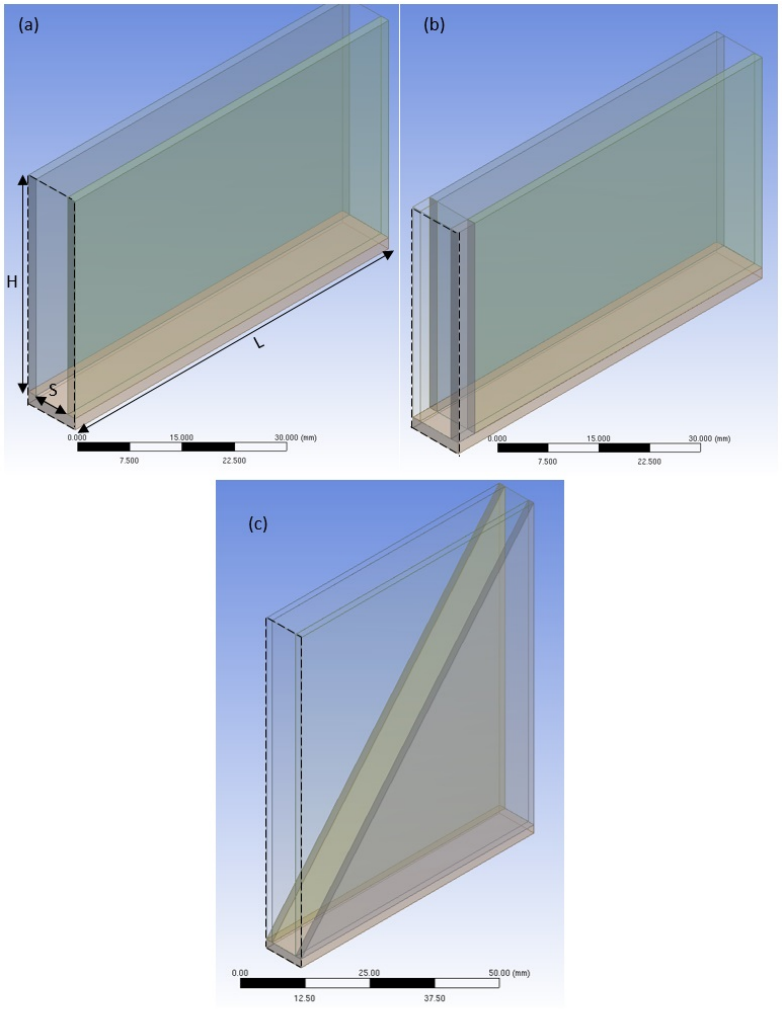

Figure 6.1: Illustration of the used fin shapes in this work. (a) rectangular fin, (b) interrupted rectangular fin, (c) inverted triangular shape. ***Dashed line indicates the symmetry plane.*** *The gravitational force vector is vertically downwards in the plane of the figure.*

In the work by Dogan et al. [46] neither the thickness of the substrate, nor the thickness of the fin was specified. The boundary condition at the substrate is expressed as a heat flux in W/m^2 in the work of Dogan et al. [46] (for example: 2250 W/m^2). However, the authors didn't specify the fin thickness. Hence, if the fin thickness increases, the total power (in W) sent to the substrate increases

accordingly for a fixed q (in W/m^2). Comparing the temperature contours provided in Dogan et al. [46] with the temperatures in our simulations, a good match was found for a fin thickness of 3 mm. Therefore, a fin thickness of 3 mm will be assumed in this work. The thickness of the substrate is taken to be 2 mm [94].

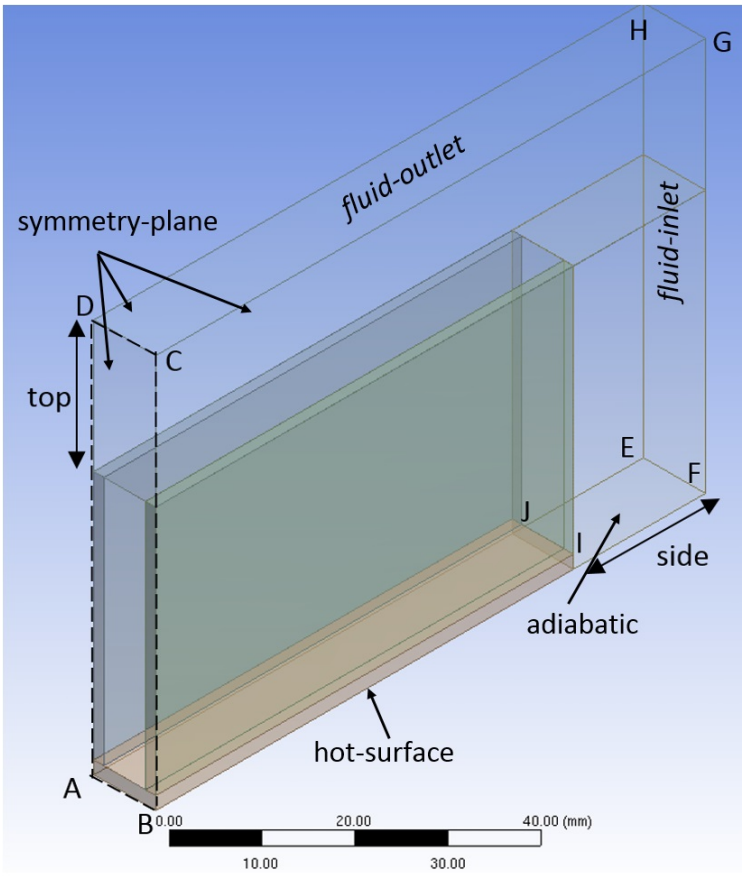

Figure 6.2: Illustration of the boundary conditions in case of a rectangular fin row ('Mesh-top20mm'). The gravitational force vector is vertically downwards in the plane of the figure.

In this work, the influence of the fluid domain on the thermal results will be assessed. More specifically, the variation of the average heat transfer coefficient on each of the fin surfaces will be determined. For all of the tested fin shapes, 8 different fluid domains were generated. In Table 6.1, the simulated geometries for each fin shape are shown. 'Side 5 mm' for example means that 5 mm of

fluid domain is added to the side of the fin shape, while 'Top 10 mm' means that 10 mm of fluid domain is added to the top of the fin shape. The geometry 'Mesh-top20mm' indicates a fin row with 20 mm of fluid domain on each of the sides and 20 mm of fluid domain on top of the fin. In total 9 different meshes are studied for each of the studied fin shapes. For the rectangular fin shape, geometry 'Mesh-top20mm' is shown in Figure 6.2 (with symmetry plane).

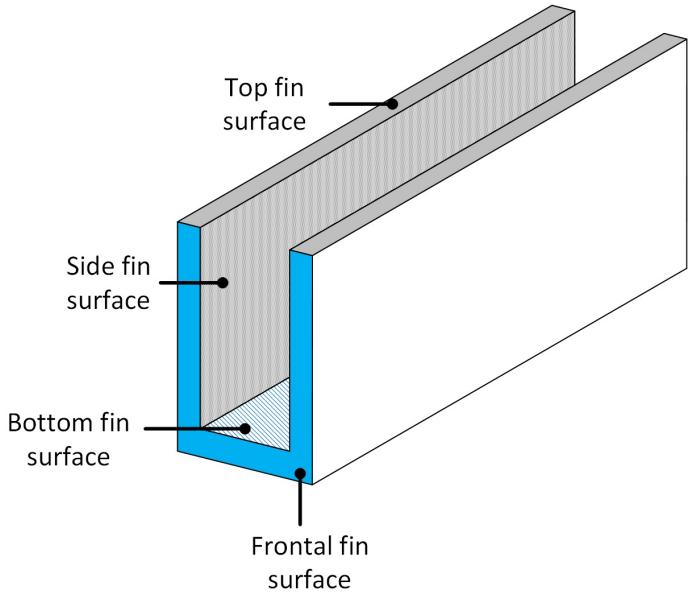

Figure 6.3: Illustration of the discussed fin surfaces. The gravitational force vector is vertically downwards in the plane of the figure.

The choice of mesh and flow domain added to the sides of the heat sink is partly based on the computational power that is needed to calculate the results (and the quality parameters like orthogonal quality and aspect ratio as defined further on, Section 6.2.3). From the case 'Mesh-top50mm' on, the length of the fluid domain on the sides was fixed at 20 mm. Likewise, increasing the height of the fluid domain at the top to 200 mm did not yield results any different from the 100 mm case. The results for the 200 mm high geometry will be discussed later in Section 6.2.4. In Figure 6.3, an illustration of the fin surfaces that will be discussed in this work is made. This particular figure is made for the rectangular fin. For the other fin designs, similar illustrations can be made. For the sake of simplicity, these figures were omitted.

The procedure for simulating conventional heat sinks is discussed in Section 6.3.

	Mesh -ref	Mesh -5mm side	Mesh -10mm side	Mesh -20mm side	Mesh top -10mm	Mesh top -20mm	Mesh top -30mm	Mesh top -50mm	Mesh top -100mm
Side 5mm		x							
Side 10mm			x		x				
Side 20mm				x		x		x	x
Side 30mm							x		
Top 10mm					x				
Top 20mm						x			
Top 30mm							x		
Top 50mm								x	
Top 100mm									x

Table 6.1: Overview of all geometries used in this Section per fin shape studied.

6.2.2 Boundary conditions

In Figure 6.2, the applied boundary conditions are illustrated for a rectangular fin row. For the two other fin shapes considered, the boundary conditions are exactly the same. Symmetrical boundary conditions are used for surfaces $ABCD$, $BCGF$ and $ADHE$. Of course it is a assumption to only simulate one fin row with symmetrical boundary condition. Surface $EFIJ$ is assumed to be adiabatic. $ABJI$ is the heated surface. Unless stated otherwise , the boundary condition at the heated surface is a fixed flux of 2250 W/m^2, in all the studied cases. Also note that the area of the substrate is the same: $0.127 \cdot 0.0094\, m^2$, in all cases. The power that is sent to the fin row is 2.69 W. This is exactly the same boundary condition which was used by Dogan et al. [46]. This corresponds to a temperature difference of +/- 33 °C. In most practical circumstances this will be the temperature difference appearing in electronics cooling (which is the focus in this work). Surface $HGEF$ is a so-called free surface where the gauge total pressure excluding hydrostatic pressure differences is set to 0 Pa. For surface $DCHG$ the gauge static pressure excluding hydrostatic pressure differences is fixed at 0 Pa. The temperature of any reversed flow at the outlet boundaries is also selected to be 293.15 K. The operating density is calculated at T_{env}.

6.2.3 Mesh and uncertainty analysis

In order to estimate the uncertainty on the numerical results, a grid discretization uncertainty analysis is performed. In this work the Roaches grid convergence index (GCI) is used to obtain an estimate of the grid discretization error [100]. The finest discretization tested has the following specifications:

- Discretization of the thickness of the fin material: 0.09 mm per cell
- Discretization of the fin height and adjacent fluid domain: 0.24 mm per cell
- Discretization of the fin length and adjacent fluid domain: 0.25 mm per cell
- Discretization of the width of the fluid domain (fin spacing): 0.08 mm/cell

The discretization is chosen in a way that both orthogonal quality, minimum orthogonal quality and maximum aspect ratio are well within the boundaries as defined by Ansys/Fluent. The reader can indeed see that sometimes no integer numbers were used. No boundary layer mesh was used, but as the GCI is low enough, it can be supposed that the results and the boundary layer is resolved [1]. This was in increase the overall quality parameters and to limit the number of cells.

[1] One can question if there is still a boundary layer in the strict definition in natural convection, of course there will be a velocity and temperature gradient. Neither of the authors, to which there is referred to in the literature survey, have used any boundary layer mesh.

In the following bullets some information is given on how Ansys/Fluent calculates these 'quality' parameters and in which ranges these parameters should be in order to get the solution converging.

- **Element quality or orthogonal quality**: provides a composite quality metric that ranges between 0 and 1. This metric is based on the ratio of the volume to the sum of the square of the edge lengths for 2D quad/tri elements, or the square root of the cube of the sum of the square of the edge lengths for 3D elements. A value of 1 indicates a perfect cube or square while a value of 0 indicates that the element has a zero or negative volume. For 3D-bodies it is calculated as:

$$element\ \ quality = C\left(\frac{volume}{\sqrt{\left(\sum(edge\ \ length)^2\right)^3}}\right), \tag{6.1}$$

  with C a parameter depending on the element that is used to mesh with. For example: C in case of a triangle is 6.92820323, while for a quadrangle it is 4.0, or a hexagon: 41.56921938.

  This parameter is calculated for each element (both solid and fluid phase).

- Minimum orthogonal quality: this value is the minimum orthogonal quality as calculated above. This value should always be larger than 0.15 in order to get the results converged.

- **Aspect ratio**: The aspect ratio is a measure of the stretching of a cell. It is computed as the ratio of the maximum value to the minimum value of any of the following distances: the distances between the cell centroid and face centroids, and the distances between the cell centroid and nodes. For a unit cube, the maximum distance is 0.866, and the minimum distance is 0.5, so the aspect ratio is 1.732. This type of definition can be applied on any type of mesh, including polyhedral. Figure 6.4 illustrates how the aspect ratio is determined. This aspect ratio is calculated in the meshing program of Ansys for each element.

- Maximum aspect ratio: this is the maximum aspect ratio as defined above. This is always below 30 in this work. However, it should be as low as possible in order to get the solution converged.

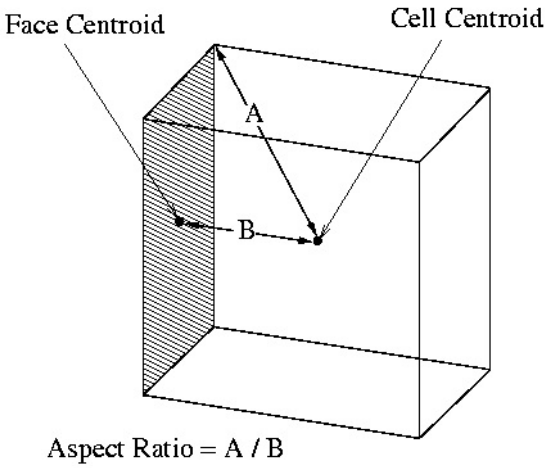

Figure 6.4: How the aspect ratio is calculated in Ansys/Fluent.

The automatic meshing program creates a mesh based on the body size maximum element which has been giving in by the user. With this meshing results, the three 'quality' parameters where calculated in Ansys/Fluent. If these are sufficient, the grid can be used to make the calculations. Otherwise, the process has to be redone[2].

The coarser grid consists of cells which are a factor of 2 larger in each direction. The results for the average heat transfer coefficient for the bottom and side fin faces are indicated in Table 6.2. Only two grids are studied. The uncertainty analysis is based on Eqs. (4.4) to (4.5). r and p in both equations stands for the factor of refinement (= 2) and order of convergence (also, = 2), respectively. Since the order of convergence was not calculated from a third grid result, Roache recommends using a safety factor of 3. The largest relative uncertainty on the heat transfer coefficient is found on the sides of the fin. When calculating with the finest grid, the GCI is 1.8%, while for the coarse grid this is 7.1%. Also other parameters are looked at to calculate a GCI. However, the most conservative value of GCI (the highest value) is obtained when looking to the heat transfer coefficient.

In next section(s), a relative uncertainty of 1.8% will be assumed.

The different fluid domains which are added on the sides and at the top of the simulated fin shape are also discretized with the same discretization as mentioned above. There is an exception for the larger fluid domains placed at the top of the heat sink, namely: 'Mesh-50mmtop' and 'Mesh-100mmtop'. For these fluid

[2]Next to this process of determining whether a grid is fine or not, also the uncertainty of the grid discretization will be looked at of course.

domains, triangular cells with a growth rate of 1.05 will be used. In the remainder of this work, only the finest discretization will be used.

	Coarse grid	Fine grid
$h_{sides}[W/m^2K]$	3.394	3.455
$h_{bottom}[W/m^2K]$	4.724	4.801
$h_{ave}[W/m^2K]$	4.621	4.697
$GCI\ h_{sides}[\%]$	7.07	1.77

Table 6.2: Uncertainty analysis for grid discretization.

A small comment before ending this section: only the uncertainty of the grid cell discretization is looked at. Of course, there are other uncertainties due to the use of symmetric boundary conditions, fluid models (e.g. incompressible ideal gas)... For these models the uncertainty is not accounted for. This is practically never done in other literature sources too. It is assumed that the uncertainty of these conditions will double the overall uncertainty, however, it is future work to study this into detail. In the next section, when 'uncertainty' is mentioned, the author means: the uncertainty due to grid cell discretization.

6.2.4 Influence of fluid domain: results

In Figure 6.5, the following heat transfer coefficients are shown for the different meshes, as shown in Table 6.1. These heat transfer coefficients are calculated automatically in the CFD software package of Fluent/Ansys:

- h_{sides}. This is the heat transfer coefficient calculated as an area-averaged value on the internal sides of the fin row (left and right) as $1/A \int_A h_{sides,i} dA$.
- h_{bottom}. This is the heat transfer coefficient calculated as an area-averaged value on the bottom side of the fin row as $1/A \int_A h_{bottom,i} dA$.
- $h_{with\ radiation}$=$Q_{tot}/(A_{fins} \cdot (T_{hot} - T_{env}))$. This heat transfer coefficient is an average heat transfer coefficient over all the available fin surfaces. If a fluid domain is added to e.g. the sides of the fin row, the heat transfer coefficient of the frontal fins will also be taken into account. Therefore $h_{with\ radiation}$ is in fact a lumped heat transfer coefficient.
- $h_{with\ radiation,\ lim}$. This is the heat transfer coefficient only for the left, right and bottom side of the fin, independent of which mesh (Table 6.1) is studied. This heat transfer coefficient is an area-averaged value of h_{sides} and h_{bottom}.

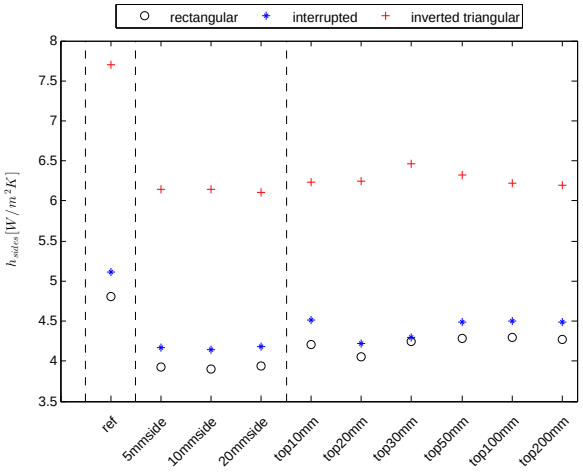

(a) h_{sides}

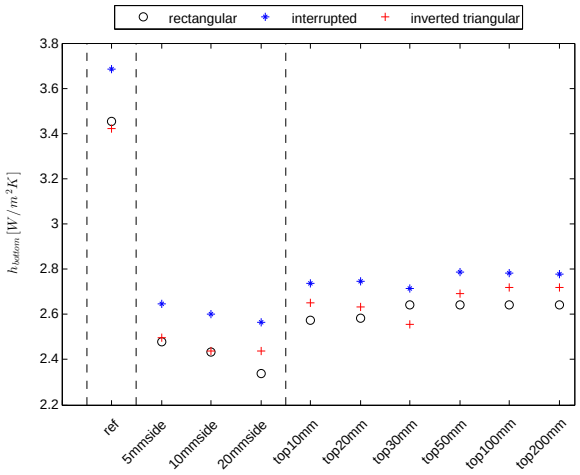

(b) h_{bottom}

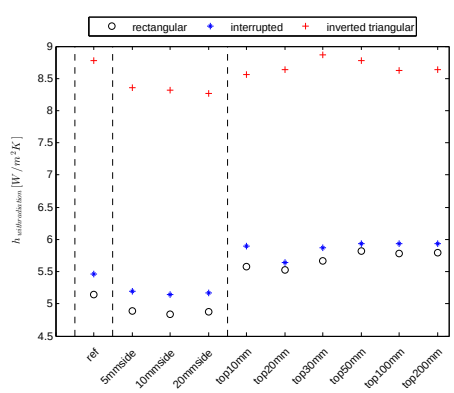

(c) $h_{with\ radiation}$

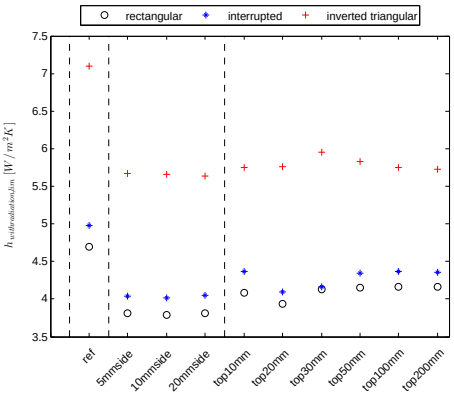

(d) $h_{with\ radiation,\ lim}$

Figure 6.5: Dependency of the heat transfer coefficient on the fluid domain on different sides of the fin row.

All the results, with their percentage difference compared to the base case ('Mesh-Ref'), are reported in Tables 6.3 and 6.4. The results for a fluid domain of 200 mm high are also given to illustrate the convergence behaviour. However, these results will not be discussed further as the boundary conditions for this grid are slightly different from the other cases. When increasing the fluid height, the unsteadiness in the flow will also increase (similar to a cigarette). This makes it impossible and/or difficult to simulate the flow steady for these large fluid domains, unless the fluid viscosity is increased with a factor two in a linear way from the zone above 100 mm to the total height of the fluid domain (200 mm). For one specific case, the author has tested if the increase in viscosity has an effect on the thermal results of the heat sink itself. It was should that this downstream effect doesn't have any effect on the thermal results. However, as this is only tested for one case (lowest temperature difference), the result isn't included in the work. The increase in viscosity has a single function: the increase in simulation time.

In order to simulate this case, the fluid viscosity was increased linearly by a factor of 10 starting from the original viscosity value at a fluid height of 100 mm (this is well above the fluid motions of interest). By doing this, the turbulence in the flow will be damped. This makes it possible to compute the steady and laminar flow.

The largest influence of the fluid domain is observed when the rectangular fin shape is compared to the inverted triangular one. The results for the interrupted rectangular fin shape are very similar to those for the rectangular fin shape. Locally the flow resistance in the middle of the interrupted fin is decreased due to the interruption[3]. However, as a single chimney pattern is observed in both the rectangular case and the interrupted case, no extra fluid will be drawn to the middle of the interrupted fin. Furthermore, the region where the fin is interrupted has a symmetric boundary condition, this makes it more difficult for air to penetrate the heat sink from the top side.

As can be seen in Figure 6.5, an increase of the fluid domain on top of the fin from 50 mm to 100 mm does not yield any significant influence on the heat transfer coefficients (the uncertainty on the grid discretization according to Table 6.2 is 1.77%).

Firstly, the influence of adding a fluid domain to the sides of the fin row on the previously defined heat transfer coefficients will be discussed (Section 6.2.4.1). Secondly, in Section 6.2.4.2, the influence of adding a fluid domain to both the sides and top of the fin row on the heat transfer coefficients will be determined.

[3]Please also note that a fin in the middle of the heat sink itself is studied. Hence there will be entrainment around the area of the interruption from the neighbouring fin (not reported in this work).

Mesh name	Rectangular fin	%-diff	Interrupted rectangular fin	%-diff	Inverted triangular fin	%-diff
h_{sides}						
Mesh -ref	4.80	-	5.11	-	7.70	-
Mesh-5mmside	3.93	-18.21	4.17	-18.35	6.15	-20.10
Mesh-10mmside	3.90	-18.74	4.14	-18.95	6.14	-20.24
Mesh-20mmside	3.94	-18.00	4.18	-18.22	6.11	-20.68
Mesh-top10mm	4.20	-12.42	4.51	-11.73	6.23	-19.08
Mesh-top20mm	4.05	-15.56	4.22	-17.55	6.24	-18.87
Mesh-top30mm	4.25	-11.48	4.30	-15.88	6.46	-16.08
Mesh-top50mm	4.28	-10.89	4.49	-12.22	6.32	-17.91
Mesh-top100mm	4.29	-10.57	4.5	-11.98	6.22	-19.19
Mesh-top200mm	4.27	-11	4.49	-12.05	6.20	-19.55
h_{bottom}						
Mesh -ref	3.46	-	3.69	-	3.42	-
Mesh-5mmside	2.48	-28.31	2.65	-28.21	2.49	-27.04
Mesh-10mmside	2.43	-29.63	2.60	-29.37	2.44	-28.73
Mesh-20mmside	2.34	-32.30	2.57	-30.36	2.44	-28.73
Mesh-top10mm	2.58	-25.47	2.74	-25.67	2.65	-22.53
Mesh-top20mm	2.58	-25.23	2.75	-25.43	2.63	-23.01
Mesh-top30mm	2.64	-23.51	2.72	-26.31	2.56	-25.24
Mesh-top50mm	2.64	-23.57	2.79	-24.36	2.69	-21.27
Mesh-top100mm	2.64	-23.51	2.78	-24.55	2.72	-20.46
Mesh-top200mm	2.64	-23.75	2.78	-24.76	2.72	-20.55

Table 6.3: Calculated values for h_{sides} $(W/(m^2K))$ and h_{bottom} $(W/(m^2K))$.

Mesh name	Rectangular fin	%-diff	Interrupted rectangular fin	%-diff	Inverted triangular fin	%-diff
$h_{with\ radiation}$						
Mesh -ref	5.14	-	5.46	-	8.78	-
Mesh-5mmside	4.89	-4.87	5.20	-4.89	8.36	-4.79
Mesh-10mmside	4.84	-5.79	5.15	-5.79	8.32	-5.19
Mesh-20mmside	4.87	-5.22	5.17	-5.32	8.27	-5.77
Mesh-top10mm	5.58	+8.63	5.90	+7.97	8.56	-2.54
Mesh-top20mm	5.52	+7.46	5.64	+3.20	8.63	-1.69
Mesh-top30mm	5.66	+10.21	5.87	+7.43	8.87	+0.99
Mesh-top50mm	5.82	+13.22	5.93	+8.60	8.77	-0.09
Mesh-top100mm	5.78	-12.40	5.93	+8.50	8.63	-1.70
Mesh-top200mm	5.79	-12.55	5.94	+8.75	8.64	-1.55
$h_{with\ radiation,\ lim}$						
Mesh -ref	4.70	-	4.98	-	7.10	-
Mesh-5mmside	3.81	-18.79	4.04	-18.82	5.67	-20.10
Mesh-10mmside	3.79	-19.37	4.01	-19.48	5.66	-20.24
Mesh-20mmside	3.81	-18.82	4.05	-18.78	5.63	-20.68
Mesh-top10mm	4.08	-13.17	4.37	-12.31	5.57	-19.08
Mesh-top20mm	3.94	-16.11	4.09	-17.84	5.76	-18.87
Mesh-top30mm	4.13	-12.16	4.17	-16.38	5.96	-16.08
Mesh-top50mm	4.15	-11.61	4.35	-12.70	5.83	-17.91
Mesh-top100mm	4.17	-11.31	4.36	-12.40	5.75	-19.01
Mesh-top200mm	4.16	-11.55	4.36	-12.55	5.73	-19.35

Table 6.4: Calculated values for $h_{with\ radiation}$ $(W/(m^2K))$ and $h_{with\ radiation,\ lim}$ $(W/(m^2K))$.

Mesh name	Rectangular fin	%-diff	Interrupted rectangular fin	%-diff	Inverted triangular fin	%-diff
$h_{frontal}$						
Mesh-5mmside	20.99	-	21.02	-	19.19	-
Mesh-10mmside	19.35	-7.82	19.36	-7.90	17.59	-8.35
Mesh-20mmside	18.24	-13.10	18.24	-13.23	16.36	-14.73
Mesh-top10mm	18.94	-9.77	18.91	-10.02	17.50	-8.82
Mesh-top20mm	17.58	-16.26	17.79	-15.37	16.18	-15.65
Mesh-top30mm	17.37	-17.26	17.24	-17.97	15.89	-17.18
Mesh-top50mm	17.72	-15.59	17.77	-15.44	16.19	-15.64
Mesh-top100mm	17.69	-15.74	17.75	-15.56	16.16	-15.78
Mesh-top200mm	17.66	-15.88	17.71	-15.75	16.15	-15.85

Table 6.5: Calculated values for $h_{frontal}$ ($W/(m^2K)$).

6.2.4.1 Influence of adding fluid at sides of fin row

Adding fluid domain to the sides of the fin material has a large impact on h_{sides} and h_{bottom}, as can be seen in Figures 6.5a and 6.5b. The heat transfer coefficient on both left, right and bottom side of the fin row decreases by adding extra fluid domain. The heat transfer coefficient h_{sides} decreases by 18% for the rectangular and interrupted fins. The impact for the inverted triangular fin is approximately the same: a relative decrease of around 20%. For the heat transfer coefficient at the bottom side of the fin row, h_{down}, the impact is even larger: a decrease of around 28% is observed, independent of the type of fin row that is simulated. From Figure 6.6, it can be observed that the velocity profile at the inlet of the fin row (for the rectangular fin) is a *single chimney pattern* [46] for the rectangular fin row without any fluid domain added. This means that the flow is drawn from one side and pushed to the top as can be seen in the streamlines in Figure 6.6. This is a typical pattern which is observed when simulating high fins (fin height over 5 mm) [70]. As shown in Figure 6.6, the direction of the velocity is forced to be perpendicular to the inlet, as was also the case in Dogan et al. [46].

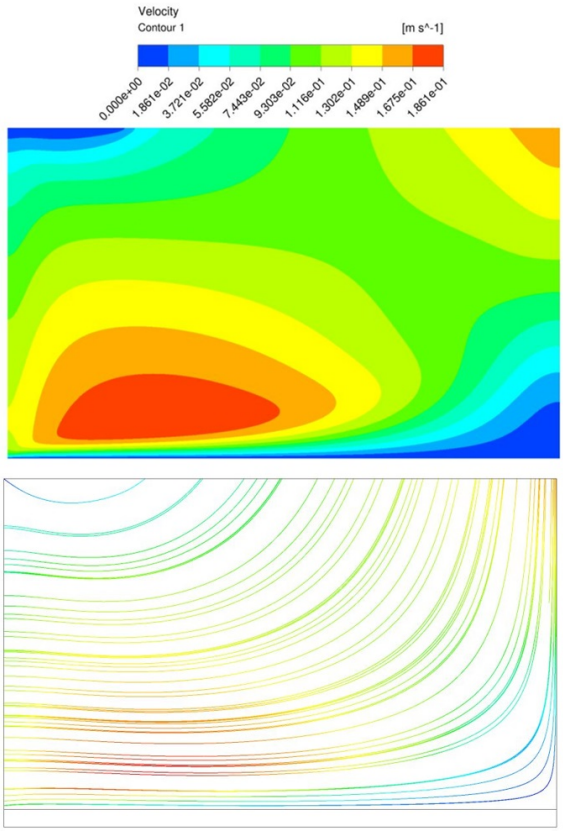

Figure 6.6: Velocity contour plot and streamlines in the middle of the rectangular fin row without any fluid domain added (Mesh-ref, right side: symmetry plane). The gravitational force vector is vertically downwards in the plane of the figure.

However, if fluid domain is added around the side of the heat sink, Figure 6.7 shows that the vector of the fluid velocity is not perpendicular any more to the (vertical) inlet of the fin, but instead enters at an angle to the inlet plane. This vector angle is downward for the upper half of the fin side, while it is upward for the lower fin side, referred to the horizontal orientation of the substrate. The fact that the lower half has an upward pushing angle is caused by the substrate: the incoming fluid heats up along the frontal fins, just before entering the fin row. This also explains why the impact on the heat transfer coefficient at the bottom side of the fin row (h_{bottom}) is, in all cases, larger compared to the impact on the heat transfer coefficient at the sides (h_{sides}) when adding fluid domain to the sides.

The combined impact on $h_{with\ radiation,\ lim}$ - an area average of h_{bottom} and h_{sides} - is thus strongly negative and independent of the kind of fin row as can be derived from Figure 6.5d. However, the impact on the heat transfer coefficient

$h_{with\ radiation}$ is much more modest compared to the case with no extra fluid domain (see Figure 6.5c). This is due to the compensation effect of the frontal fins, just before the entrance of the fin row. The results for $h_{frontal}$ are reported in Table 6.5. As can be seen the absolute values for the heat transfer coefficient $h_{frontal}$ are much larger than the values for h_{bottom} and h_{sides}, despite the frontal surface area being small.

As can be seen in Figures 6.5a to 6.5d and taking into account the relative uncertainty of ±2% on the numerical results, the difference in heat transfer coefficient of adding 5 mm, 10 mm or 20 mm to the sides of the fin row has a negligible effect. In other words, there is no need to add a large amount of fluid domain, in fact for this case 5 mm of fluid domain was enough. However, this is only the case when the effect of adding fluid domain at the top of the fin row is neglected. As will be shown in Section 6.2.4.2 where both a fluid domain at the sides and at the top will be added, the flow pattern will completely change (again).

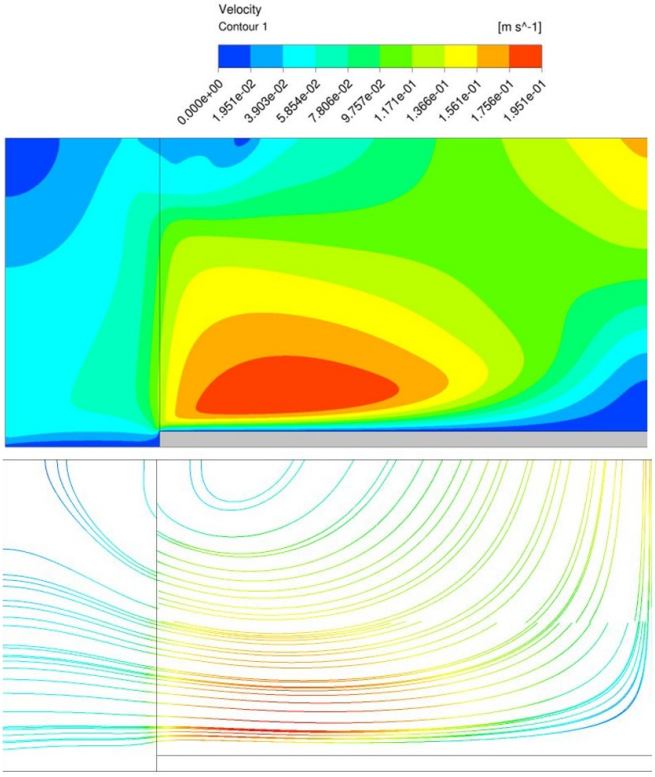

Figure 6.7: Velocity contour plot and streamlines in the middle of the rectangular fin row with 20 mm of fluid domain added at the sides ('Mesh-20mmside', right side: symmetry plane). The gravitational force vector is vertically downwards in the plane of the figure.

6.2.4.2 Influence of adding fluid at top and sides of fin row

Adding fluid domain at the top *and* both sides of the fin row will change the heat transfer coefficients further. Figure 6.5b shows the effect of adding fluid domain to top and sides on h_{bottom}. Although the impact on the heat transfer coefficient is still large and negative compared to the reference geometry ('Mesh-ref'), the relative impact is smaller compared to the case where only fluid domain was added to the sides. For the rectangular and interrupted fin design, the relative impact on h_{bottom} decreases from -28% (only adding fluid to the sides) to -24%. For the inverted triangular fin, the impact on h_{bottom} decreases from -27% to -20% (see Figure 6.5b). The fact that h_{bottom} decreases by adding fluid domain at the sides is explained in Section 6.2.4.1. The fact that the impact of adding fluid domain on the top and side is more severe for the inverted triangular shape can be explained by comparing Figure 6.8 (for the inverted triangular fin) with Figure 6.6 and 6.9 (for the rectangular fin). Figure 6.9 shows that e.g. the streamlines in the middle of the fin are oriented more to the bottom side of the fin row compared to the streamlines at the same location for inverted triangular case (Figure 6.8). This explains the differences in impact for h_{bottom} between the rectangular and inverted triangular fins when adding fluid to top and sides. In case of the rectangular fins more fluid is passing over the bottom plate.

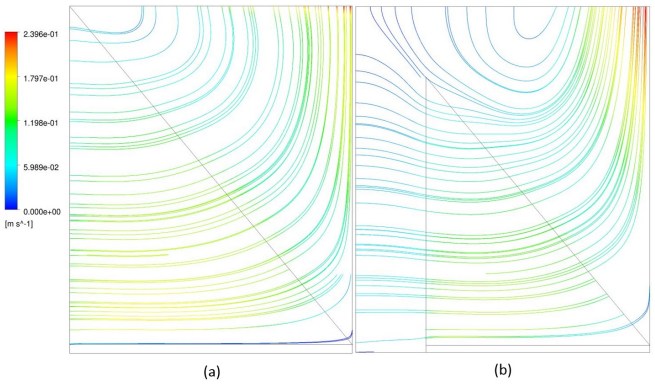

Figure 6.8: Velocity contour plot and streamlines in the middle of the inverted triangular fin row, (a) without added fluid domain ('Mesh-ref'), (b) with 20 mm of fluid domain added at the sides and top ('Mesh-top20mm', right side: symmetry plane). The gravitational force vector is vertically downwards in the plane of the figure.

Comparing the streamlines in both Figure 6.8 (inverted triangular case) and Figure 6.9 (rectangular case), it is clear that the impact of adding extra fluid domain at the top and sides of the fin row on h_{sides} is larger for the rectangular and interrupted fin row compared to the inverted triangular fin. For the first two fin rows, the impact on h_{sides} is reduced from -18% (only adding fluid at the sides

of the heat sink) to -11%. For the inverted triangular fin the impact on h_{sides} is decreased (not significantly) from -20% to -19% (see Figure 6.5a).

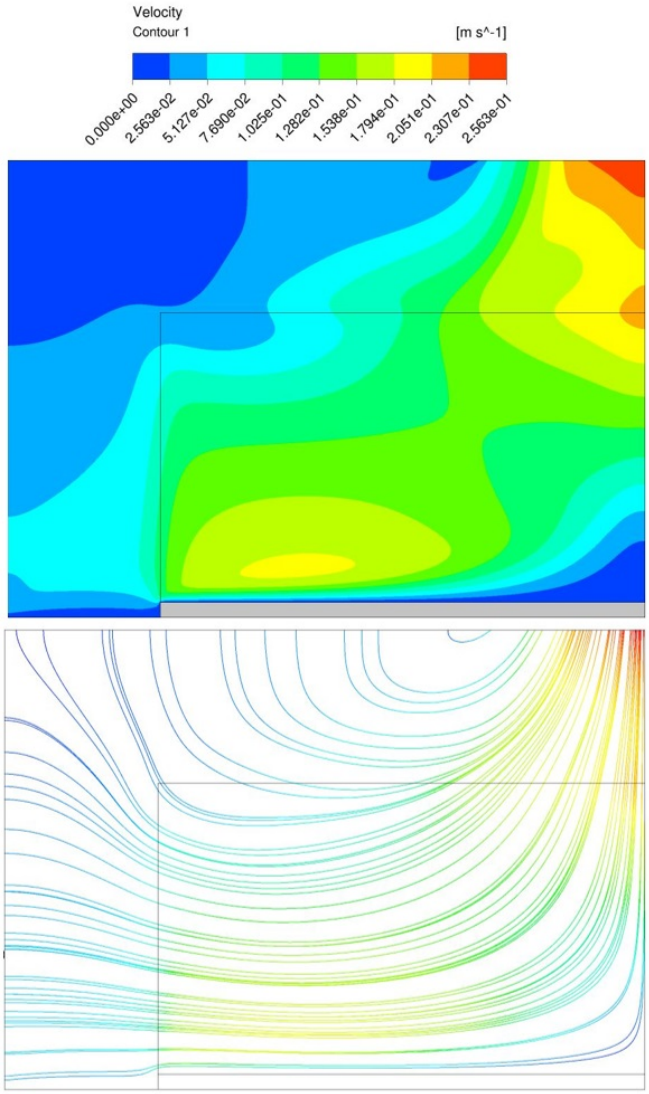

Figure 6.9: Velocity contour plot and streamlines in the middle of the rectangular fin row with 20 mm of fluid domain added at the sides and top ('Mesh-top20mm', right side: symmetry plane). The gravitational force vector is vertically downwards in the plane of the figure.

This can be explained by the fact that the heated area in case of the inverted

triangular fin row is varied in the direction from the frontal surface area deeper into the heat sink. This is due to the structure of the triangular case in comparison with the rectangular cases. Even in case of no fluid domain added to the sides or top, there is already a fluid outlet at the top of the inverted triangular fin. This is in contrast to the rectangular fin case.

The influence on the lumped heat transfer coefficient $h_{with\ radiation}$ is significant and the relative influence strongly depends on the fin shape. For the rectangular fin, the impact is large: going from a decreased heat transfer coefficient (-5%) when only fluid domain at the sides is added to an increase in the heat transfer coefficient for the case with fluid domain added to sides and top (+12%). This is completely different from the case of the inverted triangular fin where the impact goes from -5% (approximately the same as for the rectangular and interrupted fin row) to -2%, when the largest fluid domain at the top is added. This difference in impact can be explained by the frontal facing heat transfer coefficient of the fins: $h_{frontal}$. Although the absolute number of $h_{frontal}$ is approximately the same for all the fin rows studied (see Table 6.5), the relative importance of the frontal facing part of the fin row in case of the inverted triangular fin is larger compared to the rectangular case (relative difference in the frontal fin area is almost doubled in the case of an inverted triangular case).

The influence of adding extra fluid domain: going from 10 mm to 50 mm is significant in case of h_{sides} and $h_{with\ radiation}$ as can be seen in Figure 6.5a and 6.5c. The impact on $h_{frontal}$ of adding extra fluid domain on the top is limited as can be observed in Table 6.5. When at least 50 mm of fluid domain is added above the heat sink, the results no longer depend on the height of the computational domain. This corresponds to a height of 130% of the equivalent fin height (in case of a triangular fin shape, the equivalent fin height is half of the total fin height).

This minimum required fluid domain will be used in all of the following calculations.

6.2.4.3 What with other fin heights?

To check if the equivalent fin height could be taken as a parameter to estimate the necessary volume of the fluid domain at the top of the fin structure, the rectangular fin structure from Figure 6.1(a) is considered with a fin height of only half of the original case. In this case, the fin height is 19 mm instead of 38 mm. The results for this shorter fin are presented in Table 6.6. It is clear that for the fluid domain adjacent to the heat sink, only the existence of some fluid domain is enough. If our statement holds, the fluid domain that is added to the top of the heat sink should be at least 130% of 19 mm = ±25 mm[4].

[4]Please note that the author does not want to stress too much on this value of 130%. As can be seen from Table 6.6, this results most of the time in too much fluid domain. For this work, 130% can be taken as conservative value. However, more research is necessary on different fin shapes, different fin

From the results, it can be clearly seen that for a shorter fin design, the heat transfer coefficient 'converges' much faster to a steady value, when increasing the fluid domain's height above the fin itself. This indicates that the equivalent fin height could be taken as an indicator to estimate the amount of fluid height above the fin structure.

Mesh name	Rectangular fin height divided by two	%-diff
h_{sides}		
Mesh-ref	4.87	-
Mesh-5mmside	4.48	-8.7
Mesh-20mmside	4.50	-8.2
Mesh-top20mm	4.69	-3.8
Mesh-top50mm	4.72	-3.2
Mesh-top100mm	4.72	-3.1
h_{bottom}		
Mesh-ref	3.78	-
Mesh-5mmside	3.63	-4.1
Mesh-20mmside	3.65	-3.6
Mesh-top20mm	3.45	-9.6
Mesh-top50mm	3.47	-9.6
Mesh-top100mm	3.45	-9.6
$h_{with\ radiation}$		
Mesh-ref	5.36	-
Mesh-5mmside	5.47	-2.01
Mesh-20mmside	5.50	-2.5
Mesh-top20mm	6.37	+15.9
Mesh-top50mm	6.46	+17.0
Mesh-top100mm	6.49	+17.4
$h_{with\ radiation,\ lim}$		
Mesh-ref	4.71	-
Mesh-5mmside	4.36	-8
Mesh-20mmside	4.38	-7.5
Mesh-top20mm	4.51	-4.4
Mesh-top50mm	4.54	-3.7
Mesh-top100mm	4.54	-3.7

Table 6.6: Calculated results for the geometry shown in Fig. 6.1(a), but with half of the fin height.

heights and heat fluxes in order to determine whether this value can be considered as a conservative for all heat sinks studied in open literature.

6.3 Procedure to simulate conventional heat sinks

For each cell the mass (Eq. (6.2)), momentum (Eq. (6.3)) and energy equation (Eq. (6.4)) for the fluid are solved steady together with the energy conduction equation for the solid (Eq. (6.5)). For the momentum term, this is the so-called *incompressible Navier-Stokes equation in convective form* [189].

$$\nabla \cdot (\rho \overrightarrow{v}) = 0 \tag{6.2}$$

$$(\overrightarrow{v} \cdot \nabla)\overrightarrow{v} - \mu \nabla^2 \overrightarrow{v} = \frac{1}{\rho_0} \nabla p + \overrightarrow{g} \tag{6.3}$$

$$\overrightarrow{v} \cdot \nabla(\rho_0 T) = \frac{\mu}{Pr} \nabla^2 T \tag{6.4}$$

$$\nabla^2 T = 0 \tag{6.5}$$

In some of the presented cases in the next Sections, the radiative heat transfer will also be taken into account. This was also done in Ahmadi et al. [91], Shen et al. [71], Tari et al. [94] and Dogan et al. [46]. The latter two authors are using the surface to surface (S2S) model for radiation in the CFD package by Ansys/Fluent (like discussed in Section 4.1.5). This is also the model that will be used in this work. The main assumption in this model is that any absorption, emission or scattering of radiation by the fluid can be ignored. Therefore, only the energy exchange from one surface to another has to be taken into account. This energy exchange depends on the size/structure of the heat sink, separation distance and orientation. This dependence is accounted for by a function of the geometry: the view factor (as already discussed in Section 2.2.1). This view factor is calculated automatically in the CFD software from Ansys/Fluent. The used radiation model assumes all surfaces to be grey and diffuse, where the emissivity and the absorptivity of a grey surface are independent of the wavelength.

Furthermore, the pressure-velocity coupling in this work is done with the SIMPLE algorithm, while momentum and energy discretization is done second order upwind. Air is modelled as an incompressible ideal gas (like in Shen et al. [71]). Therefore the operating density (ρ_0) has to be given. This operating density is taken at environment temperature (T_{env}). Only this temperature can be used, in order to impose the correct hydrostatic pressure at the inlet of the heat sink. In most studies, it is not mentioned what value they have taken as operation density. The way ρ_0 will of course have a large influence on the results. In this way, when the environment temperature is 293.15 K, the operation density was selected 1.204 kg/m^3. When the Boussinesq approximation is not used, the operating density, ρ_0, appears in the body-force term in the momentum equations as $(\rho - \rho_0)g$.

The temperature of any reversed flow at the outlet boundaries is also selected to be 293.15 K.

The residuals, automatically calculated at each iteration step in Ansys/Fluent [28], have to be lower than 10^{-6} before the results can be accepted. However, in most cases, the residuals were even lower. In some configurations, the parameters of interest are also studied. From this, it can be concluded that residuals lower than 10^{-6} are more than low enough. This criterion holds for all residuals.

6.4 Commercially available heat sinks: base cases

Two types of heat sinks from two different manufacturers were tested in this work:

- **Pin fins.** Two types of pin fins were tested: in-lined and staggered. In Figure 6.10, both heat sinks are illustrated.

  The staggered heat sink is made by Alpha heat sinks from Japan (see Section 3.1.1.3) and has a surface-to-volume ratio of 202 $\frac{m^2}{m^3}$. The pin fin by Alpha has a hexagonal shape[5].

  The in-lined pin fin heat sink is produced by CoolInnovations from Canada (see Section 3.1.1.1) and has a surface-to-volume ratio of 417 $\frac{m^2}{m^3}$. This pin fin has a circular shape.

- **rectangular interrupted fins.** One type of plain fins is tested: the rectangular interrupted fins (see Figure 6.11). They are made by Alpha heat sinks (see Section 3.1.1.3) and have a surface-to-volume ratio of 613 $\frac{m^2}{m^3}$.

The outer dimensions of the heat sinks were chosen in a way that they can be tested with the test rig presented in Chapter 5. However, these tests were never performed due to lack of time. The height (H, h on the figures of the manufacturer) for all heat sinks is fixed on 20 mm. This neglects the uncertainties (of 0.25 mm in making the fins) given by the manufacturers.

[5] An equivalent circular shape will be tested numerically to study if the shape of the fin itself affects natural convection with pin fins

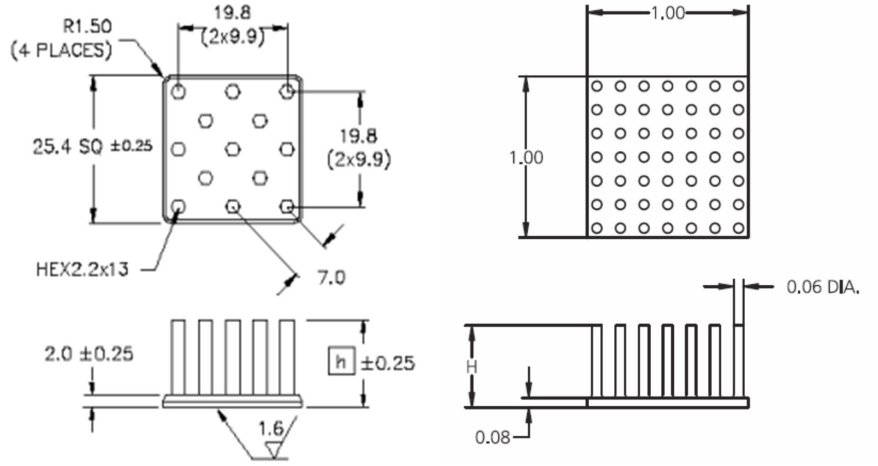

(a) pin fins from Alpha heat sinks (staggered) *(b) pin fins from CoolInnovations (in-lined)*

Figure 6.10: Illustration of the bought pin finned heat sinks in mm.

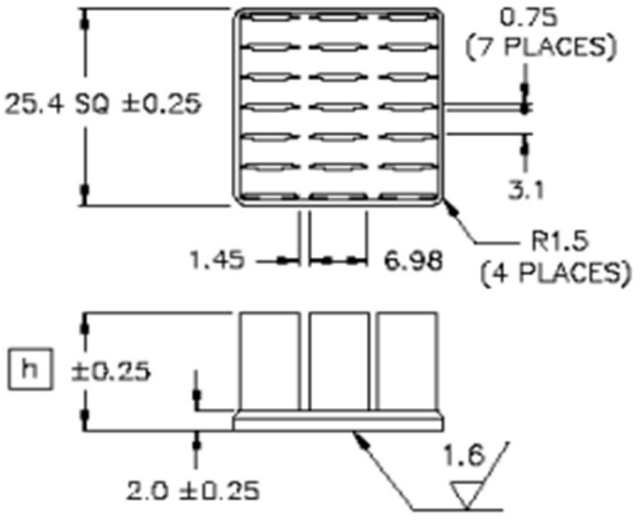

Figure 6.11: Illustration of the bought rectangular interrupted fins from Alpha heat sinks in mm

6.5 Geometry implementation & meshing in Ansys

6.5.1 Geometry

The geometry implementation to simulate the heat sinks, as described in Section 6.4, is illustrated for the hexagonal staggered pin fin geometry from Alpha heat sinks.

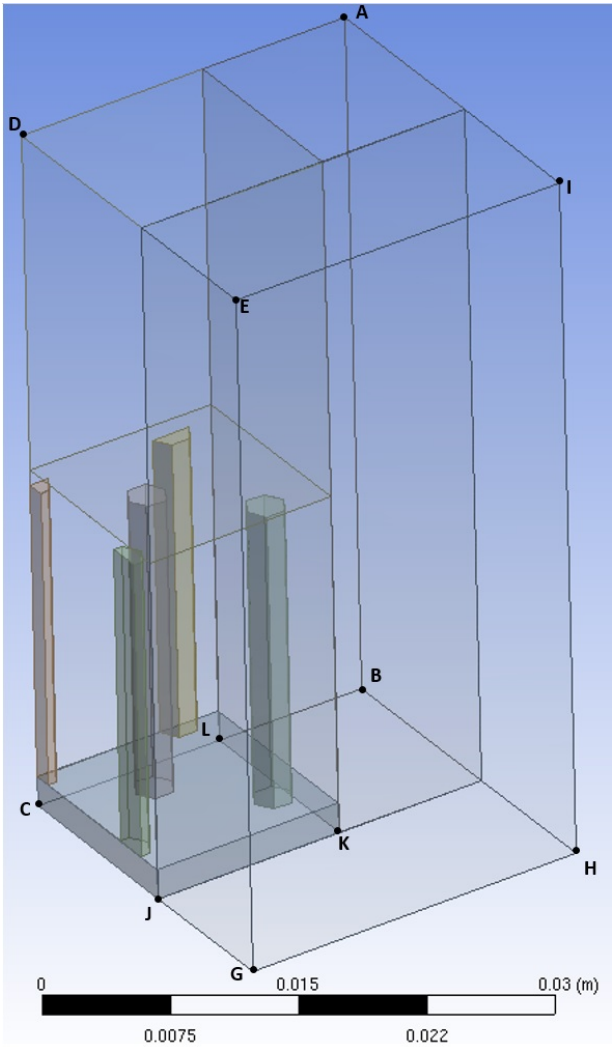

Figure 6.12: Illustration of geometry implementation of the staggered hexagonal pin fin heat sink from Alpha heat sinks. The gravitational force vector is vertically downwards in the plane of the figure.

Figure 6.12 shows the geometry implementation in Designmodeler (Ansys). For the other heat sinks which will be simulated, the implementation is done identically. In order to minimize the number of computational cells, only one quarter of the heat sink is simulated. The chamfers added by the manufacturers at the sides of the substrate of the heat sinks are not modelled, because these gave rise to very bad cell shapes. Except for this, the heat sink is modelled as it is. At least 130% of the fin height is added as a fluid domain at the top of the heat sink, while at least 15 mm of fluid domain is added at the sides of the heat sink. This is based on the results found in Section 6.2.4. In this section can be seen that even when a very small amount of fluid domain is added to the sides (5 mm was tested) it does not differ significantly from a larger amount of fluid domain to the sides (e.g. 10 mm or larger). Therefore, there is chosen for a conservative amount of 15 mm of fluid to the side. In fact, this could have been smaller.

Surfaces $ABCB$ and $DECG$ are symmetry-planes. Surface $DAEI$ is a so-called free surface where the gauge total pressure excluding hydrostatic pressure differences is set to 0 Pa. For surfaces $EIGH$ and $AIBH$ the gauge static pressure excluding hydrostatic pressure differences is fixed at 0 Pa. Surface $BLKJGH$ is assumed to be adiabatic. $CJKL$ is the heated surface. Most boundary conditions are identical to the conditions described in Section 6.2.4. The applied boundary condition is always a heat flux (in W/m^2) or a fixed temperature. The area of $CJKL$ is $\frac{25.4}{2} \cdot \frac{25.4}{2} mm^2$.

6.5.2 Mesh

For the discretization in numerical cells, a so-called body size function is selected in the Meshing program from Ansys. The fins themselves are discretized with tetrahedral cells. The complete solid three-dimensional body is also meshed with hexahedral cells if possible, otherwise with tetrahedral. As can be seen from Figure 6.12, a small fluid body is added just above the fins. This body will also be meshed using tetrahedral cells. While all the other fluid cells are discretized with hexahedral structures. This is because it is always better to mesh with hexagonals instead of tetrahedral cells: to resolve the boundary layer properly and to minimize the amount of elements [102]. However, tetrahedral cells result in better results for orthogonal quality and skewness. The size of the tetrahedral cells and rectangles is held fixed. The orthogonal quality (definition see Section 6.2.3) always has to be larger than 0.15 in order to ensure that the results converged.

Again, two different grid discretizations are used to estimate the uncertainty on the numerical results. In the first grid, the element size of the body size function is selected at 0.5 mm, while for the second (finer) grid the element size is 0.25 mm (factor 2 smaller). In case of the geometry, as presented in Figure 6.12, this results in a coarse mesh of 1 million cells and a finer mesh with 8 million cells. The finer

grid is thus a refinement with a factor 2 in each direction compared to the coarser grid[6].

	coarse grid (1M)	finer grid (8M)
$T_{solid,avg}$ in K	344.06	343.99
$T_{fluid,avg}$ in K	300.79	300.81
$h_{fins,avg}$ in W/m^2K	9.93	9.94
$GCI_{h_{fins,avg}}$ in %	**0.32**	**0.11**

Table 6.7: Grid convergence index (GCI) for the geometry discussed in Figure 6.12. A heat flux of 2250 W/m^2 is used as a boundary condition.

For a heat flux of 2250 W/m^2 and the geometry presented in Fig. 6.12, the results from both discretizations are presented in Table 6.7. It is shown that the results of interest are not so sensitive to the chosen discretization. The variations on the grid convergence index (GCI in Table 6.7) are low. In what follows, the finest discretization will be used. An illustration of this mesh in one of the symmetry planes is shown in Figure 6.13.

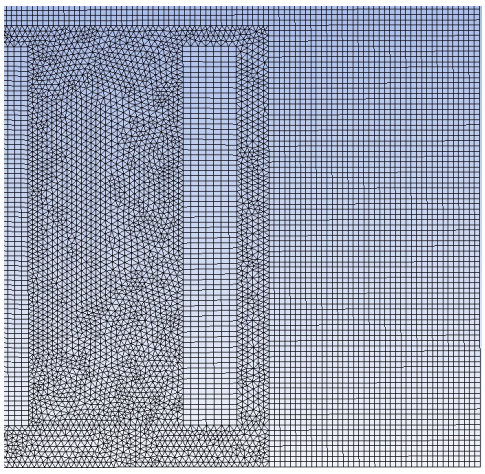

Figure 6.13: Illustration of the cell discritization in one of the two defined symmetry planes of the geometry shown in Figure 6.12. The gravitational force vector is vertically downwards in the plane of the figure.

[6]A refinement with a factor two in each direction corresponds to an increase in the cell size with a factor 8.

6.6 Parameter(s) of interest

The performance parameter wich is reported by most of the manufacturers is the **thermal resistance** R. The thermal resistance is defined in Eq. (6.6), in which T_{solid} is the area averaged temperature of the solid fin material.

The heat transfer rate Q (in W) is the convective and radiative energy that is added to the surface. This parameter is either fixed[7] or will be calculated[8].

However, which Q needs to be used in the expression for thermal resistance R (Eq. (6.6)) remains rather vague. For our CFD results, the heat transfer rate is expressed as $Q = Q_{in} = Q_{conv} + Q_{rad}$, where Q_{loss} is zero. If the thermal resistance R is reported based on experiments, the reader is referred to Section 3.2.1, where the heat transfer rate Q reported in open literature is discussed and whether or not Q_{loss} is determined properly.

The environment temperature T_{env} is another difficult parameter to determine, especially when you want to compare this numerically determined thermal resistance with its experimentally determined counterpart. However, the question is how T_{env} is determined experimentally. The reader is again referred to Section 3.2.2 in Chapter 3. In this work, the use of different T_{env} definitions will be discussed: either a volume-averaged temperature could be taken (T_{fluid}), or the fluid temperature at infinity (T_∞). Again, the author wants to stress that it is not easy to select a representative temperature. T_{fluid} as defined as a volume-average temperature, is not a proper choice, but also the temperature at infinity T_∞ is not always correct. For example: what to do in case of a heat sink in a very narrow box. What to select here as a T_{env}? The most correct and easiest way to define T_{env} is to use T_∞ because this is measurable experimentally and can be used to recalculate temperatures and fluxes from given thermal resistances.

$$R = \frac{T_{solid} - T_{env}}{Q} \; (in\ K/W) \tag{6.6}$$

This thermal resistance R is a *black-box parameter* and there are a lot of different parameters influencing this thermal resistance[9]:

- *Conduction*: the kind of material that is used to manufacture the finned heat sinks is important. The thermal conductivity of the solid material needs to be known.

  Al6063 is used for the Alpha heat sinks (thermal conductivity: 200 W/mK). For the heat sinks by CoolInnovation, it was only indicated

[7] A constant heat flux in W/m^2 can be applied in Ansys/Fluent. Because of the constant substrate surface, the heat transfer rate Q in W will also be constant

[8] In this case the temperature is fixed at the substrate.

[9] For all these types of heat transferring modes, the temperature (and consequently the heat flux) is an important parameter when determining the thermal resistance as will be seen in Section 6.7.

that aluminium was used. However, no specific alloy was given. For the calculations, again a thermal conductivity of 200 W/mK is assumed and the dependence of the conductivity is not studied (although this effect will be significant).

- *Convection*: based on the geometry of the fins the convective properties will also alter, so as the thermal resistance. All the studied geometries are discussed in Section 6.4.

- *Radiation*: depending on the emissivity of the heat sinks, the temperature field will be changed and consequently the convective heat transfer.

  As discussed in Section 6.3, the S2S radiation model will be used in this work. The view factors will be calculated automatically for each case. The only required input is the emissivity of the material. As the material emissivity is unknown, the sensitivity on this parameter needs to be discussed as well. When the heat sink is painted or anodized, the emissivity of the material is quite high and can be estimated with limited uncertainty, like discussed in Appendix B.

6.7 Results and comparison

For the geometries discussed in Section 6.5.1, a number of simulations were run.

In Section 6.7.1, a comparison between the different heat sinks studied is made based on a fixed heat flux of 2250 W/m^2. In this way the different heat sinks can be compared with one another. The choice of a fixed heat flux of 2250 W/m^2 is inspired by the work of Dogan et al. [46]. While in Section 6.7.2, the heat flux applied by the different manufacturers is used as boundary condition and the results are compared with those given by the manufacturer[10]. Depending on the kind of heat sink, other heat fluxes will be applied. Sometimes even other orientations are used by the manufacturers to report the test results. This is because the manufacturer recommends to use the heat sink in this test orientation.

In an ideal situation it was possible to compare this numerical data with experimental results. However, this was not possible due to time limitations. Furthermore, according to the knowledge of the author there are no correlations present in literature to compare the produced numerical data with. Many experiments are performed with pin fins or plain fins. Yet, the author is not able to make a correlation based on this data (e.g. for different diameters of the pins, and different compactnesses). Simply because it is very hard to find a data set for a large amount of heat sinks, e.g. with pin fins, which closely resemble each other

[10]Only the heat sinks by Alpha heat sinks are discussed here, as this is the only manufacturer who gives the boundary conditions under which the heat sinks where tested. CoolInnovations only tested the heat sinks in forced convection although they are also recommended to be used in natural convection.

in a way that a correlation is possible. Most of the time, authors are testing more complex fin shapes.

6.7.1 Comparing heat sinks with fixed Q (2250 W/m^2)

In this section, the heat flux will be held fixed at $2250W/m^2$ and the complete substrate is heated[11]. The heat flux is held fixed to compare one heat sink with another. The level at which the heat flux is held constant, is based on the work of Dogan et al. [46].

6.7.1.1 Staggered pin fin by Alpha heat sinks (Fig. 6.10a)

In Table 6.8, the thermal results for a horizontally orientated hexagonal pin fin by Alpha heat sinks are shown. The sensitivity of the radiative emissivity is tested based on three different emissivity values for the used aluminium surface: 0% (no radiation), 40% and 85% (value when the heat sink is painted black). For a fixed heat flux of $2250W/m^2$, the biggest influence of the imposed radiative heat transfer is the decrease of T_{solid}. This temperature is an area averaged parameter over all the solid cells which are in contact with the fluid domain around the heat sink (face values). In all of the simulated cases, the ambient temperature T_∞ is held fixed at $293.15K$.

From Table 6.8, it is clear that the thermal resistance R strongly depends on which temperature is chosen as the ambient temperature T_{env} in Eq. (6.6). In case of no radiation (ε = 0%), T_{fluid} and T_∞ vary by about $7.66K$. Consequently, the thermal resistance using these two temperatures as T_{env} varies by about 15%. This shows the importance of reporting the T_{env} well.

When the radiative heat transfer is increased, the difference between R_{T_∞} and $R_{T_{fluid}}$ decreases a bit as the volume averaged fluid temperature T_{fluid} also decreases by about $1K$. However, increasing the radiative heat transfer rate, has the biggest impact on the solid temperature T_{solid}. This temperature decreases by about $11.33K$, when increasing the surface emissivity by 85%. The thermal resistance decreases by 18%, this is similar to the effect of choosing another definition for T_{env}: in this case a variation of 15% is seen. This evolution in thermal resistance, also shows the impact of radiation on the performance of the system. Despite these results, this radiative influence is often neglected in numerical work [92, 95, 96, 97, 98].

[11] This will be different in Section 6.7.2 where the heat flux will be much higher and only part of the substrate is heated, according to the test procedure as described by the manufacturer

	ε = 0%	ε = 40%	ε = 85%
T_{fluid} in K	300.81	300.02	299.50
T_{solid} in K	344.108	337.21	332.78
R_{T_∞} in K/W	35.10	30.35	27.43
$R_{T_{fluid}}$ in K/W	29.83	25.62	22.93

Table 6.8: Thermal results for a horizontal hexagonal pin fin from Alpha heat sinks with heater covering complete substrate ($25.4 \cdot 25.4mm^2$ and $Q = 2250W/m^2$)

Table 6.8 shows the results for the heat sink as produced by Alpha heat sinks. The pin fins in this heat sink have a hexagonal shape. However, in many other pin fin heat sinks the pins are extruded to a circular shape. Therefore, a heat sink with the same amount of solid material but with circular pin fins is also simulated numerically[12]. The results are presented in Table 6.9. There are no significant differences observed when comparing the circular pins with the hexagonal pins (Table 6.8). Hence, the choice of making pin finned heat sinks with either hexagonal or circular pins depends on the ease of producing the two types. The thermal performance is the same.

	ε = 0%	ε = 40%	ε = 85%
T_{fluid} in K	300.78	300.01	299.49
T_{solid} in K	344.24	337.38	332.95
R_{T_∞} in K/W	35.20	30.47	27.42
$R_{T_{fluid}}$ in K/W	29.94	25.75	23.05

Table 6.9: Thermal results for a horizontal equivalent circular pin fin from Alpha heat sinks with heater covering complete substrate ($25.4 \cdot 25.4mm^2$ and $Q = 2250W/m^2$)

Furthermore, in many applications the heat sinks need to perform in a vertical orientation as well. In Table 6.10, the results for the vertical orientation are presented. By comparing the horizontal and vertical orientation, it is clear that the heat sink will perform worst in vertical orientation. In case of pin fins, the heat sink itself is equally permeable at each side of the heat sink. When the heat sink is placed horizontally, air is able to penetrate from each side of the heat sink (see Figure 6.14b). While for the vertical orientation, air is only able to enter the heat sink from below (see Figure 6.14c).

[12]The heat transferring area A for the heat sink with round pin fins is only 5% lower compared to the heat sink with hexagonal pins.

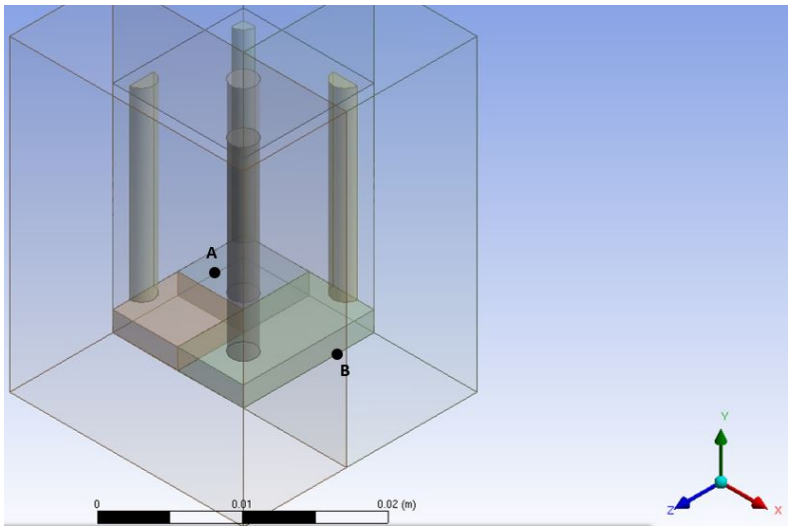

(a) Illustration of the simulated heat sink. The plane crossing point A and B is plotted in subfigures (b) and (c). For subfigure (b), the gravity is parallel to the negative y-axis. For subfigure (c), the gravity is parallel to the z-axis. A quarter of the complete heat sink is simulated.

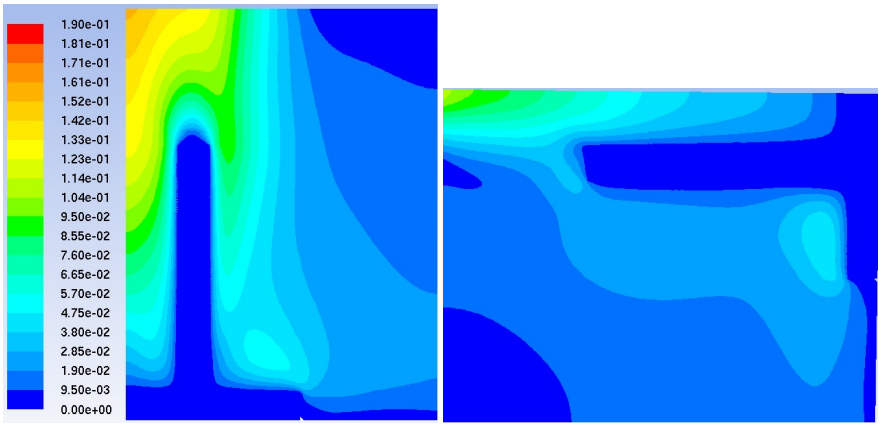

(b) horizontal orientation (ε = 85%) *(c) vertical orientation (ε = 85%)*

Figure 6.14: Velocity contour plots of the circular pin fin from Alpha heat sinks (see Fig. 6.10).

The vertical orientation also affects the solid and fluid temperature compared to the horizontal orientation. Although T_∞ remains the same, T_{fluid} is almost 2.5 K higher. The same holds for T_{solid}, this temperature is also higher because of the reduced air penetration in comparison with the horizontal orientation. This makes that when comparing the different use of T_{env} in the definition of the

thermal resistances in vertical orientation with those in horizontal orientation, the differences in performance are significant, but small. For R_{T_∞} the difference between both orientations is 9%, while for $R_{T_{fluid}}$ this is only 4.4%. This again indicates the large differences in the choice for T_{env}.

The manufacturer recommends to use the heat sink in its horizontal orientation. This is confirmed by our numerical simulations.

	ε = 0%	ε = 40%	ε = 85%
T_{fluid} in K	304.29	302.89	301.96
T_{solid} in K	351.48	342.61	336.95
R_{T_∞} in K/W	40.18	34.07	30.18
$R_{T_{fluid}}$ in K/W	32.50	27.36	24.11

Table 6.10: Thermal results for a vertical equivalent circular pin fin from Alpha heat sinks with heater covering complete substrate ($25.4 \cdot 25.4mm^2$ and $Q = 2250W/m^2$)

6.7.1.2 Rectangular interrupted fin by Alpha heat sinks (Fig. 6.11)

In Table 6.11, the thermal results for a horizontally rectangular interrupted fin by Alpha heat sinks are shown. First of all one can observe that for the horizontal case, the performance compared to the hexagonal pin fin by the same manufacturer is much higher. Without any radiative heat transfer (ε = 0%), the performance of this rectangular interrupted heat sink is 44.2% higher (based on $R_{T_{fluid}}$) compared to the hexagonal pin fin. This can be partially explained by comparing the surface-to-volume ratio of both heat sinks. As explained in Section 6.4, the difference between both heat sinks is a factor 3 in terms of surface-to-volume ratio. The fact that the difference in performance without radiation is less than a factor 3 can be explained by the difference in the possibilities for a fluid to penetrate into the heat sink: the thermal performance is always a combination of surface area A (strongly linked to the surface-to-volume ratio) and heat transfer coefficient h (strongly linked to the flow 'obstructions'). Of course, the influence of the heat sink's conductivity (and the kind of material that is used, pure aluminium or not) will result in different thermal resistances. However, the effect of conductivity is not studied.

When the radiative heat transfer is modelled (ε = 85%), the performance of the rectangular interrupted fin is only 39.0% higher compared to the in-lined pin fin. This means that the radiative influence is less pronounced for the rectangular interrupted fin in comparison with the in-lined pin fin: a decrease in $R_{T_{fluid}}$ of resp. 25.3% and 30.1% comparing the results for ε = 0% (no radiation) and ε = 85%, respectively. The difference in performance by adding radiation can be explained by the difference in view factor when comparing both fin types and the difference in heat transferring surface. Note that these differences are very

limited (only 5% points), which makes it very hard to observe these differences in performance through experiments.

	ε = 0%	ε = 40%	ε = 85%
T_{fluid} in K	302.84	301.799	301.316
T_{solid} in K	332.863	327.691	325.264
R_{T_∞} in K/W	27.36	23.79	22.12
$R_{T_{fluid}}$ in K/W	20.68	17.84	16.50

Table 6.11: Thermal results for a horizontal rectangular interrupted fin from Alpha heat sinks with heater covering complete substrate ($25.4 \cdot 25.4mm^2$ and Q = $2250W/m^2$)

As in Section 6.7.1.1, the vertical orientation is also tested. This is the orientation recommended by the manufacturer. Please note that this recommended orientation is different for the in-lined pin fin heat sink. However, Table 6.12 clearly shows that the difference between both orientations is negligible. Considering the heat sink geometry, the flow is blocked through the long plate fins both in horizontal and vertical orientation. This makes it impossible to entrain air through the sides of the heat sink. Only at the edges, where the plate fin is interrupted, there is a possibility to entrain extra air. However, it seems that this entrained air has only a small impact on the thermal performance. This can be seen in Fig. 6.15, in which it is clear that for both orientations air flows into the holes of the interruptions of the plate fins.

It is not clear why the heat sink manufacturer recommends a certain orientation for the heat sink. By creating interruptions between the fins, the effect of the orientation is negligible.

	ε = 0%	ε = 40%	ε = 85%
T_{fluid} in K	303.86	302.60	302.00
T_{solid} in K	333.46	328.14	325.62
R_{T_∞} in K/W	27.77	24.11	22.37
$R_{T_{fluid}}$ in K/W	20.39	17.59	16.27

Table 6.12: Thermal results for a vertical rectangular interrupted fin by Alpha heat sinks with heater covering complete substrate ($25.4 \cdot 25.4mm^2$ and Q = $2250W/m^2$)

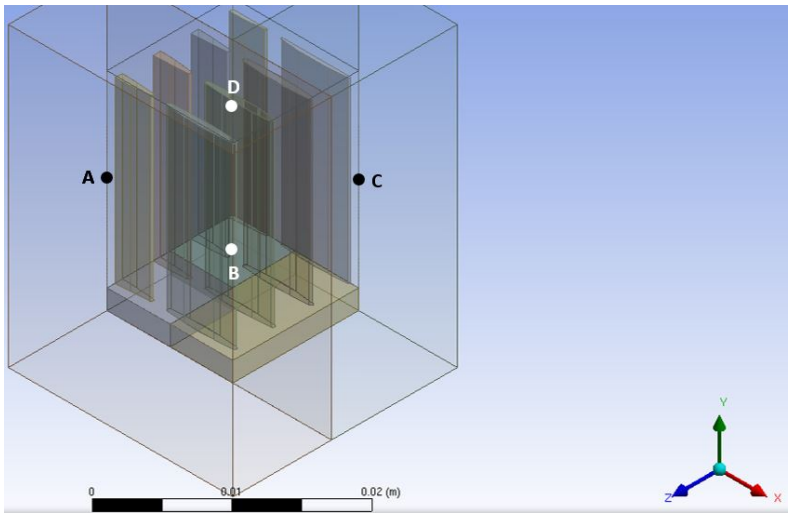

(a) Illustration of the simulated heat sink. The plane crossing point A, B, C and D at 10 mm of the fin heigth is plotted in subfigures (b) and (c). For subfigure (b), the gravity is parallel to the negative y-axis. For subfigure (c), the gravity is parallel to the negative x-axis. A quarter of the complete heat sink is simulated.

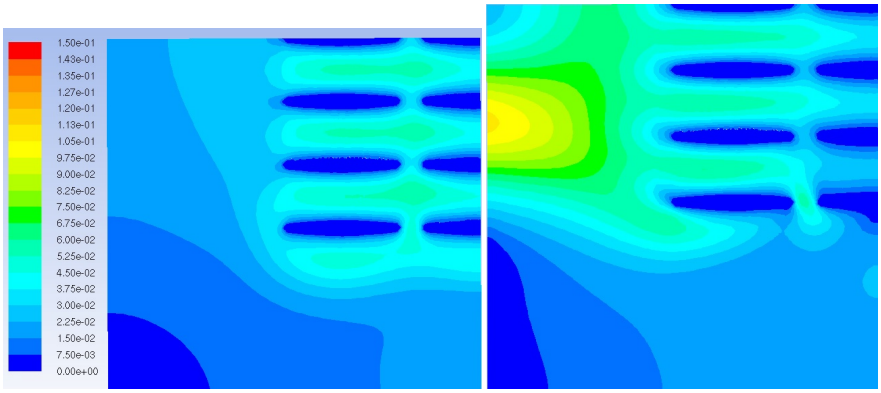

(b) horizontal orientation (ε = 85%) *(c) vertical orientation (ε = 85%)*

Figure 6.15: Velocity contour plots of the rectangular interrupted fin by Alpha heat sinks with heater covering complete substrate (see Figure 6.11). A cross section at 10 mm of the fin height is shown. Gravitional direction in each subfigure is pointed vertically from top to bottom.

6.7.1.3 In-lined pin fin by CoolInnovations (Fig. 6.10b)

The in-lined pin fin heat sink by CoolInnovation has a surface-to-volume ratio which lays between the staggered heat sink and the rectangular interrupted fin. Table 6.13 shows that $R_{T_{fluid}}$ indeed lays between the value for the rectangular

interrupted fin and the one for the staggered pin fin[13].

The fact that the in-lined pin fin is better in this case can be explained by the higher surface-to-volume ratio. However, this ratio still is a factor 2 lower compared to the rectangular interrupted fin design. However, as explained in Section 6.7.1.2, it is quite difficult for the flow to penetrate from the different sides which will limit the possibilities of this heat sink (despite the higher surface-to-volume ratio).

The radiative influence is more or less the same as for the denser rectangular interrupted fin (in terms of surface-to-volume ratio): 24.8% based on $R_{T_{fluid}}$. As discussed by Sparrow and Vemuri [81], the influence of the radiative heat transfer will decrease when the fins become more densely packed.

	ε = 0%	ε = 40%	ε = 85%
T_{fluid} in K	302.825	301.84	301.32
T_{solid} in K	334.06	328.95	326.33
R_{T_∞} in K/W	28.17	24.67	22.87
$R_{T_{fluid}}$ in K/W	21.50	18.68	17.23

Table 6.13: Thermal results for a horizontal in-lined circular pin fins from CoolInnovations with heater covering complete substrate ($25.4 \cdot 25.4mm^2$ and $Q = 2250W/m^2$)

As in the two previous sections, the vertical orientation is also tested. When comparing both orientations, for $R_{T_{fluid}}$ and $\varepsilon = 85\%$ e.g., the difference with R_{T_∞} is 18.7% and 22% . This comparison indicated a couple of things:

- Again, as was the case for the staggered heat sink, the difference between horizontal and vertical orientation depends on the definition of the thermal resistance (although the difference for both definitions is smaller here).
- Again, as was the case for the staggered heat sink, the impact of placing the heat sink vertically has a negative influence on the performance. Although CoolInnovations doesn't report a recommended orientation, the preferred orientation here is again horizontal.

[13]This shows that the surface-to-volume ratio is the most critical parameter for this heat sink. According to Zografos and Sunderland [76] the average heat transfer coefficient is higher for in-lined pin fins compared to staggered pin fins in natural convection for two heat sinks with an identical D/W-ratio (D stands for the fin diameter and W for the center-to-center spacing). Furthermore, the difference between both types of fins only becomes clear when the heat input increases. Even then the differences are moderate. For 100 W, for example, the heat transfer coefficient for the in-line pin fin is 9.3 W/m^2K, while for the staggered pin fin, it is 8.5 W/m^2K. Why in-lined pin fins perform better can be explained with similar experiments in forced convection. Soodphakdee et al. [190] explain that in-lined pin fins have a lower pressure drop, especially at low Reynolds numbers, when compared to the same setup but with a staggered lay out. This makes it easier for the fluid to penetrate into the heat sink, which is of importance in case of natural convection.

- The impact of the orientation is higher for the in-lined pin fin compared to the staggered pin fin. This result contradicts the results from Zografos and Sunderland [76], for example. These authors compared an in-lined and staggered pin fin and kept the D/W ratio fixed (which is not the case in our simulations, making a comparison even more difficult). For the in-lined heat sink, no influence of the inclination angle was obtained while for the staggered orientation effects up to 10%[14] were observed in heat transfer coefficient for a change in inclination angle of 30°. However, the authors don't give any reason for the disappearance of this difference.

  For our results, it is clear that the flow in the dense in-lined fin lay-out experiences more difficulties in penetration into the heat sink in case of the vertical orientation (see Fig. 6.17c). Comparing Fig. 6.17b with Fig. 6.17c shows that the middle pins in the vertical orientation are not able to cool down in comparison with the horizontal orientation. For the staggered pin finned heat sink even in vertical orientation there is still air flowing over the middle pin (see Fig. 6.16b and Fig. 6.16c). This result shows that the D/W ratio is more important than the difference between staggered or in-line.

- Compared to the horizontal orientation, the impact of radiation is also more pronounced. For the horizontal orientation, $R_{T_{fluid}}$ is decreased by 20% when going from ε = 0% to ε = 85%. While for the vertical orientation $R_{T_{fluid}}$ is decreased by 36.7%. This difference in the radiative heat transfer is much more modest in case of the staggered heat sink. Here, the relative difference in impact is only 5%-points.

	ε = 0%	ε = 40%	ε = 85%
T_{fluid} in K	307.28	305.99	303.98
T_{solid} in K	347.91	338.41	333.68
R_{T_∞} in K/W	37.72	31.18	27.92
$R_{T_{fluid}}$ in K/W	27.99	22.34	20.46

Table 6.14: Thermal results for a vertical in-lined circular pin fins from CoolInnovations with heater covering complete substrate ($25.4 \cdot 25.4mm^2$ and $Q = 2250W/m^2$)

[14] Which is in fact within the uncertainty levels. Please also note that this comparison can not be made with our two heat sinks, as the D/W ratio is not fixed

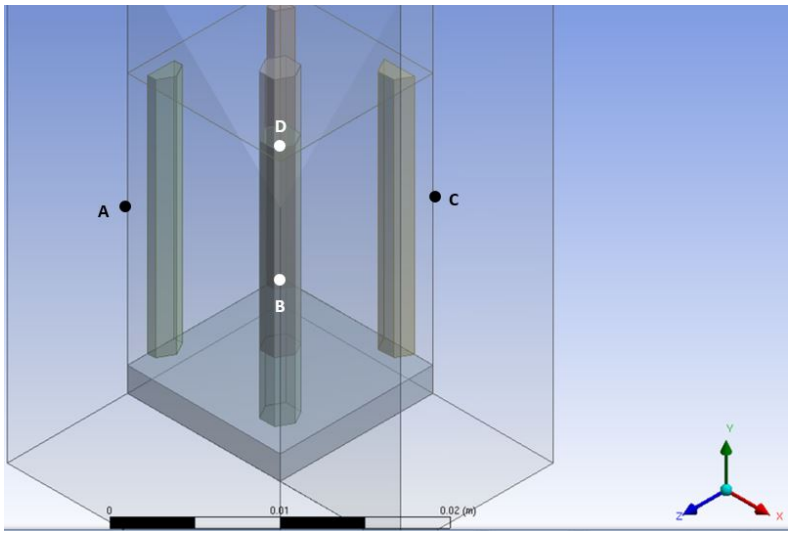

(a) Illustration of the simulated heat sink. The plane crossing point A, B, C and D at 10 mm of the fin heigth is plotted in subfigures (b) and (c). For subfigure (b), the gravity is parallel to the negative y-axis. For subfigure (c), the gravity is parallel to the z-axis. A quarter of the complete heat sink is simulated.

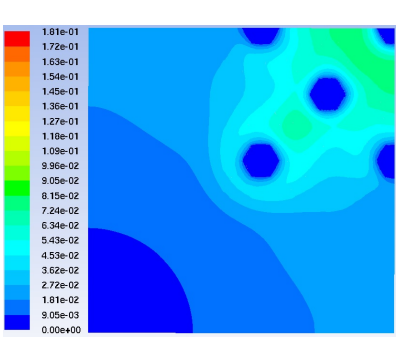

(b) horizontal orientation - staggered hexagonal pin fin (ε = 85%)

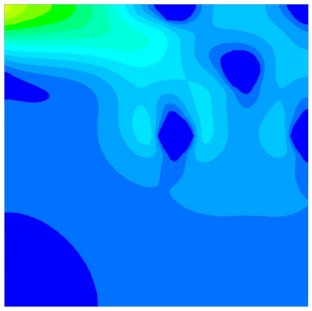

(c) vertical orientation - staggered hexagonal pin fin (ε = 85%)

Figure 6.16: Velocity contour plots of the staggered hexagonal pin fin from Alpha heat sinks.

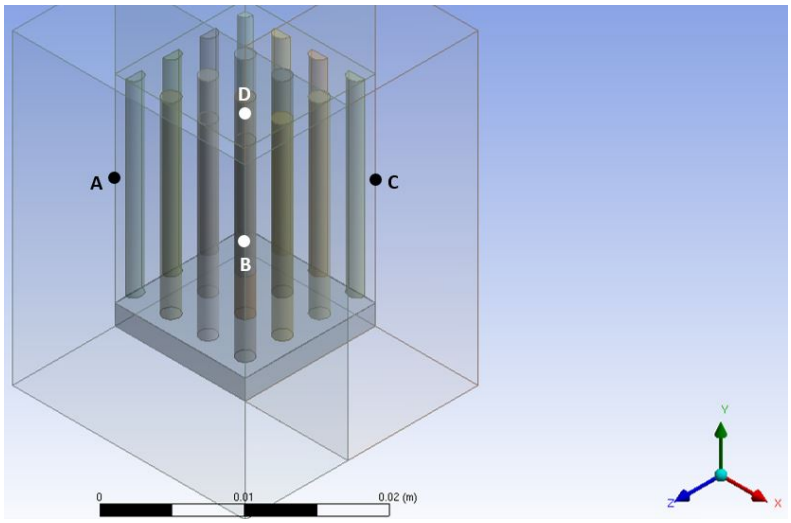

(a) Illustration of the simulated heat sink. The plane crossing point A, B, C and D at 10 mm of the fin heigth is plotted in subfigures (b) and (c). For subfigure (b), the gravity is parallel to the negative y-axis. For subfigure (c), the gravity is parallel to the negative x-axis. A quarter of the complete heat sink is simulated.

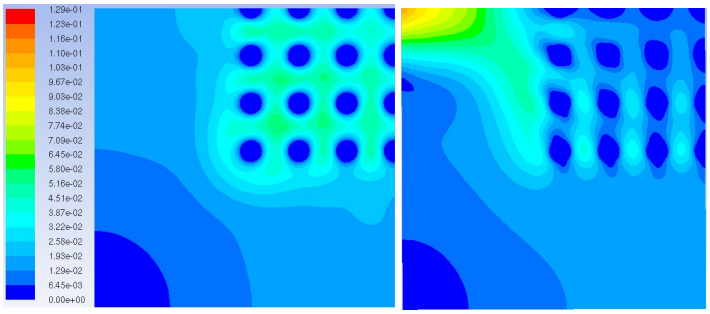

(b) horizontal orientation - in-lined pin fin (ε = 85%)

(c) vertical orientation - in-lined pin fin (ε = 85%)

Figure 6.17: Velocity contour plots of the in-lined pin finned heat sink from CoolInnovations (see Figure 6.10).

6.7.2 Comparing heat sinks based on the Q applied by manufacturer

As already mentioned in Section 6.7.1, the only manufacturer who tested their heat sinks in natural convection is Alpha heat sinks. For this reason the third heat sink by Coolinnovations will not be discussed in this Section.

In Table 6.15, the results which were measured by the manufacturer are given. As can be seen in this Table, the applied heat fluxes are much higher compared

to the ones in Section 6.7.1. The heat fluxes and the orientation in which the heat sinks are measured also vary over the discussed heat sinks. Furthermore, the heat flux itself is only applied to the middle of of heat sink itself. See Fig. 3.1, in Chapter 3, where an illustration of the test rig is shown for Alpha heat sinks.

heat sink	in-lined pin fin	rectangular interrupted fin
heat flux (in W/m^2)	21700	19530
power (in W)	3.5	3.15
orientation	*horizontal*	*vertical*
R (in K/W)	14.3	13.8

Table 6.15: Thermal results as measured by the manufacturer for different heat sinks by Alpha heat sinks.

Next to the results reported by the manufacturer, some aspects remain unknown because they were not reported:

- Radiative influences: are the heat sinks painted black before measuring them? On the website of Alpha heat sinks, the benefits of painting and/or anodizing are discussed. However, it is not mentioned if the tested heat sinks were painted. If the heat sinks are painted the emissivity will be around ε = 85%, see Appendix B.
- Determination of T_∞: how is the temperature at infinity determined? In the numerical simulations considered in this work, this is held fixed at 293.15 K. However, in a real environment this temperature will vary.
- Definition of thermal resistance: which temperatures are used to calculate the thermal resistance? How many thermocouples are used to measure T_{fluid} and T_{solid}?
- Use of insulation material. It is not specified how thick the insulating material is. Furthermore, no guard heaters are used. As discussed by Billiet et al. [16] this can lead to an extra uncertainty on Q of 15%.

6.7.2.1 Staggered pin fin from Alpha heat sinks (Fig. 6.10a)

In Table 6.16, the results for the circular staggered pin finned heat sink by Alpha heat sinks are given. As the heat flux is much higher (21 500 compared to 2 250 W/m^2), the thermal resistance will also be lower. This is also observed in Dogan et al. [46], amongst many others. $R_{T_{fluid}}$ is almost 15% lower for ε = 85%.

Higher heat fluxes also implies higher temperatures. T_{fluid} is increased by 6.5 K, while T_{solid} is increased by almost 57 K. This will increase the radiative

heat transfer rate, as this scales to the power of 4 with the temperatures. $R_{T_{fluid}}$ decreases with 33.2%, when comparing this resistance at ε = 0% and ε = 85%. This is almost 3% points higher compared to the case with Q = $2250 W/m^2$.

If it is assumed that the heat sink is painted black (ε = 85%), the difference with the reported data from the manufacturer is still 40%. As can be seen from Table 6.16, this large difference can be partially explained by the choice and measurement procedure to determine R. For ε = 85%, the difference between R_{T_∞} and $R_{T_{fluid}}$ is already 16.3%. The manufacturer also did not report where and with how many thermocouples the temperatures were measured. If T_{fluid} is measured with only one thermocouple in the hot air stream of the heat sink, for example, then the reported R from the manufacturer will be unusable. It is also a bit strange that the thermal resistance from the manufacturer is so low. One would expect a conservative value.

	ε = 0%	ε = 40%	ε = 85%
T_{fluid} in K	307.23	305.70	304.60
T_{solid} in K	401.13	385.45	375.23
R_{T_∞} in K/W	30.72	26.24	23.33
$R_{T_{fluid}}$ in K/W	26.70	22.66	20.05

Table 6.16: Thermal results for a horizontal equivalent circular pin fin by Alpha heat sinks with heater covering only a quarter of the substrate according to the testing procedure of the manufacturer ($12.7 \cdot 12.7 mm^2$ *and* Q = $21700 W/m^2$*).*

6.7.2.2 Rectangular interrupted fin from Alpha heat sinks (Fig. 6.11)

In Table 6.17, the results for the rectangular interrupted fin by Alpha heat sinks are given. The difference between both heat sinks, the pin finned and rectangular interrupted fin, although tested by the manufacturer in a different orientation is only 3.6%, while the surface-to-volume ratio differs by a factor 3. This seems strange.

In our numerical simulations, the difference between both heat sinks (the pin finned and rectangular interrupted fin from Alpha heat sinks) in case of ε = 85% and comparing $R_{T_{fluid}}$ is 46%. This is almost a factor two, as was the case in Section 6.7.1. Although the applied heat flux imposed by the manufacturer is 11% lower, T_{fluid} is higher compared to the staggered pin fin (307.23 K vs. 310.90 K, for ε = 0%). T_{solid} is much lower: 364.6 K vs. 401.13 K. All this results in a significant decrease in the thermal resistance.

	ε = 0%	ε = 40%	ε = 85%
T_{fluid} in K	310.90	308.99	307.91
T_{solid} in K	364.6	355.90	351.11
R_{T_∞} in K/W	22.68	19.92	18.40
$R_{T_{fluid}}$ in K/W	17.05	14.89	13.71

Table 6.17: Thermal results for a vertical rectangular interrupted fin by Alpha heat sinks with heater covering only a quarter of the substrate according to the testing procedure of the manufacturer ($12.7 \cdot 12.7mm^2$ *and* $Q = 19530W/m^2$*)*

It seems that the vertical measurement performed by the manufacturer is much more accurate (or is different compared to their horizontal setup), supposing that the results from the numerical simulations performed in this work are the most accurate ones. Although the author of this work has contacted the researchers from Alpha heat sinks in order to determine which test rig they had used. These researchers have send an illustration of the test rig (see Section 3.1.1.3), but have not corresponded if this test rig was used for both orientations. For this rectangular interrupted finned heat sink, the difference between the numerical and experimental results is only 0.6%. This is within the simulation uncertainty.

This shows how difficult it is to compare simulations with experiments: e.g. the exact setup of the test rig is not know, as well as the location where the temperature measurements are done, the box geometry, the used insulating material or the emissivity of the heat sinks material. Using the same conditions as reported by the manufacturer for the numerical simulations, the result differ compared to the results of the manufacturer. This can be caused by the different aspects that remain unknown: did the manufacturer paint the heat sinks black for each test, is the technique of measuring the fluid temperature (or environmental temperature) always the same, how was the experimental test rig constructed. Despite this, the Japanese manufacturer is not willing to share details about the determination of the reported thermal resistance on their website (despite numerous attempts).

6.8 Extra simulations based on the manufacturer's heat sinks

One of the open questions which still remains is: what is the effect of the flow resistance on the (thermal) performance of heat sinks in natural convection? This is also an important aspect related to metal foam heat sinks, which will be discussed in the next chapter, since metal foam has a high flow resistance.In all cases the mesh itself is created through a body mesh in the new meshing software of Ansys, explicitly looking to quality parameters like maximum aspect ratio and minimum orthogonal quality.

In this Section, some extra numerical simulations are performed based on the heat sinks from the different manufacturers, discussed previously. The geometry of these heat sinks is varied to show the effect of the flow resistance.

6.8.1 In-line vs staggered configuration

In this subsection, the staggered pin fin heat sink by Alpha heat sinks (Fig. 6.10a) is compared with an in-line lay out, see Figure 6.18.

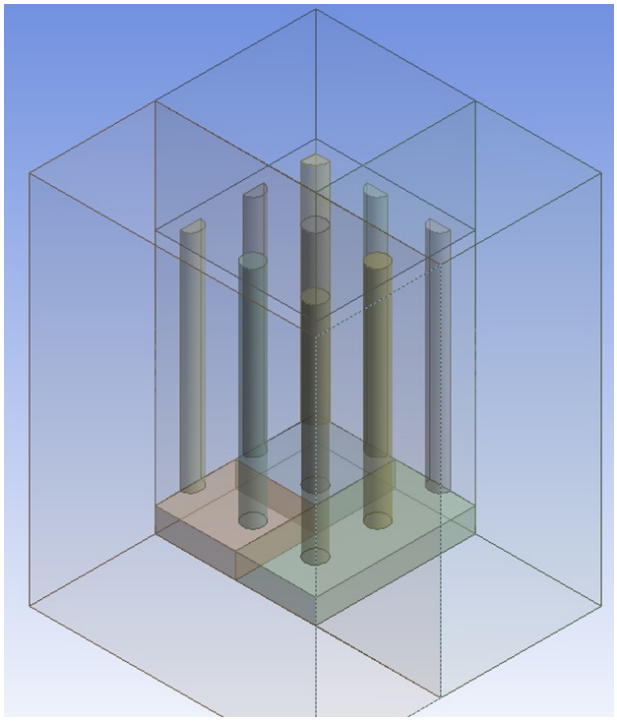

Figure 6.18: In-line variation on the staggered heat sink configuration of Alpha heat sinks (Fig. 6.10a), while holding the amount of solid material fixed d_{eq} = $1.633mm$. The gravitational force vector is vertically downwards in the plane of the figure. This is the standard tested orientation.

The in-line heat sink is a variation on the existing staggered pin fin geometry. Both heat sinks have the same amount of solid material[15]. Despite the identical amount of solid material, the heat transferring surface ($\pi \cdot d_{eq} \cdot L \cdot N_{tubes}$) is not the same for the two heat sinks. In fact, the heat sink as shown in Fig. 6.18 (in-line) has a heat transferring surface which is a factor 1.41 higher compared to the heat

[15]In case of the original hexagonal heat sink, the manufacturing technique will be the same, as the number of passes needed to make the heat sink will be the same.

sink in Fig. 6.10a (staggered). This implies that this in-line heat sink is expected to result in a higher heat transfer rate. However, the free flowing surface at the inlet of the heat sink is smaller in case of the in-line configuration. In other words, the flow resistance will be larger in the in-line configuration. This could lower the heat transfer coefficient. The question is, which of both parameters will have the strongest influence?

	$\varepsilon = 0\%$	$\varepsilon = 85\%$
T_{fluid} in K	300.93	299.80
T_{solid} in K	336.01	328.02
R_{T_∞} in K/W	29.52	24.02
$R_{T_{fluid}}$ in K/W	24.16	19.44

Table 6.18: Thermal results for the in-line variation of the staggered heat sink configuration of Alpha heat sinks (Fig. 6.18) ($25.4 \cdot 25.4mm^2$ and $Q = 2250W/m^2$)

Comparing Table 6.18 with Table 6.9, it is clear that the in-line heat sink (Fig. 6.18) performs 15.6% better for $R_{T_{fluid}}$ than the original staggered configuration ($\varepsilon = 85\%$). This is very similar to the results from Zografos and Sunderland [76], discussed in Section 6.7.1.3. Based on these results, it seems rather strange that Alpha heat sinks does not make these heat sinks with an in-line lay out.

6.8.2 Variations on the staggered heat sink by Alpha heat sinks (Fig. 6.10a)

Similar to the previous Subsection, some variations (see Figure 6.19) are made on the staggered heat sink configuration of Alpha heat sinks (Fig. 6.10a).

For the geometry in Figures 6.19a and 6.19b are generated starting from the geometry in Figure 6.10a and then doubling the amount of pin fins, again the amount of solid material is held fixed. In practice this implies that the diameter of the pins is reduced. The geometry in Figures 6.19c and 6.19d have the same number of pin fins as the geometry in Figure 6.19b. Yet the pins are arranged in a different way for each geometry. In Figure 6.19c, the pins are placed in the back of the heat sink. While for Figure 6.19d, the pins are placed in front.

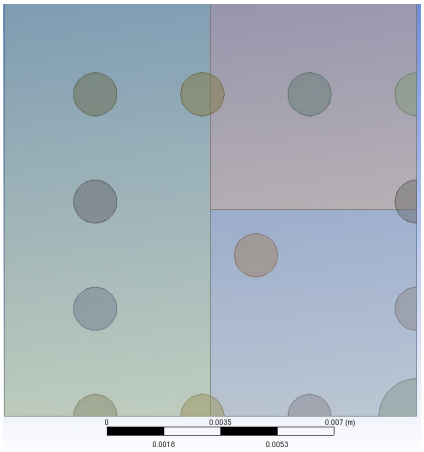

(a) Double the amount of pin fins at the side compared to Figure 6.10a, while holding amount of solid material fixed: d_{eq} = 1.334mm

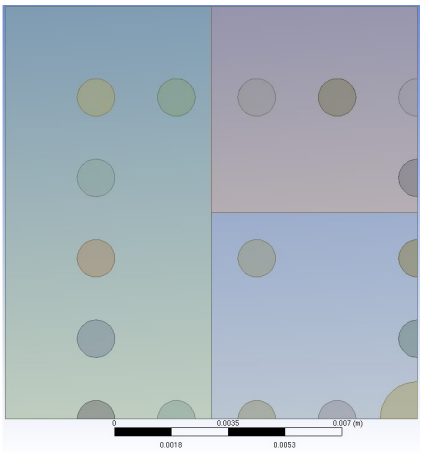

(b) Quadruple the amount of pin fins at the side compared to Figure 6.10a, while holding amount of solid material fixed:d_{eq} = 1.155mm

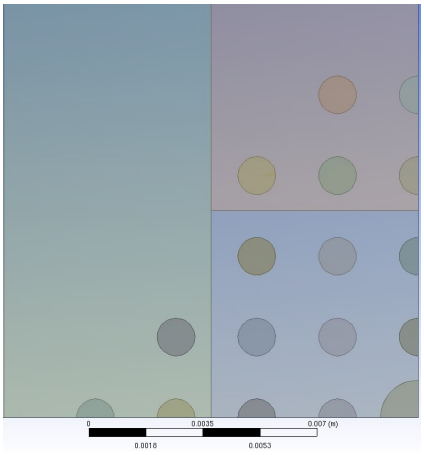

(c) Same amount of pin fins as in Figure 6.19b, but densely packed to the back of the heat sink

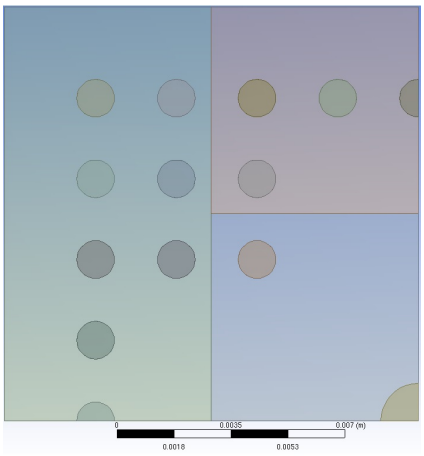

(d) Same amount of pin fins as in Figure 6.19b, but densely packed to front of the heat sink

Figure 6.19: Variations from the original geometry of the staggered pin fin heat sink (Section 6.4), while holding the amount of solid material fixed. The gravitational force vector is pointed perpendicularly in the plane of the subfigures. This is the standard tested orientation.

The geometry shown in Figure 6.20 is intended to mimic the obstructions in a metal foam heat sink. However, as is evident form this figure it is still very basic. Here the same number of vertical pins are used as in Figure 6.19a.

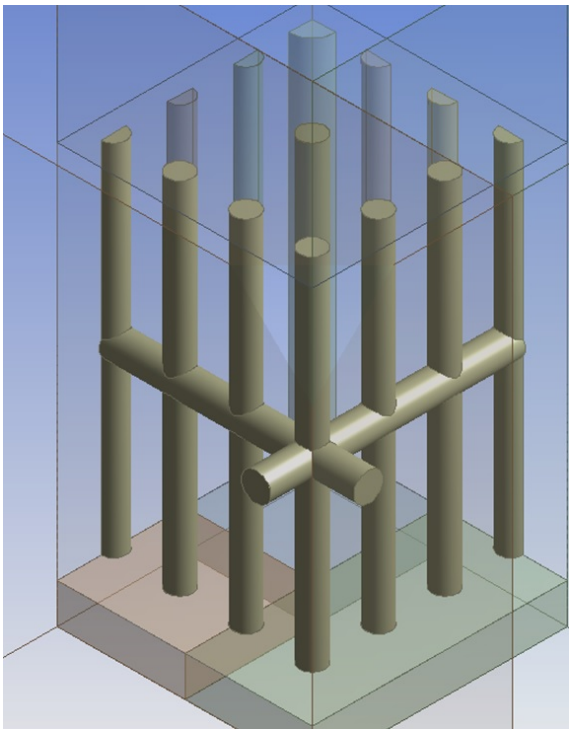

Figure 6.20: Variation from Figure 6.19a, adding horizontal bars. Holding the amount of solid material fixed: $d_{horizontal}$ = $1.45mm, d_{vertical}$ = $1.25mm$). The gravitational force vector is vertically downwards in the plane of the figure. This is the standard testing orientation.

The results for all of these variations are given in Table 6.19. To obtain these results, conjugated heat transfer is supposed, in which the conduction in the solid phase is also taken into account in order to determine the overall heat transferring performance.

Although the amount of solid material is the same, the heat transferring area A for Figures 6.19a and 6.19b is 1.73 and 2 times larger, respectively, compared to the original circular staggered pin fin by Alpha heat sinks. The results for $R_{T_{fluid}}$ are highly dependent on how the pin fins are arranged. As discussed earlier, the heat transfer rate is determined by a heat transfer coefficient h and the heat transfer area A. For the heat sink shown in Figure 6.19a, $R_{T_{fluid}}$ is decreased with 19%. This means that the thermal performance is dominated by the increase in heat transfer area for this case. However, for Figures 6.19b and 6.19d, the extra increase in heat transferring area A does not result in a substantial increase in thermal performance. This means that the increase in hydraulic resistance blocks the flow from penetrating into the heat sink. However, for the geometry in Figure

6.19c, the thermal resistance dramatically increases. This is because the incoming air is already heated (and rising) before impacting on the heat sink structure. This will limit the heat transfer coefficient and thus decrease the thermal resistance, although the heat transferring area is a factor 2 larger compared to the original heat sink by Alpha heat sinks.

For Figure 6.20 - which represents a simplified variation of open-cell metal foam - the heat transferring area A is a factor 1.89 higher compared to the original circular heat sink. This figure is based on Subfig. 6.19a. Yet, it has a heat transferring area which is almost 16%-points higher. Unfortunately, the $R_{T_{fluid}}$ is not significantly different compared to the results from Figure 6.19a. This again means that the increase in heat transferring surface area is undone by the increase in hydraulic resistance by placing horizontal bars in the middle of the pinned fins. This will have to be taken into account as in Chapter 7 open-cell foams will be studied numerically. In that Chapter, the reader will observe that the increase in hydraulic resistance will penalize the results for open-cell foam in natural convection.

Figure number	6.19a	6.19a	6.19b	6.19b	6.19c	6.19c	6.19d	6.19d	6.20	6.20
ε	0%	85%	0%	85%	0%	85%	0%	85%	0%	85%
T_{fluid} in K	301.44	300.25	302.04	300.68	303.14	300.89	302.33	300.86	301.61	300.38
T_{solid} in K	334.75	327.33	336.28	328.30	361.79	343.40	337.49	328.90	334.60	327.13
R_{T_∞} in K/W	28.66	23.55	29.71	24.22	47.29	34.61	30.55	24.63	28.56	23.41
$R_{T_{fluid}}$ in K/W	22.95	18.66	23.58	19.03	40.40	29.28	24.22	19.32	22.73	18.42

Table 6.19: Thermal results for the proposed variation from the original geometry of the staggered circular pin fin heat sink (Section 6.4), while holding the amount of solid material fixed.

6.9 Conclusion

In this chapter, the numerical simulations performed in this work on classical heat sinks are discussed. The main points and conclusions are summarized in this section.

First of all, the impact of the size of the selected fluid domain for calculation on the numerical results was studied. It was concluded that the impact of the fluid domain is dependent on the height of the fin. Globally (for a range of studied fin heights), the height of the fluid domain should be at least 1.3 times the fin height. These results on the minimum required size of the fluid domain are used to study commercially available classical heat sinks. It is shown that without any fluid domain the error is approximately 35%. However, this exact number depends on the fin that is studied: shape, fin height...

This research also shows the need of performing an uncertainty analysis on the numerical results. Based on this analysis it is shown that the uncertainty is very dependent on the numerical grid discretization. For the heat sinks studied in this work, and with the finest discretization used, the uncertainty can be lower than 2%. However, this uncertainty can rise to 7% when increasing the grid size with a factor 2. Thus, prior to the investigation an uncertainty analysis should be given. Please also take into account that this uncertainty analysis only accounts for uncertainties in grid discretization, errors resulting from the choice of fluid model, boundary conditions, cell shape etc.

Furthermore, some work is performed on commercial heat sinks to illustrate the effect of radiation and temperature determination. Some authors do not take radiation into account in numerical simulations. However, it is shown that the difference between taking radiation into account with a surface-to-surface model with an emissivity of 40% compared to neglecting radiation is up to 15% in thermal resistance. Furthermore, increasing the emissivity value of 40% to 80% leads to an additional difference of up to 10% in thermal resistance. Of course, this is again dependent on the fin structure (and the limited number of fin shapes studied in this work). There is also shown that the relative contribution of radiation is higher for lower temperature differences, this is because the convective heat transfer will increase more than the radiative heat transfer when the temperature differences increase (the radiative heat transfer will remain more or less the same). The effect of temperature in the determination of the thermal resistance is large. Most of the time, the base plate temperature can be determined unambiguously. However, the temperature of the surroundings is most of the time taken as a temperature at infinity (T_∞). Yet, in experimental circumstances this temperature is taken in the environment of the fin structure (T_{env}). It is not always mentioned which temperature is taken in numerical work[16]. This makes it even more difficult to

[16] Again, the author wants to stress that it is not easy to select a representative temperature. T_{fluid}

compare numerical results with experimental work. The differences between R_∞ and R_{env} can be up to 18%, again this is dependent on the fin structure (and the limited amount of fin structures that are tested in this work).

Next to prior results, some other conclusions can be taken. These might not be strictly related to the goals of this work, but are also noteworthy:

- A higher surface to volume ratio results in a higher flow resistance in natural convection, which makes it harder for the fluid to penetrate into the heat sink. Yet, the results from this chapter show that a higher surface to volume ratio does result in a better performing heat sink. However, the relative differences in surface to volume ratio do not result evenly in a performance difference. This is reflected by the difference in penetration resistance.

- The first heat sink studied is one produced by Alpha heat sinks, it has a staggered pinned finned structure. The pin fins were originally hexagonal. It is shown that for a same amount of aluminium material, circular pin fins perform the same. Hence, the choice between a circular or a hexagonal configuration can depend on which configuration is the easiest to manufacture.

- Another result seen in all simulations in this chapter is the large impact of the choice of T_{env} and the emissivity of the heat sink material. The simulations also show the impact of changing the orientation. As recommended by the manufacturers, the horizontal orientation performs better than the vertical one. The same holds for the in-lined pin fin. Going from horizontal to a vertical alignment limits the amount of flow that is able to penetrate into the heat sink itself. This difference in orientation is not present in case of rectangular interrupted heat sinks, at least this was not seen for the sample studied in this work. Here the impact of a vertical orientation is not negative. The plates obstruct the flow in both vertical and horizontal orientation. Hence it seems that the interruptions have a similar impact in both orientations and that this type of heat sink can also be used in vertical orientations. However, for a heat sink without interruptions the impact of the vertical orientation will be negative compared to a horizontal position.

- The third heat sink is in-lined pin finned of CoolInnovations, it has a moderate surface to volume ratio compared to the other two tested heat sink types. These heat sinks experience the largest impact of the orientation because of the more densely packed pin fins. This shows that the D/W ratio

as defined as a volume-average temperature, is not a proper choice, but also the temperature at infinity T_∞ is not always correct. For example: what to do in case of a heat sink in a very narrow box. What to select here as a T_{env}? The most correct and easiest way to define T_{env} is to use T_∞ because this is measurable experimentally and can be used to recalculate temperatures and fluxes from given thermal resistances.

(more densely packed) is more important than the influence of the lay-out of the pins (in-line or staggered).

- All tested heat sinks are commercially available. However, only Alpha heat sinks (staggered pin fins) reported the thermal resistance of their heat sinks. The difference between the manufacturer's data and the simulations for the staggered pin fin is almost 45% even when the results are based on an emissivity value of 85% and T_{env} = T_{fluid}. In comparison, the manufacturer data for the rectangular interrupted fin is exactly the same as our simulated data. This shows again how difficult it is to compare simulations with experiments. Certainly when the experiments and simulations are not done simultaneously.

- In the last section of this Chapter, the author tries to indicate that increasing the surface to volume ratio (positive impact on the thermal resistance) also increases the difficulty to penetrate into the heat sink (negative impact on thermal resistance). This work shows the difficulties of making correlations for heat sinks (pin finned or plain finned) and/or comparing with manufacturer data. All details about the experimental and/or numerical data needs to be known before one is able to compare the performance of different heat sinks.

In case of future work, it would also be interesting to study convective and radiative heat transfer apart from one another (although the combined effect is the parameter of interest in practical applications).

7 Numerical study on metal foam heat sinks

7.1 Introduction

In Chapter 4, Section 4.3, the approach to study open-cell metal foam is explained. The objective of this chapter is to simulate the experimentally measured 10 PPI metal foam heat sink (see Table 5.2), as presented in Section 5.3 and 5.4 of Chapter 5. The metal foam heat sink has a original height of 40 mm. Other foam heights (25 mm, 18 mm and 12 mm)[1] will also be simulated if possible.

Again all simulations performed in this chapter are done laminar. So the resulting Rayleigh numbers are always smaller than 10^8.

Two numerical techniques to study heat sinks will be used in this chapter:

- The VAT upscaling approach by which only the macroscopic scale will be solved. Averaging the conservation laws over a representative unit cell gives rise to closure terms (similar to turbulence modelling). As discussed in Section 4.4, many authors **use correlations to determine the closure terms**. A hybrid form of the VAT approach will be used in this work. The results of this are already published by De Schampheleire et al. [191]. In this hybrid method some closure terms are determined based on work already available in open literature, while other closure terms are determined through numerical correlations, as will be explained in the next Section.

[1] which were also measured experimentally as discussed in Chapter 5

As will be discussed, the radiative term will be calculated after the CFD calculations are done as it is not possible in Fluent to make a combined calculation of radiative, conductive and convective heat transfer when a so-called porous model is used [28].

Three-dimensional effects will also be discussed in this work (which were not included in paper of De Schampheleire et al. [191]). In this way, the results can be compared with the experimental work performed on open-cell metal foam heat sinks as presented in Chapter 5.

- **Directly solving** the steady state Navier Stokes equations on (a part of) **the application** with open-cell metal foam. In Section 4.3.2, a discussion was given on the cell counts for one PUC which was around 120 millions cells if one would like to simulate this through direct numerical simulations (DNS), which would completely resolve the flow. This would require too much computational power. Therefore as a first attempt, only *2 cells* of the 254 mm by 25.4 mm metal foam heat sink is simulated with a much coarser mesh that would be proposed for DNS. Furthermore, these two cells will be not the representation as discussed in De Jaeger [105], as this would again require too many cells due to the complex structure.

  A rectangular cell representation is rather used[2]. The results of this steady laminar calculation are given in Section 7.3. With this numerical approach, it is possible to calculate the radiative term simultaneously with the convective and conductive heat transfer.

Next to these results, the author also performed some work on *pure numerical simulations*, as discussed in Chapter 4 of this work. Inspired by the work of De Jaeger and Whitaker, the closure terms are determined as a function of the velocity. As a result, the permeability and the inertial coefficient are not a property of the material itself but are also influenced by the velocity. Furthermore, the author also studied the combined radiative-convective and convective heat transfer. Therefore, pure numerical simulations were made. The results of these simulations are presented in Appendix D, because this research is not completed yet. In this appendix it is also shown that in the VAT technique many assumptions are made.

7.2 VAT technique based on correlations

7.2.1 Determine the closure terms

In Chapter 4, Equations 4.21 to 4.24 illustrate the closure terms that appear after volume averaging the continuity, momentum and both energy equations. In this

[2]Not a cubic representation, as the foam itself due to the casting process is rectangular instead of cubic. See Chapter 2.

Section, these closure terms are determined based on correlations which can be found in open literature[3]:

- The **momentum dispersion** is described by the effective viscosity μ_e. Numerical and experimental studies have indicated that in the limit of $\phi \rightarrow 1$, effective and molecular viscosity should become equal [192] and that for a decreasing porosity, μ_e/μ increases. For highly porous media, a recent study of Nabovati and Amon [193] gave additional confirmation that the widely accepted model $\mu_e/\mu = 1/\phi$ is valid. In this work, the effective viscosity is based on this model.

- The **permeability κ and inertial coefficient** β for the momentum equation, are taken as *fixed* values. They do not vary as a function of the velocity, as in Section D.1 or as in the work of De Jaeger [105](Section 4.3.3.4).

  However, as discussed in Appendix C, there is a large scatter on the data which is reported for permeability and the inertial coefficient. One of the reasons for this is the geometrical characterization of open-cell foam (Section 6.2.1 and Ref. [194]). Therefore it is quite difficult to find correlations in open literature for both closure terms that are *trustworthy*. This is especially the case for the type of foam used in this work.

  Therefore, the permeability and inertial coefficients are determined based on the work of De Jaeger in this Section. In this work, they are assumed as a constant value as permeability is fixed for low ($Re_{d_s} < 1$) or high ($Re_{d_s} > 100$) velocities and the inertial coefficient remains fixed for high velocities ($Re_{d_s} > 1$) (see Appendix D and the PhD of De Jaeger). By using these values as a constant, this is a similar approach as in open literature where a constant value is derived from a correlation. Most of the time, the permeability and inertial coefficient are seen as a *material property*. For this simulation, the 10 PPI foam is used which is geometrically characterized in Table 5.2. The value for permeability and inertial coefficient, determined at $Re_{d_s} = 1$, is $1.65 \cdot 10^{-6} m^2$ and $105 m^{-1}$ (in the x-direction), respectively. The same is done for the y-direction. For the determination of these terms, the reader is referred to Section 4.3.3.2 of Chapter 4, Appendix D and Appendix C. In Appendix C the permeability and inertial coefficient are calculated according to the technique described in Chapter 4, including an uncertainty analysis on these properties.

- The **effective fluid thermal conductivity** $k_{f,e}$ can be expressed as a sum of the thermal dispersion k_d and the fluid conductivity k_f [195]. In buoyancy-driven convection, the dispersion term is negligible [157]. In its

[3]Except for the permeability κ and inertial coefficient β, where a *hybrid* solution will be used.

turn, the fluid conductivity is function of the tortuosity of the foam. The tortuosity is an estimate of the ratio of the chord length between two points in the fluid (or solid) phase and the effective pathway. Brun [107] reported a value of 0.98 for the fluid tortuosity for Nickel and ERG aluminium Duocel foams. As ERG foams strongly resemble the foams used in this work, the expression for the effective fluid conductivity now reads: $k_{f,e} = 0.98 \cdot \phi k_f$.

- The effective **solid thermal conductivity** $k_{s,e}$ is determined by solving the continuum-scaled heat conduction in the solid phase of a PUC, as was done by De Jaeger [196] (see Section 4.3.3.4). Based on this work, $k_{s,e}$ is taken equal to 5.4 W/mK for the flow direction (horizontal in this case) and 6.5 W/mK for the other foam direction (vertical) for the studied 10 PPI foam. These values are given in as a tensor in Ansys/Fluent The obtained value matches with the experimental results published by Schmierer and Razini [149] in vacuum conditions for aluminium foams with porosities ranging from 88.6% to 96.2%.

- Finally, the **interstitial heat transfer coefficient** h_{fs} is determined with a correlation for natural convection around a heated horizontal cylinder. So a thermal non-equilibrium model is supposed as explained in the previous literature chapter. The correlation is recommended by Raithby and Hollands [29]. This heat transfer coefficient is dependent on the fluid and solid temperature, cfr. the material and fluid properties used. The correlation is a function of the Rayleigh number and uses an average strut diameter as the characteristic length. In this work $\frac{4 \cdot (1-\phi)}{\sigma_0}$ is used as average strut diameter, taking into account the thicker nodes at the end of the strut.

A sensitivity analysis will also be performed on these parameters.

7.2.2 Implementation of the geometric model

The geometry implemented for the numerical simulations is shown in Figure 7.1 and replicates the experimental test rig shown in Figure 5.1 as well as possible. Due to the large length-to-width ratio of the tested heat sinks (10/1), a two-dimensional numerical approach is justified. The dashed area in Figure 7.1 delineates the fluid domain, while the domain indicated with MF (metal foam) is the porous zone.

Below the porous zone, an aluminium substrate with a thickness of 4 mm is modelled, together with a copper plate with a total thickness of 5 mm. Underneath the copper plate, a 1.5 mm thick layer of thermal paste is added. This single layer accounts for the contributions of the different layers of thermal paste used in the experiments. For the sake of simplicity the copper plates attached to the guard heaters and the physical thickness of the main and guard heaters are neglected in

the simulated geometry. The main and guard heaters are indicated with a green line in Figure 7.1. The thermal conductivity of AL1050, copper, the thermal paste and the insulation material is taken 220 W/mK, 387.6 W/mK, 0.8 W/mK and 0.023 W/mK, respectively [197].

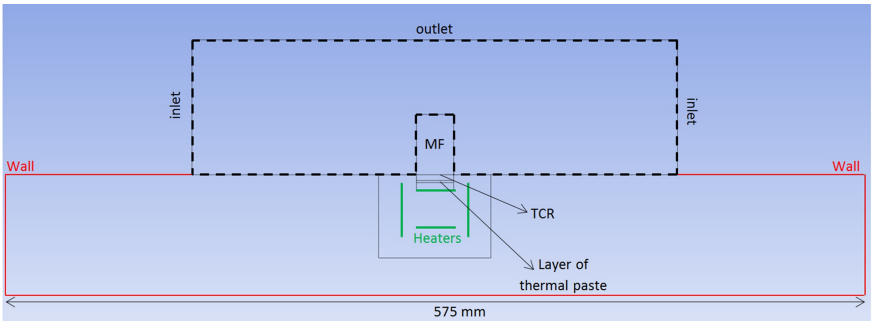

Figure 7.1: Illustration of the implementation of the experimental test rig for the numerical study. The gravitational force vector is vertically downwards in the plane of the figure.

# C.V. per mm	1	2	4	8
$Q_{conv,\,num}$ in W	20.43	20.633	20.632	20.627
Δ with *ref* in %	0.98	*ref*	0.007	0.03

Table 7.1: Mesh dependence test of numerical results for the highest foam sample (40 mm) and the highest temperature difference (ΔT = 70.6°C) tested. The reference case (ref) has 2 C.V. per mm.

To limit the number of fluid cells in the computational domain, only 150 mm of fluid domain on the left and right of the metal foam is considered. The height of the fluid domain is always 2.25 times the foam height. This is slightly different than the guideline from Chapter 6 where a factor of 2.3 was recommended, this because it is easier using integer number of the extra height of the fluid domain. So for a foam height of 40 mm, the total fluid height is 90 mm. The fluid and solid geometry is discretized with 2 control volumes per mm. However, some parts of the solid geometry, the solid parts located 30 mm from the guard heaters, are meshed triangular with the growth rate of 1.1. This growth rate was used to limit the number of grid cells. Other finer meshes are tested as well as other heights and widths for the fluid domain, with no significant differences for either the flow or energy fields. The influence of the mesh discretization is illustrated

in Table 7.1. This influence is tested for the highest foam sample and the highest temperature difference. It is clear that, compared to the reference case, there is no real difference between the total number of grid cells when comparing the heat transfer rate.

For the open boundaries where the air enters the simulated domain, the ambient pressure was used as a stagnation boundary condition with the incoming fluid having the temperature of the environment T_{env}. The static pressure was assumed to be equal to the pressure of the surrounding atmosphere where the air leaves the simulated domain. The temperature of the main heater and guard heaters were fixed at T_s. The temperature of the outer insulation is fixed at T_{env}. The heat transfer rate Q is calculated and compared to the experimental results.

Also the thermal contact resistance (TCR) between the metal foam and the substrate is taken into account. The TCR causes a temperature jump at the interface between the substrate and the foam. This interface is indicated in Figure 7.1. De Jaeger et al. [54] studied four different bonding techniques (pressed-fit, epoxy glue, co-casting and brazing) to connect the foam to the substrate and determined the respective thermal contact resistance. In the validation experiment used in this work, the foam is brazed to the substrate. For a brazed contact, De Jaeger et al. [54] reported a TCR of $0.7 \cdot 10^{-3} m^2 K/W$. The TCR between the substrate and respectively the solid and fluid phase is implemented in the numerical simulation.

The pressure correction is obtained through the SIMPLE algorithm, since steady-state calculations are performed. The COUPLED algorithm is tested, however with bad results when the VAT is used. The convective terms are discretized through a second order upwind scheme, while diffusion terms are second order accurate central differenced. The spatial discretization of the pressure term is body forced weighted. The density is calculated according to the incompressible ideal gas law. As no Boussinesq model is used, the operating density at the environment temperature has to be specified. This density is extracted from the REFPROP-database by the National Institute of Standards and Technology [198]. The macroscopic equations (Eqs. 4.21 to 4.24) are solved in the regions of the computational domain indicated as porous medium: MF in Fig. 7.1. For the porous zone, each cell holds information for both the fluid and the solid domain of the foam. In the other fluid regions, the microscopic transport equations are solved. The conservation equations in the fluid part, both for the porous zone as well as for the outer fluid region, are solved *simultaneously* as one field. The coupling between the solid and fluid phase energy transfer is achieved by computing the interstitial heat transfer rate at the fictional air/foam interface and the solid and fluid phase temperature from previous iteration.

Iterative convergence is verified by noting that the residuals drop below 10^{-11} for continuity and below 10^{-12} for velocity and energy fields, within 75 000 iterations and less than 2 hours of computing time per set point (12 dual hex core

Xeon X5690 3.46Ghz processors on board memory: 96 GB DDR3-1333 MHz RAM). Approximately 150 000 cells were needed for the 2D mesh. This shows the strength of VAT modelling. The resulting energy balance closes within 0.2%.

7.2.3 Macroscopic model implementation in Ansys-Fluent

Once the closure terms are determined, they can be used in the macroscopic model. This implementation is again done in Ansys-Fluent. Version 15 is used. In this version, it is possible to use the thermal non-equilibrium model: hence the metal foam is simulated with a fluid zone and a solid zone [4]. For this Ansys-Fluent uses a so-called Dual Cell method which consists of two porous fluid zones which are solved simultaneously and are coupled only through heat transfer and a predefined heat transfer coefficient h_{fs}. Ansys-Fluent creates an extra zone on top of the porous zone to simulate the solid material of the metal foam. Although this model seems very attractive to use, the limitation is that the solid zone is not able to exchange energy with the surrounding fluid domain. It can only transfer energy with the fluid domain to which it is connected in the Dual Cell method. This limits the accuracy of the model. Therefore, the author prefers not to work with this predefined non-equilibrium model to simulate the solid domain of the foam. Hence concerning the pre-programmed energy transport equation in the porous zone, the commercial solver will assume local thermal equilibrium.

However, the porosity is set to 1, which will cancel the solid phase contribution to the pre-programmed equation. This ensures that the standard energy equations covers the energy transport in the fluid phase. For the solid phase energy transfer, an additional transport equation is needed. This can be achieved through a so-called User Defined Scalar (UDS). This scalar will represent the solid domain of the foam and since the solid phase is considered only conductive heat transfer needs to be covered.

The implemented model is illustrated in Figure 7.2 and uses User Defined Functions (UDFs). First of all, the geometry and the boundary conditions whether or not defined through UDFs are loaded. Then, the interstitial heat transfer coefficient, h_{fs}, is calculated based on the average solid and fluid temperature of the porous material (or some default values in case of the first iteration). This value is saved in a User Defined Memory (UDM). With this input, Ansys-Fluent is able to calculate the momentum in the x-, y- and z-direction,the mass continuity equation and the energy equation in the fluid domain (both the porous zone and the surrounding fluid zones).

[4] In case of the thermal equilibrium model h_{fs} is supposed infinitely large.

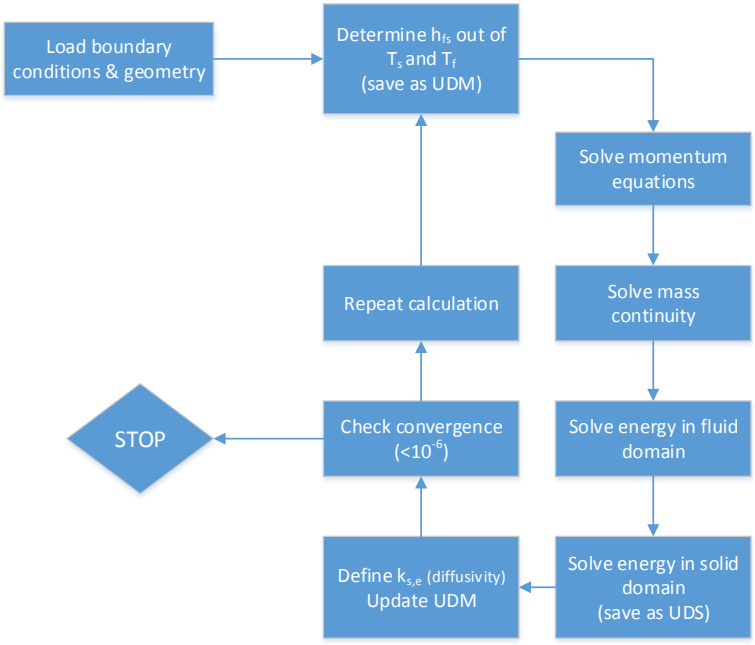

Figure 7.2: Sequence of solving the equations in Ansys-Fluent.

Next, the solid energy equation for the porous zone is solved. This is saved as a UDS value and represents the solid temperature of the foam. With this input the effective solid conductivity $k_{s,e}$ is loaded as UDS and the interstitial heat transfer coefficient h_{fs} (saved as UDM value) is updated. $k_{s,e}$ has to be entered as a diffusivity value in the porous zone and is zero elsewhere. Then the convergence for continuity, momentum, energy and UDS is checked and if these values are not lower than 10^{-6}, another iteration is performed.

7.2.4 Results, discussion and sensitivity analysis

7.2.4.1 Numerical convective results

The numerical results for all tested foam heights are summarized in Table 7.2. The 2-D numerical results in Watt per meter are rescaled for the 254 mm-long heat sink. For all foam heights, the heat transfer rate predicted by the numerical model is lower than the experimentally obtained value.

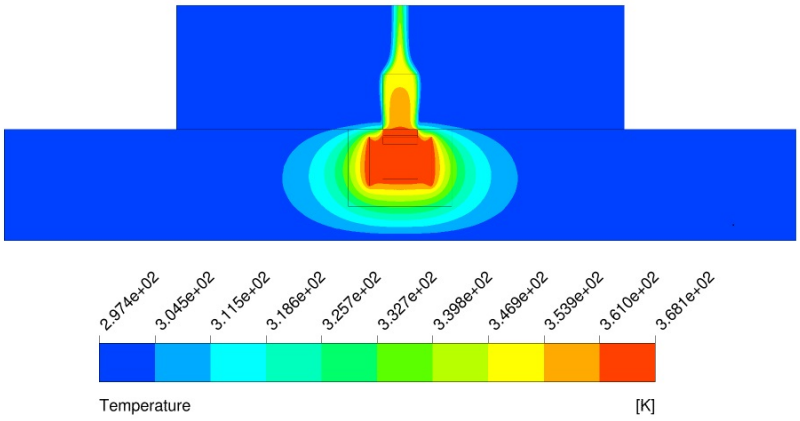

Figure 7.3: Temperature contours for a 40 mm foam heat sink and the fluid phase in the porous zone (ΔT = 70.6K). The gravitational force vector is vertically downwards in the plane of the figure.

The relative difference between the experimental and numerical results is on average 20% and does not depend much on the foam height. It will be shown in Section 7.2.4.2 that this underprediction is largely due to the neglected effect of external radiation.

Figure 7.3 shows the fluid temperature of the foam together with the temperatures of the insulating material for the highest foam sample tested, i.e. 40 mm. The simulations are performed for convective heat transfer only. It is clear that the guard heaters are working as expected (no temperature difference between the guard heaters and the main heater) and the main heater is sending a one dimensional flux to the foam substrate. Due to the large length-to-width ratio, a single chimney type flow pattern is observed. Figure 7.4 displays the velocity contours around the foam material. Due to the low permeability of the foam and high inertial coefficient, it is quite difficult for the surrounding air to penetrate into the foam. Phanikumar and Mahajan [141] observed a similar behaviour. Therefore, the fluid and solid temperature in the foam material is high as only at the foam boundaries some air is able to penetrate into the foam. Only at these boundaries the foam is cooled slightly. The solid temperature of the foam is displayed in Figure 7.5. The decrease of the solid temperature over the foam domain is not very large. This implies that the fin efficiency, also called foam efficiency, is quite high. This is expected for buoyancy driven flow [199]. For this 40 mm foam sample and the highest investigated temperature difference, the temperature decrease from bottom to top of the solid foam matrix is smaller than 13 K.

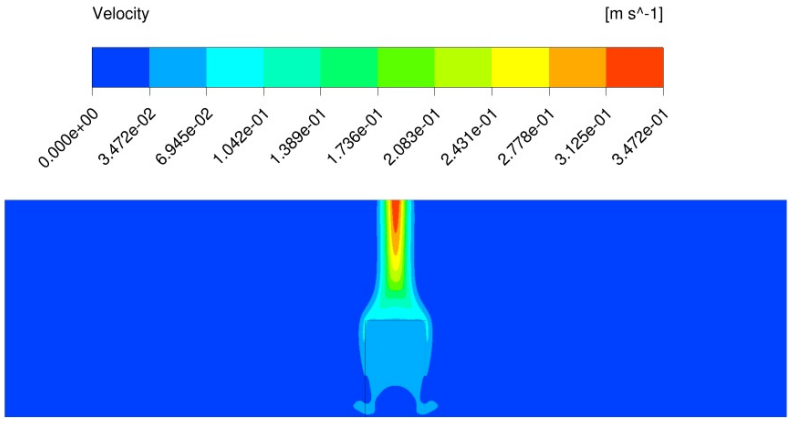

Figure 7.4: Velocity contours for a 40 mm foam heat sink (ΔT = 70.6K). The gravitational force vector is vertically downwards in the plane of the figure.

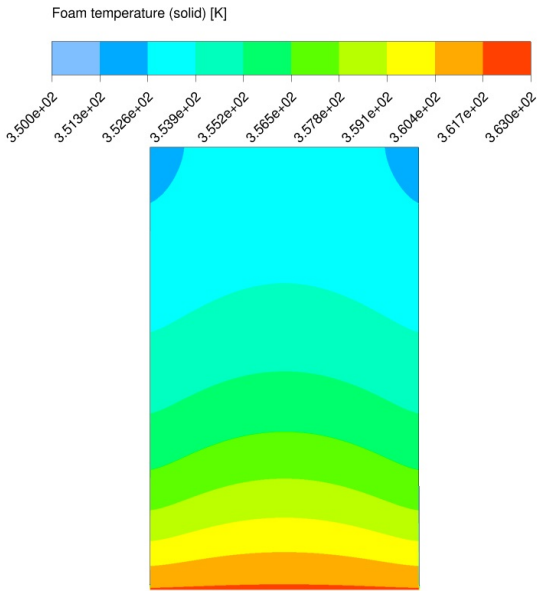

Figure 7.5: Solid temperature contours for a 40 mm foam heat sink (ΔT = 70.6K)

As can be seen in Figure 7.5, the highest local convection coefficients are at the two top ends (left and right top end). There the lowest foam temperatures are observed. Above the heat sink, a hot air plume is observed. In that plume, the maximum velocity is observed. Yet, the average velocity in the foam domain for the highest foam sample and the highest temperature difference tested is 0.04 m/s.

foam height	$\Delta T[^\circ C]$	$Q_{exp}[W]$	$Q_{conv,num}[W]$	$\lvert 1-\frac{Q_{conv}}{Q_{exp}}\rvert$	$Q_{conv+rad,num}[W]$	$\lvert 1-\frac{Q_{conv+rad,num}}{Q_{exp}}\rvert$
40 mm	33.2	10.10	7.36	0.27	10.40	0.030
	37.4	11.76	8.66	0.26	12.11	0.030
	41.8	13.58	10.15	0.25	14.05	0.035
	46.2	15.40	11.57	0.25	15.95	0.036
	50.6	17.42	13.16	0.24	18.05	0.037
	55.4	19.47	14.79	0.24	20.21	0.038
	59.7	21.39	16.34	0.23	22.29	0.042
	66.1	24.33	18.87	0.22	25.47	0.047
	70.6	26.34	20.63	0.22	27.80	0.056
25.4 mm	36.6	9.6	7.65	0.20	10.19	0.061
	43.3	12.07	9.69	0.2	12.79	0.059
	50.2	14.7	11.95	0.19	15.62	0.063
	56.9	17.33	14.16	0.18	18.45	0.064
	63.6	20.00	16.54	0.1	21.46	0.073
18 mm	36.8	8.21	6.62	0.19	8.73	0.063
	41.3	9.68	7.85	0.19	10.26	0.06
	43.5	10.38	8.45	0.19	11.02	0.062
	45.8	11.09	9.07	0.18	11.80	0.064
	50.4	12.60	10.40	0.17	12.51	0.007
	55.0	14.15	11.76	0.17	15.15	0.071
	57.2	14.92	12.43	0.17	16.00	0.072
	59.5	15.71	13.13	0.16	16.88	0.074
	64.1	17.31	14.65	0.15	18.76	0.084
	68.7	18.97	16.16	0.18	20.65	0.089
12 mm	37.5	7.28	5.14	0.29	6.94	0.048
	42.1	8.52	6.09	0.28	8.13	0.045
	46.6	9.69	7.03	0.27	9.33	0.036
	51.2	11.00	8.09	0.26	10.67	0.029
	55.8	12.30	9.10	0.26	11.98	0.026
	60.3	13.63	10.16	0.26	11.98	0.022
	64.9	15.00	11.27	0.25	14.75	0.016

Table 7.2: Comparison with the experimental results for different foam heights ('10 PPI' foam with brazed contact technology)

7.2.4.2 Influence of radiation

One of the most important assumptions made in the simulation results shown in the previous section is that the effect of radiation is neglected, as in Refs. [141] and [170]. To determine whether this assumption is acceptable, the effect of external radiation is estimated through the simplified Stefan-Boltzmann law ($Q_{rad} = \varepsilon\sigma A(T_{hot}^4 - T_{env}^4)$)[5].

In this equation, the view factors to the surroundings are neglected. Furthermore, ε is the emissivity of the foam material, A is the external surface area exposed to the surroundings, T_{env} is the temperature of the surroundings and T_{hot} is the temperature of the foam at the surface of the foam exposed to the surroundings. This T_{hot} is calculated for each set point as an average temperature over the surface.

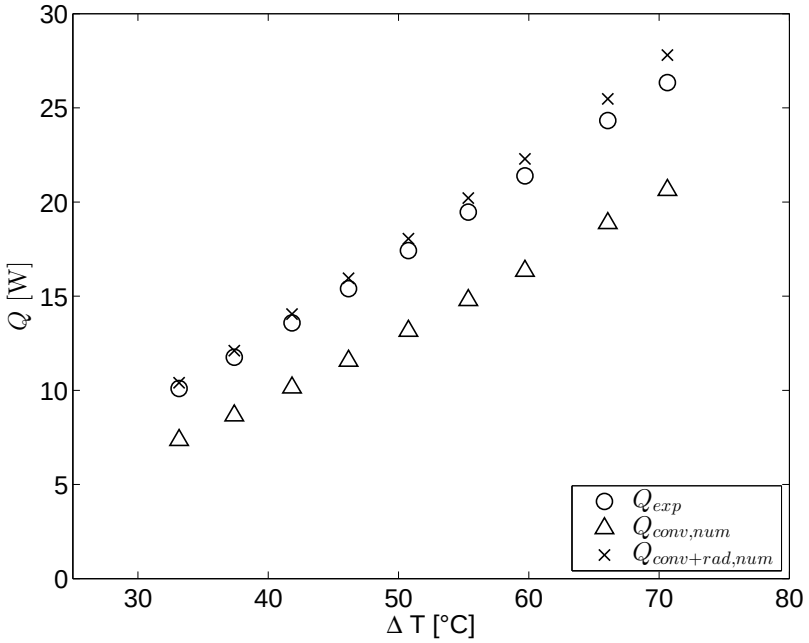

Figure 7.6: Influence of radiation for the highest foam simulated (40 mm) and comparison with experimental results.

The emissivity depends on the surface finish of the foam (grey, white or shiny),

[5]This is a first approach. With the introduction of radiation, there will also be a temperature drop in the solid phase of the foam. This will thermohydraulicly influence the convective heat transfer as it will lead to a drop in solid temperature and thus a drop in heat transfer coefficient. The Stefan-Boltzmann law ($Q_{rad} = \varepsilon\sigma A(T_{hot}^4 - T_{env}^4)$) also supposes heat transfer from a hot body to a cold body. However, in reality this is not the case, so the radiative heat transfer rate will certainly be overestimated.

as well as on the geometrical characteristics. An emissivity value of 55% is used in this work [200] [6]. The resulting Q_{rad} yields an indication of the influence of external radiation for these heat sinks. The results are reported in Table 7.2. Generally, the simulations now slightly over-predict the experimental data. The influence of radiation is the highest for the largest foam height, up to 30% of the total heat transfer rate. This is well within the expected range of 25-40% [81]. The trends also show a decrease of the relative influence of radiation to the experimental values when the temperature difference increases. The same trends were observed by Sparrow and Vemuri [81]. These results clearly show that for buoyancy driven convection in open-cell metal foam the radiative share in the total heat transfer cannot be neglected.

In Figure 7.6, the influence of the radiative heat transfer is shown graphically for the largest foam height which was simulated. Three heat transfer rates were reported: the experimental Q_{exp}, the purely convective $Q_{conv,num}$ and the combined convection/radiation $Q_{conv+rad,num}$. For the foam sample with the largest height, the differences between the combined heat transfer rate and the experimental one are very small: lower than 5% for each simulated temperature difference. For the other foam heights, the difference between Q_{exp} and $Q_{conv+rad,num}$ stays below 9%. From Figure 7.6, it can be seen that the numerical results for pure convection show a similar trend when compared to the experimental results.

7.2.4.3 Sensitivity analysis

A sensitivity analysis is performed to assess the influence of the different closure term models, the selection of the effective properties and some other details linked to the experimental test rig and the foam heat sinks. The sensitivity of ten parameters is studied. For the closure terms, the permeability κ, the inertial coefficient β and the interstitial heat transfer coefficient h_{fs} are investigated. For the effective properties, the effective solid and fluid conductivity $k_{s,e}$ and $k_{f,e}$ are varied. Considering the test rig, the substrate temperature T_s, the temperature of the environment T_{env} and the value of the thermal conductivity of the thermal paste layer k_{paste} are selected for investigation. Finally, for the foam samples, the width and height of the heat sink are studied in this sensitivity analysis. The analysis is performed for the highest (40 mm) and lowest (12 mm) foam height studied. For both heights, the lowest and highest temperature differences are tested. The following steps are undertaken consecutively for this sensitivity:

1. Calculate the numerical case as is.

[6] This is a slight underestimation of the value reported in Appendix B. Of course, there are also uncertainties on the values reported in Appendix B. 55% is taken here as reported in Ref. [200].

2. Request the local values for $k_{f,e}$ and h_{fs} in each foam cell and calculate the average value over the foam domain.

3. Make a new model where $k_{f,e}$ and h_{fs} are constant over the entire foam domain and equal to the average values determined in the previous step and recalculate the heat transfer rate from the model.

4. For each of the four cases, ten parameters (one at a time) are varied and the resulting heat transfer rate is compared with the result from Step 3.

Based on the results of Step 4, a sensitivity parameter is calculated according to Eq. 7.1 for each parameter and each of the four cases, assuming a linear approximation suffices. In fact, the aim is to calculate the partial derivative of heat flux with respect to the ten parameters by numerically approximating it. Hence, the parameter variation has to be limited. The higher the sensitivity parameter, the higher the impact on the results and the greater the attention which should be spent on a proper selection of these parameters, as is done in this work.

$$\vartheta = \left| \frac{\frac{Q_{new} - Q_{old}}{Q_{old}}}{\frac{\omega_{new} - \omega_{old}}{\omega_{old}}} \right| \tag{7.1}$$

In Equation 7.1, ω represents the different parameters. In this way, the heat transfer rate, by varying the different parameters, is scaled linearly. Most of the parameters are varied by only 1%: κ, β, $k_{s,e}$, $k_{f,e}$, k_{paste} and h_{fs}. The substrate temperature and temperature of the environment is varied with 1 K. Since the difference between these two temperatures is considered, similar results are expected for both temperatures. An exception on this are the fluid properties and the operating density, which will be affected in a different way by these temperatures. The width of the heat sink is varied with 1 mm (4% variation), while the height is increased with 1 mm for the foam heat sink with the largest height (2.5% variation) and only 0.5 mm for the 12 mm high foam (4% variation). The results for the sensitivity parameter are reported in Table 7.3. Next to each value of the sensistivity parameter the relative importance is shown between brackets for each case (1 stands for the most important and 10 is the least important) in Table 7.3.

These results show that the temperature of the substrate and the environment are very important parameters: they have the highest influence on the heat transfer rate, independent of the foam height. However, the uniformity of the copper plates and the substrate are vital for a proper determination of T_s. The same holds for T_{env}, which has to be determined at several locations around the heat sink, as performed in this work. For example, in case of the 40 mm high foam and a temperature difference of 70.6 K, the uncertainty on the temperature is already of 1.2 K. This is already quite a significant uncertainty considering that a 1 K

temperature increase of the substrate leads to a relative increase in heat transfer rate of up to 4%. Furthermore, as mentioned in Chapter 3, not all authors in open literature perform experiments with great care, this could lead to even higher uncertainties.

ϑ	40 mm foam ΔT = 33.2K	40 mm foam ΔT = 70.6K	12 mm foam ΔT = 37.5K	12 mm foam ΔT = 64.9K
κ	0.120 (6)	0.122 (7)	0.137 (7)	0.133 (7)
β	0.197 (5)	0.204 (4)	0.217 (5)	0.218 (5)
k_{paste}	0.081 (9)	0.102 (8)	0.052 (8)	0.062 (8)
$k_{f,e}$	0.047 **(10)**	0.035 **(10)**	0.032 (9)	0.022 **(10)**
$k_{s,e}$	0.112 (7)	0.131 (6)	0.027 **(10)**	0.032 (9)
h_{fs}	0.103 (8)	0.097 (9)	0.180 (6)	0.185 (6)
foam height	0.242 (4)	0.174 (5)	0.786 (3)	0.783 (3)
foam width	0.764 (3)	0.827 (3)	0.501 (4)	0.521 (4)
T_s	1.318 (2)	1.257 (2)	1.372 (2)	1.318 (2)
T_{env}	1.463 **(1)**	1.575 **(1)**	1.527 **(1)**	1.652 **(1)**

Table 7.3: Sensitivity parameters for two cases (12 mm and 40 mm high foam) and two different temperature differences.

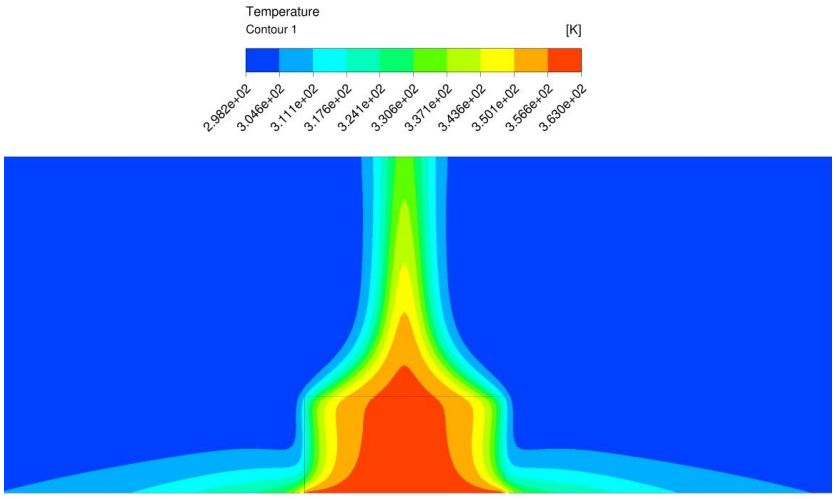

Figure 7.7: Temperature contours for a 12 mm foam heat sink and the fluid phase in the porous zone (ΔT = 64.9K). The gravitational force vector is vertically downwards in the plane of the figure.

In case of the highest foam sample, the foam width is more important compared to the height. For the lowest foam sample, it is the other way around and the foam height is more important. The reason for this is the same as why the influence of $k_{s,e}$ is much smaller for the lowest foam compared to the foam with the largest height. As can be seen from Figure 7.7, the solid and fluid temperature in the porous zone of a 12 mm-high heat sink is much higher compared to the 40 mm foam. As expected, the foam with smaller height has a higher foam efficiency. This explains why an increase in $k_{s,e}$ has less influence on the heat transfer rate. Furthermore, an increase in the height of the 12 mm-high foam, has a more severe impact compared to the 40 mm foam as the temperature at the boundaries of the porous domain are higher compared to the 40 mm foam.

For the other parameters, some changes in importance are observed when comparing the foam with the largest and smallest height. It is clear that the impact of the interstitial convection coefficient h_{fs} is small, as well as the impact of k_{paste} and $k_{f,e}$. The two momentum closure terms κ and β have a limited importance on the heat transfer rate. Hence, this indicates that for accurate modelling of buoyancy driven heat transfer with open-cell aluminium foams, research should not be focussed on convection coefficient correlations.

Finally, a small remark, the sensitivity on the different parameters can not explain the different between the numerical simulations and the measurements. This has been tested by performing the simulation with some variations in heat sink dimension, for example.

7.2.4.4 Three-dimensional effects

Next to radiation, the three-dimensional effects are not studied by authors working on VAT modelling in metal foam [141, 167, 170]. In this Section, these effects are studied separately for all foam heights considered in this work. For this study, the determination of the closure terms and the implementation of the geometric model are done the same way as explained in the previous Sections (7.2.1 and 7.2.2). The only difference is that the geometrical model is three-dimensional. The geometry, as shown in Fig. 7.1, is extruded in Ansys-Designmodeller. However, only one quarter of the heat sink is simulated. This because of the limited computational power that is available: the mesh for one quarter of the 40 mm high foam counts more than 17 million elements.

The results for the studied foam heights (40 mm, 25.4 mm, 18 mm and 12 mm) are reported in Table 7.4. Only the highest and lowest temperature difference is tested, just to show the influence of the three-dimensional effects. For all foam heights over 18 mm, the 3-D effects are quite limited. These effects are positive and vary between +3.6% and +5.2% compared to the 2-D case. The results for the 40 mm-high foam is also comparable to the 2-D results: a single chimney effect is observed (see Fig. 7.8).

foam height	%-diff. 2D results ΔT lowest tested	%-diff. 2D results ΔT highest tested
40 mm	+3.8	+5.2
25.4 mm	+4.9	+5.2
18 mm	+4.4	+3.6
12 mm	+11.8	+4.6

Table 7.4: Three-dimensional effects of studying the foam at different height and temperature differences through the VAT modelling technique. The %-difference against $Q_{conv+rad,num}$ is reported.

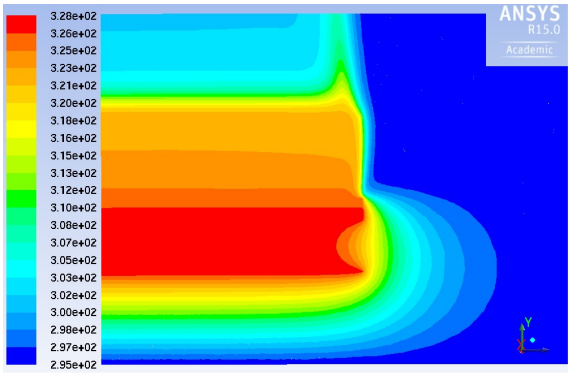

Figure 7.8: Illustration of the 3D-effects in 40 mm high foam at the lowest tested temperature difference (ΔT = 33.2K). A cross-section in the lateral direction in the middle of the heat sink is shown. The gravitational force vector is vertically downwards in the plane of the figure.

On the other hand, for the lowest foam height studied (12 mm) the 3-D effects are much more severe. For the lowest tested temperature difference, sliding chimney effects[7] are observed (see Fig. 7.9a). This results in a thermal impact of +11.8%. For the highest temperature difference, the impact is much more modest (+4.6%). Due to the higher buoyancy forces, sliding chimneys are not observed any more in this case (see Fig. 7.9b). After doing these calculations, one can also look to Table 7.2 once again. From this Table, it can be seen that for all foam heights, except for 12 mm, the numerical results ($Q_{conv+rad,num}$) slightly overpredict the experimental results. In contrast, the results for the 12 mm foam underpredict the experimental results. The higher 3D-effect could be the reason for this.

[7]This term is given by Harahap and McManus [69] and is called to the oscillating but steady motion along the fin channel.

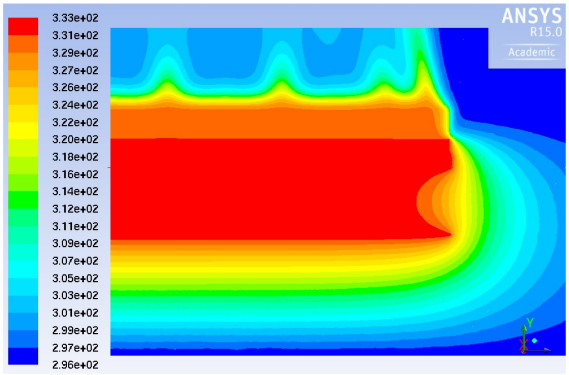

(a) Lowest temperature difference (ΔT = 37.5K).

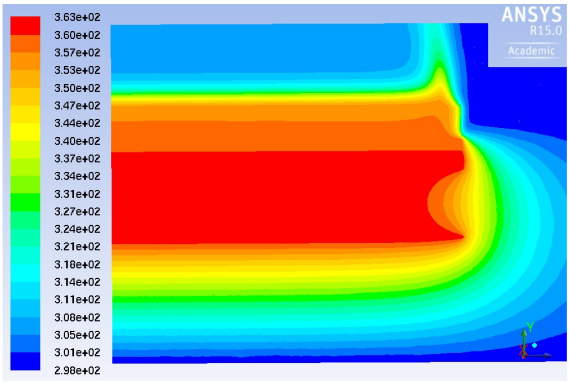

(b) Highest temperature difference (ΔT = 64.9K).

Figure 7.9: Illustration of the 3D-effects in 12 mm high foam. A cross-section in the lateral direction in the middle of the heat sink is shown. The gravitational force vector is vertically downwards in the plane of the figure.

7.3 Steady laminair calculations

Although the results of VAT are promising, there are still some imperfections in the way open-cell metal foam heat sinks can be calculated with this technique, as explained in Appendix D. In this Appendix it is shown that a pure numerical simulation results in a flow pattern which does not resemble experimental results. The volume averaged model also supposes that the flow is completely developed as soon as it enters the foam. This does not seem to be a correct assumption, especially for buoyancy-driven convection; where the foam itself imposes a large resistance against flow penetration. Therefore, researchers also need to look to other methods to numerically study open-cell metal foam heat sinks.

A steady laminar calculation, without using the volume averaging theory, could

be an alternative way to numerically study open-cell metal foam. The main disadvantage this calculation is the computational impact. Therefore, the number of calculations is also very limited: only one calculation was performed. This was also due to time limitations.

7.3.1 Used geometry

The geometry that will be replicated is the same geometry as used and simulated in the previous section: the 10 PPI foam as characterized in Table 5.2.

Due to computational limitations, the only foam sample which can be calculated is the 12 mm high foam. All the other foam heights require too much computational effort. Even with this limited foam height, the maximum number of complete metal foam cells that can be simulated is 2.

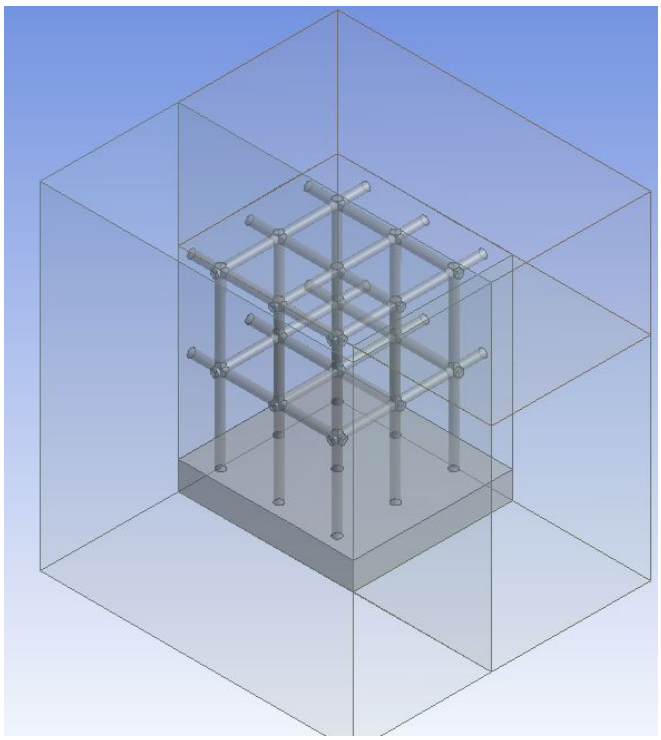

Figure 7.10: Illustration of the geometry used to simulate a 10 PPI open-cell metal foam (d_1 = 6.22mm, d_2 = 4.22mm). The gravitational force vector is vertically downwards in the plane of the figure.

Figure 7.10 represents the geometrical domain. One can see the base plate underneath a rectangular representation of the foam itself. The dimensions of the

foam sample are given in Chapter 5 together with the experimental results. The foam is surrounded with fluid domain: 10 mm at each side. At the sides of the fluid domain a pressure inlet boundary condition is applied, the top of the fluid domain is defined as a pressure outlet. The faces where the foam is not surrounded by fluid have a symmetrical boundary condition. By applying these symmetrical boundary conditions, one is able to calculate the complete width of the original foam that is tested experimentally: 25.4 mm. The total length of the foam is however still limited: 23 mm. So one could expect an overestimation on the thermal results.

7.3.2 Calculation technique

This geometry is meshed using a body size function. The resulting mesh has the following properties:

- Minimal face area: $5.1510^{-12}m^2$
- Maximum face area: $1.79610^{-7}m^2$
- Number of cells: 16.1 million cells
- Number of nodes: 3.2 million nodes
- Number of faces: 33.0 million faces
- Minimal orthogonal quality: 1.9610^{-1} (see definition Section 6.2.3)
- Maximum aspect ratio: 2.4710^{+1} (see definition Section 6.2.3)

The calculations are performed with the 'Warmte13' of the Ghent University. This server has to following properties:

- Intel(R) Xeon(R) CPU E5-2680 v3 @ 2.50GHz
- 2x12 cores
- 132 GB memory

The solution model is very similar to the one used in the previous Section (of course no porous model is used here). Again a gravity term is used, together with a second-order discretization of the momentum and energy term. The pressure-velocity coupling is performed through a SIMPLE scheme. Only for the energy term, some under relaxation is used which is not implemented by default in Fluent15[8]. For the radiation term, a surface-to-surface model is used as standardly implemented in Fluent15. The view factors were calculated automatically. The emissivity is taken as a standard emissivity value for aluminium [17] of 40%. Of course, the emissivity value depends on the surface finish of the material and is not an exact material property.

[8] By default 1 is used, for this calculation 0.99 is used

7.3.3 Results

For this small foam sample, the resulting total heat transfer was 0.25 W. Some impressions of the temperature and velocity results are given in Figure 7.11. The subfigures were taken at the middle of the foam sample.

If this would be a full foam sample (25.4 mm by 254 mm) the heat transfer rate would be 11.21 W[9].

Compared to the experimental result of 7.28 W, presented in Chapter 5, the difference between both results is only 35%, which is not so bad taking into account the limitations on this numerical CFD calculation. It is also evident that the heat transfer result (11.21 W compared to 7.28 W) is larger compared to the experimental result; this is because the numerical result is performed with the assumption that the foam is only 23 mm long and surrounded with an infinite amount of fluid. The other assumption is that the surrounding air at 10 mm from the heat sink is at ambient temperature, in reality, this will not be the case. The same holds for the insulation underneath the heat sink. In the numerical result it is supposed that the insulation is perfect, while in the experiments, there will be some leakage of energy to the surroundings. Furthermore, the foam replication of the geometry is not correct. For example, the porosity of the used geometry (Fig. 7.10) is 96%, this shows that the representation of the geometry itself is not so accurate when comparing to the obtained results of the real foam sample: 93.3% (see Table 5.2). In this subsection, the author used a rectangular representation, while the real foam structure is of course much more complicated. Also a very limited amount of cells is simulated. Again, this will have its contributions to the resulting heat transfer rate.

Although 35% is a large uncertainty if the goal is to optimize heat sinks, it does show that the steady laminar calculations could provide a proper alternative to numerically simulate open-cell metal foam heat sinks. A supercomputer, together with a clever choice of grid discretization, could make it possible for researchers to simulate larger samples of foam. This could give a more proper determination of the heat transfer rate and can be considered as future work.

[9] 0.25389 W is the exact result for the total heat transfer, this has to be multiplied with a factor 2 to obtain a 25.4 mm wide foam (through the symmetrical boundary condition) and again with a factor 2 to obtain the 23 mm foam length (again with the symmetrical boundary condition). Subsequently, one has to multiply this with a factor *254 (mm) / 23 (mm)* to obtain the full 254 mm length.

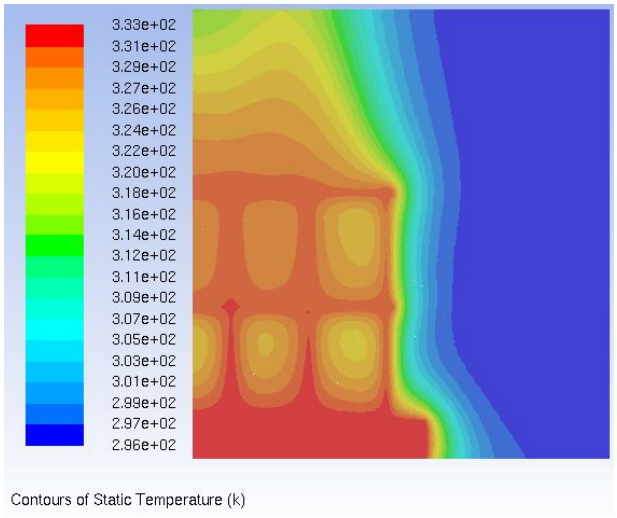

(a) Illustration of the temperature field in the middle of the 10 PPI foam sample.

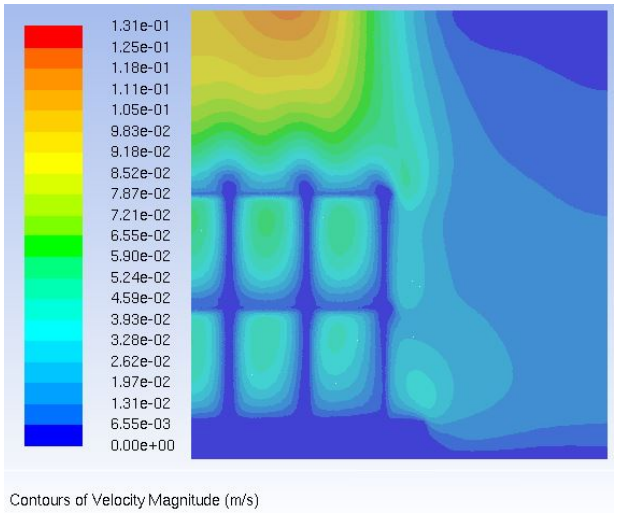

(b) Illustration of the velocity field in the middle of the 10 PPI foam sample.

Figure 7.11: Illustration of the steady laminair calculations of a 12 mm high 10 PPI foam sample (see Figure 7.10). A cross-section in the laterial direction in the middle of the heat sink is shown. The gravitational force vector is vertically downwards in the plane of the figure.

7.4 Conclusion

In this Chapter, different ways of numerically simulating open-cell metal foam heat sinks are presented.

In the first section of this Chapter a macroscopic model is developed based on a **hybrid form of the VAT method** which allows to simulate buoyancy driven convection in heat sinks with open-cell aluminium foam as an extended surface and air as the working medium. Experiments for 10 PPI brazed aluminium foam with a porosity of 93.3% are compared with a 2-D numerical model based on the volume averaging technique. In total four foam heights are studied: 40 mm, 25.4 mm, 18 mm and 12 mm. When radiative heat transfer is not taken into account, the relative differences between the numerical results and the experiments are always smaller than 29%. When radiation is included in the numerical model, by applying the Stefan-Boltzmann equation, the numerical results differ less than 9% from the experimental results. This shows that the radiative heat transfer to the surroundings has to be taken into account for buoyancy driven convection in open-cell foam, even at low temperatures. This has never been stated before.

To assess the influence of some parameters on the model predictions, a sensitivity analysis is performed. Ten parameters of the macroscopic model and the experimental setup are varied. It is shown that the construction and dimensions of the experimental facility have the largest impact on the heat transfer rate and not the convection coefficient as is often assumed.

Finally, the 3D-impact of VAT modelling is shown. This effect is the highest for the lowest foam height, for which the performance is increased by 12% for the lowest temperature difference tested. It is for this temperature difference that sliding chimneys are observed. These 3D-effects show the difficulties of doing only 2D-simulations: for high foam samples this 3D-impact is limited, for low foam samples 3D-simulation are a must. This is confirmed by the experimental results.

Another approach based on a **pure VAT modelling approach** (where the closure terms were determined based on the fluid's velocity) was also considered. In this approach the closure terms are determined based on steady laminar calculations on the PUC. In Section 6.2.1 of Chapter 4 a discussion is given on the geometrical representation of (casted) open-cell metal foam. Furthermore, a numerical modelling approach for each of these terms, including the permeability κ and inertial coefficient β, is given in Section 4.3.3 of Chapter 4. This is based on the work of De Jaeger [105]. As mentioned in Chapter 4 this method still needs to be investigated further before it can be widely used. Furthermore it is questionable whether the VAT technique or an approach based on it is usable to numerically investigate open-cell metal foam heat sinks. As this technique assumes the flow to be fully developed at the moment it enters the heat sink. For open-cell metal foam

this assumption is clearly not the case. It should be investigated further to which extent this assumption will influence the results for open-cell metal foam heat sinks. A preliminary investigation for this further research was made in this work. However, since it doesn't solve all of the remaining issues, it is not incorporated in the main text of this work but in Appendix D.

Finally, open-cell metal foam as an example of a metal foam heat sink is simulated through a steady laminar calculation of a very simplified structure. This simplified rectangular structure is meant to resemble open-cell metal foam. Although the simulation is quite limited: only 23 mm of the foam structure is actually drawn and calculated, it shows the potential value of this technique. Against the experimental results presented in Chapter 5, the numerical result differs less than 35%. Of course, this difference is still large. This can be attributed to the limited amount of foam that is simulated and to the simplification of the foam itself. For example, the resulting porosity from the representation (96%) is different to the actual porosity of the real foam sample (93.3%). However, some future work needs to be done to reveal if this steady laminar calculation of the Navier Stokes equations should be used in the future instead of simulations based on the volume averaging theory. Perhaps the use of the supercomputer available at the Ghent University and a more clever design of the grid discritization algorithm could be useful.

8 Conclusions

8.1 Conclusions

This work both experimentally and numerically studies natural convection in classical heat sinks (pin fins and plain fins) and heat sinks made out of open-cell metal foam.

In this work, a literature review is given on both the experimental and numerical work done on classical and open-cell metal foam heat sinks in open literature. Based on this overview, the issues and gaps in the existing work on both topics were identified. More specifically for classical heat sinks, the difficulties in comparing different literature sources with one another, both for experimental and numerical work were pointed out. The author has shown that in order to be able to compare different literature sources, the following questions need to be answered:

- Which temperature is measured to report e.g. the thermal resistance? And what is the value of that temperature?
- Which material emissivity is assumed to perform the simulations? Is thermal radiation included? How important is it to include radiation?
- How is the experimental test rig constructed? Are guard heaters used? Is insulation placed around the test rig?
- How is the numerical simulation performed? What is the size of the fluid domain around the heat sink?

This PhD shows that it is not straightforward to test *classical heat sinks*, both in numerical and experimental studies. Furthermore, this work illustrates how this complexity rises further going from classical heat sinks to metal foam heat sinks, which is a much more complex fin type. Both types have their own particularities. To study metal foam heat sinks numerical one has to use specialized techniques such as the volume averaging approach. This approach is explained extensively in Chapter 4.

In **Chapter 5**, the **experimental results** of a test rig designed for open-cell metal foam is used to draw some general conclusions useful to experimentally characterize all kinds of heat sinks. The main points which should be taken into account when designing a test rig are listed here, for further details the reader is referred to Chapter 3. This can also lead to a standardization of the experimental work.

- *Location of temperature measurements*: dependent on the used materials and the dimensions of those materials (which needs to be reported carefully), this location can have a significant effect on the measured temperature. This is mainly the case for the substrate temperature. This large variation of the measured temperature is due to the non-uniformities in the test setup. The magnitude of the effect depends on the setup and the measurement location, but can be estimated conservatively at a difference of up to 5°C. Please refer to Chapter 5, where the non-uniformity is only 0.8°C. Thus it is possible to create a test rig with a uniform temperature at the substrate. The temperature of the environment should be taken at 'infinity', as this is the only temperature which can be measured accurately.

- *Guard heaters and the location of the guard heaters*: to limit the losses and non-uniformities in the test setup, the use of guard heaters is imperative. Also the location of the guard heaters in the setup has a large effect on their usefulness. There are no general rules on how these heaters should be placed, this has to be investigated for each test facility individually. This can be done through numerical simulations. Even when using guard heaters there will be an energy leakage from the main heater to the environment, however, this can be measured through numerical simulations. When using no guard heaters, an extra uncertainty can be created of more than 10% on Q going to the heat sink's substrate.

  In some cases even no guard heater can be used, please refer to chapter 4, to see an example of this in open literature.

- *The box geometry*: generally the effect of the enclosure around the tested sample on the test results is limited. However, for small box geometries this effect can become significant. Hence it is important to pay attention

to this parameter. In this work, the effect of the box geometry was up to 7.5% based on the heat transfer coefficient. Thus, in fact, in each case, the heat sink itself doesn't have one heat transfer coefficient, or one thermal resistance. Its thermal parameters should be linked with the box geometry in which the heat sink is supposed to operate.

- *Effect of the emissivity of the material*: this was not studied in chapter 5, due to the difficulties of studying radiation experimentally in an accurate way. However, this effect was studied numerically, as will be discussed later on in this work. As will be shown in the numerical study, the effect of radiation can be up to 30% depending on the fin geometry. Reporting the emissivity will make it possible for other researcher to compare and could make it possible to separate convective and radiative data from each other.

For metal foam heat sinks one extra issue is present: the way the structure is *bonded* to the base plate, as classical heat sinks are most of the time extruded. The effect of the bonding method can be quite large, e.g. between brazing and epoxy contact this can be up to 15% as illustrated in this work. This makes it more complex to study metal foam heat sinks, next to the geometry determination of course, as extensively discussed in Chapters 3 and 5. Most ideally, one is able to subtract the type of bonding method from the convective results.

Based on this itemization and the results for open-cell metal foam heat sinks, there can be thought of some standardisation in the experimental work that will be undertaken in the future by (academic) researchers. It is shown that it is highly important to report each part of the test rig and test samples, including all material properties (like insulation, bonding technique, emissivity of the material). The location of the temperature measurements (and amount of thermocouples used, including the exact location) should also be mentioned. Preferably the researchers take the base plate temperature as close to the substrate of the heat sink as possible. Of course the type of bonding technique will also induce a temperature drop, this has to be taken into account. Or subtract this effect of the convective thermal results. The temperature of the environment is taken as far of the heat sink as possible. A heat sink should always be characterised, giving a specific constraint/box geometry. By doing so, this experimental work can be used for numerical validation studies. Guard heaters should be used, but these can be used in different arrangements, like is shown in the literature survey too. The locations where the guard heaters are placed should be linked with numerical calculations.

Ideally, the radiative term should be subtracted and only the convective results should be given. This is certainly of interest in case of academic research in order to optimize. In this way the experiments are also useful for numerical validation. A way to do this is to polish the heat sink itself, so the emissivity is close to 0 (of course this is not possible with complex heat sinks, like the ones made out

of open-cell metal foam). Or/and to perform some tests in a vacuum chamber. However, in industrial purposes the radiative term is present and will significantly influence the thermal performance. So in real cases, both effects (convection and radiation) should be looked combined.

The remaining parts (Chapters 6 and 7) of this work are dedicated to **numerical work**. Although the results for numerical work are the same as for experimental work: characterization of the heat sink itself, there are other techniques that are used for that characterization. Therefore the standardised way in which researchers should work is listed below. In this work, the simulations were performed laminar without the use of a turbulence model. So the results are valid for Rayleigh numbers lower than 10^8

The first chapter on this topic (**Chapter 6**) focuses on numerical simulations of classical heat sinks. Even for these rather simple geometries, there are many issues which have to be considered. First of all, the impact of the fluid domain on the numerical results was studied. It was concluded that the impact of the fluid domain is dependent on the height of the fin. Globally (for a range of studied fin heights), the height of the fluid domain should be at least 1.3 times the fin height. These results on the minimum required size of the fluid domain are used to study commercially available classical heat sinks. It is shown that without any fluid domain the error is approximately 35%. However, the exact number depends on the studied fin: shape, fin height, boundary conditions, radiation term...

This research also shows the need of performing an *uncertainty analysis* on numerical simulations. Based on this analysis is it shown that the uncertainty is very dependent on the numerical grid discretization. For the heat sinks studied in this work, and with the finest discretization used, the uncertainty can be lower than 2%. However, this uncertainty can rise to 7% when increasing the grid size with a factor 2. Thus, prior to the investigation an uncertainty analysis should be given.

Furthermore, some work is performed on commercial heat sinks to illustrate the *effect of radiation and temperature determination*. Some authors do not take radiation into account in numerical simulations. However, it is shown that the difference between taking radiation into account with a surface-to-surface model with an emissivity of 40% compared to neglecting radiation is up to 15% in thermal resistance. Increasing the emissivity value of 40% to 80% leads to an additional difference of up to 10% in thermal resistance. Of course, this is again dependent on the fin structure (and only a limited number of fin shapes was studied in this work). The effect of temperature in the determination of the thermal resistance is large. Most of the time, the base plate temperature can be determined unambiguously. However, the temperature of the surroundings is most of the time taken as a temperature at infinity (T_∞). Yet, in experimental circumstances this temperature is taken in the environment of the fin structure (T_{env}). It is not always mentioned which temperature is taken in numerical work. This makes it even more difficult to

compare numerical results with experimental work. The differences between R_∞ and R_{env} can be up to 18%, again this is dependent on the fin structure. In fact, to define the thermal resistance, T_{env} should be defined as the temperature at T_∞ and the temperature of the solid should be defined as the temperature at the substrate, as this temperature is also measurable.

Finally, in **Chapter 7**, the additional issues which arise when metal foam heat sinks are numerically studied are highlighted. In this Chapter, two ways of numerically simulating open-cell metal foam heat sinks are presented.

In the first section of this Chapter a macroscopic model is developed which allows to simulate buoyancy driven convection in heat sinks with open-cell aluminium foam as an extended surface and air as the working medium. Experiments for 10 PPI brazed aluminium foam with a porosity of 93.3% are compared with a 2D numerical model based on the volume averaging technique. In total four foam heights are studied: 40 mm, 25.4 mm, 18 mm and 12 mm. When radiative heat transfer is not taken into account, the relative differences between the numerical results and the experiments are always smaller than 29%. When radiation is included in the numerical model, by applying the Stefan-Boltzmann equation, the numerical results differ less than 9% from the experimental results. This shows that the radiative heat transfer to the surroundings has to be taken into account for buoyancy driven convection in open-cell foam, even at low temperatures.

To assess the influence of some parameters on the model predictions, a sensitivity analysis is performed. Ten parameters of the macroscopic model and the experimental setup are varied. It is shown that the construction and dimensions of the experimental facility have the largest impact on the heat transfer rate and not the convection coefficient as is often assumed.

In a second section of this chapter, a metal foam heat sink is simulated through a steady state laminar calculation of a very simplified structure. This simplified rectangular structure is meant to resemble the metal foam structure. Although the simulation is quite limited: only a 23 mm-long part of the very simplified foam structure is actually drawn and calculated, it shows potential value. Against the experimental results presented in Chapter 5, the numerical result differs less than 35%. This can also be studied latter.

8.2 Future work

As stated throughout this work, some aspects were not investigated due to lack of time and/or they were to far from the scope of this work. These and other points can be the subject of future work. The main domains where future work might be located are (in case of the experimental work, some steps are already taken in the previous section):

- *Experimental work on classical/metal foam heat sinks*: is it possible to make an industrial standard to test heat sinks against? In this way it is more easy to compare and select heat sinks in a particular circumstance. Now it is very hard for academic researchers and industrial clients to select or compare a particular heat sink with the heat transfer performance given by the manufacturer. Especially in academics it is very difficult to compare data from one research with each other. It is future work to spread these results more in the academic and industrial world. It would mean a start of a better approach to compare heat sinks between one another.

- *Numerical work on classical heat sinks*: is it possible to make an optimization routine which is capable to select a proper grid discritization, to test a lot of different classical structures and to optimize a heat sink to fit in a particular case? Some work on optimization is already done, but many researchers do not include radiation or a grid uncertainty analysis. Also the influence of the fluid domain placed upon the heat sink has to be taken into account. Next to a proper optimization routine. In this way, one can design very effective heat sinks for different applications.

  The influence of fluid domain on the top of the heat sink can be studied more detailed: e.g. by testing more different fins and more temperatures/heat fluxes to see if there are any effects of these parameters of the fluid height that is necessary to do the simulations. If this work is done, a correlation can be made.

  One should also try to substrate (conductive,) convective and radiative effects from each other. This can be done in numerical work quite easily, however, this is not done in this work. It is an advantage if one would be able to compare both radiative and convective effects in between each other. One should also try, in future work, to compare heat sinks based on a fixed temperature instead of a fixed heat flux. Work on the effect of both approaches should be performed.

- *Numerical work on metal foam heat sinks*: is it possible to make an alternative model to the VAT model, in which the researchers are capable to efficiently simulate metal foam heat sinks? Maybe there is no length scale separation on these long and narrow metal foam heat sinks, as studied in this work. Maybe extra boundary conditions, like pressure jump conditions should be added to the model in order to simulate the entrance and exit effects more properly.

  Or is it possible to perform laminar steady state simulations on a simplified geometry in a way that the results better match the experiments? One of the questions is: how large does the domain of the heat sink have to be chosen

in order to minimize the uncertainty? What is a proper representation of a metal foam heat sink? For this last question, a sensitivity analysis could be useful.

A

Uncertainty analysis for experimental results

The measured value of a physical property in experimental research always differs from the actual value. This deviation is called the uncertainty. The uncertainty consists of:

- The **systematic uncertainty** which is due to the inaccuracy of the measuring device.
- The **random uncertainty** caused by random deviations on the measuring device. This random uncertainty can be treated statistically and can be reduced by performing more independent measurements of exactly the same experiment.

To incorporate the uncertainty on a specific measurement, often an interval $x + \delta x$ is given in which the 'real' value lies. The confidence interval used in this work is 95% (2σ). For uncertainty propagation the textbook of Taylor [184] is used. Not all error propagations which are used in this work are given here. Only the one who where not directly interpretable.

A.1 Uncertainty on Q

The terminology that will be used here is based on Eq. (3.1). Q_{in} is the power dissipated by the heater. This is a combination of Q_{conv}, Q_{loss} and Q_{rad}. As

Q_{conv} and Q_{rad} are quite difficult to separate, certainly in experiments, both will be combined to $Q_{heat\ sink}$.

A.1.1 Power dissipated Q_{in}

The power dissipated by the heater is calculated as

$$Q_{in} = \overline{V} \cdot \overline{I} \tag{A.1}$$

The accuracy of the power supply is respectively:

- $\delta V = 50mV \pm 0.1\%$
- $\delta I = 0.1mA \pm 0.3\%$

With these values, the uncertainty on $\overline{V}$ and $\overline{I}$ can be calculated according to Eq. (A.2) and (A.3). Finally the uncertainty on the total power dissipated by the heater Q_{in} is calculated in Eq. (A.4).

$$\delta\overline{V} = \sqrt{(\delta V)^2 + (\delta 2\sigma_{\overline{V}})^2} = \sqrt{(0.05 + 0.001\overline{V})^2 + \left(\frac{2\sigma_V}{\sqrt{n}}\right)^2} \tag{A.2}$$

$$\delta\overline{I} = \sqrt{(\delta I)^2 + (\delta 2\sigma_{\overline{I}})^2} = \sqrt{(0.0001 + 0.003\overline{I})^2 + \left(\frac{2\sigma_I}{\sqrt{n}}\right)^2} \tag{A.3}$$

$$\delta Q_{in} = \sqrt{(\overline{I} \cdot \delta\overline{V})^2 + (\delta\overline{I} \cdot \overline{V})^2} \tag{A.4}$$

A.1.2 Heat loss through the insulation Q_{loss}

The heat loss through the insulation Q_{loss} is calculated through CFD calculations.

The model geometry is shown in Fig. A.1. Only a quarter of the actual test setup is modelled in 3D. A uniform mesh is created for the aluminium substrate, copper plates and the insulation nearby the substrate. Following boundary conditions where used:

- The guard heaters are kept at the same temperature as the main heaters
- The effect of radiation is negligible
- The ambient temperature is taken at $300K$
- The heat transfer coefficient of the insulating wall is taken at 5 W/m^2K
- Material properties of the insulation material: $k = 0.023W/mK$

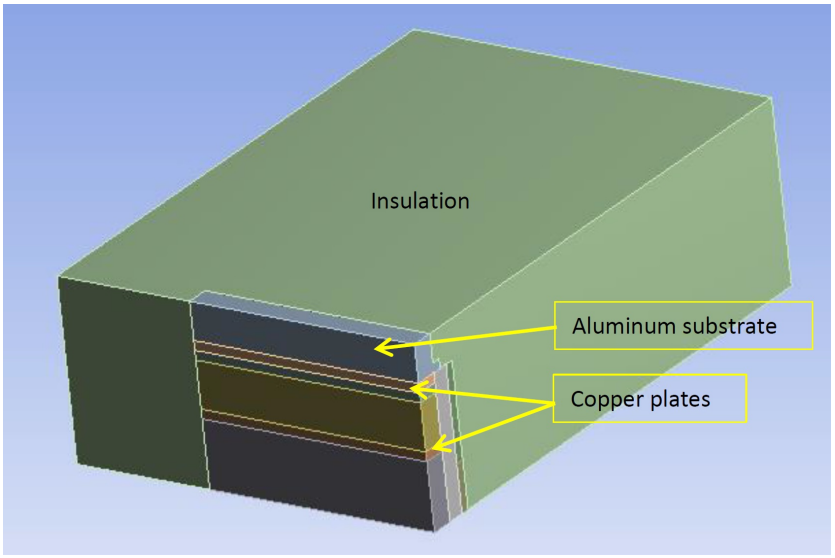

Figure A.1: Illustration of the geometry used in CFD.

In Table A.1, nine different cases are shown. By varying T_{heater} and $h_{heat\ sink}$ one by one to obtain Q_{loss} in function of those two parameters. For these nine cases, Q_{loss} is calculated and reported in this same table.

Case nr	T_{heater} in $°C$	$h_{heat\ sink}$ in $W/(m^2K)$	Q_{loss} in W
1	40	10	0.05805
2	70	10	0.1943
3	100	10	0.3288
4	40	25	0.058
5	70	25	0.1937
6	100	25	0.329015
7	40	40	0.05762
8	70	40	0.1921
9	100	40	0.3287

Table A.1: Basic calculation cases for calculation of Q_{loss}

A least squares fit is determined for two independent variables $\Delta T = T_{heater} - T_\infty$ and $h_{heat\ sink}$ according to:

$$Q_{loss} = f(T,h) = a + b \cdot \Delta T + c \cdot h \tag{A.5}$$

Solving the equations results in a = -0.0001, b = 0.0045 and c = 0 (so there is no influence of $h_{heat\ sink}$ on Q_{loss}).

δQ_{loss} can be calculated as $\sqrt{(b \cdot \delta \Delta T)^2 + (c \cdot \delta h)^2}$ or

$$\delta Q_{loss} = 0.0045 \delta \Delta T \tag{A.6}$$

A.1.3 Power sent to the heat sink

$Q_{heat\ sink}$ is defined as $Q_{in} - Q_{loss}$. The uncertainty due to the heat loss through the insulation Q_{loss} is determined in Section A.1.2, while the uncertainty on Q_{in} is determined in Section A.1.1. Consequently the uncertainty on $Q_{heat\ sink}$ is determined through Eq. (A.7).

$$\delta \overline{Q}_{heat\ sink} = \sqrt{(\delta \overline{Q}_{in})^2 + (\delta \overline{Q}_{loss})^2} \tag{A.7}$$

A.2 Uncertainty on the geometrical dimensions

If all dimensions are measured with a Vernier caliper, the uncertainty will be $\pm 0.05mm$. All copper plates, heat sinks and aluminium substrates were measured with such a Vernier caliper. The maximum uncertainty on the copper plates, due to the lack of flatness, was 0.1 mm. Consequently, this will also be the thickness of the thermal paste layer.

A.3 Uncertainty on the measured temperatures

To reduce the systematic error of the temperature measurement, the accuracy of the thermocouple has to be improved. The bought thermocouples were made according to the EC 60584-2 class 2 standard. This means that the standard accuracy of these thermocouples is $\pm 2.5°C$. To improve this accuracy, the thermocouples were calibrated against a more precise thermometer. The calibration will determine the relationship between the sensor output and the real value. The precise measuring device used is a Fluke 1523 Reference Thermometer. This thermometer uses a PT-100 temperature probe (Fluke 5610-9). The combined accuracy of the temperature measurement by the Fluke 1523 and Fluke 5610-9 is 0.064 $°C$. This was determined by a certified calibration centre, Dimed NV in Antwerp/Belgium. The calibration oven used is a Druck DBC 150. The accuracy of the analog to digital converter (ADC) which is in this case a Keithley 2700 is $\pm 0.001°C$.

In this work a third order polygon is used as a calibration curve. Least-squares fitting is used to find this polygon ($y = A \cdot x^3 + B \cdot x^2 + C \cdot x + D$). For each

thermocouple which is used 10 equally distanced measurements have been taken between 10 $^{\circ}C$ and 100 $^{\circ}C$ to determine the calibration curve.

$$\sigma_{TC,\ calibration,\ i} = \sqrt{\frac{1}{n-4}\sum_{j=1}^{n}\left(y_{ij} - A_i\ x_{ij}^3 - B_i\ x_{ij}^2 - C_i\ x_{ij} - D_i\right)^2} \quad \text{(A.8)}$$

The uncertainty on each thermocouple i is then determined as:

$$\begin{aligned}\delta_{TC,i}(in\ ^{\circ}C) &= \delta_{PT-100} + \delta_{ADC} + 2\sigma_{TC,\ calibration,\ i} \\ &= \left(0.064 + 0.001 + 2\sqrt{\frac{1}{n-4}\sum_{j=1}^{n}(y_{ij} - A_i\ x_{ij} - B_i)}\right)\end{aligned} \quad \text{(A.9)}$$

With this calibration technique, the average uncertainty on the thermocouples is $\pm 0.11^{\circ}C$, while the maximum uncertainty is $\pm 0.2^{\circ}C$.

The ambient temperature is determined based on N temperature measurements (N = 12 in our case), each measurement is performed n times in steady state condition (n = 100 in our case). Hence, the uncertainty on the substrate temperature is:

$$\delta_{\overline{T},ambient} = \sqrt{\left(\frac{\sum_{TC_i}^{TC_{i+N}}(\delta_{TC,i})^2}{N}\right)^2 + \left(2\frac{\sigma_{T,ambient}}{\sqrt{n}}\right)^2} \quad \text{(A.10)}$$

All error propagation rules that were used are explained in Ref. [184]. So, to determine the uncertainty on the heater and substrate temperature, the temperature difference between substrate and ambient temperature and the different thermal resistances, the technique described in Taylor can be used [184].

B

Emissivity measurements of some metal foam samples

B.1 Measuring principle

The conventional determination of emissivity of any object by means of infrared thermometer, a temperature controlled sample and reference surfaces requires an excessive amount of time and funds.

An exact measurement of the surface temperatures and strict corresponding with controlled thermal conditions of the surroundings are of absolute necessity. To achieve a fast and reliable process control, such an expense is not acceptable. In this work, a TIR-100 measuring device wil be used (see Figure B.1). This measuring device is manufactured by Inglas. This device is able to measure the integral emissivity within a few seconds. Furthermore, the measurement can be performed directly at the original part and even structured and curved surfaces can be measured. Figure B.2 explains the measuring principle. The surface of interest is exposed to the thermal radiation of a black body with a defined temperature. This temperature is held constant at $100°C$. Depending on the emissivity value, the black body radiation is reflected on the sample surface and detected by a sensor, which is mounted in an opening of the radiator. In order to achieve a complete and homogeneous illumination of the measuring surface, the radiator has been styled in the form of a half sphere. Hence, even rough and structured surfaces can be detected.

Figure B.1: TIR-100 measuring equipment to measure the integral emissivity (manufacturer: Inglas/Germany)

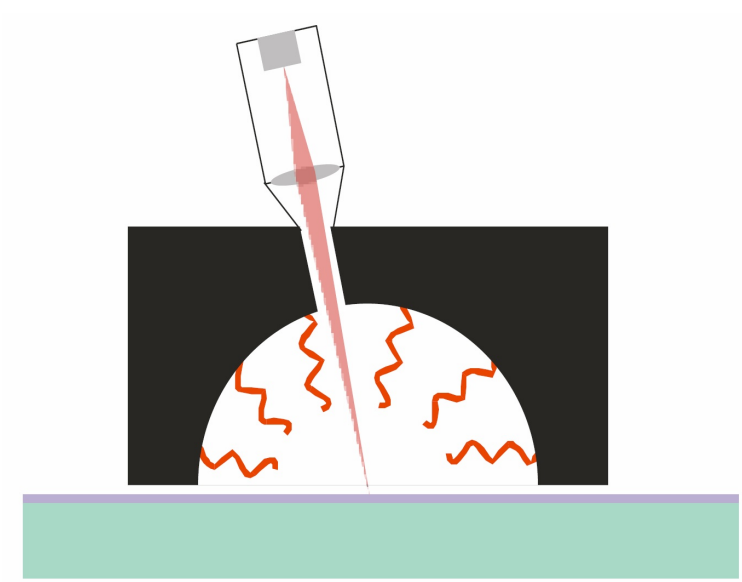

Figure B.2: Illustration of the measuring principle (TIR-100 from Inglas)

Using a Fresnell lens the sensoring area is focused to a small part of the sample

surface. As a result, the smallest samples and even rods can be measured with a sufficient precision. In the same time this assembly guarantees that the sensor has sufficient energy for a highly precise measurement. The radiators' temperature has been chosen in such a way, that there is a thermal spectrum with the center wavelength of λ = 8 μm. Its spectral distribution corresponds to the conditions that are relevant for applications at room temperature.

The sensor is a so-called Thermopile, a serial connection of several thermocouples, which absorb radiation energy in a broad band and linear manner. The temperature difference between the measuring and the referencing thermocouples generates a voltage signal which is proportional to the reflected thermal energy. The temperature of the referencing elements must either be kept constant or it must be measured separately. In the latter case it will be necessary to superpose it over the radiation signal as a correction signal.

The emissivity is determined by comparing the measuring result of the sample with the values of two well-known standards. To do so the sensor signals (U) of a low emitting (ε_N, U_N) and a highly emitting (ε_H, U_H) reference are measured. The reference materials that were used were a so-called 'mirror side' with an emissivity of 0.012 and a 'black side' with emissivity of 0.960 (series numbers: 2015-0.139).

Then the measured value is found based on the following equation:

$$\varepsilon = \varepsilon_H + (\varepsilon_H - \varepsilon_N)\frac{(U_H - U)}{(U_N - U_H)} \tag{B.1}$$

It is a basic condition, that the standards and the sample are measured at the same temperature. As long as the sample is of massive quality and of high thermal conductance, any heating of the sample during the measurement can be neglected. On the contrary, thin and thermally insulating materials shall heat up very quickly and lead to an emissivity value which is continually changing towards smaller values. In such cases care must be taken to perform a measurement as quickly as possible, in order to assure that the sample temperature remains the same as the ambient temperature as much as possible ($\Delta T \leq 1°C$).

B.2 Metal foam samples

Four different samples of open-cell metal foam are used. Only one of the samples is painted black with a spray, as no big difference in effect are expected between different foams samples when painting them black (see numerous of publications by our research group). The spray which is used to paint these samples is by Kontakt Chemie: Graphit 33 which is a conductive coating.

The following samples are tested[1]:

[1] Only some samples were scanned through μCT.

- Sample 1: 10 PPI metal foam sample with porosity 93.3% (d_1 = $4.22mm$, d_2 = $6.23mm$, A_0 = $0.0998mm^2$). Foam manufacturer: M-Pore.
- Sample 2: 10 PPI metal foam sample with porosity 96.9%. Foam manufacturer: M-Pore.
- Sample 3: 20 PPI metal foam sample with porosity 93.6% (d_1 = $2.77mm$, d_2 = $4.15mm$, A_0 = $0.0377mm^2$). Foam manufacturer: M-Pore.
- Sample 4 and 5: 10 PPI metal foam sample with porosity 95.1% (d_1 = $4.28mm$, d_2 = $6.42mm$, A_0 = $0.0615mm^2$). Foam manufacturer: Alhedron (in-house production). This sample is produced twice: one sample is tested as is (sample 4) and one is painted black (sample 5).

The PPI value which is reported is the PPI value determined by the manufacturer. The porosity is calculated in-house by measuring both dimensions and weight.

B.3 Results

The relevant standard for the test is EN16012:2012. No information is given upon the absolute uncertainties. Only the repeatability is tested by measuring each sample 10 times in random sequence. Hence, next to an average value also the standard deviation is given (σ):

- Sample 1: 10 PPI metal foam sample with porosity 93.3%. **Average value: 0.694.** Standard deviation: 0.0022
- Sample 2: 10 PPI metal foam sample with porosity 96.9%. **Average value: 0.754.** Standard deviation: 0.0036
- Sample 3: 20 PPI metal foam sample with porosity 93.6%. **Average value: 0.583.** Standard deviation: 0.0026
- Sample 4: 10 PPI metal foam sample with porosity 95.1%. **Average value: 0.540.** Standard deviation: 0.0032
- Sample 5: 10 PPI metal foam sample with porosity 95.1%. *Painted black.* **Average value: 0.894.** Standard deviation: 0.0045.

These results show no observable trend between the emissivity and the PPI and porosity values. This can be caused by several factors. First of all: the PPI value itself is a not an adequate parameter to compare different foams. Secondly the surface finish is not the same for the different foams. This surface finish depends on the specific manufacturing process, which will certainly be different for the

foam samples by M-Pore and Alhedron in terms of cooling process, used ceramics, curing time...

In fact for each different foam which is tested, especially in natural convection, the emissivity should be measured. However, the measurement equipment from Inglas (TIR-100) is quite expensive: 10 000 EUR.

C

A new interpretation of the Darcy equation

This appendix considers open-cell metal foam as an example of a multidimensional heat sink.

This appendix gives an alternative way to calculate the permeability and inertial coefficient through a numerical approach, based on the viscous and pressure forces that are acting on the porous medium. This approach is explained in Chapter 4 and will be used further in Appendix D.

The permeability is used in the famous Darcy equation, the alternative way of calculating the permeability gives a new interpretation of this Darcy law. This will also be discussed in this Appendix.

C.1 Introduction and possible ways to calculate κ and β

The creeping flow through porous media is described by the Darcy equation which relates pressure drop to velocity (Eq. (C.1)). In Eq. (C.1), κ is the permeability of the porous medium. It is experimentally shown that after the transitional regime the pressure drop becomes quadratic with the velocity (Eq. (C.2)). The equation to capture this behavior is called the Darcy-Forchheimer equation (or Hazen-Dupuit-Darcy). In this equation, β stands for the inertial coefficient. Both permeability and inertial coefficient are classically seen as material properties

[157]. They are exclusively related to the structure of the porous medium.

$$\nabla P = \frac{\mu}{\kappa}\vec{V}, \tag{C.1}$$

$$\nabla P = \frac{\mu}{\kappa}\vec{V} + \rho\beta\vec{V}^2, \tag{C.2}$$

Dukhan et al. [201] mentioned that the Darcy equation accounts for the viscous drag while the Forchheimer term ($\rho\beta V^2$) corresponds to the form drag. This is also linked with the generally known interpretation of the Reynolds number. The Reynolds number represents the ratio of the momentum flux to the viscous stress. For many (but not all) applications, this can also be interpreted as the ratio between the inertial forces and the viscous forces. For low Reynolds numbers the viscous forces are dominant and for high Reynolds numbers the inertial forces will become dominant. It is expected that when viscous stress dominates, the relation between pressure drop and velocity is linear. However, for higher flow velocities, the linear pressure drop does not follow the Darcy equation. Du Plessis and Woudberg [202] provided an expression for the critical Reynolds number for departure from the Darcy regime, which only depends on the porosity of the porous medium (c_d in Eq. (C.3) is 1.9). Of course, this determination of the critical Reynolds number is only a first attempt in order to determine this departure from Darcy regime. There are many open questions on this correlation itself to which the author will not go into detail.

$$Re_c = \frac{\left(50.8\phi(1-\phi)^{1/3}\right)}{c_d\left[1-(1-\phi)^{1/3}\right]} \tag{C.3}$$

Experimental approach

A first approach to investigate the effect of velocity on the permeability and the inertial factor is to perform experiments[1]. Foam with a porosity of 93.2% (d_1:4.22 mm, d_2:6.23 mm and A_0:0.0988 mm^2) with a thickness of 40 mm is placed in a wind tunnel with a cross dimensional test section of 256 mm by 447 mm. The construction of the wind tunnel is explained in De Schampheleire et al. [203]. Pressure drop data for a velocity range between 0 and 26 m/s is gathered and fitted to a second order polynomial to determine κ and β. To determine this parameters, the entrance and exit effects as discussed in the PhD of De Jaeger [105] are also accounted for. For this specific case these values were 5.77 $10^{-6}m^2$ and 118.59 $1/m$, respectively. With these values the Darcy-term ($\mu/\kappa V$) and Forchheimer term ($\rho\beta V^2$) are determined and compared to the global pressure drop in Figure C.1. The characteristic length for the Reynolds number is the average strut diameter: $d_s = \frac{4(1-\phi)}{\sigma_0}$ which can be interpreted as the diameter of a cylinder with a length equal to the total strut length and a volume equal to the

[1]For this work, the author are acknowledge the work of De Jaeger [105], which was his successor

solid phase volume [151]. The relative uncertainty is calculated through the error propagation rules as described in the textbook by Taylor [184]. This uncertainty varies between 4.5% and 10%.

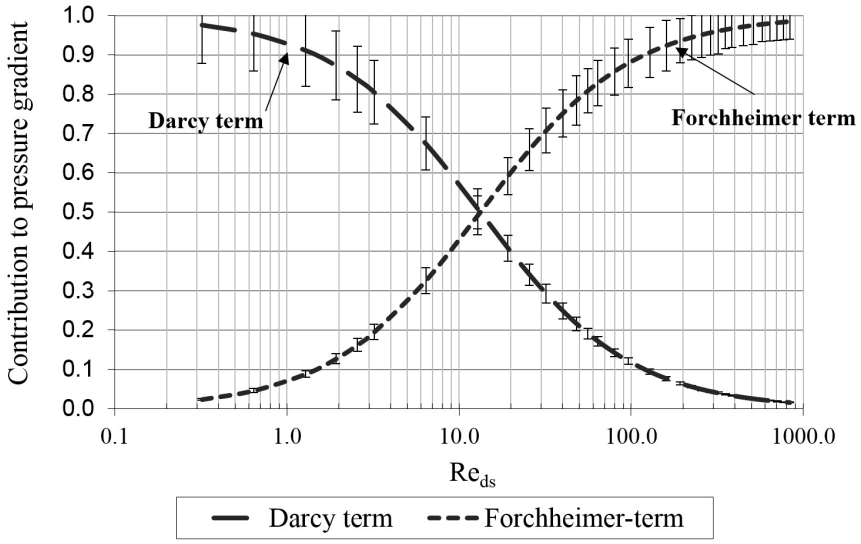

Figure C.1: Contribution of the Darcy and Forchheimer term to the pressure gradient for a foam with following dimensions: d_1:4.22 mm, d_2:6.23 mm and A_0:0.0988 mm^2

In the region of low Reynolds numbers, which corresponds to creeping flow, the Darcy term in Eq. (C.2) is dominant and shows a nearly linear relation with the Reynolds number. The Forchheimer term becomes significant (more than 3% of the total pressure gradient) when the transition to the steady laminar regime occurs [196]. It indicates that inertial forces start to become significant. The share of the Forchheimer term increases significantly, until it contributes approximately 63% of the total pressure gradient [204]. The corresponding Reynolds number indicates the onset for the formation of regular vortex shedding from the struts, i.e., transition to the unsteady laminar regime. The onset of transitional flow regime is clearly observed when the Forchheimer term contribution is approximately 83% [205] . However, for the transition to the turbulent flow regime Seguin et al. [205] state that the inception takes place when the Forchheimer contribution reaches 91% of the total pressure gradient. The Darcy term accounts for the viscous drag, while the Forchheimer term corresponds to the form drag [201]. However, using numerical simulations, it is also possible to directly evaluate the viscous drag and the form drag separately.

Numerical approach: calculation of κ and β^2

[2]Some of the equations and explanation given here is a repetition from Chapter 4. Also for this

The permeability κ and inertial coefficient β are numerically determined through Eqs. C.4 and C.5 based on the viscous and pressure forces, respectively. In this equations, the superficial average is used. The tested foam is the same as for the numerical approach (d_1:4.22 mm, d_2:6.23 mm and A_0:0.0988 mm^2). Both tensors are symmetrical and the non-diagonal components are zero [151, 206, 207]. For orthotropic media, Scheidegger [207] analyzed experimental data and revealed a symmetric behavior. This was later proven by Whitaker [206]. Thus, when permeability is determined along the principal directions, only the three diagonal components need to be determined. For the inertial loss factor though, symmetry is not guaranteed. However, Magnico [151] investigated this factor for shear-deformed open-cell nickel foams and found that the eigenvectors were nearly orthogonal and they followed the shear angles. This led to the conclusion that the inertial loss factor of foams, could be practically considered to be symmetrical. Furthermore, the permeability and inertial coefficient along the z-direction is the same as the one along the x-direction ($\kappa_{*,xx} = \kappa_{*,zz}$ and $\beta_{*,xx} = \beta_{*,zz}$). There are therefore just two unknown components in each tensor, which can be obtained by imposing flow in two different directions. Pressure gradients of different magnitudes are imposed, once in the x direction and once in the y direction. The calculations are done using a commercial CFD software package. The convective terms are discretized using a second-order upwind scheme and a coupled pressure-velocity scheme is used. No turbulence model is used. All residuals have to be lower than 10^{-6} before the solution is accepted.

$$\mu\langle\vec{v}\rangle \cdot \overline{\overline{\kappa}}_*^{-1} = \vec{f}_v \tag{C.4}$$

$$\langle\vec{v}\rangle \cdot \overline{\overline{\beta}}_* = \frac{1}{\rho\|\phi\vec{v}\|}\vec{f}_p \tag{C.5}$$

Shear stress calculation in laminar flow ($\vec{f}_v$) requires a sufficiently fine mesh at the boundary layer to accurately resolve the gradient. In order to be certain that changing the size of the cells of the computational grid does not influence the results for $\overline{\overline{\kappa}}_*$ and $\overline{\overline{\beta}}_*$, a grid discretization study is performed. In this work the Roaches grid convergence index (GCI) is used to estimate the grid discretization error [99, 100]. Three different grid sizes are tested each with a 10% refinement of all cells in each direction. For the finest mesh the first boundary layer cell was 4 μm thick. The growth ratio was taken 1.1 and a maximum size cell of 60 μm is imposed. For the PUC reported in Figure C.2 this leads to a computational domain of 10.5 million cells[3]. In Table C.1 the GCI for the finest grid is reported. Even for this fine grid, the relative uncertainty on $\kappa_{*,yy}$ is quite high (15.4%). However,

section, the author wants to acknowledge the work of De Jaeger [105], which is co-author in the original peer-reviewed paper that was written on this topic.

[3]This figure was taken from the PhD work of Peter De Jaeger, figure 5.7 on page 174 [105]

the uncertainties are acceptable in comparison to the experimental results, where uncertainties over one order of magnitude are reported (see Bonnet et al. [142]).

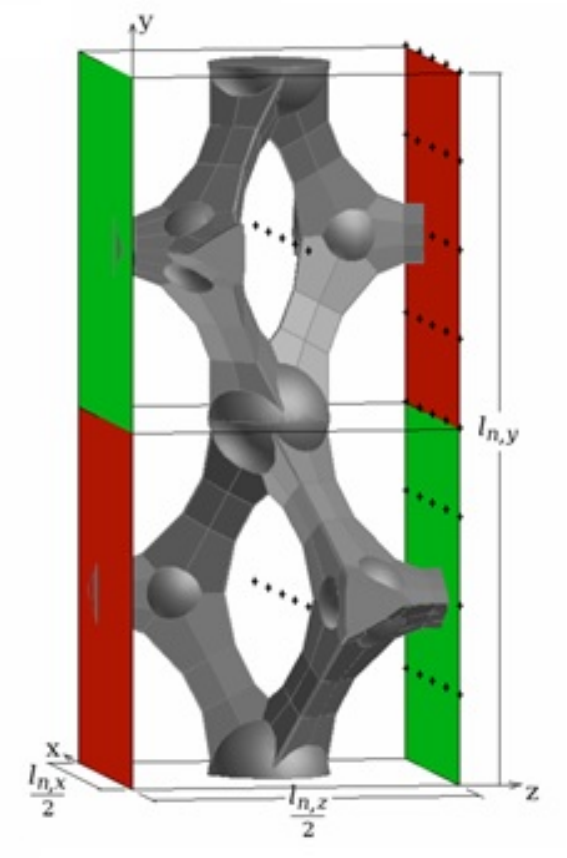

Figure C.2: Illustration of the periodic unit cell used of the foam with dimensions: d_1:4.22 mm, d_2:6.23 mm and A_0:0.0988 mm^2 [105].

The results for the different pressure gradients that were simulated are reported in Table C.2 and Figures C.3 and C.4. The focus of this paper is on low velocities: only steady calculations were performed. The permeability in both directions remains constant for $Re_{d_s} < 0.25$, see Figure C.3 and Table C.2. The flow regime here is creeping flow. For higher Reynolds numbers, the viscous force (shear stress) will start to increase and by observing the trend, it can be stated that the viscous force increases slightly more than linearly with the Darcian velocity. According to Eq. C.4, this results in a decrease of the permeability.

	Coarse mesh start size: 5 μm	Finer mesh start size: 4.5 μm	Finest mesh start size: 4 μm	$\Delta_{coarse-finest}$	$GCI_{finest\ grid}$
$\kappa_{*,xx}$	1.584 $\cdot 10^{-6} m^2$	1.610 $\cdot 10^{-6} m^2$	1.632 $\cdot 10^{-6} m^2$	3 %	7.2%
$\kappa_{*,yy}$	6.318 $\cdot 10^{-7} m^2$	6.527 $\cdot 10^{-7} m^2$	6.700 $\cdot 10^{-7} m^2$	6 %	15.4%
$\beta_{*,xx}$	72.36 $1/m$	72.66 $1/m$	73.74 $1/m$	1.9 %	8.7%
$\beta_{*,yy}$	142.75 $1/m$	143.70 $1/m$	144.54 $1/m$	1.2 %	3.44%

Table C.1: Determination of grid discretization error for a pressure gradient of 100 Pa over the PUC.

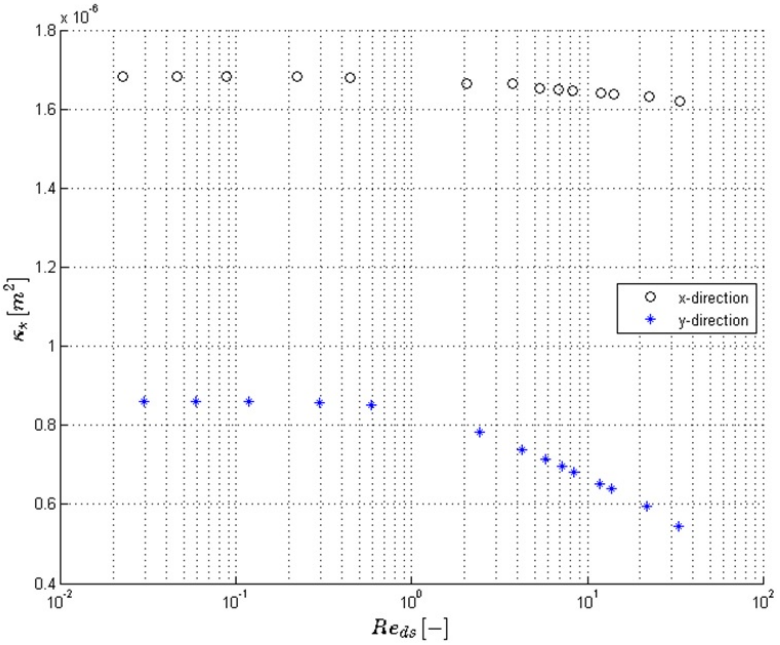

Figure C.3: The permeability in the x- and y-direction ($\kappa_{*,xx}$ and $\kappa_{*,yy}$) determined through numerical calculations plotted against the Reynolds number.

$Re_{d_s,x}[-]$	$Re_{d_s,y}[-]$	$\kappa_{*,xx}[m^2]$	$\kappa_{*,yy}[m^2]$	$\beta_{*,xx}[1/m]$	$\beta_{*,yy}[1/m]$
0.02244	0.02982	1.682E-06	8.600E-07	28744	28062
0.04581	0.05889	1.682E-06	8.600E-07	14374	14037
0.08834	0.1178	1.682E-06	8.600E-07	7191.5	7029.9
0.2225	0.2977	1.681E-06	8.580E-07	2888.6	2843
0.4450	0.5857	1.680E-06	8.510E-07	1464.6	1472.7
2.0384	2.4474	1.664E-06	7.820E-07	360.79	444.38
3.7659	4.2338	1.663E-06	7.380E-07	218.26	311.63
5.3462	5.7618	1.654E-06	7.130E-07	165.99	260.38
6.8218	7.1327	1.649E-06	6.950E-07	138.24	231.67
8.2059	8.3926	1.645E-06	6.810E-07	120.93	212.72
11.9227	11.7460	1.639E-06	6.530E-07	94.22	180.00
14.0919	13.7320	1.637E-06	6.400E-07	85.39	167.31
22.5039	21.8332	1.632E-06	5.960E-07	69.85	138.94
33.5792	33.0721	1.620E-06	5.430E-07	65.65	126.75

Table C.2: Results for the permeability and inertial coefficient based on the numerical calculation method.

The inertial coefficient in the direct formulation is defined as the ratio of the (volume averaged) pressure force to the kinetic energy of the fluid (Eq. (C.5)). Upstream of a strut, there is a stagnation zone where kinetic energy descends to zero, which results in a region with high pressure. Downstream, a distinction has to be made between flow regimes with or without recirculation regions in the wakes behind the struts. In case of no recirculation ($Re_{d_s} < 10$, see Figure C.4), the inertial loss factor decreases with increasing Reynolds number. This indicates that the pressure force increases at a rate lower than the average kinetic energy in the flow domain. For higher Reynolds numbers, it is expected that the increment of pressure force will be balanced by the increase of velocity. This will be again characterised by a nearly constant inertial coefficient. This can be again observed in Table C.2 for the Reynolds numbers in laminar regime.

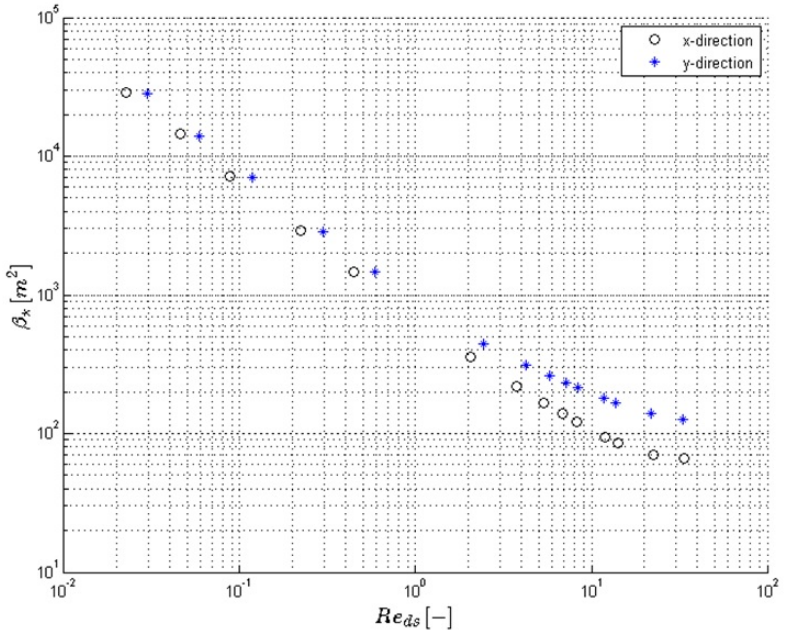

Figure C.4: The inertial coefficient in the x- and y-direction ($\beta_{*,xx}$ and $\beta_{*,yy}$) determined through numerical calculations plotted against the Reynolds number.

C.2 Discussion on the Darcy equation

To provide more detail, Table C.3 reports the viscous and pressure forces over the simulated range of Reynolds numbers in the x-direction with these forces, the inertial coefficient and permeability were determined. Similar results hold for the y-direction. Next to both the viscous and pressure forces, also the influence of the

viscous force to the total force ($\frac{f_{v,x}}{f_{v,x}+f_{p,x}}$)) is reported in Table C.3.

$Re_{d_s,x}$	$f_{p,x}$	$f_{v,x}$	$\frac{f_{v,x}}{f_{v,x}+f_{p,x}}$
0.02243	$1.77 \cdot 10^{-9}$	$8.14 \cdot 10^{-10}$	0.315
0.0458	$3.54 \cdot 10^{-9}$	$1.63 \cdot 10^{-9}$	0.315
0.0883	$7.08 \cdot 10^{-9}$	$3.26 \cdot 10^{-9}$	0.315
0.2225	$1.77 \cdot 10^{-8}$	$8.13 \cdot 10^{-9}$	0.315
0.4450	$3.55 \cdot 10^{-8}$	$1.62 \cdot 10^{-8}$	0.313
2.0384	$1.84 \cdot 10^{-7}$	$7.48 \cdot 10^{-8}$	0.290
3.7659	$3.79 \cdot 10^{-7}$	$1.38 \cdot 10^{-7}$	0.267
5.3462	$5.8 \cdot 10^{-7}$	$1.95 \cdot 10^{-7}$	0.251
6.8219	$7.87 \cdot 10^{-7}$	$2.47 \cdot 10^{-7}$	0.239
8.2059	$9.96 \cdot 10^{-7}$	$2.96 \cdot 10^{-7}$	0.229
11.9227	$1.64 \cdot 10^{-6}$	$4.29 \cdot 10^{-7}$	0.208
14.0920	$2.07 \cdot 10^{-6}$	$5.1 \cdot 10^{-7}$	0.197
22.5040	$4.33 \cdot 10^{-6}$	$8.42 \cdot 10^{-7}$	0.163
33.5792	$9.05 \cdot 10^{-6}$	$1.28 \cdot 10^{-6}$	0.124

Table C.3: Results for the pressure and viscous forces acting on the PUC for different Reynolds numbers.

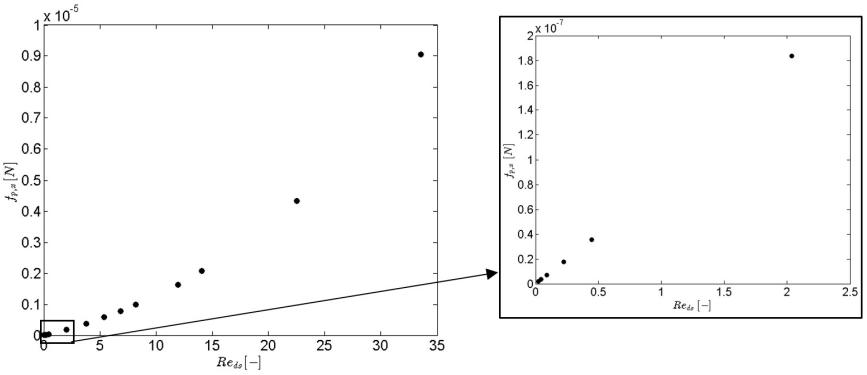

Figure C.5: The pressure force in the x-direction is plotted against the Reynolds number.

The maximum influence of the viscous forces is only 32%. Although both forces increase with increasing Reynolds numbers, the relative influence of the viscous forces rapidly decreases. As expected, for high Reynolds numbers the inertial contribution to the drag becomes constant. Furthermore, from Figure C.5 and Table C.3 it is also clear that the pressure force varies linearly with velocity for small Reynolds numbers ($Re_{d_s} < 2$). For this velocity range, $\beta_{\star,xx}$ and $\beta_{\star,yy}$

can be written as a constant value divided by the velocity ($\overrightarrow{f_p} \sim \overrightarrow{v}$). In case of the studied foam, $\beta_{\star,xx} = 19.76/v_x$ for $Re_{d_s} < 2$ and $\beta_{\star,yy} = 25.68/v_y$ for $Re_{d_s} < 2$.

The large influence of pressure forces at low velocities can be explained with the theory of Stokes flow. Rewriting the momentum equations in dimensionless form, it can be shown that for very low Reynolds numbers, the material derivative of the velocity can be neglected. Equivalently, this means that inertial effects are neglected. However, it is important to note that the pressure gradient can still be significant in comparison to the viscous term. Only neglecting the inertial term but keeping the pressure term results in the so-called Stokes equation [208] (Eq. (C.6)). In this equation the pressure is made dimensionless with respect to $\mu U/L$, where U is the free stream velocity and L is a characteristic length scale.

$$\nabla p - \mu \nabla^2 \overrightarrow{v} = 0 \tag{C.6}$$

For a 3-D sphere, an exact analytical solution for the drag exists. With a, the radius of the sphere and V, the unidirectional incoming velocity, it is given by Eq. (C.7) [208]:

$$D = \underbrace{3\pi\mu aV \int_0^{\pi} cos^2\theta d\theta}_{\text{pressure}} + \underbrace{3\pi\mu aV \int_0^{\pi} sin^3\theta d\theta}_{\text{viscous}} = 2\pi\mu aV + 4\pi\mu aV = 6\pi\mu aV \tag{C.7}$$

In the case of a 3-D sphere, one-third of the drag is due to pressure forces and two-thirds is due to viscous forces. This is also verified with the CFD software used in this work. However, from Table C.3, even higher influences of the pressure forces are observed in the case of metal foam. This is because the struts themselves do not have the shape of a sphere. However, this case can be approximated by flow around a cylinder or a triangular prism. Furthermore, the flow is not around a single strut, but around a staggered array of struts, which has different flow characteristics.

To illustrate the influence of the pressure forces, some additional calculations are performed on the following geometries: (1) a standalone circle and (2) three circles in staggered layout (see Figure C.6). For these simulations, the solution techniques and discretization of the geometry is done in exactly the same way as in case of the finest mesh discussed above. Of course, instead of using the volume averaged equations, the classical Navier-Stokes equations are used here. If the circle diameter is D, the surroundings are $10D$ (see Fig. C.6). The influence of the viscous force on the total force is reported in Figure C.7 for a single circle and three circles placed in a staggered configuration. As can be seen, the staggered layout of the circles results in a lower relative influence of the viscous forces. Furthermore, the middle circle of the staggered layout experiences an even lower influence of viscous forces: only 37%. These observations are consistent with the

observations from Table C.3: the contribution of the viscous forces are very low in a real foam.

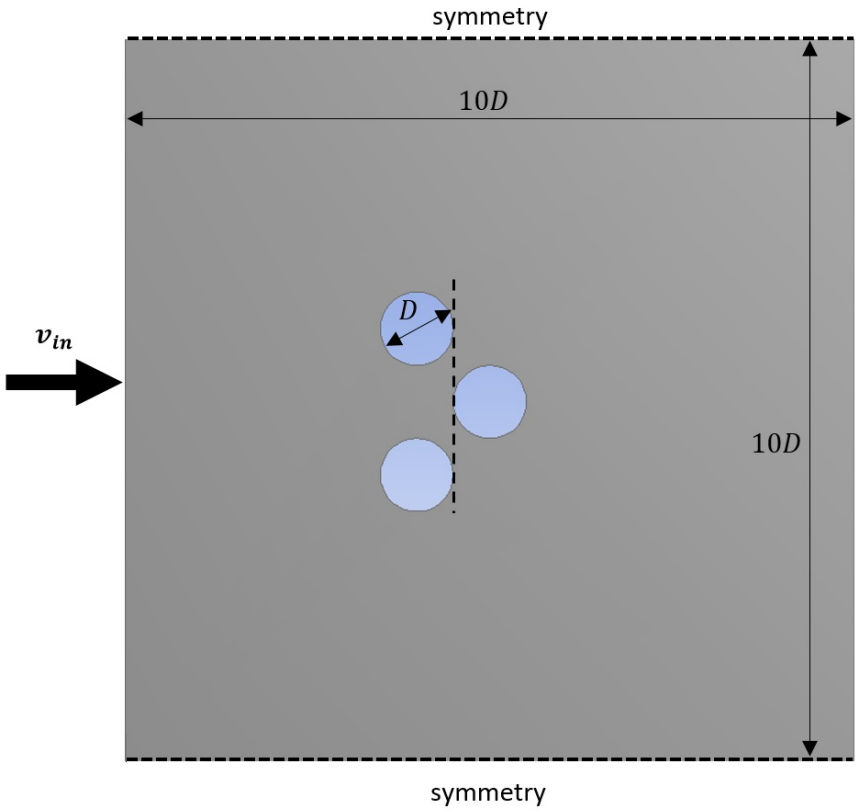

Figure C.6: Illustration of the boundary conditions for the staggered case with circles.

As illustrated in Figure C.7, the pressure influences are not negligible at low velocities. Furthermore, from Figure C.5 it is clear that the pressure drop for $Re_{d_s} < 2$ varies linearly with the velocity. So the pressure drop over the foam can be written as a combination of viscous and pressure forces (over a microscopic element):

$$\frac{dp}{dx} = \underbrace{\frac{\mu}{\kappa_{vis}} V}_{\text{viscous}} + \underbrace{Cv}_{\text{pressure}} \tag{C.8}$$

Note again that this equation is different compared to the classical Darcy equation where the permeability is a combination of viscous and inertial influences. C in Eq. (C.8) is a constant parameter representing the influence of the

pressure drag on the pressure drop. In order to rewrite Eq. (C.8) to the generally known Darcy equation, C should vary linearly with the molecular viscosity, such that it can be written as $C = \frac{\mu}{\kappa_{inertial}}$.

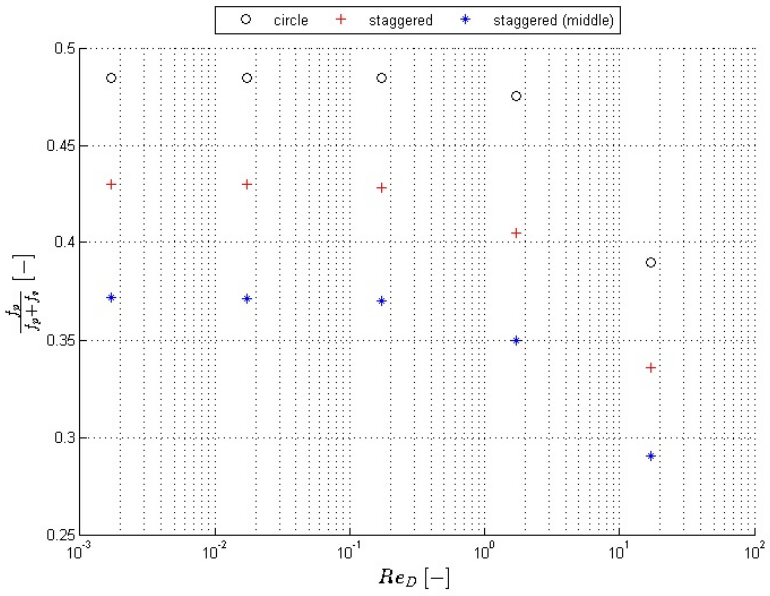

Figure C.7: Illustration of the influence against the velocity of the viscous forces to the total forces acting on the surface of the foam.

To investigate this, the simulations of the staggered layout are repeated but with an increase of the fluid viscosity with a factor of 2. Increasing the viscosity will also increase the viscous forces with the same factor, since there is a linear relation between both. From the dimensionless relation for the pressure in the Stokes flow, it is expected that the pressure gradient will also scale linearly with the viscosity. The results are depicted in Figure C.8. It is confirmed that in creeping flow where inertial effects are negligible and Stokes flow is valid, for $Re_{d_s} < 2$, the pressure drag indeed varies linearly with the viscosity. This means that the Darcy law is still valid, see Eq. (C.9), with $\kappa_{classical} = \kappa$ as reported in open literature. However, one needs to be careful with the interpretation of the Darcy equation. Dukhan et al. [201] state that the Darcy equation represents the viscous drag, yet the permeability as reported in the Darcy equation is really a combination of a viscous and pressure drag component.

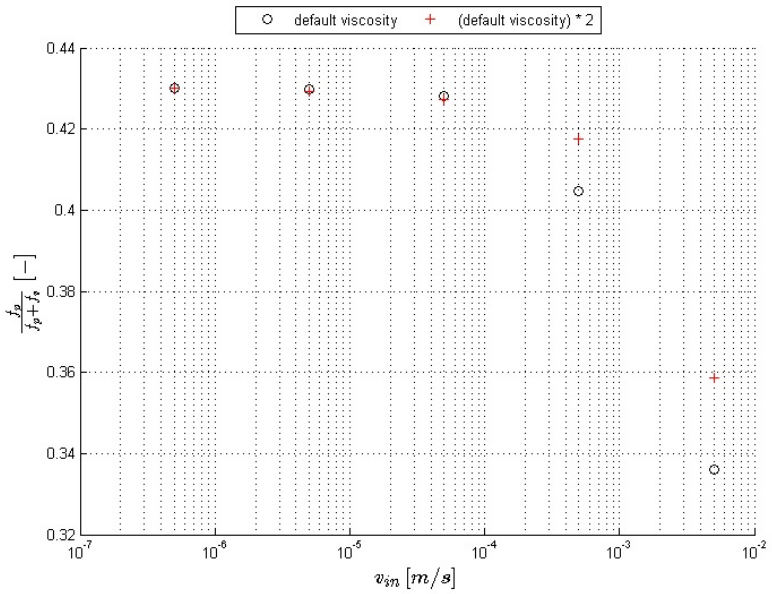

Figure C.8: Illustration of the influence against the velocity of the viscous forces to the total forces acting on the surface of the foam for the staggered circle lay-out and two different viscosities.

$$\frac{dp}{dx} = \frac{\mu}{\kappa_{vis}} v + \frac{\mu}{\kappa_{pressure}} v = \frac{\mu}{\kappa_{classical}} v \tag{C.9}$$

The direct formulation of the permeability and the inertial coefficient shows velocity-dependent behaviour, which is due to two reasons. Firstly, the linear term of the pressure drop is not purely due to the shear stress, since the pressure drag also exhibits linear behaviour for low Reynolds numbers. Similarly, it is not really correct to lump the pressure drag into the inertial term for these low velocities, as in reality it has a linear behaviour and not a quadratic behaviour. Secondly, the real pressure drag versus velocity behaviour is not exactly given by a second order polynomial, which results in velocity-dependent values for the permeability and the inertial coefficient even in the phenomenological approach of the Darcy law.

C.3 Conclusion

This study has pointed out that here is another way to calculate permeability and inertial coefficient. Based on a numerical approach, both closure terms are calculated depending on resp. the viscous and pressure forces acting on a

representative elementary volume of the studied open-cell foam. It was shown that in the creeping flow regime, the linear term in the Darcy law was due to both pressure forces and viscous forces. Furthermore for creeping flow and based on the Stokes equation, it is shown that this pressure force influence is more important than the viscous contribution with a ratio of 70%/30%. Finally, in the volume averaging theory, the pressure forces are associated with inertial effects (quadratic in function of the velocity), which is, strictly speaking, not valid for the creeping flow regime. This results in the inertial coefficient in the direct formulation going to infinity as the velocity goes to zero, varying as the reciprocal of the flow velocity.

D

Preliminary results for VAT technique based on DNS results

D.1 Introduction

In this Appendix, the closure terms will be determined *purely* numerically (as was already introduced in Chapter 4 and Appendix C)[1]. Certainly for the momentum closure terms this is a completely other approach than what is found in open literature. This modelling work, based on the PhD work of De Jaeger [105] (as extensively explained in Section 4.3.3.4), has proved good agreement with experiments in case of a forced convective application [164]. However, this work shows many imperfections in case of natural convection (for forced convective applications these imperfections seem less problematic). Further work is required to study if these problems can be solved. There are still several questions to be solved (although, the author will not go into detail on these issues):

- The foam samples that are studied in natural convection have to be long and narrow. In this way it is possible for air to penetrate easily into the material. However, this makes that there are only a few cells in the width direction of the foam. Regarding the PhD work of Brun [107] and De Jaeger [196] this suggest the question: is there still a length scale separation? And can the VAT technique still be used?

[1] The numerical study from Chapter 7 was a hybrid version between determining the closure terms purely experimentally or purely numerically.

- What about the boundary around the heat sink itself? As the VAT technique supposes that the fluid is completely developed as soon as it enters the heat sink, there could be looked for a boundary condition, a so-called pressure jump condition, to overcome this issue.

The geometry that will be studied is the same geometry as used and simulated in the Chapter 7: the 10 PPI foam as characterized in Table 5.2 of Chapter 5.

D.2 Determine the closure terms

D.2.1 Momentum closure terms

As explained in Appendix C and Section 4.3, there are basically two ways to calculate the momentum closure terms (the permeability and inertial coefficient). One possible approach is to determine these parameters experimentally through wind tunnel experiments. However, as discussed in different chapters of this PhD, the work of Bonnet et al. [142], Innocentini et al. [209, 210] and Dukhan et al. [118, 211, 212] there are a lot of particularities which are not taken into account when doing those experiments, like: geometry characterization, velocity range, wall effects, procedure of curve fitting, entrance and exit effects. Innocentini et al. [209, 210] and Dukhan et al. [118, 211, 212] observed, only for the permeability, differences up to 75% over different literature sources. Based on the results of Innocentini et al., Dukhan et al. came up with the idea of using two permeabilities to characterize the foam: one in the Darcy regime and one for the Forchheimer regime. However, still both permeabilities are determined experimentally. This basic idea of Dukhan is then expanded to a continuous approach in the work of De Jaeger [105]. Recently, the work of De Schampheleire et al. [213] (see Appendix C) has tackled this problem further. To calculate the permeability and inertial coefficient, one needs to calculate the viscous and pressure forces over a representative elementary volume (see Eqs. C.4 and C.5). The determination of such a volume is discussed in Section 6.2.1 and Appendix C. The determination of the viscous force can be done automatically in Ansys-Fluent. For the pressure forces, acting on the surface, a User Defined Function (UDF) has to be written in Ansys-Fluent. Especially for the determination of the viscous forces, the mesh at the boundary layer need to be fine enough. However, in De Jaeger [105] the influence of the fineness of this boundary layer mesh is not discussed. For *'Foam1'* in the work of De Jaeger [105], the number of cells was only 1.03 million, while in this work the number of cells to calculate the momentum closure terms will be higher than 8 million. The reason for this is the fineness of the boundary layer mesh. For this a grid refinement study is done. The results of this refinement study were presented in Table C.1. The results of this momentum closure term modelling for the 10 PPI metal foam (Table 5.2) is shown in Figures C.3 and C.4.

Two orientations are calculated: the x-direction and y-direction. It is shown that the results for the z-direction were the same as for the x-direction. This is a direct result from the geometrical representation of the foam (see Figure C.2). For the sake of simplicity, these results are omitted in this Section.

The **permeability** κ remains constant for low velocities (creeping flow: $Re_{d_s} < 0.25$). For higher Reynolds numbers, the viscous force will start to increase and by observing the trend, it can be stated that the viscous force increases slightly more than linearly with the Darcian velocity. Therefore, the permeability starts to decrease.

The **inertial coefficient** β in the direct formulation is defined as the ratio of the (volume averaged) pressure force to the kinetic energy of the fluid, see Eq. C.4. Upstream of a strut, there is a stagnation zone where kinetic energy descends to zero, which results in a region with high pressure. Downstream, a distinction has to be made between flow regimes with or without recirculation regions in the wakes behind struts. In case of no recirculation ($Re_{d_s} < 10$), the inertial loss factor decreases with increasing Reynolds number. This means that the pressure force increases at a rate lower than the average kinetic energy in the flow domain. For higher Reynolds numbers, it is expected that the increment of pressure force will be balanced by the increase of velocity. This will be again characterised by a nearly constant inertial coefficient.

The determination of the **momentum dispersion** term is the same as in Section 7.2. Again the model for the effective viscosity of Nabovati and Amon [193] is followed and thus $\mu_e/\mu = 1/\phi$

D.2.2 Energy closure terms

The **effective fluid conductivity** $k_{f,e}$ is identical to the one proposed by Brun [107]: $k_{f,e} = 0.98 \cdot \phi k_f$.

The **effective solid conductivity** $k_{s,e}$ is anisotropic in nature. Casted metal foam cells e.g. are elongated as explained in Fig. 1.5[2]. As a result this metal foam has a different conductivity in x- and y-direction. The conductivity in the z-direction is identical to the x-direction, cfr. the construction of the geometrical model. The way in which the conductivities are calculated is identical to the ones presented in Chapter 7. For the x-direction $k_{s,e,x} = 5.4W/mK$. While for the y-direction $k_{s,e,y} = 6.5W/mK$. Also for this solid phase, a grid dependence study is performed. The results will not be mentioned here.

On the other hand, the **interstitial heat transfer coefficient** h_{fs} is determined purely numerically. This is in contrast to the previous Section where it is determined based on experimental results. h_{fs} is calculated following the routine as explained in the PhD of De Jaeger (see Eq. 4.38).

[2]This is one of the reasons why casted metal foam is so difficult to characterize.

D.3 Implementation of the geometric model

The implemented geometry, Figure D.1, is very similar to Figure 7.1. The only difference is the rectangle indicated by 'MF' in Figure 7.1. This 2-D geometric model is meshed with rectangles, the last cell row, which is in contact with the surrounding fluid domain serves as a separate structure (consisting of three rectangles around the metal foam). In this extra solid structure, it is possible to superpose an extra source term. This source term represents the thermal radiation.

The source term that is used to present this thermal radiation is inspired on the Boltzmann equation (see Eq. 2.6). The UDF that is written for this purpose is shown in Figure 7.4.

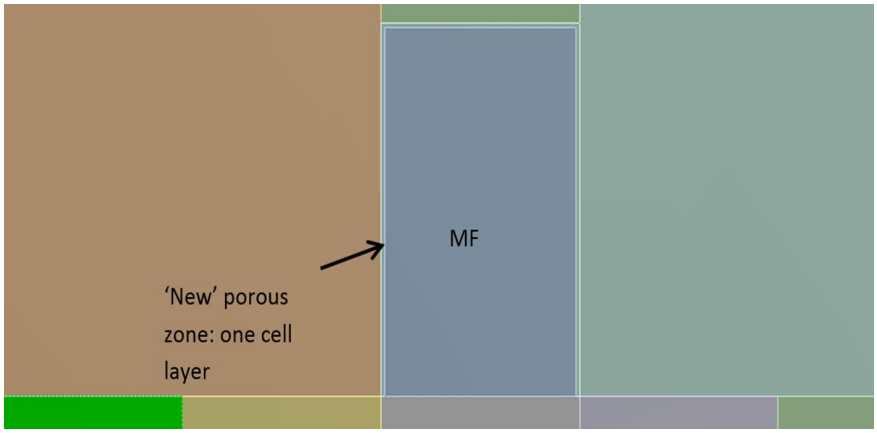

Figure D.1: Illustration of the implementation of the extra porous zone to represent the thermal radiation.

In Section 7.2, this thermal radiation was calculated afterwards. In buoyancy-driven convection, this approach is acceptable as the temperature differences over the solid structure are not so large, see Figure 7.5 for example. However, the radiative heat transfer will lower the solid temperature which will decrease the buoyancy forces and thus the heat transfer coefficient. Therefore, to be more precise the previously discussed approach will be taken to implement radiation directly.

The discretization of the geometric model is done exactly the same way as in Section 7.2.

For a more detailed overview, the readers are referred to the review paper of De Schampheleire et al. [194].

D.4 Preliminary results, discussion and conclusions

The results for the temperature and velocity profile of the fluid are shown in Figures D.3 and D.4, respectively. The temperature profile of the foam itself is given in Figure D.5. It is clear that no fluid is able to penetrate into the foam. This is different compared to Fig. 7.4.

Figure D.2: Illustration of the penetration of air flow through metal foam. Measurement done by Billiet et al. [16] for a 150x100 mm^2 metal foam sample.

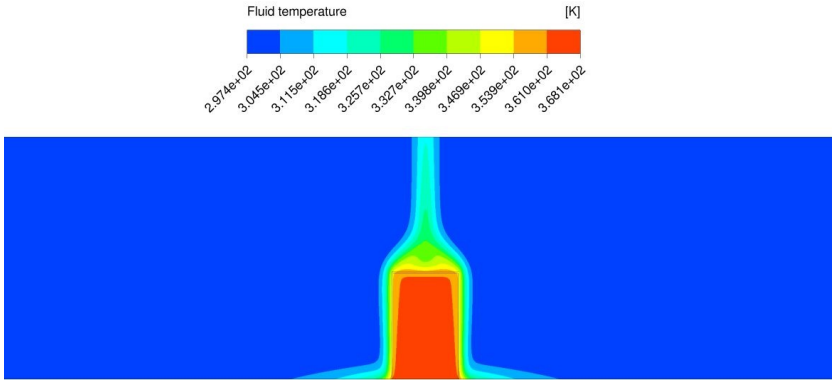

Figure D.3: Temperature contours for a 40 mm foam heat sink and the fluid phase in the porous zone (ΔT = 70.6K). Closure terms are determined through DNS results.

The major difference between this and the previous section is the determination of the closure terms. For low velocities in the foam, the results for permeability

will be the same. However, the inertial coefficient keeps on increasing for decreasing velocities[3]. Due to this the flow resistance to penetrate into the foam will also increase, which decreases the fluid flow even further.

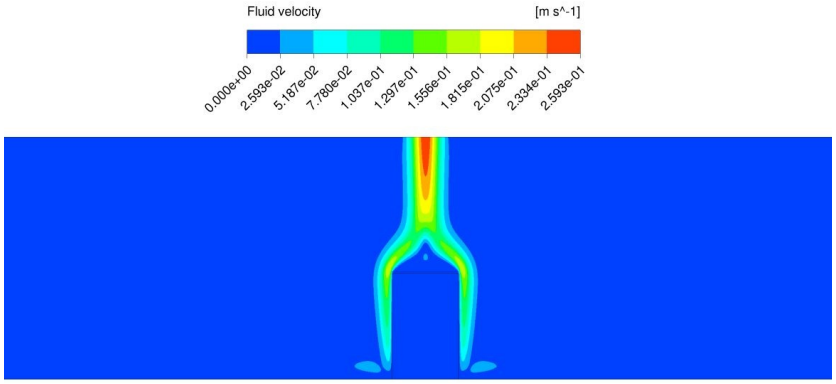

Figure D.4: Velocity contours for a 40 mm foam heat sink (ΔT = 70.6K). Closure terms are determined through DNS results.

The numerical and experimental results show no match. Due to the different determination of the closure terms, there are no fluid velocities in the foam domain. However, compared to the experimental results of Billiet et al. [16] there should be clearly some fluid in the foam.

[3]The fact that the inertial coefficient increases for decreasing velocities is explained in Appendix C. This Appendix is based on the work of De Schampheleire et al. [213].

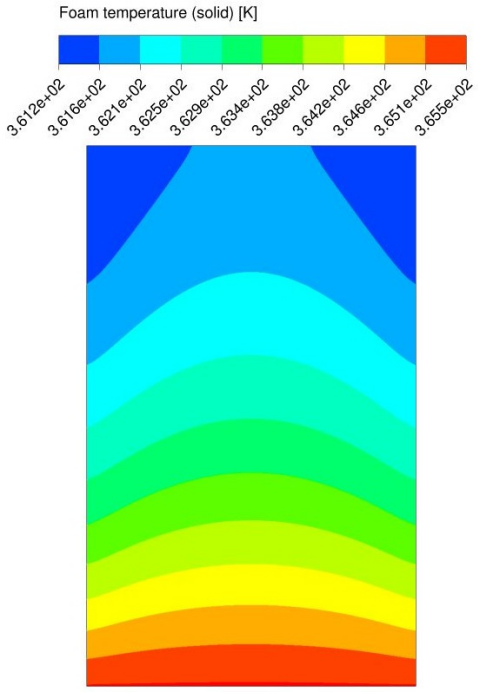

Figure D.5: Solid temperature contours for a 40 mm foam heat sink (ΔT = 70.6K). Closure terms are determined through DNS results.

The difference between the numerical and experimental results bring us to the following question, which has never been brought up before in open literature: can buoyancy-driven convection in multi-dimensional heat sinks be modelled through a volume averaged model?. The fact that volume averaging assumes that the flow is completely developed as soon as it enters the porous structure, does seem to make this a valuable question. This assumption is certainly not valid for the materials and dimensions studied in this work. Future research is necessary to further investigate the possibilities of VAT for multidimensional heat sinks in natural convection.

E
Publications

E.1 Related publications in peer reviewed international journals

- Lehmhus D., Vesenjak M., De Schampheleire S. and Fiedler T. *From Stochastic Foam to Designed Structure: Balancing Cost and Performance of Cellular Metals*. Materials; 10, 922, doi:10.3390/ma10080922, 2017.

- De Schampheleire S., De Kerpel K., Ameel B., Bacgi O., De Paepe M. *Discussion on the Effect of a Fluid Domain around Fins and Grid Discretization in Buoyancy-Driven Convection*. Heat Transfer Engineering; p. 1531-1546, 38(18), 2017.

- De Schampheleire S., De Kerpel K., Ameel B., De Jaeger P., Bacgi O., De Paepe M. *A discussion on the interpretation of the Darcy equation in case of open-cell metal foam based on numerical simulations*. Materials; 9(6), 409, 2016.

- De Schampheleire S., De Jaeger P., De Kerpel K., Ameel B., Huisseune H., De Paepe M. *How to study thermal applications of open-cell metal foam: experiments and computational fluid dynamics*. Materials; 9(2), 94, 2016.

- De Schampheleire S., De Kerpel K., De Jaeger P., Huisseune H., Ameel B., De Paepe M. *Buoyancy Driven Convection in Open-cell Aluminium Foam*

Using the Volume Averaging Technique. Applied Thermal Engineering; 79:225 - 233, 2015.

- De Schampheleire S., De Jaeger P., Reynders R., De Kerpel K., Ameel B., T´Joen C. and De Paepe M. *Experimental study of buoyancy-driven flow in open-cell aluminium foam heat sinks.* Applied Thermal Engineering, 59(1-2):30 - 40, 2013.
- De Schampheleire S., De Jaeger P., Huisseune H., Ameel B., T´Joen C., De Kerpel K. and De Paepe M. *Thermal hydraulic performance of 10 PPI aluminium foam as alternative for louvered fins in an HVAC heat exchanger.* Applied Thermal Engineering; 51(1-2):371 - 382, 2013.

E.2 Other publications in peer reviewed international journals

- De Kerpel K., De Schampheleire S., De Keulenaer T., and De Paepe M. *Effect of the bend geometry on the two-phase frictional pressure drop and flow behaviour in the vicinity of the bend*. Applied Thermal Engineering, 104:403 413, 2016.
- De Kerpel K., De Schampheleire S., Steuperaert H., and De Paepe M. *Experimental study of the effect of felt wick porosity on capillary-driven heat pipes*. Applied Thermal Engineering, 96:690 - 698, 2016.
- De Kerpel K., De Schampheleire S., De Keulenaer T., and De Paepe M. *Two-phase frictional pressure drop and flow behaviour up- and downstream of a sharp return bend*. Applied Thermal Engineering, 93(C):824 - 838, 2016.
- De Schampheleire S., De Kerpel K., Ameel B., Huisseune H. and De Paepe M. *Thermal Analysis of a Commercial Plate Fin Heat Exchanger with Non-uniform Inlet Flow Conditions*. Heat Transfer Engineering; 37(17), 2016.
- Billiet M., De Schampheleire S., Huisseune H. and De Paepe M. *Influence of orientation and radiative heat transfer on aluminum foams in Buoyancy-induced convection*. Materials; 8(10):6792-6805, 2015.
- De Kerpel K., De Schampheleire S., De Keulenaer T. and De Paepe M. *Two-phase flow regime assignment based on wavelet features of a capacitance signal*. International Journal of Heat and Fluid Flow, 56(C):317 - 323, 2015.
- Huisseune H., De Schampheleire S., Ameel B. and De Paepe M. *Comparison of metal foam heat exchangers to a finned heat exchanger for low*

Reynolds number applications. International Journal of Heat and Mass Transfer, 89:1 - 10, 2015.

- De Schampheleire S., De Kerpel K., Deruyter T., De Jaeger P. and De Paepe M. *Experimental Study of Small Diameter Fibres as Wick Material for Capillary-driven Heat Pipes*. Applied Thermal Engineering; 78:258 267, 2015.

- De Kerpel K., De Keulenaer T., De Schampheleire S. and De Paepe M. *Capacitance sensor measurements of upward and downward two-phase flow in vertical return bends*. International Journal of Multiphase Flow, 64:1 - 10, 2014.

- Ameel B., Degroote J., Huisseune H., De Schampheleire S., Vierendeels J. and De Paepe M. *Accounting for the effect of the heat exchanger length in the performance evaluation of compact fin and tube heat exchangers*. Applied Thermal Engineering, 65(1-2):544 - 553, 2014.

- De Kerpel K., Ameel B., De Schampheleire S, T´Joen C., Canière H. and De Paepe M. *Calibration of a capacitive void fraction sensor for small diameter tubes based on capacitive signal features*. Applied Thermal Engineering, (3):77 - 83, 2014.

- Lecompte S., Huisseune H., van den Broeck M., De Schampheleire S and De Paepe M. *Part load based thermo-economic optimization of the Organic Rankine Cycle (ORC) applied to a combined heat and power (CHP) system*. Applied Energy, 111:871-881, 2013.

- De Jaeger P., T´Joen C., Huisseune H., Ameel B., De Schampheleire S. and De Paepe M. *Influence of geometrical parameters of open-cell aluminum foam on thermohydraulic performance*. Heat Transfer Engineering, 34(14):1202-1215, 2013.

- Huisseune H., T´Joen C., De Jaeger P., Ameel B., De Schampheleire S. and De Paepe M. *Performance enhancement of a louvered fin heat exchanger by using delta winglet vortex generators*. International journal of heat and mass transfer, 56(1-2):475-487, 2013.

- Huisseune H., T´Joen C., De Jaeger P., Ameel B., De Schampheleire S. and De Paepe M. *Influence of the louver and delta winglet geometry on the thermal hydraulic performance of a compound heat exchanger*. International journal of heat and mass transfer, 57(1):58-72, 2013.

- Huisseune H., T´Joen C., De Jaeger P., Ameel B., De Schampheleire S. and De Paepe M. *Performance analysis of a compound heat exchanger by screening its design parameters*. Applied Thermal Engineering, 51(1-2).:490-501, 2013.

- Ameel B., Degroote J., T´Joen C., De Jaeger P., Huisseune H., De Schampheleire S., Vierendeels J. and De Paepe M. *Optimization of X-shaped louvered fin and tube heat exchangers while maintaining the physical meaning of the performance evaluation criterion*. Applied Thermal Engineering, 58(1-2):136 - 145, 2013.

- De Jaeger P., T´Joen C., Huisseune H., Ameel B., De Schampheleire S. and De Paepe M. *Assessing the influence of four cutting methods on the thermal contact resistance of open-cell aluminum foam*. International Journal of Heat and Mass Transfer, 55(21-22):6142-6151, 2013.

- De Jaeger P., T´Joen C., Huisseune H., Ameel B., De Schampheleire S. and De Paepe M. *Assessing the influence of four bonding methods on the thermal contact resistance of open-cell aluminum foam*. International Journal of Heat and Mass Transfer, 55(21-22):6200-6210, 2013.

E.3 Publication in peer reviewed journals (not included in WOS)

- De Schampheleire S. and De Paepe M. *Biomass conversion opportunities in Belgium: complexity and available technologies*. Revue E - Tijdschrift E, 128(3):16-22, 2012.

E.4 Related publications in proceedings of international conferences

- De Schampheleire S., De Kerpel K., Ameel B., Sharif A., Bagci O. and De Paepe M. *On the numerical simulation of fins in natural convection*. 11th International Conference on Heat Transfer, Fluid Mechanics and Thermodynamics, Proceedings. Costa del Sol, Spain, 2016.

- De Schampheleire S., De Jaeger P., De Kerpel K., Ameel B., Huisseune H., Bagci O. and De Paepe M. *On the scatter of experiments done with open-cell metal foam in open literature*. 11th International Conference on Heat Transfer, Fluid Mechanics and Thermodynamics, Proceedings. Costa del Sol, Spain, 2016.

- De Schampheleire S., De Kerpel K., Ameel B., Sharif A., Bagci O. and De Paepe M. *How to perform numerical simulations on fins in buoyancy-driven heat transfer?*. 7^{th} European Thermal Sciences Conference, Proceedings. Krakow, Poland, 2016.
- De Schampheleire S., De Kerpel K., Deruyter T. and De Paepe M. *Study of new wick material for capillary-driven heat pipes*. UK Heat Transfer Conference, Proceedings. Edinburgh, UK, 2015.
- De Schampheleire S., De Kerpel K., Huisseune H. and De Paepe M. *Numerical study on a metal foam heat sink in Buoyancy driven convection*. 9th International Conference on Porous Metals and Metallic Foams, Proceedings. Barcelona, Spain, 2015.
- De Schampheleire S., De Kerpel K., Huisseune H., De Jaeger P., Ameel B. and De Paepe M. *Applying the volume averaging theory to open-cell metal foam in natural convection/radiation*. 11th International Conference on Heat Transfer, Fluid Mechanics and Thermodynamics, Proceedings. Kruger Park, South-Africa, 2015.
- De Schampheleire S., De Kerpel K., Deruyter T. and De Paepe M. *Small diameter fibres as new wick material for capillary-driven heat pipes*. 11th International Conference on Heat Transfer, Fluid Mechanics and Thermodynamics, Proceedings. Kruger Park, South-Africa, 2015.
- De Schampheleire S., De Kerpel K., De Jaeger P., Huisseune H., and De Paepe M. *Natural convection in open-cell aluminium foam using the volume averaging technique*. Cellular Materials, Proceedings. Dresden, Germany, 2014.
- De Schampheleire S., De Kerpel K., Kennof G., Pirmez P., Huisseune H. and De Paepe M. *Comparison of aluminium foam finned heat sinks and effect of painting and orientation in buoyancy-driven convection*. International Heat Transfer Conference, Proceedings. Kyoto, Japan: International heat transfer conference, 2014.
- De Schampheleire S., De Jaeger P., De Kerpel K., Ameel B., Huisseune H. and De Paepe M. *Experimental study of free convection in open-cell aluminum foam*. 8th International Conference on Porous Metals and Metallic Foams, Proceedings. Orlando, U.S.A., 2014.
- De Schampheleire S., De Kerpel K., Kennof G., Pirmez P., Huisseune H., Ameel B. and De Paepe M. *Thermal performance study of finned foam heat sinks and the effect of painting and inclination angle in natural convective heat transfer*. 10th International Conference on Heat Transfer, Fluid

Mechanics and Thermodynamics, Proceedings. Orlando, Florida, USA, p. 2337-2343, 2014.

- De Schampheleire S., De Kerpel K., Ameel B., Huisseune H. and De Paepe M. *Thermal influence of non-uniform inlet flow conditions for a commercial plate fin heat exchanger*. 10th International Conference on Heat Transfer, Fluid Mechanics and Thermodynamics, Proceedings. Orlando, Florida, USA, p. 216-223, 2014.

- De Schampheleire S., De Jaeger P., Huisseune H., Ameel B., De Kerpel K. and De Paepe M. *Numerical and experimental investigation of a pressed-fit 10 PPI aluminium foam heat exchanger*. 6^{th} European Thermal Sciences Conference, Proceedings. Poitiers, France, 2013.

- De Schampheleire S., De Jaeger P., De Kerpel K., Ameel B., Huisseune H. and De Paepe M. *Hydraulic characterisation of the porous properties in open-cell aluminum foam*. Eurotherm Seminar n96 on Convective Heat Transfer Enhancement, Proceedings. Brussels, Belgium, 2013.

- De Schampheleire S., De Jaeger P., De Kerpel K., Ameel B., Huisseune H. and De Paepe M. *Influences of bonding technology, pore density and foam height for natural convection in open-cell aluminum foam heat sinks*. 8^{th} World Conference on Experimental Heat Transfer, Fluid Mechanics and Thermodynamics, Proceedings. Lisbon, Portugal, 2013.

- De Schampheleire S., De Jaeger P., Huisseune H., Ameel B., TJoen C. and De Paepe M. *10 PPI metal foam as alternative for louvered fins in a HVAC heat exchanger*. 6^{th} European Thermal Sciences Conference, Proceedings. Poitiers, France, 2012.

- De Schampheleire S., De Jaeger P., Huisseune H., Ameel B., TJoen C. and De Paepe M. *Thermo-hydraulic comparison of 10 PPI metal foam and louvered fins for low velocity applications* 9^{th} International Conference on Heat Transfer, Fluid Mechanics and Thermodynamics, Proceedings. Malta, p. 445-453, 2012.

E.5 Book editor

- De Schampheleire S., Lehmhus D., Vesenjak M. and Fielder T. *Bookeditor: Special Issue 'Metal foams: synthesis, characterization and applications', Journal Materials.* Publisher: MDPI AG, Basel, Switzerland, 2016.

E.6 Book chapters

- De Schampheleire S., De Kerpel K. and De Paepe M. *Biomass conversion technologies for countries with low biomass production potential*. Bioenergy, in Energy Science and Technology 7. Studium Press LLC, Houston, Texas, U.S.A., 2014.

References

[1] C. Kittel and H. Kroemer. *Thermal Physics*. W. H. Freeman, 1980.

[2] *Lawrence Livermore National Laboratory - Energy flow charts (2015)*. https://flowcharts.llnl.gov/. Accessed: 2016-05-20.

[3] *What is Moore's law*. http://www.extremetech.com/extreme/210872-extremetech-explains-what-is-moores-law. Accessed: 2016-05-20.

[4] *The Economist explains: The end of Moore's law*. http://www.economist.com/blogs/economist-explains/2015/04/economist-explains-17. Accessed: 2016-05-20.

[5] *Different Intel Core i7 Microprocessors*. https://en.wikipedia.org/wiki/List_of_Intel_Core_i7_microprocessors. Accessed: 2016-05-20.

[6] C.Y. Zhao, T.J. Lu, H.P. Hodson, and J.D. Jackson. *The temperature dependence of effective thermal conductivity of open-celled steel alloy foams*. Mater. Sci. Eng. A, 367(12):123 – 131, 2004.

[7] ERG Materials and Aerospace. *Duocel foam*. Accessed on November 4 2015, through http://www.ergaerospace.com/Aluminum-properties.html.

[8] D. Walz. *Reticulated Foam Structure*, 1976. Oakland, California, U.S.A., US Patent - 3946039.

[9] M-Pore. *Casted foam from M-Pore*. Accessed on November 4 2015, through http://www.m-pore.de/.

[10] Alveotec. *Information on how casted metal foam is produced with a stacked bed of solvable spheres*. Accessed on November 4 2015, through http://www.alveotec.fr/fr/innovation.html.

[11] Constellium. *Foam made by constellium (production with stacked bed of solvable spheres)*. Accessed on November 4 2015,

through http://www.constellium.com/media/news-and-press-releases/press-releases-only/constellium-showcases-its-innovative-aluminium-technologies-at-the-duesseldorf-aluminium-trade-fair-from-vision-to-reality.

[12] M. Borovinsek and Z. Ren. *Computational modelling of irregular open-cell foam behaviour under impact loading*. Materialswiss Werkst, 39(2):114–120, 2008.

[13] C. T'Joen, P. De Jaeger, H. Huisseune, S. Van Herzeele, N. Vorst, and M. De Paepe. *Thermo-hydraulic study of a single row heat exchanger consisting of metal foam covered round tubes*. Int. J. Heat Mass Transfer, 53(1516):3262 – 3274, 2010.

[14] Tuchinskiy Lev. *Novel fabrication technology for metal foams*. J. Adv. Mater., 37:60–65, 2005.

[15] Loupi. *Dissipateur pour led LOUPI*. Accessed on November 4 2015, through http://www.alveotec.fr/fr/nos-realisations/dissipateur-pour-led-loupi_10.html.

[16] M. Billiet, S. De Schampheleire, H. Huisseune, and M. De Paepe. *Influence of Orientation and Radiative Heat Transfer on Aluminum Foams in Buoyancy-Induced Convection*. Materials, 8(10).

[17] G. Nellis and S. Klein. *Heat Transfer*. Cambridge University Press, 2009.

[18] J.H. Lienhard. *A Heat Transfer Textbook: Fourth Edition*. Dover Civil and Mechanical Engineering. Dover Publications, 2013.

[19] T. Ohmura, M. Tsuboi, and T. Tomimura. *Estimation of the Mean Thermal Conductivity of Anisotropic Materials*. International Journal of Thermophysics, 23(3):843–853, 2002.

[20] W.M. Rohsenow, J.P. Hartnett, and Y.I. Cho. *Handbook of heat transfer*. McGraw-Hill handbooks. McGraw-Hill, 1998.

[21] Ludwig Boltzmann. *On certain questions of the theory of gases*. Nature, 51:413–415, 1895.

[22] J.R. Howell, M.P. Menguc, and R. Siegel. *Thermal Radiation Heat Transfer, 5th Edition*. CRC Press, 2010.

[23] G. Ellison. *Thermal Computations for Electronics: Conductive, Radiative, and Convective Air Cooling*. CRC Press, 2010.

[24] Herrmann Schlichting and Klaus Gersten. *Boundary-layer theory*. Springer Science & Business Media, 2003.

[25] H. Huisseune. *Performance evaluation of louvered fin compact heat exchangers with vortex generators*. PhD thesis, Ghent University, Belgium, 2011.

[26] R.K. Shah and D.P. Sekulic. *Fundamentals of Heat Exchanger Design*. Wiley, 2003.

[27] K. Takeishi, Y. Oda, Y. Miyake, and Y. Motoda. *Convective Heat Transfer and Pressure Loss in Rectangular Ducts With Inclined Pin-Fin on a Wavy Endwall*. ASME Journal of engineering gas turbines power, 2013.

[28] *ansys user guide (ansys release 2015)*. http://148.204.81.206/Ansys/readme.html. Accessed: 2016-05-20.

[29] *heat sinks from Aavid for natural convective purposes*. http://www.aavid.com/solutions/extruded. Accessed: 2016-05-20.

[30] Y.A. Çengel. *Heat Transfer: A Practical Approach*. McGraw-Hill series in mechanical engineering. McGraw-Hill, 2003.

[31] *Fanless Apple Macbooks 12"*. http://www.computerworld.com/article/2894581/apple-demotes-air-with-new-fanless-12-in-retina-macbook-as-its-lightest-thinnest-computer.html. Accessed: 2016-05-20.

[32] *Texas instruments: semiconductor and IC package thermal metrics*. http://www.ti.com/lit/an/spra953b/spra953b.pdf. Accessed: 2016-05-20.

[33] M.G. Cooper, B.B. Mikic, and M.M. Yovanovich. *Thermal contact conductance*. International Journal of Heat and Mass Transfer, 12(3):279 – 300, 1969.

[34] N Vutz and SW Angrist. *Thermal contact resistance of anisotropic materials*. Journal of Heat Transfer, 92(1):17–20, 1970.

[35] C.V. Madhusudana. *Thermal Contact Conductance*. Mechanical Engineering Series. Springer International Publishing, 2013.

[36] Karthik Narendra Babu. *Thermal contact resistance: experiments and simulations*. http://publications.lib.chalmers.se/records/fulltext/223157/223157.pdf, 2015. Accessed: 2016-05-20.

[37] M. Grujicic, C.L. Zhao, and E.C. Dusel. *The effect of thermal contact resistance on heat management in the electronic packaging*. Applied Surface Science, 246(13):290 – 302, 2005.

[38] Seri Lee. *Calculating spreading resistance in heat sinks*. Electronics Cooling, 4:30–33, 1998.

[39] Bjorn Vermeersch and Gilbert De Mey. *A fixed-angle heat spreading model for dynamic thermal characterization of rear-cooled substrates*. In Semiconductor Thermal Measurement and Management Symposium, 2007. SEMI-THERM 2007. Twenty Third Annual IEEE, pages 95–101. IEEE, 2007.

[40] *Surface-embedded heat pipe heat sinks*. http://www.dau-at.com/741_Embedded-Heat-Pipe-Heat-Sink-Solutions.aspx?LNG=en. Accessed: 2016-05-20.

[41] Sven De Schampheleire, Peter De Jaeger, Robin Reynders, Kathleen De Kerpel, Bernd Ameel, Christophe T'Joen, Henk Huisseune, Steven Lecompte, and Michel De Paepe. *Experimental study of buoyancy-driven flow in open-cell aluminium foam heat sinks*. Applied Thermal Engineering, 59(12):30 – 40, 2013.

[42] N. Nagarani, K. Mayilsamy, A. Murugesan, and G. Sathesh Kumar. *Review of utilization of extended surfaces in heat transfer problems*. Renewable and Sustainable Energy Reviews, 29:604 – 613, 2014.

[43] Md. Farhad Ismail, Muhammad Noman Hasan, and Suvash C. Saha. *Numerical study of turbulent fluid flow and heat transfer in lateral perforated extended surfaces*. Energy, 64:632 – 639, 2014.

[44] E.A.M. Elshafei. *Natural convection heat transfer from a heat sink with hollow/perforated circular pin fins*. Energy, 35(7):2870 – 2877, 2010.

[45] Abdullah H. AlEssa and Mohamad I. Al-Widyan. *Enhancement of natural convection heat transfer from a fin by triangular perforation of bases parallel and toward its tip*. Applied Mathematics and Mechanics, 29(8):1033–1044, 2008.

[46] M. Dogan, Mecit Sivrioglu, and Onder Ylmaz. *Numerical analysis of natural convection and radiation heat transfer from various shaped thin fin-arrays placed on a horizontal plate-a conjugate analysis*. Energy Conversion and Management, 77:78 – 88, 2014.

[47] David Calamas and John Baker. *Tree-like branching fins: Performance and natural convective heat transfer behavior*. International Journal of Heat and Mass Transfer, 62:350 – 361, 2013.

[48] Yue-Tzu Yang and Huan-Sen Peng. *Numerical study of the heat sink with un-uniform fin width designs*. International Journal of Heat and Mass Transfer, 52(1516):3473 – 3480, 2009.

[49] Yue-Tzu Yang and Huan-Sen Peng. *Numerical study of pin-fin heat sink with un-uniform fin height design*. International Journal of Heat and Mass Transfer, 51(1920):4788 – 4796, 2008.

[50] Adrian Bejan. *Constructal-theory network of conducting paths for cooling a heat generating volume*. International Journal of Heat and Mass Transfer, 40(4):799 – 816, 1997.

[51] Henry Darcy. *Les fontaines publiques de la ville de Dijon*. 1856.

[52] O. Laguerre, S. Ben Amara, G. Alvarez, and D. Flick. *Transient heat transfer by free convection in a packed bed of spheres: Comparison between two modelling approaches and experimental results*. Applied Thermal Engineering, 28(1):14 – 24, 2008.

[53] Carlos Teixeira. *Direct numerical simulation of fixed-bed reactors: effect of random packing*. 2013.

[54] P. De Jaeger, C. TJoen, H. Huisseune, B. Ameel, S. De Schampheleire, and M. De Paepe. *Assessing the influence of four bonding methods on the thermal contact resistance of open-cell aluminum foam*. International Journal of Heat and Mass Transfer, 55(2122):6200 – 6210, 2012.

[55] CoolInnovations. *Products available at CoolInnovations for natural convection purpose*. Accessed on November 4 2015, through http://www.coolinnovations.com/products/heatsinks/natural-convection/overview.

[56] *heat sinks from ATS heat sinks for natural convective purposes*. http://www.qats.com/eShop.aspx?productGroup=0&subGroup=0&group=All&q=Profile. Accessed: 2016-05-20.

[57] *heat sinks from Alpha heat sinks for natural convective purposes*. http://www.micforg.co.jp/en/temeasuree.html. Accessed: 2016-05-20.

[58] A. Bhattacharya and R.L. Mahajan. *Metal Foam and Finned Metal Foam Heat Sinks for Electronics Cooling in Buoyancy-Induced Convection*. Journal of Electronic Packaging, 128:256–266, 2005.

[59] Younghwan Joo and Sung Jin Kim. *Comparison of thermal performance between plate-fin and pin-fin heat sinks in natural convection*. International Journal of Heat and Mass Transfer, 83:345 – 356, 2015.

[60] Bin Li and Chan Byon. *Investigation of natural convection heat transfer around a radial heat sink with a concentric ring*. International Journal of Heat and Mass Transfer, 89:159 – 164, 2015.

[61] Gustavo Ledezma and Adrian Bejan. *Heat sinks with sloped plate fins in natural and forced convection*. International Journal of Heat and Mass Transfer, 39(9):1773 – 1783, 1996.

[62] R. Bahadur and A. Bar-Cohen. *Thermal design and optimization of natural convection polymer pin fin heat sinks*. IEEE Transactions on Components and Packaging Technologies, 28(2):238–246, June 2005.

[63] Pankaj Singh and Anil K. Patil. *Experimental investigation of heat transfer enhancement through embossed fin heat sink under natural convection*. Experimental Thermal and Fluid Science, 61:24 – 33, 2015.

[64] Rajesh Baby and C. Balaji. *Thermal optimization of $\{PCM\}$ based pin fin heat sinks: An experimental study*. Applied Thermal Engineering, 54(1):65 – 77, 2013.

[65] Yong Kang Khor, Yew Mun Hung, and Boon Kian Lim. *On the role of radiation view factor in thermal performance of straight-fin heat sinks*. International Communications in Heat and Mass Transfer, 37(8):1087 – 1095, 2010.

[66] K. K. Sikka, K. E. Torrance, C. U. Scholler, and P. I. Salanova. *Heat sinks with fluted and wavy plate fins in natural and low-velocity forced convection*. IEEE Transactions on Components and Packaging Technologies, 25(2):283–292, 2002.

[67] Pradeep. M. Kamath, C. Balaji, and S.P. Venkateshan. *Experimental investigation of flow assisted mixed convection in high porosity foams in vertical channels*. International Journal of Heat and Mass Transfer, 54(2526):5231 – 5241, 2011.

[68] Umesh V. Awasarmol and Ashok T. Pise. *An experimental investigation of natural convection heat transfer enhancement from perforated rectangular fins array at different inclinations*. Experimental Thermal and Fluid Science, 68:145 – 154, 2015.

[69] Filino Harahap and Daru Setio. *Correlations for heat dissipation and natural convection heat-transfer from horizontally-based, vertically-finned arrays*. Applied Energy, 69(1):29 – 38, 2001.

[70] S. G. Taji, G. V. Parishwad, and N. K. Sane. *Experimental investigation of heat transfer and flow pattern from heated horizontal rectangular fin array under natural convection*. Heat and Mass Transfer, 50(7):1005–1015, 2014.

[71] Qie Shen, Daming Sun, Ya Xu, Tao Jin, and Xu Zhao. *Orientation effects on natural convection heat dissipation of rectangular fin heat sinks mounted on LEDs*. International Journal of Heat and Mass Transfer, 75:462 – 469, 2014.

[72] Roody Charles and Chi-Chuan Wang. *A novel heat dissipation fin design applicable for natural convection augmentation*. International Communications in Heat and Mass Transfer, 59:24 – 29, 2014.

[73] A. Güvenç and H. Yüncü. *An experimental investigation on performance of fins on a horizontal base in free convection heat transfer*. Heat and Mass Transfer, 37(4):409–416.

[74] H. Yüncü and G. Anbar. *An experimental investigation on performance of rectangular fins on a horizontal base in free convection heat transfer*. Heat and Mass Transfer, 33(5):507–514.

[75] Filino Harahap, Herry Lesmana, and Poetro Lebdo Sambegoro. *Concurrent calorimetric and interferometric studies of steady-state natural convection from miniaturized horizontal single plate-fin systems and plate-fin arrays*. Heat and mass transfer, 46(8-9):929–942, 2010.

[76] Antonios I. Zografos and J. Edward Sunderland. *Natural convection from pin fin arrays*. Experimental Thermal and Fluid Science, 3(4):440 – 449, 1990.

[77] V. Rammohan Rao and S.P. Venkateshan. *Experimental study of free convection and radiation in horizontal fin arrays*. International Journal of Heat and Mass Transfer, 39(4):779 – 789, 1996.

[78] Ren-Tsung Huang, Wen-Junn Sheu, and Chi-Chuan Wang. *Orientation effect on natural convective performance of square pin fin heat sinks*. International Journal of Heat and Mass Transfer, 51(910):2368 – 2376, 2008.

[79] Ahmet Ali Sertkaya, efik Bilir, and Suna Kargc. *Experimental investigation of the effects of orientation angle on heat transfer performance of pin-finned surfaces in natural convection*. Energy, 36(3):1513 – 1517, 2011.

[80] D. Sahray, H. Shmueli, G. Ziskind, and R. Letan. *Study and Optimization of Horizontal-Base Pin-Fin Heat Sinks in Natural Convection and Radiation*. Journal of heat transfer, 132(1):012503, 2009.

[81] E.M. Sparrow and S.B. Vemuri. *Orientation effects on natural convection/radiation heat transfer from pin-fin arrays*. International Journal of Heat and Mass Transfer, 29(3):359 – 368, 1986.

[82] Massimo Corcione. *Natural convection heat transfer above heated horizontal surfaces*. In 5th WSEAS International Conference on Heat and Mass Transfer (HMT08), Acapulco, Mexico, Jan, pages 25–27, 2008.

[83] W.H. McAdams. *Heat transmission*. McGraw-Hill series in chemical engineering. McGraw-Hill, 1954.

[84] F.P. Incropera. *Fundamentals of heat and mass transfer*. Number v. 1 in Fundamentals of Heat and Mass Transfer. John Wiley, 2007.

[85] E Sadeghi, S Hsieh, and M Bahrami. *Thermal conductivity and contact resistance of metal foams*. Journal of Physics D: Applied Physics, 44(12):125406, 2011.

[86] Christopher T. DeGroot, Derek Gateman, and Anthony G. Straatman. *The Effect of Thermal Contact Resistance at Porous-Solid Interfaces in Finned Metal Foam Heat Sinks*. Journal of electronic packaging, 132, 2010.

[87] Indranil Ghosh. *Heat-transfer analysis of high porosity open-cell metal foam*. Journal of Heat Transfer, 130(3):034501, 2008.

[88] V. Kathare, J.H. Davidson, and F.A. Kulacki. *Natural convection in water-saturated metal foam*. International Journal of Heat and Mass Transfer, 51(1516):3794 – 3802, 2008.

[89] Zhiguo Qu, Tiansong Wang, Wenquan Tao, and Tianjian Lu. *Experimental study of air natural convection on metallic foam-sintered plate*. International Journal of Heat and Fluid Flow, 38:126 – 132, 2012.

[90] H. Mahdi, P. Lopez, A. Fuentes, and R. Jones. *Thermal performance of aluminium-foam CPU heat exchangers*. International Journal of Energy Research, 30(11):851–860, 2006.

[91] Mehran Ahmadi, Golnoosh Mostafavi, and Majid Bahrami. *Natural convection from rectangular interrupted fins*. International Journal of Thermal Sciences, 82:62 – 71, 2014.

[92] L. Dialameh, M. Yaghoubi, and O. Abouali. *Natural convection from an array of horizontal rectangular thick fins with short length*. Applied Thermal Engineering, 28(1718):2371 – 2379, 2008.

[93] Mehdi Mehrtash and Ilker Tari. *A correlation for natural convection heat transfer from inclined plate-finned heat sinks*. Applied Thermal Engineering, 51(12):1067 – 1075, 2013.

[94] Ilker Tari and Mehdi Mehrtash. *Natural convection heat transfer from horizontal and slightly inclined plate-fin heat sinks*. Applied Thermal Engineering, 61(2):728 – 736, 2013.

[95] Seung-Jae Park, Daeseok Jang, and Kwan-Soo Lee. *Thermal performance improvement of a radial heat sink with a hollow cylinder for {LED} downlight applications*. International Journal of Heat and Mass Transfer, 89:1184 – 1189, 2015.

[96] Seung-Hwan Yu, Daeseok Jang, and Kwan-Soo Lee. *Effect of radiation in a radial heat sink under natural convection*. International Journal of Heat and Mass Transfer, 55(13):505 – 509, 2012.

[97] Vtor A.F. Costa and Antnio M.G. Lopes. *Improved radial heat sink for led lamp cooling*. Applied Thermal Engineering, 70(1):131 – 138, 2014.

[98] Daeseok Jang, Seung-Hwan Yu, and Kwan-Soo Lee. *Multidisciplinary optimization of a pin-fin radial heat sink for {LED} lighting applications*. International Journal of Heat and Mass Transfer, 55(4):515 – 521, 2012.

[99] Patrick J Roache. *Verification and validation in computational science and engineering*. Hermosa, 1998.

[100] Patrick J Roache, Kirti N Ghia, and Frank M White. *Editorial policy statement on the control of numerical accuracy*. Journal of Fluids Engineering, 108(1):2–2, 1986.

[101] David C Wilcox et al. *Turbulence modeling for CFD*, volume 2. DCW industries La Canada, CA, 1998.

[102] ANSYS, Inc. *Ansys Fluent Theory Guide*. 2013.

[103] M Quintard. *Transfers in porous media (keynote)*. In Proceedings of the 15th International Heat Transfer Conference, IHTC-15, August 10-15, 2014, Kyoto, Japan, page 20, 2014.

[104] F.A.L. Dullien and H. Brenner. *Porous Media: Fluid Transport and Pore Structure*. Elsevier Science, 2012.

[105] P. De Jaeger. *Thermal and Hydraulic Characterisation and Modelling of Open-Cell Aluminum Foam*. PhD thesis, Ghent University, Belgium, 2013.

[106] Roderic Lakes. *Materials with structural hierarchy*. Nature, 361(6412):511–515, 1993.

[107] E. Brun. *De l'imagérie 3D des structures a l'étude des mécanismes de transport en milieux cellulaires*. PhD thesis, Aix Marseille Université, France, 2009.

[108] John H. Cushman, Lynn S. Bennethum, and Bill X. Hu. *A primer on upscaling tools for porous media*. Adv. Water Resour., 25(812):1043 – 1067, 2002.

[109] S. Whitaker. *The method of volume averaging*, volume 13. Springer, Dordrecht, the Netherlands, 1999.

[110] Luc Tartar. *The general theory of homogenization: a personalized introduction*, volume 7. Springer Science & Business Media, 2009.

[111] K Hooman, A. Tamayol, and M.R. Malayeri. *Impact of Particulate Deposition on the Thermohydraulic Performance of Metal Foam Heat Exchangers: A Simplified Theoretical Model*. Journal of heat transfe, 134(9):092601, 2012.

[112] Indranil Ghosh. *Heat-Transfer Analysis of High Porosity Open-Cell Metal Foam*. Journal of heat transfer, 130:034501, 2007.

[113] Wen-Yea Jang, Andrew M. Kraynik, and Stelios Kyriakides. *On the microstructure of open-cell foams and its effect on elastic properties*. Int. J. Solids Struct., 45(78):1845 – 1875, 2008.

[114] Nihad Dukhan, Pablo D. Quiones-Ramos, Edmundo Cruz-Ruiz, Miguel Vlez-Reyes, and Elaine P. Scott. *One-dimensional heat transfer analysis in open-cell 10-ppi metal foam*. International Journal of Heat and Mass Transfer, 48(2526):5112 – 5120, 2005.

[115] A. Kopanidis, A. Theodorakakos, E. Gavaises, and D. Bouris. *3D numerical simulation of flow and conjugate heat transfer through a pore scale model of high porosity open cell metal foam*. International Journal of Heat and Mass Transfer, 53(1112):2539 – 2550, 2010.

[116] D. Weaire and R. Phelan. *A counter-example to Kelvin's conjecture on minimal surfaces*. Philosophical Magazine Letters, 69(2):107–110, 1994.

[117] Shankar Krishnan, Jayathi Y Murthy, and Suresh V Garimella. *Direct simulation of transport in open-cell metal foam*. Journal of heat transfer, 128(8):793–799, 2006.

[118] Nihad Dukhan and Ahmed S. Suleiman. *Simulation of Entry-Region Flow in Open-Cell Metal Foam and Experimental Validation*. Transport in Porous Media, 101(2):229–246, 2014.

[119] Shankar Krishnan, Suresh V Garimella, and Jayathi Y Murthy. *Simulation of thermal transport in open-cell metal foams: effect of periodic unit-cell structure*. Journal of Heat Transfer, 130(2):024503, 2008.

[120] V.V. Calmidi and R.L. Mahajan. *Forced convection in high porosity metal foams*. J. Heat Transfer, 122(3):557–565, 2000.

[121] Karthik K. Bodla, Jayathi Y. Murthy, and Suresh V. Garimella. *Microtomography-Based Simulation of Transport through Open-Cell Metal Foams*. Numer. Heat Transfer, Part A, 58(7):527–544, 2010.

[122] Salvatore Cunsolo, Maria Oliviero, William M. Harris, Assunta Andreozzi, Nicola Bianco, Wilson K.S. Chiu, and Vincenzo Naso. *Monte Carlo determination of radiative properties of metal foams: Comparison between idealized and real cell structures*. Int. J. Therm. Sci., 87:94 – 102, 2015.

[123] C. Veyhl, I.V. Belova, G.E. Murch, and T. Fiedler. *Finite element analysis of the mechanical properties of cellular aluminium based on micro-computed tomography*. Mat Sci Eng A-Struct, 528(1314):4550 – 4555, 2011.

[124] T. Fiedler, E. Solrzano, F. Garcia-Moreno, A. chsner, I.V. Belova, and G.E. Murch. *Computed tomography based finite element analysis of the thermal properties of cellular aluminium*. Materialwiss Werkst, 40(3):139–143, 2009.

[125] Proceedings of SPIE 4503 pp. 103-115. *Quantitative analysis of three dimensional x-ray tomographic images*, 2002.

[126] J. Ohser and K. Schladitz. *3D images of materials structures: processing and analysis*. Vch Pub, 2009.

[127] J. Vlassenbroeck, M. Direrick, B. Masschaele, V. Cnudde, L. Van Hoorebeke, and P. Jacobs. *Software tools for quantification of X-ray microtomography at the UGCT*. Nucl. Instrum. Meth. A, pages 442–445, 2007.

[128] Camille Perrot, Raymond Panneton, and Xavier Olny. *Periodic unit cell reconstruction of porous media: Application to open-cell aluminum foams*. Journal of Applied Physics, 101(11):113538, 2007.

[129] Peter De Jaeger, Christophe TJoen, Henk Huisseune, Bernd Ameel, and Michel De Paepe. *An experimentally validated and parameterized periodic unit-cell reconstruction of open-cell foams*. Journal of Applied Physics, 109(10):103519, 2011.

[130] Prashant Kumar and Frederic Topin. *Impact of anisotropy on geometrical and thermal conductivity of metallic foam structures*. Journal of Porous Media, 18(10), 2015.

[131] Sergey Kanaun and Oleksandr Tkachenko. *Effective conductive properties of open-cell foams*. International Journal of Engineering Science, 46(6):551 – 571, 2008. Special Issue: Micromechanics of Materials.

[132] P. De Jaeger, C. TJoen, H. Huisseune, B. Ameel, S. De Schampheleire, and M. De Paepe. *Assessing the influence of four cutting methods on the thermal contact resistance of open-cell aluminum foam*. International Journal of Heat and Mass Transfer, 55(2122):6142 – 6151, 2012.

[133] Shadi Mahjoob and Kambiz Vafai. *A synthesis of fluid and thermal transport models for metal foam heat exchangers*. Int. J. Heat Mass Transfer, 51(1516):3701 – 3711, 2008.

[134] Prieur Du Plessis, Agnes Montillet, Jacques Comiti, and Jack Legrand. *Pressure drop prediction for flow through high porosity metallic foams*. Chem. Eng. Sci., 49(21):3545 – 3553, 1994.

[135] J G. Fourie and J P. Du Plessis. *Pressure drop modelling in cellular metallic foams*. Chem. Eng. Sci., 57(14):2781 – 2789, 2002.

[136] V.V. Calmidi. *Transport phenomena in high porosity metal foams*. PhD thesis, University of Colorado, 1998.

[137] W.Q. Li, Z.G. Qu, Y.L. He, and W.Q. Tao. *Experimental and numerical studies on melting phase change heat transfer in open-cell metallic foams filled with paraffin*. Appl. Therm. Eng., 37:1 – 9, 2012.

[138] E. Sauret and K. Hooman. *Particle size distribution effects on preferential deposition areas in metal foam wrapped tube bundle*. Int. J. Heat Mass Transfer, 79:905 – 915, 2014.

[139] Joakim Lindblad. *Surface area estimation of digitized 3D objects using weighted local configurations*. Image and Vision Comput., 23(2):111 – 122, 2005. Discrete Geometry for Computer Imagery.

[140] Robert J. Moffat. *Describing the uncertainties in experimental results*. Exp. Therm. Fluid Sci., pages 3–17, 1998.

[141] M.S. Phanikumar and R.L. Mahajan. *Non-Darcy natural convection in high porosity metal foams*. Int. J. Heat Mass Transfer, 45(18):3781 – 3793, 2002.

[142] Jean-Philippe Bonnet, Frederic Topin, and Lounes Tadrist. *Flow Laws in Metal Foams: Compressibility and Pore Size Effects*. Transp. Porous Media, 73(2):233–254, 2008.

[143] Xiaohu Yang, Tian Jian Lu, and Tongbeum Kim. *An analytical model for permeability of isotropic porous media*. Phys. Lett. A, 378(3031):2308 – 2311, 2014.

[144] S. Brunauer, P. Emmett, and E. Teller. *Adsorption of gases in multimolecular layers*. J. Am. Chem. Soc., 60:309–319, 1938.

[145] Choondal B Sobhan and George P Peterson. *Microscale and nanoscale heat transfer: fundamentals and engineering applications*. CRC Press, Florida, U.S.A., 2008.

[146] K. Sing, D. Everett, R. Haul, L. Moscou, R. Pierotti, J. Rouquerol, and T. Siemieniewska. *IUPAC Recommendations 1984: reporting physisorption data for gas/solid systems with special reference to the determination of surface area and porosity*. Pure Appl. Chem., 57:603–619, 1985.

[147] Burhan Ozmat, Bryan Leyda, and Burton Benson. *Thermal Applications of Open-Cell Metal Foams*. Mater. Manuf. Processes, 19(5):839–862, 2004.

[148] Johann Friedrich Gülich. *Centrifugal pumps*. Springer, Berlin, Germany, 2008.

[149] A. Razani E. N. Schmierer. *Self-consistent open-celled metal foam model for thermal applications*. J. Heat Transfer, 128:1194–1203, 2006.

[150] Paola Ranut, Enrico Nobile, and Lucia Mancini. *High resolution microtomography-based {CFD} simulation of flow and heat transfer in aluminum metal foams*. Applied Thermal Engineering, 69(12):230 – 240, 2014.

[151] P. Magnico. *Analysis of permeability and effective viscosity by {CFD} on isotropic and anisotropic metallic foams*. Chemical Engineering Science, 64(16):3564 – 3575, 2009.

[152] A. Della Torre, G. Montenegro, G.R. Tabor, and M.L. Wears. *{CFD} characterization of flow regimes inside open cell foam substrates*. International Journal of Heat and Fluid Flow, 50:72 – 82, 2014.

[153] William G. Gray. *A derivation of the equations for multi-phase transport*. Chemical Engineering Science, 30(2):229 – 233, 1975.

[154] J.Alberto Ochoa-Tapia and Stephen Whitaker. *Momentum transfer at the boundary between a porous medium and a homogeneous fluidI. Theoretical development*. International Journal of Heat and Mass Transfer, 38(14):2635 – 2646, 1995.

[155] W.J. Minkowycz, A. Haji-Sheikh, and K. Vafai. *On departure from local thermal equilibrium in porous media due to a rapidly changing heat source: the Sparrow number*. Int. J. Heat Mass Transfer, 42(18):3373 – 3385, 1999.

[156] Jean-Michel Hugo and Frederic Topin. *Metal Foams Design for Heat Exchangers: Structure and Effectives Transport Properties*, volume 13 of *Advanced Structured Materials*. Springer Berlin Heidelberg, 2012.

[157] M. Kaviany. *Principles of Heat Transfer in Porous Media*. Mechanical Engineering Series, Springer, New York, second edition, 1995.

[158] M. Steven, A. Mach, F. von Issendorff, M. Altendorfner, and A. Delgado. *Numerical simulation of combustion of a low caloric gas mixture in a porous inert medium taking anisotropic dispersion into account*. In Third European Combustion Meeting ECM 2007, Chania, Crete, 11-13 April 2007, 2007.

[159] D. Koch and J. Brady. *The effective diffusivity of fibrous media*. AIChE J., 32:575 – 591, 1986.

[160] Irfan Kurtbas and Nevin Celik. *Experimental investigation of forced and mixed convection heat transfer in a foam-filled horizontal rectangular channel*. Int. J. Heat Mass Transfer, 52(56):1313 – 1325, 2009.

[161] Tzer-Ming Jeng, Sheng-Chung Tzeng, and Ying-Huei Hung. *An analytical study of local thermal equilibrium in porous heat sinks using fin theory*. Int. J. Heat Mass Transfer, 49(1112):1907 – 1914, 2006.

[162] A. Zukauskas. *Heat Transfer From Tubes in Crossflow*. Advances in heat transfer, volume 8, Academic Press, New York, 1972.

[163] A. Tamayol and K. Hooman. *Thermal assessment of forced convection through metal foam heat exchangers*. J. Heat Transfer, 133(11):111801–1 – 111801–, doi:10.1115/1.40045307, 2011.

[164] Henk Huisseune, Sven De Schampheleire, Bernd Ameel, and Michel De Paepe. *Comparison of metal foam heat exchangers to a finned heat exchanger for low Reynolds number applications*. International Journal of Heat and Mass Transfer, 89:1 – 9, 2015.

[165] Jean Michel Hugo, Emmanuel Brun, Frédéric Topin, and Jérôme Vicente. *Conjugate Heat and Mass Transfer in Metal Foams: A Numerical Study for Heat Exchangers Design*. In Diffusion in Solids and Liquids V, volume 297 of *Defect and Diffusion Forum*, pages 960–965. Trans Tech Publications, 4 2010.

[166] Xu H.J., Qu Z.G., Lu T.J., He Y.L., and Tao W.Q. *Thermal Modeling of Forced Convection in a Parallel-Plate Channel Partially Filled With Metallic Foams*. Journal of Heat Transfer, 133(9):092603, 2011.

[167] C.Y. Zhao, L.N. Dai, G.H. Tang, Z.G. Qu, and Z.Y. Li. *Numerical study of natural convection in porous media (metals) using Lattice Boltzmann Method (LBM)*. International Journal of Heat and Fluid Flow, 31(5):925 – 934, 2010. Sixth International Symposium on Turbulence, Heat and Mass Transfer, Rome, Italy, 14-18 September 2009.

[168] Djomice Beugre, Sbastien Calvo, Grard Dethier, Michel Crine, Dominique Toye, and Pierre Marchot. *Lattice Boltzmann 3D flow simulations on a metallic foam*. Journal of Computational and Applied Mathematics, 234(7):2128 – 2134, 2010. Fourth International Conference on Advanced Computational Methods in Engineering (ACOMEN 2008).

[169] VV Calmidi and RL Mahajan. *The effective thermal conductivity of high porosity fibrous metal foams*. Journal of Heat Transfer, 121(2):466–471, 1999.

[170] C.Y. Zhao, T.J. Lu, and H.P. Hodson. *Natural convection in metal foams with open cells*. International Journal of Heat and Mass Transfer, 48(12):2452 – 2463, 2005.

[171] John G. Georgiadis and I. Catton. *Dispersion in cellular thermal convection in porous layers*. International Journal of Heat and Mass Transfer, 31(5):1081 – 1091, 1988.

[172] J. W. Paek, B. H. Kang, S. Y. Kim, and J. M. Hyun. *Effective Thermal Conductivity and Permeability of Aluminum Foam Materials1*. International Journal of Thermophysics, 21(2):453–464, 2000.

[173] K. Boomsma and D. Poulikakos. *On the effective thermal conductivity of a three-dimensionally structured fluid-saturated metal foam*. International Journal of Heat and Mass Transfer, 44(4):827 – 836, 2001.

[174] Stuart W. Churchill and Humbert H.S. Chu. *Correlating equations for laminar and turbulent free convection from a vertical plate*. International Journal of Heat and Mass Transfer, 18(11):1323 – 1329, 1975.

[175] Marzio Piller and Enrico Stalio. *Numerical investigation of natural convection in inclined parallel-plate channels partly filled with metal foams*. International Journal of Heat and Mass Transfer, 55(2324):6506 – 6513, 2012.

[176] Ramvir Singh and H.S Kasana. *Computational aspects of effective thermal conductivity of highly porous metal foams*. Applied Thermal Engineering, 24(13):1841 – 1849, 2004.

[177] B Alazmi and K Vafai. *Analysis of variants within the porous media transport models*. Journal of Heat Transfer, 122(2):303–326, 2000.

[178] Yan Su, Jane H. Davidson, and Francis A. Kulacki. *A geometry factor for natural convection in open cell metal foam*. International Journal of Heat and Mass Transfer, 62:697 – 710, 2013.

[179] Robin Reynders. *Experimentele prestatiestudie van metaalschuim als koelvin bij natuurlijke convectie*, 2011. Master thesis, Ghent University, promotor prof. Michel De Paepe.

[180] Heleen Steuperaert. *Experimental study of the constraints of metal fibres as wick material in heat pipes*, 2015. Master thesis, Ghent University, promotor prof. Michel De Paepe.

[181] A. Willockx. *Using the inverse heat conduction problem and thermography for the determination of local heat transfer coefficients and fin effectiveness for longitudinal fins*. PhD thesis, Ghent university, Belgium, 2009.

[182] Anandaroop Bhattacharya and Roop L Mahajan. *Finned metal foam heat sinks for electronics cooling in forced convection*. Journal of Electronic Packaging, 124(3):155–163, 2002.

[183] Robert J Moffat, John K Eaton, and Andrew Onstad. *A method for determining the heat transfer properties of foam-fins*. Journal of Heat transfer, 131(1):011603, 2009.

[184] J.R. Taylor. *An Introduction to Error Analysis: The Study of Uncertainties in Physical Measurements*. A series of books in physics. University Science Books, 1997.

[185] K. Kadoya, N. Matsunaga, and A. Nagashima. *Viscosity and Thermal Conductivity of Dry Air in the Gaseous Phase*. Journal of Physical and Chemical Reference Data, 14(4), 1985.

[186] D. P. Sekulic, Y.M. Dakhoul, H. Zhao, and W. Liu. *Aluminum foam compact heat exchanger: brazing technology development vs. thermal performance*. In Gunter Stephani Kieback and Bernd, editors, Cellular metals for structural and functional applications (CELLMET2008), pages 5–10, Dresden, Germany, 2009. Fraunhofer Institute.

[187] Jos Fernndez-Seara, Francisco J. Uha, Jaime Sieres, and Antonio Campo. *A general review of the Wilson plot method and its modifications to determine convection coefficients in heat exchange devices*. Applied Thermal Engineering, 27(1718):2745 – 2757, 2007.

[188] R. A. Toupin. *Saint-Venant's Principle*. Archive for Rational Mechanics and Analysis, 18(2):83–96, 1965.

[189] John Wendt. *Computational fluid dynamics: an introduction*. Springer Science & Business Media, 2008.

[190] Denpong Soodphakdee, Masud Behnia, and David Watabe Copeland. *A Comparison of Fin Geometries for Heatsinks in Laminar Forced ConvectionPart I: Round, Elliptical, and Plate Fins in Staggered and In-Line Configurations*. Int. J. Microcircuits Electron. Packag, 24(1):68–76, 2001.

[191] Sven De Schampheleire, Kathleen De Kerpel, Peter De Jaeger, Henk Huisseune, Bernd Ameel, and Michel De Paepe. *Buoyancy driven convection in open-cell metal foam using the volume averaging theory*. Applied Thermal Engineering, 79:225 – 233, 2015.

[192] Nicos S. Martys. *Improved approximation of the Brinkman equation using a lattice Boltzmann method*. Physics of Fluids, 13(6), 2001.

[193] Aydin Nabovati and Cristina H. Amon. *Hydrodynamic Boundary Condition at Open-Porous Interface: A Pore-Level Lattice Boltzmann Study*. Transport in Porous Media, 96(1):83–95, 2013.

[194] Sven De Schampheleire, Peter De Jaeger, Kathleen De Kerpel, Bernd Ameel, Henk Huisseune, and Michel De Paepe. *How to Study Thermal Applications of Open-Cell Metal Foam: Experiments and Computational Fluid Dynamics*. Materials, 9(2):94, 2016.

[195] M. Quintard, M. Kaviany, and S. Whitaker. *Advances in Heat Transfer in Porous Media Two-medium treatment of heat transfer in porous media: numerical results for effective properties*. Advances in Water Resources, 20(2):77 – 94, 1997.

[196] P. De Jaeger. *Thermal and Hydraulic Characterisation and Modelling of Open-Cell Aluminum Foam*. PhD thesis, Ghent university, Belgium, 2012.

[197] ASM International. *ASM Ready Reference - Thermal properties of metals*. Accessed on August 3 2016, through http://www.asminternational.org/documents/10192/3449989/ACFAAB7.pdf/279ed959-4984-4914-a942-097876e3a6b3.

[198] The National Institute of Standards and Technology (NIST). *NIST Standard Reference Database 23 (NIST Reference Fluid Thermodynamic and Transport Properties Database (REFPROP): version 9.0, 2012*, 2012. Standard Reference Data Program, Gaithersburg, United States of America.

[199] Indranil Ghosh. *Heat transfer correlation for high-porosity open-cell foam*. International Journal of Heat and Mass Transfer, 52(56):1488 – 1494, 2009.

[200] C.Y. Zhao, S.A. Tassou, and T.J. Lu. *Analytical considerations of thermal radiation in cellular metal foams with open cells*. International Journal of Heat and Mass Transfer, 51(34):929 – 940, 2008.

[201] Nihad Dukhan and Carel A. Minjeur. *A two-permeability approach for assessing flow properties in metal foam*. Journal of Porous Materials, 18(4):417–424, 2011.

[202] *Pore-scale derivation of the Ergun equation to enhance its adaptability and generalization*. Chemical Engineering Science, 63(9):2576 – 2586, 2008.

[203] Sven De Schampheleire, Peter De Jaeger, Henk Huisseune, Bernd Ameel, Christophe T'Joen, Kathleen De Kerpel, and Michel De Paepe. *Thermal hydraulic performance of 10 PPI aluminium foam as alternative for louvered fins in an HVAC heat exchanger*. Applied Thermal Engineering, 51(12):371 – 382, 2013.

[204] D Seguin, A Montillet, and J Comiti. *Experimental characterisation of flow regimes in various porous mediaI: Limit of laminar flow regime*. Chemical Engineering Science, 53(21):3751 – 3761, 1998.

[205] D Seguin, A Montillet, J Comiti, and F Huet. *Experimental characterization of flow regimes in various porous mediaII: Transition to turbulent regime*. Chemical Engineering Science, 53(22):3897 – 3909, 1998.

[206] Stephen Whitaker. *The Forchheimer equation: A theoretical development*. Transport in Porous Media, 25(1):27–61, 1996.

[207] Adrian E Scheidegger. *The Physics of Flow Through Porous Media.* Soil Science, 86(6):355, 1958.

[208] Stephen Childress. *An Introduction to Theoretical Fluid Dynamics*. 2008.

[209] M. D. M. Innocentini, L. P. Lefebvre, R. V. Meloni, and E. Baril. *Influence of sample thickness and measurement set-up on the experimental evaluation of permeability of metallic foams*. Journal of Porous Materials, 17(4):491–499, 2010.

[210] Murilo DM Innocentini, Vania R Salvini, Victor C Pandolfelli, and José R Coury. *Assessment of Forchheimer's equation to predict the permeability of ceramic foams*. Journal of the American Ceramic Society, 82(7):1945–1948, 1999.

[211] Nihad Dukhan and Mohamed Ali. *Strong wall and transverse size effects on pressure drop of flow through open-cell metal foam*. International Journal of Thermal Sciences, 57:85 – 91, 2012.

[212] Nihad Dukhan and Krunal Patel. *Effect of sample's length on flow properties of open-cell metal foam and pressure-drop correlations*. Journal of Porous Materials, 18(6):655–665, 2011.

[213] Sven De Schampheleire, Kathleen De Kerpel, Bernd Ameel, Peter De Jaeger, Ozer Bagci, and Michel De Paepe. *A Discussion on the Interpretation of the Darcy Equation in Case of Open-Cell Metal Foam Based on Numerical Simulations*. Materials, 9(6):409, 2016.